DISSERTATION

DEFECT TOLERANCE, ANHARMONICITY, AND ORGANIC-INORGANIC COUPLING IN HYBRID ORGANIC-INORGANIC SEMICONDUCTORS

Submitted by

Annalise E. Maughan

Department of Chemistry

In partial fulfillment of the requirements

For the Degree of Doctor of Philosophy

Colorado State University

Fort Collins, Colorado

Fall 2018

Doctoral Committee:

Advisor: James R. Neilson

Amy L. Prieto
Melissa M. Reynolds
James R. Sites

ABSTRACT

DEFECT TOLERANCE, ANHARMONICITY, AND ORGANIC-INORGANIC COUPLING IN HYBRID ORGANIC-INORGANIC SEMICONDUCTORS

Implementing and improving sustainable energy technologies is predicated upon the discovery and design of new semiconducting materials. Perovskite halides represent a paradigm shift in solar photovoltaic technologies, as devices utilizing perovskites as the active semiconductor can achieve power conversion efficiencies rivaling those of commercial solar cells after less than a decade of dedicated research. In contrast to conventional semiconductors, perovskites are unique in that they exhibit excellent photovoltaic performance despite the presence of significant materials disorder. This disorder manifests as (1) a large concentration of crystallographic defects introduced by low-temperature processing, and (2) as dynamic disorder due to the deformable metal-halide framework and the presence of dynamic organic species within the crystalline voids. Vacancy ordered double perovskites of the general formula A_2BX_6 are a defect-ordered variant of the archetypal perovskite structure comprised of isolated $[BX_6]$ octahedral units bridged by cationic species at the A-site. The presence of ordered vacancies and relatively decoupled octahedral units presents an ideal system to investigate defects and lattice dynamics as they pertain to optical and electronic properties of perovskite halide semiconductors.

This work aims to illuminate the fundamental structure-dynamics-property relationships in vacancy-ordered double perovskite and hybrid organic-inorganic semiconductors through a combination of advanced structural characterization, optical and electrical measurements, and insight from computation.

We begin with a study of the $Cs_2Sn_{1-x}Te_xI_6$ series of vacancy-ordered double perovskites to inform the chemical and bonding characteristics that impact defect chemistry in vacancy-ordered double perovskites. While the electronic properties of Cs_2SnI_6 are tolerant to the pres-

ence of crystallographic defects, introducing tellurium at the *B*-site yields an electronic structure that renders Cs_2TeI_6 defect-intolerant, indicating the importance of the *B*-site chemistry in dictating the optoelectronic properties in these materials.

Next, we elucidate the interplay of the *A*-site cation with the octahedral framework and the subsequent influence upon lattice dynamics and optoelectronic properties of several tin-iodide based vacancy-ordered double perovskites. The coordination and bonding preferences of the *A*-site drive the structural and dynamic behavior of the surrounding octahedra and in turn dictate charge transport. *A*-site cations that are too small produce structures with cooperative octahedral tilting, while organic-inorganic coupling via hydrogen bonding yields soft, anharmonic lattice dynamics characterized by random octahedral rotations. Both regimes yield stronger electron-phonon coupling interactions that inhibit charge transport relative to undistorted analogs.

The final study presented here details the discovery of two hybrid organic-inorganic semiconductors containing the organic tropylium cation within tin- and lead-iodide frameworks. In $C_7H_7PbI_3$, the tropylium electronic states couple to those of the lead iodide framework through organic-inorganic charge transfer. Electronic coupling between the organic and inorganic sublattices within a singular material provides an avenue to elicit unique optical and electronic properties unavailable to either components individually.

The above work is then placed in context of other recent studies of vacancy-ordered double perovskite semiconductors, and a set of design principles are constructed. Future avenues of research are proposed. These structure-dynamics-property relationships represent an important step towards rational design of vacancy-ordered double perovskite semiconductors for potential optoelectronic applications.

ACKNOWLEDGEMENTS

Words do not seem adequate to describe the gratitude I feel for the mentorship, friendship, and support I have received during my doctoral journey. I will try my best here, knowing that it will never be sufficient to convey the depth of my appreciation.

I would first like to thank my advisor, Jamie Neilson. Over the years, Jamie's steadfast patience, never-ending encouragement, and seemingly boundless positivity – particularly during the myriad frustrations associated with research and graduate school – has been instrumental in my development as a scientist. Thank you for pushing me to question everything and to never take anything for granted. Finally, thank you for reminding me that life is too short for boring socks.

I am grateful to have worked with an incredible group of people throughout my time in the Neilson lab. Thank you for the overwhelmingly positive and constructive work environment. It wouldn't have been as enjoyable without you. I would also like to thank my undergraduate colleagues Mitchell, Juliette, Mohammed, Andrew, and Alex, without whom much of this work would not have been possible. You're all doing a great job.

I would like to specifically thank Dr. Alex Ganose and Dr. David Scanlon, whose expertise in computational chemistry and contributions therein were crucial to the success and impact of this work. It has been an absolute pleasure collaborating with you both.

I am grateful for the incredible friendships that have buoyed me throughout graduate school. Kim, your friendship is a constant in times of turbulence and uncertainty, despite the many miles between us. I can always count on you to laugh out loud at my less-than-funny jokes, and I am truly grateful for you. To the numerous friends I've made throughout my time here at CSU: Thank you for baking nights, rock climbing, yoga, card games, jogging, brunch, laser tag, biking, Pizza Casbah, knitting parties, hiking, movie nights, pool parties, and so much more. But most of all, thank you for your friendship.

To my parents: Thank you, endlessly. Thank you for instilling in me the value of hard work and encouraging me to never settle for less than my absolute best. Thank you for teaching me humility in success and perseverance through difficulty. Momma, thank you for always being a shoulder to lean on and an ear to bend. Dad, thank you for pushing me to ask the hard questions and to dig for answers beneath the surface. You are both more wonderful and supportive beyond anything I could have ever asked for. Thank you both for always believing in me. I would not be who I am or where I am today without you both.

To Kyle: Thank you for being an awesome (little!) brother. Thank you for always making me laugh and for being there for me. You're the best.

I am forever grateful for the never-ending support I have received from my extended and chosen families. Thank you for always being there for me and believing in me.

Finally, to my husband Weston: Thank you. I would not be who or where I am without your unwavering love and support. Thank you for challenging me to be the best version of myself, as a scientist and otherwise. Thank you for skiing and boarding adventures, spirited discussions about science, Saturday morning homemade lattes, and late-night games. You are my rock and my best friend, and there is no one with whom I would rather share the twists, turns, and loop-de-loops of life. I love you, forever and ever.

TABLE OF CONTENTS

ABSTRACT ii
ACKNOWLEDGEMENTS iv
LIST OF FIGURES viii

Chapter 1 Introduction 1
1.0.1 Perovskite Halides for Emerging Photovoltaics 1
1.0.2 Defect Tolerance 4
1.0.3 Lattice Dynamics and Electron-Phonon Coupling 7
1.0.4 Vacancy-Ordered Double Perovskites 10
1.0.5 Hybrid Organic-Inorganic Materials 13
1.0.6 Summary of Dissertation 16

Chapter 2 Defect Tolerance to Intolerance in the Vacancy-Ordered Double Perovskite Semiconductors Cs_2SnI_6 and Cs_2TeI_6 20
2.1 Introduction 20
2.2 Methods and Materials 23
2.3 Results and Discussion 28
2.3.1 Electronic Properties 28
2.3.2 Crystal Structures 29
2.3.3 Optical Spectroscopy and Electronic States 36
2.3.4 Intrinsic Defects 44
2.4 Conclusions 48

Chapter 3 Anharmonicity and Octahedral Tilting in Hybrid Vacancy-Ordered Double Perovskites 49
3.1 Introduction 49
3.2 Methods and Materials 52
3.3 Results and Discussion 57
3.4 Conclusions 73

Chapter 4 Tolerance Factor and Cooperative Tilting Effects in Vacancy-Ordered Double Perovskite Halides 74
4.1 Introduction 74
4.2 Methods and Materials 77
4.3 Results 81
4.3.1 Structural Characterization 81
4.3.2 Electronic and Optical Properties 85
4.3.3 Local Coordination Environment 86
4.3.4 Electronic Structure Calculations 89
4.4 Discussion 95
4.5 Conclusions 98

Chapter 5 Bond Valences and Anharmonicity in Vacancy-Ordered Double Perovskite Halides . . . 100
5.1 Introduction . . . 100
5.2 Methods and Materials . . . 103
5.3 Results . . . 105
5.4 Discussion . . . 115
5.5 Conclusion . . . 118

Chapter 6 Hybrid Inorganic–Organic Materials with an Optoelectronically-Active Aromatic Cation:$(C_7H_7)_2SnI_6$ and $C_7H_7PbI_3$ . . . 119
6.1 Introduction . . . 119
6.2 Methods and Materials . . . 122
6.3 Results and Discussion . . . 125
6.3.1 FT-IR and ^{1}H NMR Studies . . . 126
6.3.2 The crystal structures of tropylium tin iodide, $(C_7H_7)_2SnI_6$, and tropylium lead iodide, $C_7H_7PbI_3$ . . . 128
6.3.3 Optical Properties and Electronic Structures . . . 135
6.4 Conclusions . . . 139

Chapter 7 Perspectives and Design Principles of Vacancy-Ordered Double Perovskite Semiconductors . . . 141
7.1 Introduction . . . 141
7.2 Optical Gap and Band Alignment . . . 141
7.3 Electronic Dispersion and Charge Transport . . . 149
7.4 Defect Chemistry . . . 153
7.5 Mixed Valence . . . 155
7.6 Lattice Dynamics and Electron-Phonon Coupling . . . 157
7.7 Concluding Remarks . . . 160
7.8 Outlook and Future Directions . . . 161
Bibliography . . . 164

Appendix A Analysis of Total Scattering Data . . . 203

Appendix B Rigid-Body Modeling of Anharmonicity in Hybrid Vacancy-Ordered Double Perovskites . . . 208

LIST OF FIGURES

1.1 Crystal structure comparison of diamond-like semiconductors with the general perovskite structure. In (a), structural representations of the diamond-like semiconductors silicon (Si), cadmium telluride (CdTe), and gallium arsenide (GaAs) are shown. The unit cell representation of the general cubic perovskite structure of the general formula ABX_3 is shown in (b); *A*-site cations are shown in purple, *B*-site cations are shown in teal, and *X*-site anions are shown as orange spheres. 2

1.2 Crystal structure of the perovskite methylammonium lead iodide ($CH_3NH_3PbI_3$). The zoom region is shown to highlight the dynamic nature of the methylammonium cation within the cuboctahedral void. Lead atoms are grey, iodine atoms are purple, carbon atoms are brown, nitrogen atoms are light blue, and hydrogen atoms are beige. 3

1.3 A simplified energy band diagram of a semiconductor. The valence and conduction bands are denoted by the blue and orange slabs, respectively. Electrons are shown as magenta circles, and holes are represented by black open circles. Dotted lines represent localized energy states introduced by defects. E_{gap} is the band gap, and $k_B T$ is the product of the Boltzmann constant and temperature. 5

1.4 Experimental realization of defect tolerance in $CH_3NH_3PbI_3$. The energy difference between the Fermi level and valence band maximum (ΔE_v) determined by X-ray photoelectron spectroscopy is plotted as a function of I:Pb stoichiometric ratio. Figure reproduced with permission from Steirer, Schulz, Teeter, Stevanovic, Yang, Zhu, Berry, *ACS Energy Lett.*, **2016**, *1*, 360–366.[1] Copyright 2016 American Chemical Society. 6

1.5 A schematic of the relationship between the archetypal perovskite (ABX_3) and vacancy-ordered double perovskite (A_2BX_6) structures. 10

1.6 Crystal structures of Cs_2TeI_6, Rb_2TeI_6, and K_2TeI_6 as representative examples of common octahedral tilting motifs observed in the vacancy-ordered double perovskite family. 11

1.7 Classification of hybrid organic-inorganic materials based upon the dimensionality of the inorganic polyhedral connectivity and the metal-organic-metal connectivity. The first row (purple text) denotes hybrid materials with varying degrees of inorganic connectivity with non-coordinating organic moieties. Figure adapted with permission from Rao, Cheetham, Thirumurugan, *J. Phys.: Condens. Matter*, **2008**, *20*, 083202.[2] Copyright 2008 IOPScience. 14

2.1 (a) Crystal structure of the vacancy-ordered double perovskites, Cs_2SnI_6 and Cs_2TeI_6. (b) Reorientation of the unit cell reveals the isolated octahedral units. Panel (c) illustrates the cubic close-packed iodine sublattice, and panel (d) shows how the cubic close-packed iodine sublattice is decorated with Sn atoms to yield the isolated octahedral units. Teal spheres are cesium, grey are tin/tellurium, and purple are iodine. . 21

2.2 (a) The temperature dependence of the electrical resistivity for the solid solution $Cs_2Sn_{1-x}Te_xI_6$. The data for Cs_2SnI_6 (black circles) indicate semiconducting behavior, as described by variable range hopping conductivity from T = 130–300 K (orange line). Temperature-dependent curves are also shown for x = 0.05 (purple squares) and x = 0.1 (green triangles). (b) The room-temperature resistivity for x = 0, 0.05, 0.1, and x = 0.25 in $Cs_2Sn_{1-x}Te_xI_6$. The x = 0.5, 0.75, 0.9, and x = 1 samples were too resistive for accurate measurements. (c) The carrier concentration, n_e (filled teal triangles), and carrier mobility, μ_e (open pink diamonds), for x = 0, 0.05 and x = 0.1 are reduced upon Te substitution, as determined by Hall voltage measurements. Error bars denote the propagation of uncertainty from the sample dimensions for all samples, except for x = 0.05 which denotes the standard deviation of 3 transport specimens. 29
2.3 Rietveld refinements of high-resolution time-of-flight neutron scattering data of (a,c) Cs_2SnI_6 and (b,d) Cs_2TeI_6 collected from wavelength frame 2 on the POWGEN diffractometer at the Spallation Neutron Source, Oak Ridge National Laboratory. Data collected at T = 300 K are shown in panels (a) and (b) and data collected at T = 10 K are shown in panels (c) and (d). Refinements were performed using data collected from wavelength frames 2 and 4 of the POWGEN diffractometer. Black circles are the data, the orange line is the fit, and the blue line is the difference. The pink tick marks indicate the location of predicted Bragg reflections for the cubic structure. 30
2.4 Rietveld refinements of high-resolution time-of-flight neutron scattering data of (a,c) Cs_2SnI_6 and (b,d) Cs_2TeI_6 collected from wavelength frame 4 of the POWGEN diffractometer at the Spallation Neutron Source, Oak Ridge National Laboratory. Data collected at T = 300 K are shown in panels (a) and (b) and data collected at T = 10 K are shown in (c) and (d). The structural models were refined jointly against data from wavelength frames 2 and 4. Black circles are the data, the orange line is the fit, and the blue line is the difference. The pink tick marks indicate the location of predicted Bragg reflections for the cubic structure. 31
2.5 Heat capacity data of Cs_2SnI_6 (a,b) and Cs_2TeI_6 (c,d). The data are shown as filled black circles for Cs_2SnI_6 and open black squares for Cs_2TeI_6. The orange line is the total fit to the sum of the Debye and Einstein models of the heat capacity, and the separate contributions from each model are shown in pink dotted (Debye) and teal dashed (Einstein) lines. In (c) and (d) the data are shown at C_p/T^3 to highlight the deviation of the Debye model from the data at low temperatures. 32
2.6 (a) High-resolution synchrotron X-ray diffraction data (11-BM) and Rietveld refinements of the solid solution series $Cs_2Sn_{1-x}Te_xI_6$ collected at room temperature (black circles represent data, colored lines represent the fit, and blue lines are difference curves). (b) The strongest reflection, {222} at Q = 1.87 Å^{-1} shifts to lower Q with increasing tellurium substitution. 32

2.7 Crystal structure parameters across the solid solution series, $Cs_2Sn_{1-x}Te_xI_6$, as determined from high-resolution synchrotron X-ray diffraction at room temperature. (a) The refined lattice parameters are plotted as a function of nominal x in $Cs_2Sn_{1-x}Te_xI_6$. The dashed line represents Vegard's law interpolated from the end members. (b) The average polyhedral volumes of the BI$_6$ octahedra and $\square$I$_6$ void regions show that the voids become smaller as the [BI$_6$] octahedra become larger. (c) The average B–I bond distances and I–I contact distances along the ⟨110⟩ directions in the unit cell reflect the trend shown in (b). Dashed lines in (b) and (c) are linear regressions. 33
2.8 Synchrotron X-ray pair distribution function analysis of all compounds in the solid solution series from data collected at room temperature. The XPDF data for all compounds can be constructed by a linear combination of the XPDF data for the end members (*i.e.*, XPDF = (1–x)XPDF$_{Sn}$ + (x)XPDF$_{Te}$. The data are shown as solid colored lines, and the computed linear combinations for each member are overlain as a black dotted line. The difference between the data and the linear combinations are shown as blue lines. The difference curve shown below x = 1 (green line) is the difference between end-members and illustrates the apparent shift in bond lengths across the solid solution. Note the split x-axis to highlight the nearest-neighbor (B–I) and next-nearest-neighbor (I–I) pair correlations. 34
2.9 Charge density isosurfaces of the occupied ns^2 states in Cs_2SnI_6 and Cs_2TeI_6. Sn, Te, and I atoms are denoted by grey, gold, and purple spheres, respectively. Contours shown from 0 (blue) to 0.002 eV Å^{-3} and 0.0034 eV Å^{-3} (red) for Cs_2SnI_6 and Cs_2TeI_6, respectively. 35
2.10 Optical gaps of the solid solution series determined from UV-visible diffuse reflectance data. The optical gaps (shown as yellow circles) are determined by converting the reflectance data to absorbance, fitting linear functions to the baseline and onset regions of the data, and determining the intersection. The blue bars represent a range of values for optical gaps determined by extracting the data by various methods and are shown to highlight the ambiguity in determining the value of the optical gap by diffuse reflectance spectroscopy. The red square represents the magnitude of the DFT-calculated optical gap arising from the dipole-allowed transition below the valence band maximum (See Figure 2.13). 37
2.11 Room-temperature photoluminescence (PL) measurements of (a) Cs_2SnI_6 and (b) Cs_2TeI_6. 37
2.12 Band structures, including orbital projection analysis, of (a) Cs_2SnI_6 and (b) Cs_2TeI_6, showing the contributions of: the I p states in red, the B 5s states in blue, and the B 5p states in green. 38
2.13 Band structure of Cs_2SnI_6 depicting the fundamental band gap at Γ. The bands resulting in the fundamental allowed optical band gap are indicated in green. The valence band maximum is set to 0 eV. 39
2.14 Crystal orbital Hamilton population (COHP) analysis of (a) Cs_2SnI_6 and (b) Cs_2TeI_6, in which the density of states is partitioned for Sn–I and Te–I interactions, with the sign indicating bonding or anti-bonding character, and the magnitude related to the strength of the interaction. The valence band maximum is set to 0 eV. 40

2.15 Comparison of DFT-calculated band alignments for Cs_2SnI_6 and Cs_2TeI_6 (HSE06 + SOC) to experimentally-determined band alignments. The experimental valence band maximum position of Cs_2SnI_6 was determined by XPS and the conduction band minimum was positioned 0.97 eV above (HSE06 + SOC band gap). The experimental values are shown for $CsSnI_3$,[3] $MASnI_3$,[4] and $MAPbI_3$[5] (where MA = $CH_3NH_3^+$). 41
2.16 Fundamental band gaps calculated using HSE06+SOC for several members of the solid solution. The calculated dipole-allowed optical transition for Cs_2SnI_6 is shown as a red square for reference. 42
2.17 X-ray photoelectron spectroscopy data for Cs_2SnI_6. (a) The work function is extrapolated from the secondary electron cutoff. (b) The DOS convoluted with a 350 meV Gaussian allows interpolation of the XPS data to yield the valence band maximum with respect to Fermi level. 43
2.18 Illustration of the accessible chemical potential ranges of (a) Cs_2SnI_6 and (b) Cs_2TeI_6. Constraints imposed by the formation of competing binary and ternary compounds result in the stable region indicated in orange. 45
2.19 Formation energies for iodine vacancies in Cs_2SnI_6 (teal) and Cs_2TeI_6 (orange), under tin-poor conditions (point C in Figure 2.18). Sloped lines indicate the +1 charge state, and the solid dots represent the transitions levels $\epsilon(q/q')$. The dashed lines represent the fundamental band gap of each material. 46

3.1 Laboratory powder X-ray diffraction patterns and Rietveld refinements showing phase purity of the A_2SnI_6 series, where $A = Cs^+$, $CH_3NH_3^+$ (methylammonium), and $CH(NH_2)_2^+$ (formamidinium). Data are shown as black circles, the fit is the colored line, and difference curves are shown as grey lines. 58
3.2 Structures of Cs_2SnI_6, $(CH_3NH_3)_2SnI_6$, and $(CH(NH_2)_2)_2SnI_6$ showing the isolated octahedral units. Tin atoms are shown in blue, iodine are purple, cesium are yellow, carbon are brown, nitrogen are light blue, and hydrogen are eggshell. The structures are shown with random orientations of the methylammonium and formamidinium cations. 59
3.3 Electrical resistivity as a function of temperature for each member of the A_2SnI_6 series. Data were collected on cold-pressed polycrystalline pellets using a 4-wire configuration with Au paste for $A = Cs^+$ and $CH_3NH_3^+$ and Ag paste for $CH(NH_2)_2^+$. 60
3.4 Carrier concentrations (blue squares) and carrier mobilities (orange circles) for the A_2SnI_6 series determined by Hall effect measurements. The dotted lines are shown as a guide to the eye. 61
3.5 UV-visible diffuse reflectance spectra collected for the A_2SnI_6 series. The data were converted to pseudo-absorbance, F(R), by the Kubelka-Munk function, and the absorption onsets determined by extrapolating the linear onset region to zero absorbance. The transformed data are shown as colored lines and the fits the the linear regions are shown as black lines. Zero absorbance is demarcated by the dashed grey line. . . 62
3.6 Band structures calculated using HSE06+SOC for cesium tin(IV) iodide, methylammonium tin(IV) iodide, and formamidinium tin(IV) iodide. The valence band maximum is set to 0 eV in all cases. 63

3.7 Band structure calculations of the cubic vacancy-ordered double perovskite structure of Cs_2SnI_6 in which both the Cs and Sn cations are removed, the Sn cations are removed, and Cs_2SnI_6. The structures used in the calculations are shown above. The states at the bottom of the conduction band are colored pink for clarity. 64
3.8 Experimental mobility, μ_e plotted as a function of band effective mass, m_e^{*-1}. Fits to the data for m_e^{*-1} (pink solid line), m_e^{*-2} (orange dotted line), and $m_e^{*-5/2}$ (blue dashed line). 66
3.9 X-ray pair distribution function analysis of cesium tin(IV) iodide, methylammonium tin(IV) iodide, and formamidinium tin(IV) iodide. The data were modeled with the cubic structural models determined by powder X-ray diffraction, with fit ranges of $2 \leq r \leq 5.5$ Å (left panels) and $5.5 \leq r \leq 30$ Å (right panels). The data are shown as black circles, the fit is the colored line, and the difference is the grey line. 67
3.10 Supercells for a) Cs_2SnI_6, b) $(CH_3NH_3)_2SnI_6$, and c) $(CH(NH_2)_2)_2SnI_6$ with the corresponding θ_{max} determined by the pseudo-rigid-body modeling routine. 69
3.11 X-ray pair distribution function analysis of cesium tin(IV) iodide, methylammonium tin(IV) iodide, and formamidinium tin(IV) iodide with fits from the tilted models shown in Figure B.2. In the left panels, the data are fit from $2 \leq r \leq 5.5$ Å, while the right panels show the fits from $5.5 \leq r \leq 30$ Å. Black circles are the data, colored lines are the fit, and grey lines are the difference curve.[6] 69
3.12 Comparison of powder X-ray diffraction data convolved with a Gaussian to diffraction patterns ($I(Q)$) calculated from $G(r)$ of the tilted supercells. Black lines are the convolved data, while colored lines represent the calculated $I(Q)$ for each compound in the A_2SnI_6 series. 70
3.13 Mean-force potentials calculated from the structural models with tilted octahedra shown in Figure B.2. The intra-octahedral I–I potentials are shown as the grey dashed line, while the inter-octahedral I–I potentials are shown as solid colored lines. 72

4.1 Crystal structures of Rb_2SnI_6 at $T = 295$ K and $T = 100$ K. In (a) and (c), the structures are projected down the c-axis to highlight the octahedral tilting and rotation, while unit cell descriptions are shown in b) and d). Rubidium atoms are shown in pink, tin atoms in blue, and iodine atoms are shown in purple. 82
4.2 Rietveld refinements of the tetragonal and monoclinic structural models of Rb_2SnI_6 against high resolution synchrotron powder X-ray diffraction patterns collected at $T = 295$ K (a,b) and $T = 100$ K (c,d) on the high-resolution 11-BM diffractometer. Data are shown as black circles, the fit is the orange line, and the difference is shown in blue. Plots b) and d) highlight the splitting of the most intense reflection (202) at $Q \sim 1.9$ Å^{-1} upon cooling through the phase transition. 83
4.3 Neutron diffraction data of Rb_2SnI_6 collected upon cooling on the 31° bank of the NOMAD instrument. In a), the data are shown from $Q = 1.5$–4.0 Å^{-1}. In panel b), the data are shown over shorter Q-ranges ($Q = 1.75$–2.5 Å^{-1}) to highlight the most intense reflections in the diffraction pattern. The white horizontal line at $T = 189$ K denotes the estimated phase transition temperature of Rb_2SnI_6. 84
4.4 Monoclinic β angle plotted as a function of temperature extracted from sequential Rietveld refinements of the $P2_1/n$ structural model of Rb_2SnI_6 against neutron diffraction data collected on the NOMAD instrument. 85

4.5 Temperature-dependent resistivity data of rubidium tin(IV) iodide collected using a 4-probe configuration with Pt wires and Ag paste. 86
4.6 UV-visible diffuse reflectance spectrum for Rb_2SnI_6. The data were converted to pseudo-absorbance via the Kubelka-Munk transform and the optical gap was determined by extrapolating the onset region to zero absorbance, as shown by the black fit. The pink line is the transformed data, the fit is the black line, and zero absorbance is shown as the grey dashed line. The intersection point of the fit and zero absorbance is shown by the black dot. 87
4.7 The X-ray pair distribution function of Rb_2SnI_6 fit to the a) tetragonal ($P4/mnc$) and b) monoclinic ($P2_1/n$) structural models. In a), the XPDF is fit to the tetragonal ($P4/mnc$) model using anisotropic atomic displacement parameters for iodine and rubidium ions, and in b) the XPDF is fit to the monoclinic ($P2_1/n$) structural model using isotropic displacement parameters for all atoms. The thermal ellipsoids in the corresponding structural models are shown at 95% probability. 88
4.8 a) Temperature-dependent neutron pair distribution function analysis (nPDF) of Cs_2SnI_6 extracted from neutron total scattering collected on NOMAD. The x-axis is split to highlight the low-r pair correlations. Rietveld refinements of the corresponding neutron diffraction patterns collected from bank 2 (31° bank) of NOMAD are shown in b). Both the nPDF and neutron diffraction data are modeled by the cubic ($Fm\bar{3}m$) structural model at all temperatures. Black circles are the data, the orange lines are the fits, and the blue lines are difference curves. In b), the grey tick marks indicate the positions of predicted reflections from the $Fm\bar{3}m$ structure. 89
4.9 a) Temperature-dependent neutron pair distribution function analysis (nPDF) of Rb_2SnI_6 extracted from neutron total scattering collected on NOMAD. The nPDFs are best modeled by the monoclinic ($P2_1/n$) structure at all temperatures. The x-axis is split to highlight the low-r pair correlations, and the data are offset vertically for clarity. Rietveld refinements of the neutron diffraction data from bank 2 (31° bank) of NOMAD are shown in b). For $T > 150$ K, the data are modeled with the tetragonal ($P4/mnc$) structure. For $T \leq 150$ K, the data are modeled by the monoclinic ($P2_1/n$) structure. Black circles are the data, the orange lines are the fits, and the blue lines are difference curves. In b), the grey tick marks indicate the positions of predicted reflections from the $P4/mnc$ and $P2_1/n$ structures. The x-axis is split to highlight the lower-Q reflections, and the data are offset vertically for clarity. 90
4.10 Band structures calculated using HSE06+SOC for the a) $P4/mnc$ and b) $P2_1/n$ phases of Rb_2SnI_6. The color of the band indicates the orbital contribution to that band, with Sn 5s, Sn 5p, and I 5p represented by red, green and blue, respectively. The resulting color of the bands is obtained by mixing each color in proportion to the orbital contributions. The valence band maximum is set to 0 eV in all cases. 91
4.11 Calculated band alignment (HSE06+SOC) of the $P4/mnc$ and $P2_1/n$ structured phases of Rb_2SnI_6 relative to those of Cs_2SnI_6. 92

4.12 The phonon band structure of rubidium tin(IV) iodide in the tetragonal $P4/mnc$ structure ($a^0a^0c^+$). The lowest-frequency optic mode at 0.25 THz (1.03 meV, 8.27 cm^{-1}) (denoted by the orange circle) corresponds to displacements of the rubidium and iodine atoms, as shown by the displacement vectors in the structural representations. Together, these displacements map to the octahedral tilting out of the *ab* plane coupled with Rb^+ displacements observed in the lower-symmetry monoclinic structure, ($a^-a^-c^+$). 95
4.13 Experimentally- ($\mu_{e,\text{expt.}}$) and computationally-derived Hellwarth (μ_e^H) electron mobilities of the A_2SnI_6 vacancy-ordered double perovskites plotted as a function of perovskite tolerance factor. Experimental electron mobilities are shown as filled purple circles on the left axis, while the calculated Hellwarth electron mobilities are denoted by open orange squares on the right axis. Values for the carrier mobilities of Cs_2SnI_6, $(CH_3NH_3)_2SnI_6$, and $(CH(NH_2)_2)_2SnI_6$ are taken from a previous study.[6] For Rb_2SnI_6, the μ_e^H value is calculated from the tetragonal structure. 98

5.1 Unit cell representation of the cubic vacancy-ordered double perovskite structure. *A*-site cations are shown in teal, *B*-site cations are shown in blue, and *X*-site anions are shown in purple. Panels (a) and (c) highlight the isolated BX_6 octahedral units. In (b) and (d), the grey, transparent octahedra represent the ordered vacancies, denoted as $\square X_6$. 102
5.2 (a) X-ray pair distribution functions of the solid solution $Cs_2Sn_{1-x}Te_xI_6$ modeled with the cubic vacancy-ordered double perovskite structure with isotropic, harmonic atomic displacement parameters. The data are shown as black circles, the fits are colored lines, and the difference is shown in grey. The *x*-axis is split to highlight the low-*r* pair correlations, particularly the asymmetry of the next-nearest neighbor pair correlation at $r \sim 4.1$ Å. The R_{wp} for each fit is shown in (b). 107
5.3 Structural parameters for the $Cs_2Sn_{1-x}Te_xI_6$ solid solution from refinement of the cubic structural models against high-resolution synchrotron powder X-ray diffraction (SXRD) data (filled symbols) and X-ray pair distribution function analysis (open symbols). In (a), the lattice parameters for each member of the solid solution follow Vegard's law. In (b), the average *B*–I bond lengths increase linearly with substitution of the larger tellurium ion at the expense of the interoctahedral I–I contact distance along the ⟨110⟩ direction shown in (c). In (d), the average Cs–I bond length increases. The dashed lines represent linear regressions performed for each data set. Error bars are shown for the parameters extracted from the XPDF fits. The error bars for the SXRD parameters are within the size of the symbol and are therefore omitted for clarity. The structural parameters from the SXRD data are taken from Ref.[7] 108
5.4 Rietveld refinements of temperature-dependent neutron diffraction of Cs_2SnI_6 at T = 10, 90, 300, and T = 500 K from the 31° bank (bank 2) of the NOMAD instrument at the Spallation Neutron Source, Oak Ridge National Laboratory. The data are modeled with the cubic vacancy-ordered double perovskite structure at all temperatures. Black circles are the data, the orange line is the fit, the blue line is the difference, and the grey tick marks represent positions of anticipated reflections for the $Fm\bar{3}m$ vacancy-ordered double perovskite structure. The data at T = 10, 90, and T = 300 K have been previously reported.[8] 109

5.5 Temperature-dependent neutron pair distribution function analysis of Cs_2SnI_6 at T = 10, 90, 300, and T = 500 K. The data are modeled with the cubic vacancy-ordered double perovskite structure at all temperatures. Black circles are the data, orange lines are the fits, and grey lines are the difference curves. The x-axis is split to highlight the low-r pair correlations and the increasing asymmetry of the next-nearest-neighbor pair correlation at $r \sim 4$ Å with increasing temperature. The nPDFs at T = 10, 90, and T = 300 K have been previously reported and are re-fit here for comparison with the T = 500 K data.[8] 110
5.6 Atomic displacement parameters (ADPs) extracted from the temperature-dependent neutron diffraction data for Cs_2SnI_6 using Rietveld analysis. Isotropic atomic displacement parameters were refined for cesium and tin. The ADPs for iodine were refined anisotropically, such that U_{11} corresponds to iodine displacements along the Sn–I bond and $U_{22} = U_{33}$ corresponds to displacements perpendicular to the Sn–I bond. The dotted lines are a guide to the eye to highlight the trends in ADP for each atom. 111
5.7 Supercell structures of Cs_2SnI_6 and Cs_2TeI_6 optimized from pseudo-rigid-body RMC simulations. 112
5.8 Calculated $G(r)$ and $S(Q)$-1 from pseudo-rigid-body RMC-optimized supercells of Cs_2SnI_6 and Cs_2TeI_6 compared against the experimental $G(r)$ and $S(Q)$-1 from X-ray total scattering data. Experimental data are shown as open circles, the fits from the RMC optimizations are shown as orange lines, and the difference curves are shown as blue lines. The x-axes in (a) and (b) are split to highlight the low-r pair correlations. 112
5.9 Partial radial distribution functions for I–I_{intra} (a,b), I–I_{inter} (c,d), and Cs–I (e,f) pair correlations in Cs_2SnI_6 and Cs_2TeI_6 obtained from pseudo-rigid-body Reverse Monte Carlo simulations (circles). The distributions are fit with Gaussian functions, shown by the orange line. The difference curves are shown in blue and reveal asymmetries in the I–I_{inter} and Cs–I RDFs. 113
5.10 (a) Toda potential fits to the next-nearest-neighbor pair correlation in the X-ray pair distribution function analysis for $Cs_2Sn_{1-x}Te_xI_6$. The data are shown as black circles and the fit is the orange line. The PDF data are fit with one Toda potential peak, and are offset vertically for comparison and clarity. In (b) and (c), the interatomic distance (b) and degree of anharmonicity (β) are plotted as a function of x in $Cs_2Sn_{1-x}Te_xI_6$, respectively. The colored tick marks in (a) represent the contact distances for Cs–I (teal), intraoctahedral I–I (pink), and interoctahedral I–I (purple) atom pairs taken from the refinements of the cubic model against the XPDF data from Figure 5.2. Dashed lines in (b) and (c) represent linear regressions. 114
5.11 The degree of anharmonicity from the Toda potential fits plotted as a function of the Cs^+ bond valence sum. 116

6.1 DFT-relaxed crystal structures of tropylium tin iodide ((a), (b)), and tropylium lead iodide ((c), (d)). Lavender spheres denote tin, purple denote iodine, charcoal denote lead, brown denote carbon, and eggshell denote hydrogen. 126
6.2 FT-IR spectra of tropylium iodide, tropylium tin iodide, and tropylium lead iodide, indicating the vibrational modes of the aromatic (Ar) $[C_7H_7]^+$ ring. "oop" refers to "out-of-plane" bending. 127

6.3 ^{1}H NMR spectra of tropylium iodide, tropylium tin iodide, and tropylium lead iodide redissolved in d_6-DMSO. The singlet at δ = 9.33 ppm corresponds to the seven hydrogens of the aromatic tropylium ion, which are highlighted in red for clarity. Tetramethylsilane (TMS) was used as an internal standard. 128
6.4 Visualization of the residual electron density after location of the heavy atoms in tropylium tin iodide (a) and tropylium lead iodide (b). Crystal structures of tropylium tin iodide (c) and tropylium lead iodide (d) superposed on the respective Fourier difference maps. Hydrogen atoms have been omitted for clarity, lavender spheres denote tin atoms, charcoal are lead, purple are iodine, and brown are carbon. 129
6.5 Joint Rietveld refinement of high-resolution X-ray powder diffraction data (a) with high-resolution time-of-flight neutron diffraction data (b). The right panel in (a) is multiplied by 8 to show the sharp decrease in intensity at $Q > 4$ Å^{-1} and diffuse features. The grey tick marks indicate the locations of predicted Bragg reflections of $(C_7H_7)_2SnI_6$. Refinement parameters can be found in Table 6.1. 131
6.6 Rietveld refinement of tropylium lead iodide. The data for $Q > 3.2$ Å^{-1} are multiplied by 8 in order to enhance the diffuse features at higher Q. The grey tick marks indicate the locations of predicted Bragg reflections for $C_7H_7PbI_3$. 132
6.7 X-ray PDF analysis of (a) tropylium tin iodide and (b) tropylium lead iodide over a fit range of $2 < r < 24$ Å. The insets of (a) and (b) show the refinements resulting from a fit range of $2 < r < 8.5$ Åand $2 < r < 8$ Å, respectively. The large feature in (a) at r = 2.83 Å corresponds to the octahedral tin-iodide bond distance, while the peak at r = 4.44 Å reflects the distance between iodine atoms within an octahedron. In (b) the arrows show that, over shorter refinement ranges, the predicted intensity of the feature at r~6.4 Å is improved. 133
6.8 Tauc plots of UV-visible diffuse reflectance spectra used to determine the (a) direct optical gaps and (b) indirect optical gaps of tropylium iodide, tropylium tin iodide, and tropylium lead iodide (diluted in $BaSO_4$). The insets in (a) are brightfield photographs of the sample powders of tropylium iodide, tropylium tin iodide, and tropylium lead iodide. 135
6.9 Total and local density of states for tropylium tin iodide (a) and tropylium lead iodide (c). The contribution from the inorganic constituents are shown in the upper panels, while the contribution from the tropylium rings is shown in the lower panels. The calculated band diagrams for tropylium tin iodide and tropylium lead iodide are shown in (b) and (d), respectively. The Fermi energy is referenced to the top of the valence band, set to 0 eV. 137
6.10 Band decomposed charge densities for tropylium tin iodide and tropylium lead iodide. Panel (a) shows the charge density associated with the highest occupied band (HOB) of tropylium tin iodide, while (b) shows the charge density of the tropylium tin iodide lowest unoccupied band (LUB). The band decomposed charge densities of tropylium lead iodide are shown in (c) and (d), where (c) illustrates the charge density of the HOB and (d) shows the charge density for the LUB. The tropylium rings have been omitted from panels (a) and (b) for clarity. 139

7.1 DFT-calculated band gaps of the A_2BX_6 compounds in which the *A*-, *B*-, and *X*-sites were systematically varied. Figure reproduced with permission from Cai, Xie, Ding, Chen, Thirumal, Wong, Mathews, Mhaisalkar, Sherburne, Asta, *Chem. Mater.*, **2017**, *29*, 7740–7749.[9] . . . 142
7.2 Molecular orbital theory perspective of the frontier states of (a) Cs_2SnI_6, (b) Cs_2SnBr_6, and (c) Cs_2SnCl_6 considering the interactions between the Sn and I orbitals. 143
7.3 Comparison of the experimentally- and computationally-determined ionization potentials and electron affinities of several members of the vacancy-ordered double perovskite family. Dashed lines represent the reported Fermi levels. Values were taken from (a),[10] (b),[11] (c),[7] (d),[3] (e),[12] (f),[13] (g),[10] (h),[10] (i),[10] (j),[10] (k),[10] (l),[14] (m),[7] (n),[8] (o),[8] (p),[8] (q).[7] . . . 145
7.4 Molecular orbital theory perspective of the frontier states of (a) Cs_2SnI_6 and (b) Cs_2TeI_6 with orbital representations of the highest occupied and lowest unoccupied states of $[SnI_6]$ and $[TeI_6]$ octahedra calculated using GAMESS. . . . 147
7.5 Band structure of Cs_2SnI_6, highlighting the A_{1g} antibonding states. Simplified bonding diagram (a and d) and charge density isosurfaces (c and e) of the highlighted band at the Γ and X points. The isosurface level was set to 0.008 eV Å^{-3}. Figure reproduced with permission from A. M. Ganose Copyright 2018 University of College London.[15] . . . 152
7.6 Crystal structure representation of $Cs_2Sb^{III}_{0.5}Sb^{V}_{0.5}X_6$ in the charge ordered tetragonal structure. The isolated and ordered $[Sb^{III}X_6]$ and $[Sb^{V}X_6]$ octahedra are differentiated as blue and red, respectively. Cesium ions are shown in grey and the *X*-site anions are shown in orange. . . . 156
7.7 The experimental and calculated electron mobilities of the A_2SnI_6 vacancy-ordered double perovskites as a function of perovskite tolerance factor. The experimentally-determined electron mobilities are shown as filled purple circles on the left axis, while the calculated Hellwarth electron mobilities are denoted by open orange squares on the right axis. Figure reproduced with permission from Maughan, Ganose, Almaker, Scanlon, Neilson, *Chem. Mater.*, **2018**, *30*, 3909–3919.[8] . . . 160

A.1 Comparison of powder X-ray diffraction data convolved with a Gaussian to diffraction patterns ($I(Q)$) calculated from $G(r)$ of the tilted supercells. Black lines are the convolved data, while colored lines represent the calculated $I(Q)$ for each compound in the A_2SnI_6 series. . . . 207

B.1 X-ray pair distribution functions of Cs_2SnI_6, $(CH_3NH_3)_2SnI_6$, and $(CH(NH_2)_2)_2SnI_6$. The XPDFs are modeled with the cubic vacancy-ordered double perovskite structure observed in the powder X-ray diffraction data. While the Sn–I peak at ~2.9 Å is well described, significant tailing of the next-nearest-neighbor I–I pair correlation at ~4 Å is observed in the hybrid compounds and cannot be modeled by the cubic structural models. . . . 215
B.2 Supercells for a) Cs_2SnI_6, b) $(CH_3NH_3)_2SnI_6$, and c) $(CH(NH_2)_2)_2SnI_6$ with the corresponding θ_{max} determined by the pseudo-rigid-body modeling routine. . . . 215

B.3 X-ray pair distribution functions of Cs_2SnI_6, $(CH_3NH_3)_2SnI_6$, and $(CH(NH_2)_2)_2SnI_6$. The XPDFs are modeled with the tilted supercells of the vacancy-ordered double perovskite structures shown in Figure B.2. 216

Chapter 1

Introduction

1.0.1 Perovskite Halides for Emerging Photovoltaics

Transitioning to alternative, sustainable sources of energy is a challenge that is fundamentally rooted in the discovery, development, and design of solid-state materials. Photovoltaic (PV) technology is a source of renewable energy generation that has the potential to mitigate the dependence upon fossil fuel and combustion-based energy sources by transforming solar radiation into electricity. In a photovoltaic cell, incident photons in the ultraviolet and visible region of the solar spectrum are absorbed by the active semiconducting material and converted into electricity. Commercial photovoltaic technology utilizes silicon or cadmium telluride as the active light-absorbing semiconductors, and modules utilizing single crystalline silicon (*sc*-Si) can achieve up to ~26% power conversion efficiencies.[16] However, there are several fundamental materials properties that limit the maximum efficiency that can be realized by silicon-based devices. Silicon possesses an indirect band gap of E_g = 1.12 eV,[17] which yields a low absorption coefficient, a weak absorption onset, and subsequently inefficient absorption of photons. A larger volume of absorber material can enhance light absorption, but this in turn increases the probability of electron-hole recombination processes that limit efficiencies and increases both cost and weight of the PV module. Optimization of these parameters for a silicon-based solar cell with a band gap of 1.1 eV yields a calculated maximum photovoltaic efficiency of ~30% for a single junction solar cell, which is commonly known as the Shockley-Queisser limit.[18] While utilizing solar energy to produce electricity encourages a societal shift to renewable energy sources, the limitations of silicon-based solar cells inhibit their ubiquitous implementation. Improved photovoltaic technology therefore relies on the discovery and development of new semiconducting materials.

Perovskite halides have recently emerged as promising semiconductor materials for applications in inexpensive, high-efficiency photovoltaic technologies. In only a decade of dedicated research, photovoltaic devices containing hybrid perovskite halides as the active semiconductor have achieved power conversion efficiencies up to ~22%,[19] which are competitive with those of commercial silicon-based devices. Further, the low-temperature solution-based materials processing routes and thin-film device architecture enables facile, inexpensive fabrication of perovskite solar cells. However, the ease of material and device preparation and resultant rapid growth in power conversion efficiencies has left unanswered questions regarding the fundamental structure-property relationships that give rise to their advantageous performance.

Perovskite materials are structurally distinct from other diamond-like semiconducting materials (*i.e.* silicon, cadmium telluride, or gallium arsenide) that are conventionally used for photovoltaics. In Figure 1.1a, the crystalline structures of diamond-like semiconductors are compared to the general perovskite structure. The canonical perovskite structure, named for the perovskite mineral $CaTiO_3$, is described by the general stoichiometry ABX_3. The structure is formed by a framework of vertex-sharing anionic $[BX_6]$ octahedral units with the A-site cation residing in the 12-coordinate cuboctahedral void formed by the X-site anions, as shown in Figure 1.1b.

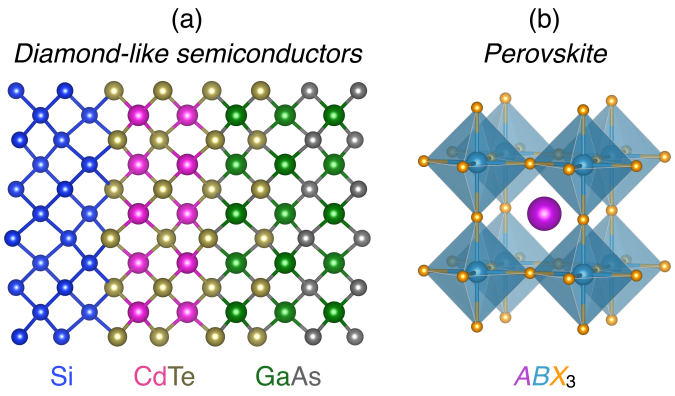

Figure 1.1: Crystal structure comparison of diamond-like semiconductors with the general perovskite structure. In (a), structural representations of the diamond-like semiconductors silicon (Si), cadmium telluride (CdTe), and gallium arsenide (GaAs) are shown. The unit cell representation of the general cubic perovskite structure of the general formula ABX_3 is shown in (b); A-site cations are shown in purple, B-site cations are shown in teal, and X-site anions are shown as orange spheres.

The highest efficiency perovskite material in photovoltaic devices is a compositional derivative of the hybrid organic-inorganic perovskite methylammonium lead iodide ($CH_3NH_3PbI_3$). As shown in Figure 1.2, Pb^{2+} ions occupy the *B*-site and are coordinated by six I^- ions, while the *A*-site is occupied by a dynamically disordered organic $CH_3NH_3^+$ cation. In the highest efficiency solar cells, there is compositional mixing at all three sites;[19] at the *A*-site, methylammonium ($CH_3NH_3^+$) is substituted with the smaller cesium (Cs^+) and larger formamidinium ($CH(NH_2)_2^+$) cations. The *B*-site is occupied by Pb^{2+} and Sn^{2+}, while the *X*-site is occupied by I^-, Br^-, and Cl^- in varying stoichiometric ratios.

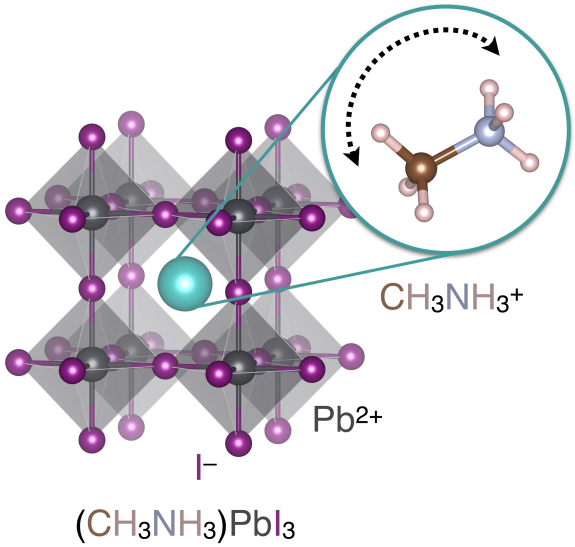

Figure 1.2: Crystal structure of the perovskite methylammonium lead iodide ($CH_3NH_3PbI_3$). The zoom region is shown to highlight the dynamic nature of the methylammonium cation within the cuboctahedral void. Lead atoms are grey, iodine atoms are purple, carbon atoms are brown, nitrogen atoms are light blue, and hydrogen atoms are beige.

Perovskite halides, such as methylammonium lead iodide, exhibit unusual photophysical properties that have been strongly implicated in their advantageous performance in solar cells. Of particular note is the observance of long carrier excited state lifetimes > 1 ms[20–22] and long carrier diffusion lengths > 1 μm[20–23] in methylammonium lead iodide. Longer excited state lifetimes and diffusion lengths increase the probability of harvesting photoexcited carriers and subsequently improve power conversion efficiencies in photovoltaic devices. These observa-

tions suggest that excited state carriers are mobile through the perovskite framework and are protected from electron-hole recombination pathways that typically limit device efficiencies. The exceptionally long carrier excited state lifetimes and diffusion lengths in $CH_3NH_3PbI_3$ are hypothesized to originate from (1) the apparent tolerance of the electrical properties of perovskite halides to the presence of crystallographic defects that often originate from the low-temperature solution-based processing[24] and (2) polaron formation via electron-phonon coupling between photoexcited charge carriers and the deformable metal-halide framework to protect mobile charge carriers.[25] The presence of significant crystallographic disorder and the influence of lattice dynamics upon charge transport behavior in perovskite halides provides a unique paradigm to understand and develop structure-dynamics-property relationships in functional semiconductors. The following sections will address the research efforts directed at understanding materials defects and lattice dynamics and the subsequent implications for charge transport in perovskite halide semiconductors.

1.0.2 Defect Tolerance

Materials defects are ubiquitous and often strongly influence the optical and electronic properties of semiconducting materials. Point defects, such as interstitials, vacancies, and site substitutions, can be introduced into a semiconductor intentionally to yield *p*-type vs.*n*-type behavior; these defects are referred to as dopants and can be used to chemically engineer the carrier transport characteristics of a semiconductor. Dopants or "shallow" defects typically introduce localized states within a few tens of millielectronvolts within the conduction and valence band edges, and electrons can be thermally excited into/out of these acceptor/donor states to yield free carriers. In contrast, point defects may also form highly localized "trap" states deep within the band gap that serve as recombination centers and impede charge transport.[26] These defects are represented in the simplified energy diagram shown in Figure 1.3.

"Defect tolerance" refers to the ability of a semiconductor to retain its optical and electronic properties despite the presence of crystallographic defects. Using Cu_3N and GaN as a test case,

Zakutayev *et al.* classified semiconductors with antibonding states at the valence band maximum and bonding states at the conduction band minimum as "defect tolerant," as the dangling bonds formed at these defect sites result in electronic states that are resonant with the conduction and valence bands rather than trap states deep within the band gap.[27] In Cu_3N, the lowest enthalpy of formation defects form as donor or acceptor states near or within the band edges, and thus the formation of these defects are not anticipated to be detrimental to charge transport properties. In contrast, the native defects in GaN form as deep traps within the band gap, demonstrating the inherent intolerance of this material to crystallographic defects. Similarly, the electronic properties of conventional semiconductors such as Si and GaAs are quite sensitive to the presence of point defects, and high-temperature and high-precision processing techniques are required to mitigate the formation of detrimental defects in these materials.[28]

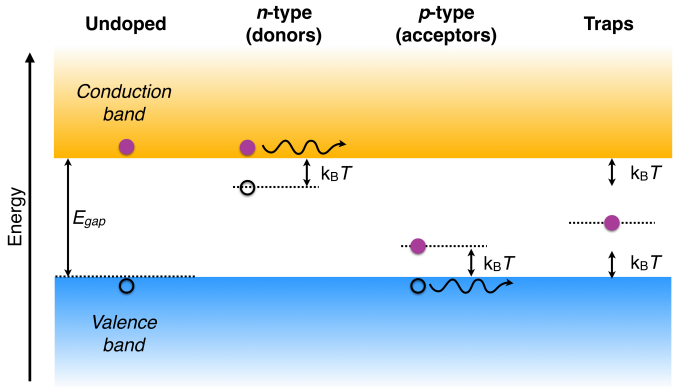

Figure 1.3: A simplified energy band diagram of a semiconductor. The valence and conduction bands are denoted by the blue and orange slabs, respectively. Electrons are shown as magenta circles, and holes are represented by black open circles. Dotted lines represent localized energy states introduced by defects. E_{gap} is the band gap, and $k_B T$ is the product of the Boltzmann constant and temperature.

Perovskite halides appear to challenge the notion that significant defect concentrations diminish photovoltaic efficiencies, in that they exhibit excellent electrical performance despite the presence of significant crystallographic disorder introduced by the often low-temperature solution-processing routes that result in imperfect materials with small grain sizes. Defect tolerance in $CH_3NH_3PbI_3$ was addressed in an X-ray photoelectron spectroscopy (XPS) study by

Steirer *et al.*[1] Upon irradiation by X-rays *in vacuo*, $CH_3NH_3PbI_3$ decomposes via evolution of CH_3NH_2(g) and HI(g) to yield $CH_3NH_3^+$ and I^- vacancies ($V_{CH_3NH_3^+}/V_{I^-}$). Despite the formation of these defects, the energy difference between the Fermi level and valence band maximum (ΔE_v) remains constant until a significant number of defects are created to yield a mixed phase region, in which both PbI_2 and $CH_3NH_3PbI_3$ coexist (Figure 1.4). The marginal changes in electronic structure despite the large concentration of crystallographic defects indicates that $V_{CH_3NH_3^+}$ and V_{I^-} defects do not form localized states deep within the band gap, but rather form close to or resonant with the conduction and valence band edges, consistent with computational studies of the defect chemistry of $CH_3NH_3PbI_3$.[29,30] This is also consistent with the classification of "defect tolerance" proposed by Zakutayev *et al.*,[27] as the band structure of methylammonium lead iodide is formed by antibonding states at the valence band maximum and bonding states at conduction band minimum.[31] The inherent defect tolerance of methylammonium lead iodide offers an explanation for the long carrier diffusion lengths and excited state lifetimes and subsequently high photoconversion efficiencies, despite low-temperature solution-based materials processing.

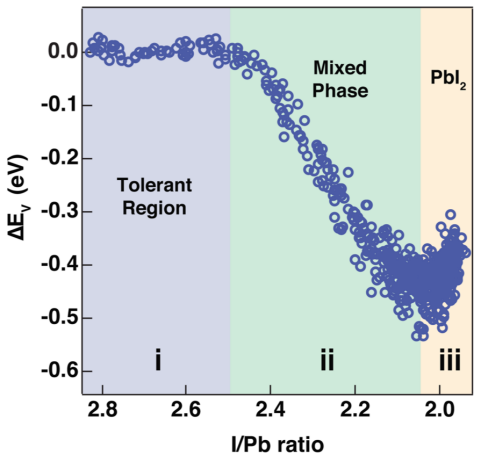

Figure 1.4: Experimental realization of defect tolerance in $CH_3NH_3PbI_3$. The energy difference between the Fermi level and valence band maximum (ΔE_v) determined by X-ray photoelectron spectroscopy is plotted as a function of I:Pb stoichiometric ratio. Figure reproduced with permission from Steirer, Schulz, Teeter, Stevanovic, Yang, Zhu, Berry, *ACS Energy Lett.*, **2016**, *1*, 360–366.[1] Copyright 2016 American Chemical Society.

1.0.3 Lattice Dynamics and Electron-Phonon Coupling

Lattice dynamics are well-known to influence charge transport in semiconducting materials. Electron-phonon scattering processes often reduce carrier mobilities and are responsible for thermalization of "hot carriers" with above-bandgap energies to the conduction band minimum, which is a factor that dictates device efficiencies.[18] Electrons may also interact with lattice vibrations via the formation of polarons. A polaron is a quasiparticle consisting of a localized lattice distortion formed via electrostatic interactions with an electron, which screens the charge of the electron.[32] This effect is more pronounced in ionic crystals due to the strong coulomb interaction between the electron and the charged ionic species compared to that of neutral atoms in covalently-bonded materials.[33] The strength of the electron-phonon coupling interaction for a given material, called the Frölich coupling constant, is inversely proportional to the frequency of the lowest-energy longitudinal optical phonon, and as such, materials with large dielectric constants and softer lattice dynamics typically exhibit stronger electron-phonon coupling interactions.[34] The electron dressed by the lattice distortion experiences variations in charge transport mechanism based upon the electron-phonon coupling strength and the resultant size of the polaron. In the "small polaron" case, short-range lattice deformations localize the electron at a single atomic site and charge transport is dominated by thermally-activated hopping conductivity of the polaron from site to site within the crystal.[35,36] In the "large polaron" case, the lattice distortion may persist over multiple unit cell lengths and the transport in band-like in nature, but with reduced mobility relative to the undressed electron.[37,38]

The lattice dynamics of halide perovskites are well-suited to facilitate electron-phonon coupling interactions. In contrast to the highly covalent diamond lattice of conventional semiconductors, the ionic perovskite halide structure is soft and deformable, characterized by low Young's moduli,[39,40] low speeds of sound,[41] and low thermal conductivity.[41–43] Cooperative octahedral tilting is a well-known origin of perovskite lattice dynamics. At elevated temperatures, octahedral tilting occurs as a spontaneous and dynamic process, which yields a time-averaged untilted structure.[44–46] As the thermal energy of the system is reduced upon cooling, these tilt-

ing vibrational modes progressively soften and crystallographic phase transitions to structures with frozen-in tilted octahedra are observed.[47] The propensity of a given perovskite to exhibit cooperative octahedral tilting is governed by the relative radii of the constituent atoms and can be predicted by the Goldschmidt tolerance factor, $t = (r_A + r_X)/(\sqrt{2}(r_B + r_X))$, which expresses the ratio of the side lengths of a cubic perovskite in terms of the ionic radii of the constituent *A*, *B*, and *X* ions.[48] The Goldschmidt tolerance factor is strongly correlated with phase transition temperatures and phonon softening within compositional families of the perovskite structure, and can therefore be used to predict the presence (and to some extent, the temperature) of these symmetry-lowering phase transitions.[49,50]

The formation of large polarons is hypothesized to prolong carrier excited state lifetimes in perovskite halides, as polaron formation is hypothesized to screen the excited electron from electron-electron, electron-defect, and electron-phonon interactions that contribute to recombination processes.[25,51–53] Charge carrier-lattice coupling has been demonstrated through experiment and supported by computational studies.[54,55] Terahertz absorption spectroscopic studies of $CsPbI_3$, $CH_3NH_3PbI_3$, and $CH(NH_2)_2PbI_3$ reveal spectral features at energies associated with dynamics of the lead iodide framework upon photoexcitation.[56,57] This process has also been observed by optical Kerr effect spectroscopy of $CsPbBr_3$ and $CH_3NH_3PbBr_3$.[58] The structural effects of carrier-lattice coupling have also been directly probed by ultrafast electron diffraction studies and differential pair distribution function analysis of $CH_3NH_3PbI_3$. Upon photoexcitation, Wu *et al.* observe broadening of the I–I pair correlation, indicating that electron-phonon coupling results in I–Pb–I bending.[59] These studies indicate that polaron formation occurs predominantly within the inorganic octahedral framework. The formation of large polarons is further supported by the observation that halide perovskites exhibit only modest carrier mobilities, a hallmark of large polaron transport.[60,61]

The presence of dynamic, organic molecular cations imbues hybrid halide perovskites with additional dynamic degrees of freedom. In $CH_3NH_3PbI_3$ and $CH(NH_2)_2PbI_3$, the organic cations undergo rapid molecular reorientations on picosecond timescales.[62–66] The cation re-

orientations in $CH_3NH_3PbI_3$ are coupled to dynamic tilting modes of the lead iodide framework,[67] and have been shown to affect the octahedral tilting progression observed during temperature-dependent phase transitions. This is exemplified by comparison of $CH_3NH_3PbBr_3$ and $CsPbBr_3$. While $CsPbBr_3$ exhibits in-phase octahedral tilting motifs upon cooling,[68] replacing Cs^+ with $CH_3NH_3^+$ instead yields out-of-phase tilting.[62,69] The temperatures at which the hybrid halide perovskites undergo crystallographic phase transitions are correlated with freezing out of the methylammonium reorientational dynamics,[70–73] and it has been suggested that coupling between the organic cations and the octahedral framework via hydrogen bonding interactions drives these phase transitions.[73–76]

Organic cation dynamics and organic-inorganic coupling affect electron-phonon coupling processes in hybrid perovskite halides. While polaron formation is observed in both hybrid and all-inorganic perovskite halides,[57] electron-phonon coupling occurs on faster timescales in $CH_3NH_3PbBr_3$ than in $CsPbBr_3$ due to participation of coupled organic-inorganic modes in the polaron formation process.[58] This notion is supported by a terahertz spectroscopy study of $CH_3NH_3PbI_3$, in which Guzelturk *et al.* observed that photoexcitation is accompanied by emission features at energies associated with I–Pb–I bending as well as coupled organic-inorganic modes.[56] Furthermore, the presence of rapidly reorienting dipolar organic cations has been suggested to influence polaron transport behavior via "dielectric drag," in which movement of charges as large polarons is accompanied by rotational relaxation of the dipolar organic cations.[77] This phenomenon is hypothesized to reduce carrier mobility in hybrid perovskite halides containing dynamically disordered dipolar organic cations, as these rotating dipoles provide additional friction to the polaron and result in slower charge transport processes. The influence and necessity of organic cations upon carrier excited state lifetimes in perovskite halide semiconductors is still an active area of debate within the literature.[53]

1.0.4 Vacancy-Ordered Double Perovskites

The presence of ordered defects and the absence of polyhedral connectivity in vacancy-ordered double perovskites provide an excellent structural framework to understand defect chemistry and lattice dynamics as they pertain to the optical and electronic properties of perovskite halide semiconductors. Vacancy-ordered double perovskites are a structural derivative of the archetypal perovskite structure. The structure is derived from the conventional perovskite by doubling the ABX_3 unit cell along all three crystallographic axes and then replacing every-other B-site cation with a vacancy, as illustrated in the schematic in Figure 1.5. The structure can alternatively be thought of as an antifluorite arrangement of A-site cations and anionic BX_6 units, to which these materials are often referred.

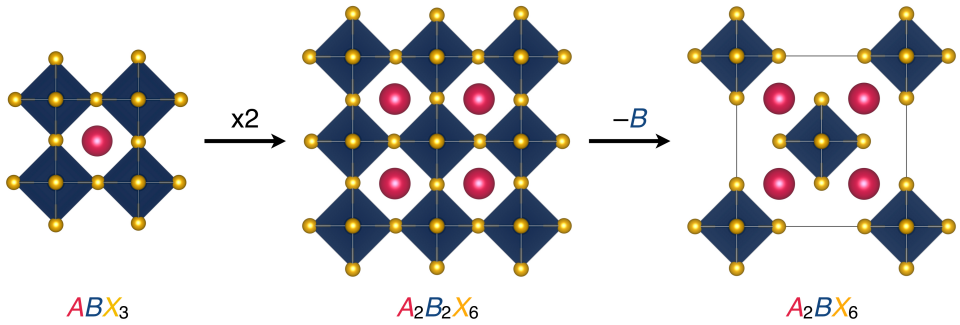

Figure 1.5: A schematic of the relationship between the archetypal perovskite (ABX_3) and vacancy-ordered double perovskite (A_2BX_6) structures.

Early research efforts of vacancy-ordered double perovskites were devoted to understanding the structural and dynamic behavior of these molecular-like crystals. Vacancy-ordered double perovskites exhibit cooperative octahedral tilting motifs familiar to ordered double perovskites,[78,79] which are nominally driven by a size mismatch between the A-site cations and the surrounding BX_6 octahedral framework. The tendency of a given composition to exhibit octahedral tilting at room temperature can be predicted by the geometric "radius ratio," which is defined as the ratio of the A-site cation ionic radius to the radius of the enclosing void formed by twelve X-site anions.[9,80] The radius ratio (R) is calculated as $R = r_A/(D_{xx} - r_X)$, where r_A is

the radius of the A-site cation, D_{xx} is the interoctahedral $X-X$ bond length, and r_X is the radius of the X-site anion. When $0.89 < R < 1$, no octahedral tilting is expected at room temperature. Smaller A-site cations yield $R < 0.89$, and the octahedral framework will undergo cooperative tilting to optimize coordination to the A-site cation.[81] This is exemplified by the A_2TeI_6 (A = Cs^+, Rb^+, K^+) family; while Cs_2TeI_6 adopts the cubic vacancy-ordered double perovskite structure (space group $Fm\bar{3}m$),[82] replacing the larger Cs^+ cation with the smaller Rb^+ and K^+ cations yields cooperative octahedral tilting to lower symmetry structures ($P4/mnc$ and $P2_1/n$, respectively), as illustrated in Figure 1.6.[83,84]

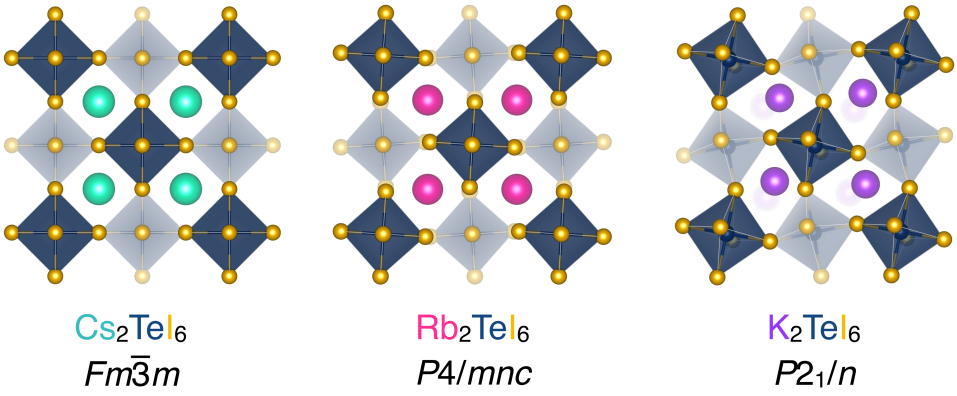

Figure 1.6: Crystal structures of Cs_2TeI_6, Rb_2TeI_6, and K_2TeI_6 as representative examples of common octahedral tilting motifs observed in the vacancy-ordered double perovskite family.

Temperature-dependent structural phase transitions in vacancy-ordered double perovskites follow the octahedral tilting progression shown in Figure 1.6 upon cooling. Through a nuclear quadrupole resonance study of the vacancy-ordered double perovskite K_2ReCl_6, O'Leary and Wheeler determined that the temperature-dependent phase transitions corresponded with softening of the [$ReCl_6$] octahedral rotary phonon mode corresponding to rigid-body rotations of the octahedra.[85] Subsequent studies of K_2ReCl_6 and other members of the vacancy-ordered double perovskite family by nuclear quadrupole resonance and inelastic neutron scattering attributed octahedral rotations as the primary source of dynamics and the origin of the temperature-dependent phase transitions in this family of materials.[86–93] It follows that the energy of the octahedral rotary phonon is correlated with the size of the A-site cation,

which is exemplified by the increase in frequency of the [$PtCl_6$] rotary phonon from 55 cm^{-1} to 64 cm^{-1} to 75 cm^{-1} with increasing size of the alkali cation across the A_2PtCl_6 ($A = K^+$, Rb^+, Cs^+) series.[87] A comprehensive review of the temperature-dependent structural evolutions and the influence of lattice dynamics upon phase transition behavior in 5*d* transition metal vacancy-ordered double perovskite halides can be found elsewhere.[94]

Incorporation of *A*-site cations such as ammonium (NH_4^+) or methylammonium ($CH_3NH_3^+$) influences phase transition behavior through hydrogen bonding interactions. In the vacancy-ordered double perovskites $(NH_4)_2SiF_6$, $(NH_4)_2SnBr_6$, and $(NH_4)_2SnCl_6$, reorientations of the NH_4^+ cations are coupled to rotations of the [BX_6] octahedral units and are suggested to hinder octahedral rotations at higher temperatures.[95,96] Furthermore, deuteration of the ammonium group in $(ND_4)_2SeCl_6$ has been shown to affect the phase transition behavior relative to the hydrogenated analog, and $(ND_4)_2SeCl_6$ exhibits three additional phase transitions where only one is observed in $(NH_4)_2SeCl_6$.[97] The larger methylammonium ($CH_3NH_3^+$) cation also undergoes rapid molecular reorientations in plastic crystals such as $(CH_3NH_3)_2SnCl_6$ and $(CH_3NH_3)_2PtCl_6$, and these dynamic reorientations have been implicated in the phase transition behavior of these materials.[98–102] The absence of extended polyhedral connectivity in vacancy-ordered double perovskites alleviates the competition between cooperative octahedral tilting and hydrogen bonding interactions often observed in ABX_3 perovskites,[72] and therefore the phase transitions in hybrid vacancy-ordered double perovskites are predominantly driven by organic-inorganic coupling through hydrogen bonding interactions.

While the structural and dynamic behavior of vacancy-ordered double perovskites has been well characterized, the optical and electronic properties of these materials have only recently been explored. The vacancy-ordered double perovskite Cs_2SnI_6 exhibits optical and electronic properties relevant for applications in photovoltaics. Cs_2SnI_6 possesses a direct optical gap of 1.3 eV, corresponding to its deep black color.[11,103] Electrical resistivity and Hall effect measurements indicate that Cs_2SnI_6 is a native *n*-type semiconductor with a moderate electron mobil-

ity of 310 $cm^2\ V^{-1}\ s^{-1}$, which is of the same order of magnitude as the value of 585 $cm^2\ V^{-1}\ s^{-1}$ reported for $CsSnI_3$, despite the presence of ordered vacancies in Cs_2SnI_6.[104] Lee *et al.* demonstrated that *p*-type conductivity could be achieved under appropriate doping conditions, yet the hole mobilities (42 $cm^2\ V^{-1}\ s^{-1}$) were notably lower than the electron mobilities.[11] A computational study of the defect chemistry in Cs_2SnI_6 suggested that the ambipolar doping and charge transport in Cs_2SnI_6 was due to the formation of *n*-type iodide vacancies/tin interstitials or *p*-type cesium vacancies.[105] Despite the lower hole mobilities, a dye-sensitized solar cell utilizing Cs_2SnI_6 as a hole-transporting material was reported to achieve 7.8% power conversion efficiency.[11] The presence of formally tetravalent tin in Cs_2SnI_6 is suggested to improve air and moisture stability relative to the Pb^{2+}- and Sn^{2+}-based ABX_3 perovskites, as well as mitigate toxicity concerns associated with the use of lead. The advantageous properties of Cs_2SnI_6 motivates further study of the structure-property relationships in vacancy-ordered double perovskites for potential optoelectronic applications.

1.0.5 Hybrid Organic-Inorganic Materials

Hybrid materials, in which both inorganic and organic components coexist in a single crystalline phase, have been the subject of research interest beyond hybrid perovskite halides. Hybrid materials offer a uniquely tunable structural framework, as both the organic moiety and inorganic framework can be modified (somewhat independently) to afford these materials with desirable functional properties. Further, hybrid materials are often processed by solution-based routes at low temperatures, a useful trait for fabrication of devices by processes such as spin-coating or drop casting.

Rao *et al.* classified hybrid organic-inorganic materials according to the "dimensionality" of the organic and inorganic lattices based upon the metal-organic connectivity and the connectivity of inorganic polyhedra (Figure 1.7).[2] While there is significant research devoted to hybrid materials with metal-organic-metal connectivity (*e.g.*, metal-organic frameworks, coordination polymers), the present work will focus upon hybrids consisting of polyhedral inorganic

frameworks with non-coordinating organic ions, as shown in the first row of the grid in Figure 1.7 denoted by purple text. Zero-dimensional hybrid materials, also known as "molecular complexes," are those with isolated inorganic polyhedra. One-dimensional hybrid materials contain chains of inorganic polyhedra, and two-dimensional hybrids are composed of layers of inorganic polyhedra. Three-dimensional hybrids form extended inorganic lattices in all dimensions. In all cases, the organic species reside within the crystalline voids and charge balance the inorganic framework.

Dimensionality of Inorganic Connectivity

Metal-Organic-Metal Connectivity

	0	1	2	3
0	**Molecular Complexes**	**Inorganic Chains**	**Inorganic Layers**	**3-D Inorganic Framework**
1	Chain Coordination Polymers	Mixed Organic-Inorganic Layers	Mixed Organic-Inorganic 3-D Framework	———
2	Layered Coordination Polymers	Mixed Organic-Inorganic 3D Framework	———	———
3	3-D Coordination Polymers	———	———	———

Figure 1.7: Classification of hybrid organic-inorganic materials based upon the dimensionality of the inorganic polyhedral connectivity and the metal-organic-metal connectivity. The first row (purple text) denotes hybrid materials with varying degrees of inorganic connectivity with non-coordinating organic moieties. Figure adapted with permission from Rao, Cheetham, Thirumurugan, *J. Phys.: Condens. Matter*, **2008**, *20*, 083202.[2] Copyright 2008 IOPScience.

Alteration to the connectivity of the inorganic framework can significantly influence functional properties in hybrid materials. Mitzi *et al.* prepared a series of layered two-dimensional Ruddlesden-Popper hybrid perovskite materials in which the thickness of the inorganic layers was varied.[106] Upon increasing the thickness (and thus the dimensionality) of the inorganic layers, the electronic conductivity of the materials increased and eventually transitioned from semiconducting to metallic behavior. A more recent study by Stoumpos *et al.* further showed that the optical absorption of similar Ruddlesden-Popper perovskites can be progres-

sively tuned by increasing the inorganic layer thickness, with thinner layers resulting in larger optical gaps concomitant with a gradual color change across the series.[107] As the optical and electronic properties of hybrid materials are often dictated by the inorganic lattice, hybrid materials containing 1D chains and 2D layers of polyhedra may result in anisotropic functional properties, and these materials are often considered as 1D electronic wires or 2D quantum wells.[108,109]

Although organic species typically do not participate directly in charge transport or visible light absorption in most hybrid materials, the choice of organic may indirectly influence these properties by dictating the dimensionality of the inorganic framework or templating certain inorganic structural motifs.[110–113] Small organic cations such as methylammonium ($CH_3NH_3^+$), formamidinium ($CH(NH_2)_2^+$), or guanidinium ($C(NH_2)_3^+$) may fit within the smaller crystalline voids in three dimensional frameworks, such as in the 3D hybrid halide perovskites.[114,115] Large organics often result in structural topologies with reduced dimensionalities; incorporation of the large cycloheptylammonium and cyclooctylammonium cations within lead iodide frameworks yields chains of corner-sharing PbI_6 octahedra and sheets of face-sharing PbI_6 octahedra respectively.[116] While larger organics often require lower-dimensional frameworks, the corollary is not true; smaller organics do not exclusively produce structures of high-dimensionality. This is evidenced by hybrid compounds such as $(CH_3NH_3)_3Bi_2I_9$, which adopts a structure composed of face-sharing bismuth iodide octahedral dimers with methylammonium cations in the voids.[117] Hybrid compounds often include organic cations in which the positive charge is localized on an ammonium group, which can then act as a hydrogen bond donor to drive certain structural topologies.[111] In the 1-D hybrids ABiI$_5$, the differences in steric constraints between the organic cations strongly influences the packing of the corner-sharing bismuth iodide octahedral chains within the crystal structure.[112] The spatial organization of the organic species is dictated by weak van der Waals interactions between the organic molecules, such as in pi stacking in aromatic systems such as the layered tin iodide perovskites containing halogen-

substituted phenylethylammonium organic species[110,118] or aliphatic stacking motifs observed in hybrids with long-chain hydrocarbons.[119]

Synergy between the the organic and inorganic sublattices can to give rise to interesting and emergent phenomena unavailable to inorganic solid-state materials or organic compounds individually. Incorporating organic chromophores, such as pyrene, within lead-halide layered perovskites can enhance phosphorescence through charge transfer between the inorganic and organic sublattices.[120,121] Studies of hybrid compounds containing tetrathiofulvalene (TTF) within metal halide inorganic framework demonstrate the influence of organic-inorganic coupling upon electrical properties. An early report by Kondo *et al.* revealed semiconducting behavior in the hybrid compounds (TTF)SnX_6 ($X = Cl^-$ or Br^-) arising from a layered organization of the TTF species that enables two-dimensional electronic conductivity.[122] More recent work by Evans *et al.* of (TTF)Pb_2I_5 reveals low-energy features in the UV-visible absorption spectrum, which was attributed to charge transfer between the $TTF^{+\cdot}$ radical and the inorganic lead iodide framework.[123] Similarly, the electrical conductivity observed in (TTF)$BiI_4$and $(TTF)_4BiI_6$ is attributed to both the connectivity of the inorganic framework as well as stacking motifs of the TTF ions within the crystallographic voids.[124] Unique functional behavior may therefore be realized in hybrid materials by coupling and exploiting the functionalities of both the organic and inorganic sublattices.

1.0.6 Summary of Dissertation

The following body of work is aimed at understanding the crystal-chemistry of vacancy-ordered double perovskite halides and hybrid organic-inorganic materials, in order to inform materials design principles relevant for potential optoelectronic applications.

Chapter two focuses on the defect chemistry of the vacancy-ordered double perovskites $Cs_2Sn_{1-x}Te_xI_6$, and in particular, what specific structure and bonding characteristics are necessary to achieve defect-tolerant perovskite halide semiconductors. In Cs_2SnI_6, iodine vacancies are the lowest enthalpy of formation defect with states that form as donor states that are nearly

degenerate with the conduction band, giving rise to the native *n*-type conductivity observed experimentally. However, substituting Te^{4+} for Sn^{4+} results in defect-intolerance; the more covalent Te–I interactions inhibit the formation of iodine vacancy defects and push the conduction band higher in energy, such that any defect states that do form result in trap states deep within the band gap. From these observations, a set of bonding principles is then constructed to inform the design of new, defect-tolerant semiconductors.

Chapter three reports the vacancy-ordered double perovskites Cs_2SnI_6, $(CH_3NH_3)_2SnI_6$, and $(CH(NH_2)_2)_2SnI_6$ and correlates trends in electronic and optical properties with anharmonicity that manifests in the local bonding environment. By modeling the local coordination environment with random rotations of the SnI_6 octahedral units, insights are drawn regarding the influence of soft, anharmonic lattice dynamics on the charge transport behavior of these materials. It is further proposed that the anharmonicity arises from dynamic reorientations of the organic methylammonium ($CH_3NH_3^+$) and formamidinium ($CH(NH_2)_2^+$) cations coupled to rotations of the SnI_6 octahedral units via hydrogen bonding. The presence of soft, anharmonic lattice dynamics results in stronger electron-phonon coupling that reduces electron mobilities. These conclusions are put in perspective of the charge transport behavior of other hybrid perovskite halide semiconductors.

In chapter four, incorporation of the Rb^+ ion into the tin(IV) iodide vacancy-ordered double perovskite lattice is results in cooperative octahedral tilting to improve coordination to the *A*-site cation. Rb_2SnI_6 undergoes a phase transition upon cooling, characterized by further octahedral tilting relative to the high-temperature structure. It is found that the low-temperature structure is observed in the local coordination environment at all temperatures, consistent with the presence of dynamic octahedral rotations that "freeze in" to yield the low temperature structure observed by powder X-ray diffraction. Reduced electronic conductivity relative to Cs_2SnI_6 arises from stronger electron-phonon coupling due to a larger number of low-frequency phonon modes introduced by the lower symmetry of Rb_2SnI_6 that contribute to the dielectric response of the lattice. This study further exploits these observations to derive a set of

design principles for the charge transport characteristics of vacancy-ordered double perovskites based upon the geometric perovskite tolerance factor.

In chapter five, a study of the local coordination environment of the vacancy-ordered double perovskites $Cs_2Sn_{1-x}Te_xI_6$ reveals asymmetry of the Cs–I/I–I pair correlation that increases concomitantly with the concentration of tin. From Reverse Monte Carlo simulations, this asymmetry is captured by rotations of the isolated [BX_6] octahedra coupled with displacements of Cs^+ cations. As this asymmetry appears to increase at higher temperatures in Cs_2SnI_6, suggesting that it originates from anharmonic lattice dynamics rather than from a static structural distortion. The anharmonicity across the $Cs_2Sn_{1-x}Te_xI_6$ series is directly correlated with the bond valence of the Cs^+ cation within the cuboctahedral void, in that the smallest degree of anharmonicity is observed when the coordination preference of the Cs^+ cation is most satisfied by the twelve surrounding iodide ions. As the charge transport properties of perovskite materials are highly dependent upon lattice dynamics, this study provides insight into the structure and bonding characteristic that give rise to anharmonicity in vacancy-ordered double perovskite materials.

Chapter six details the discovery and characterization of two new hybrid organic-inorganic materials containing the seven-membered aromatic tropylium ring. The structures of tropylium lead(II) iodide ($C_7H_7PbI_3$) and tropylium tin(IV) iodide ($(C_7H_7)_2SnI_6$) were solved *ab initio* from high-resolution powder X-ray diffraction patterns. The large size of the tropylium ring prohibits the formation of perovskite structural topologies and structures containing 1D chains of face-sharing lead iodide octahedra and isolated tin iodide octahedra are observed instead. From computational analysis, it is found that the bright red-orange color of tropylium lead(II) iodide arises from charge transfer from the electronic states of the inorganic framework at the top of the valence band to the lowest-unoccupied electronic states of the tropylium ring at the conduction band minimum. In tropylium tin(IV) iodide, the organic states are energetically out-of-range for inorganic–organic charge transfer processes to occur; rather, the deep black color arises from transitions within the Sn–I framework. The presence of organic-inorganic

electronic coupling in tropylium lead(II) iodide provides insight into the design of new hybrid materials with advantageous optical properties.

The final chapter summarizes the insights and structure-property relationships of vacancy-ordered double perovskite semiconductors deduced from the above work. The findings are placed in the context of other studies and used to construct a set of design principles that may be used to elicit particular optical, electronic, and dynamic properties of these materials. From this, future avenues of study are proposed.

The appendices of this document contain *ad hoc* Python code used in chapter 3, as well as a description of the mathematical relationships used to derive the pair distribution function from total scattering data.

Chapter 2

Defect Tolerance to Intolerance in the Vacancy-Ordered Double Perovskite Semiconductors Cs_2SnI_6 and Cs_2TeI_6[2]

2.1 Introduction

Hybrid inorganic/organic and all-inorganic halide-based perovskites, such as $CsSnI_3$ and $(CH_3NH_3)PbI_3$, have been recently shown to exhibit advantageous optical and electronic properties for applications in field-effect transistors,[125,126] light-emitting diodes,[127,128] and efficient photovoltaic devices.[104,129–132] These materials challenge conventional wisdom in that they exhibit excellent electrical performance despite the inexpensive, low-temperature solution-based preparatory routes that result in imperfect materials with small grain sizes.[133–137] Many of these perovskite halides suffer from several issues that currently preclude their widespread use in commercial applications, including lead toxicity,[138,139] air and moisture sensitivity,[114,140–144] and crystalline phase stability.[104,145–148]

The immense compositional and structural diversity of the perovskite family provides many opportunities to circumvent the challenges that accompany the $A\mathrm{Sn}X_3$ and $A\mathrm{Pb}X_3$ perovskite halides. As in the perovskite oxides,[149] the halides also undergo symmetry-lowering phase transitions upon cooling, manifesting as cooperative tilting of the $B\mathrm{I}_6$ octahedra, which influence the band gap and conductivity.[68,70,104,150,151] The halides can also form ordered double perovskites, of the general formula $A_2B'B''X_6$, in which there is rock-salt ordering of the B' and B'' metals; the ordering is often driven by a large charge difference between the two metals.[152]

[2]Substantial portions of this chapter have been reproduced with permission from A. E. Maughan, A. M. Ganose, M. M. Bordelon, E. M. Miller, D. O. Scanlon, and J. R. Neilson, *J. Am. Chem. Soc.*, **2016**, *138*, 8453–8464.[7] ©2016 the American Chemical Society

The recently-reported double perovskite halides, Cs_2AgBiX_6 ($X = Cl^-, Br^-$),[153,154] absorb visible light with long carrier recombination lifetimes, which provide new opportunities for non-toxic and air-stable alternatives to Pb^{2+}- and Sn^{2+}-based ABX_3 perovskites.

Replacing one B-site cation with a vacancy in the $A_2B'B''X_6$ double perovskite yields the vacancy-ordered double perovskites, A_2BX_6 (*e.g.*, $A_2B\square X_6$, where $\square$ is a vacancy). Often referred to as anti-fluorite materials, these defect-variant perovskites adopt the K_2PtCl_6 structure type, which can be described as isolated $[BX_6]^{2-}$ octahedra bridged by A^+ cations. These A_2BX_6 perovskites exhibit several similarities to ABX_3 perovskites. Although every-other $[BX_6]$ octahedron is removed, the close-packed anionic lattice familiar to ABX_3 perovskites is retained. Additionally, the vacancy-ordered structure type undergoes cooperative octahedral tilting and rotations in symmetry-lowering phase transitions upon cooling.[155–158] As in ABX_3 perovskites, these phase transitions are driven by a mismatch in ionic radii of the constituent atoms; in ABX_3 perovskites, structural stability is predicted by the Goldschmidt tolerance factor,[159,160] while the "radius ratio" of A-site cation radius to the radius of the 12-coordinate void has been used in the A_2BX_6 perovskites.[80]

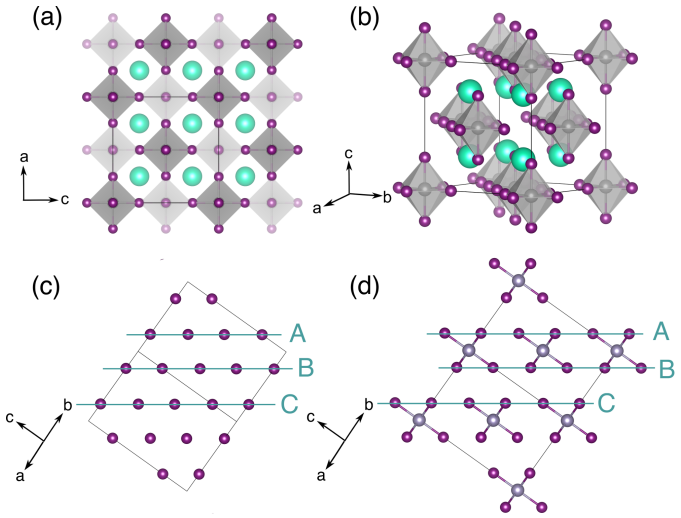

Figure 2.1: (a) Crystal structure of the vacancy-ordered double perovskites, Cs_2SnI_6 and Cs_2TeI_6. (b) Reorientation of the unit cell reveals the isolated octahedral units. Panel (c) illustrates the cubic close-packed iodine sublattice, and panel (d) shows how the cubic close-packed iodine sublattice is decorated with Sn atoms to yield the isolated octahedral units. Teal spheres are cesium, grey are tin/tellurium, and purple are iodine.

Cs_2SnI_6 adopts the cubic structure at room temperature ($Fm\bar{3}m$), as predicted by its radius ratio ~ 0.94,[80] and the compound exhibits intrinsic *n*-type electrical conductivity, air and moisture stability, and strong visible light absorption – all are advantageous properties for photovoltaic devices.[11,12] Despite the presence of regularly-ordered *B*-site vacancies, the room-temperature carrier mobility of Cs_2SnI_6 is reported to be of the same order of magnitude to that of $CsSnI_3$ ($\mu \sim 310$ cm^2 V^{-1} s^{-1} and 585 cm^2 V^{-1} s^{-1}, respectively);[11,104] yet, a more recent report on Cs_2SnI_6 thin films has determined a moderate electron mobility ($\mu_e \sim 3$ cm^2 V^{-1} s^{-1}).[12] The origin of conductivity in Cs_2SnI_6 has been hypothesized to stem from (a) the presence of dispersive conduction band states and (b) the formation of iodine vacancies which serve as electron donors that contribute to conductivity.[11,12,103] The seemingly inherent "defect-tolerance" of Cs_2SnI_6 motivates exploration of these molecular perovskites and the effect of composition on their tolerance to crystallographic defects. The concept of defect tolerance has been employed to identify materials that are insensitive to charge localization due to intrinsic defects,[27] and has previously been applied to ABX_3 perovskites.[161,162]

In this contribution, we describe the structure-property relationships of the solid solution, $Cs_2Sn_{1-x}Te_xI_6$, which characterizes Cs_2SnI_6 as a defect-tolerant semiconductor, thus illustrating how the close-packed anionic lattice of the vacancy-ordered perovskite halides can yield advantageous electronic properties, despite the lack of *B*–*X*–*B* connectivity. In these materials, the tin(IV) ion, (formal [Kr]$4d^{10}5s^0$ electron configuration), is substituted with the larger tellurium(IV) ion (formal [Kr]$4d^{10}5s^2$ electron configuration) to yield a solid solution with no distortions of the local coordination environment, despite the presence of the tellurium lone pair. In this work, we refer exclusively to formal oxidation state of the Sn and Te ions in these materials (*i.e.*, Sn^{4+} and Te^{4+}), as the actual charge is likely reduced through covalent bonding interactions.[163,164] The larger Te(IV) ion is accommodated into the structure by expansion of the [BI_6] octahedra at the expense of the inter-octahedral void region. Despite the reduced I–I separation between neighboring octahedra and higher predicted carrier mobilities, substitution of tellurium is accompanied by a significant reduction in electrical conductivity from a

dramatically reduced carrier concentration and carrier mobility. There is a non-linear change in the optical gap with increasing Te substitution, yet no distortions of the crystal structure or local coordination environment are observed across the solid solution, as determined by analysis of high-resolution time-of flight neutron and synchrotron X-ray diffraction data and X-ray pair distribution function analysis. From density functional calculations, we have identified iodine vacancies as the lowest energy defect in Cs_2SnI_6, which act as shallow electron donors. In contrast, iodine vacancies in Cs_2TeI_6 have a higher enthalpy of formation and form deep in the band gap, a consequence of increased Te–I covalency, which renders Cs_2TeI_6 defect intolerant. While the close-packed halogen sublattice provides a framework for mobile charge carriers in these vacancy-ordered double perovskites, the interaction between the *B*-site cation and *X*-site anions serves to set the magnitude and character of the band gap and dictates the tolerance of these materials to point defects in the lattice.

2.2 Methods and Materials

Note on author contributions: This chapter was published in *Journal of the American Chemical Society*, **2016**, volume 138, pages 8453–8464 by Annalise E. Maughan, Alex M. Ganose, Mitchell M. Bordelon, Elisa M. Miller, David O. Scanlon, and James R. Neilson. AEM and MMB performed the syntheses and experiments and analyzed the data. JRN, AMG, and DOS performed density functional calculations, and EMM performed X-ray photoelectron spectroscopy measurements. AEM wrote the initial draft of the manuscript, and JRN supervised the project. All authors contributed to editing and finalization of the manuscript.

Synthesis of SnI_4 and TeI_4

Two equivalents of solid I_2 were added to one equivalent of either elemental Sn or Te in a silica ampoule and sealed under dynamic vacuum. The reaction was heated to $T = 200°C$ until the purple iodine vapor in the tube had subsided ($\sim$ 60 h), resulting in bright orange (SnI_4) and dark grey (TeI_4) products, as confirmed with powder X-ray diffraction. Yields are quantitative.

Synthesis of $Cs_2Sn_{1-x}Te_xI_6$

The compounds in the solid solution series $Cs_2Sn_{1-x}Te_xI_6$ were synthesized by modification of the method described by Lee *et al.*[11] In a beaker, ~0.5 mmol of Cs_2CO_3 was added to 3 mL of 57% hydriodic acid (aqueous, 1.5% H_3PO_2) and stirred to dissolve. Solid Cs_2CO_3 was added slowly to hydroiodic acid in order to account for the vigorous reaction between Cs_2CO_3 and HI, which produces heat and CO_2(g). In a separate beaker, the appropriate ratio of SnI_4/TeI_4 precursor was dissolved in 15 mL of absolute ethanol and 2 mL of 57% hydriodic acid (aqueous, 1.5% H_3PO_2), to which excess elemental iodine was added to consume the hypophosphorus acid stabilizing agent. The beaker containing the BI_4 precursors was gently heated to $T \sim 60$ °C to encourage solubility. Once the solids had completely dissolved into their respective solutions, the Cs_2CO_3/HI solution was quickly added to the BI_4 solution, resulting in a black precipitate that immediately crashed out of solution. The reaction was stirred for an additional 30 m. The precipitate was collected by centrifugation and washed three times with absolute ethanol. The final products were dried at 60 °C for 24 h. Phase purity was verified by powder X-ray diffraction. Synthetic yields range from 87–94% for the solid solution, as determined by comparing the amount of product collected from the synthesis to the theoretical mass of product calculated from precursor amounts.

Characterization

Powder X-ray diffraction data were collected on a Scintag X-2 Diffractometer with CuKα radiation. Diffraction data were quantitatively analyzed using the Rietveld method as implemented in GSAS/EXPGUI.[165,166] High-resolution time-of-flight neutron powder diffraction was performed on the POWGEN diffractometer at the Spallation Neutron Source, Oak Ridge National Laboratory at T = 300 K and T = 10 K. High-resolution synchrotron powder X-ray diffraction data were collected on the 11-BM-B beamline at the Advanced Photon Source, Argonne National Laboratory.[167] X-ray pair distribution function data were calculated from X-ray total scattering collected at the 11-ID-B beamline at the Advanced Photon Source, Argonne National

Laboratory. Two-dimensional diffraction images were calibrated and radially integrated using the FIT2D software.[168] The PDFs were extracted using PDFgetX3 after correcting for the empty Kapton® capillary container[169] and were quantitatively modeled using PDFgui.[170] The crystal structures were visualized using VESTA.[171]

Electrical resistivity measurements were performed using a Physical Properties Measurement System (Quantum Design, Inc.) on cold-pressed pellets of the members of the solid-solution series using a 4-wire configuration with Au-paste contacts and Pt wires. Measurements were performed upon cooling and then again upon heating to ensure reproducibility. Analysis of the temperature dependent resistivity data was performed as in Ref.[172] Hall measurements were performed using a Physical Properties Measurement System (PPMS, Quantum Design, Inc.) in the van der Pauw configuration on cold-pressed polycrystalline pellets. Measurements on the Te-substituted samples were not possible due to the highly insulating nature of the specimens.

UV–visible diffuse reflectance spectroscopy was performed on powdered samples of the solid solution series diluted to 10wt% in $BaSO_4$, using $BaSO_4$ as a baseline; spectra were acquired using a Thermo Nicolet Evolution 300 spectrophotometer with a Praying Mantis mirror setup from $\lambda = 200$ to 1000 nm at a scan rate of 240 nm/min. Heat capacity measurements were performed on pelleted samples of Cs_2SnI_6 and Cs_2TeI_6 using the quasi-adiabatic heat-pulse technique implemented in the Quantum Design, Inc. PPMS from $T = 3$–150 K.

Photoluminescence (PL) spectra were collected from cold-pressed polycrystallline pellets of Cs_2SnI_6 and Cs_2TeI_6 mounted on glass substrates. The compounds were excited with an LED head at 780 nm. The excitation beam was modulated at 50 Hz and loosely focused (spot size roughly 0.8 cm in diameter) on the samples. The incident angle of the excitation beam was $\sim 45°$, and the resulting PL were collected at an angle perpendicular to the excitation beam and detected by an amplified Ge photodiode routed to a lock-in amplifier. The 830 nm long-pass filters were placed before the detector to remove excitation light. The PL spectra were corrected for monochromator and detector efficiencies using a calibrated lamp.

The XPS (hν = 1486.7 eV) measurements for Cs_2SnI_6 were performed on a PHI 5600 XPS instrument, which has been previously described in detail.[173] For the XPS core level, valence band, and workfunction measurements, the pass energy was set to 11.75 eV, 5.85 eV, and 2.95 eV with a step size of 0.10 eV, 0.050 eV, and 0.025 eV, respectively. The spectrometer was calibrated with metallic Fermi edges and atomic core levels from Au, Ag, Cu, or Mo. The instrumental response of the XPS spectrometer was 350 meV, respectively, and is determined from comparing the measured and calculated Fermi function for a particular instrument condition. The energy uncertainty of XPS (± 0.050 eV) is a statistical quantity determined from multiple measurements of the Fermi energy. The Cs_2SnI_6 pellet did not charge as verified with power dependent measurements. To determine the E_F-E_{VBM} value, we used two methods. First, we fit both the baseline and main valence band feature to a line, and the intersection was taken as the onset value, E_F-E_{VBM} = 1.44 eV ± 0.05 eV. Second, we used the calculated density of states (DOS). We broaden the DOS with a ~ 350 meV FWHM Gaussian line shape, which is the instrument response of the spectrometer. Because the DOS calculation does not account for the XPS cross-section, we only fit the broadened DOS to the rising edge of the experimental spectrum, similar to that used by Kraut, *et al.* and Chambers, *et al.*, E_F-E_{VBM} = 1.49 eV ± 0.05 eV.[174,175]

Density Functional Theory Calculations

First-principles calculations were performed using the Vienna *Ab initio* Simulation Package (VASP),[176–179] a periodic density functional theory (DFT) code utilizing a plane-wave basis set, with interactions between the core and valence electrons described using the Projector Augmented Wave (PAW) method.[180] This study employed the HSE06 functional,[181] which combines 75% exchange and 100% of the correlation energies from the Perdew, Burke and Ernzerhof (PBE) functional[182] together with 25% exact Hartree-Fock (HF) exchange at short ranges. HSE06 has been shown to accurately reproduce the lattice constants and electronic properties of a wide range of solid-state semiconductors.[183–185] For band structure and density of states calculations, special attention was paid to accurately modelling the relativistic effects seen in

Sn, Te and I, through use of scalar relativistic PAW pseudopotentials and explicit treatment of spin-orbit coupling (SOC) effects.[186] A plane wave cut-off of 350 eV and *k*-point sampling of Γ centered 3 × 3 × 3 for the 9 atom unit cells of Cs_2SnI_6 and Cs_2TeI_6 were used. For structural relaxations the ionic forces were converged to 0.01 eV Å^{-1}, using a larger cutoff energy (455 eV) in order to avoid errors arising from Pulay stress.

Electronic structure calculations of the solid solution were calculated by constructing a 2 × 2 × 2 supercell (containing 288 atoms) of the Cs_2SnI_6 standard $Fm\bar{3}m$ unit cell. Compositions corresponding to 25%, 50%, 75%, 88%, and 91% Te concentration were generated based on the quasi-random structure (SQS) approach,[185,187] in which an appropriate number of Sn atoms are replaced with Te (8, 16, 24, 28, and 29 atoms, respectively). Due to the solid solution nature of the alloys observed by experiment, these random structures are expected to demonstrate properties representative of each composition. Each structure was geometrically relaxed using the HSE06 functional at a single *k*-point before the band gap was calculated using HSE06+SOC.

Phonon calculations were carried out on 2 × 2 × 2 supercells of the standard cell structures of Cs_2SnI_6 and Cs_2TeI_6, containing 288 atoms. These calculations were performed at a single *k*-point (Γ) and employed the PBEsol functional without the use of SOC; explicit treatment of relativistic effects greatly increases computational complexity and has been shown to have a minimal effect on lattice vibrations.[188,189] Lattice-dynamics calculations were carrier out using the Phonopy package,[190] using the finite difference approach to calculate the interatomic force constants (IFCs). Dielectric constants and Born effective charges were calculated within the framework of density functional perturbation theory (DFPT) at a denser *k*-point mesh of 4 × 4 × 4, using the PBEsol functional both with and without SOC effects. These were used to make non-analytical corrections to the calculated phonon frequencies, in order to determine the splitting between the longitudinal and transverse optical phonons (LO-TO splitting).

COHPs were calculated using the LOBSTER program based on wavefunctions calculated using HSE06.[191,192] The optical transition matrix elements were calculated using the transversal

approximation and used to construct the imaginary dielectric function and corresponding optical absorption.[193] Band alignments were performed using a slab model (45 Å slab, 35 Å vacuum), with the corresponding electrostatic potential averaged along the *c*-direction, using the MacroDensity package.[194–196] The energy of the potential at the plateau was used as the external vacuum level. The slab calculations were performed using the HSE06, PBE, and PBEsol functionals, with corrections to the valence band energy and band gap in each case taken from the HSE06+SOC, PBE+SOC, and PBEsol+SOC calculated bulks. All defects were calculated using HSE06 in a 3 × 3 × 3 (243 atom) supercell, employing a single *k*-point at Γ. All the competing phases required to construct the chemical potential limits were structurally converged using HSE06. Bader charge analysis was calculated using the bader code[197,198] with the GPU port of VASP[199,200] using the HSE06 functional and explicit treatment of spin-orbit coupling.

2.3 Results and Discussion

2.3.1 Electronic Properties

Cs_2SnI_6 exhibits properties consistent with an intrinsically-doped, *n*-type semiconductor. As measured on a cold-pressed polycrystalline pellet, the resistivity of Cs_2SnI_6 at T = 300 K is $\rho \sim 13$ Ω·cm. The exponential increase in resistivity on cooling is consistent with semiconducting behavior (Figure 2.2a), and the data follow, $\rho = \rho_0 \exp([\frac{T_0}{T}]^p)$, where $p = 0.56$, consistent with Efros-Shklovskii variable range hopping (ES-VRH).[201,202] However, the precise nature of the transport is yet inconclusive due to the polycrystalline nature of the specimens. Measurement of the Hall voltage at T = 300 K confirms intrinsic *n*-type behavior, with a carrier concentration of $n_e \sim 5(1) \times 10^{16}$ cm^{-3} and a carrier mobility of $\mu_e \sim 8.6(5)$ cm^2 V^{-1} s^{-1} (Figure 2.2c).

Partial substitution of Sn by Te in the solid solution series $Cs_2Sn_{1-x}Te_xI_6$ increases electrical resistivity of the materials. At 5% tellurium substitution (x = 0.05), a 50-fold increase in resistivity is observed, and samples containing more than 25% Te are too insulating for accurate measurements (Figure 2.2b). Measurements of the Hall voltage for the 5% and 10% Te samples reveal that, while the dominant carriers are still electrons, the carrier concentrations and

mobility are dramatically reduced (Figure 2.2c). Therefore, detailed analyses of the crystal and electronic structures are necessary to determine the nature of resistivity increase.

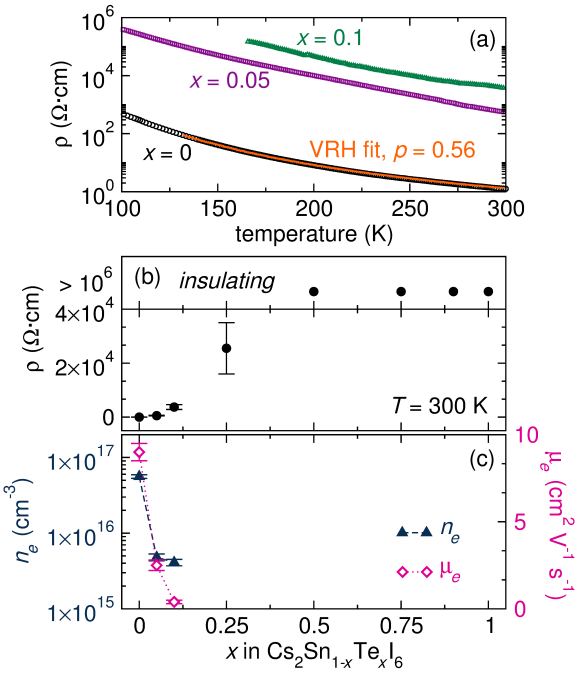

Figure 2.2: (a) The temperature dependence of the electrical resistivity for the solid solution $Cs_2Sn_{1-x}Te_xI_6$. The data for Cs_2SnI_6 (black circles) indicate semiconducting behavior, as described by variable range hopping conductivity from T = 130–300 K (orange line). Temperature-dependent curves are also shown for x = 0.05 (purple squares) and x = 0.1 (green triangles). (b) The room-temperature resistivity for x = 0, 0.05, 0.1, and x = 0.25 in $Cs_2Sn_{1-x}Te_xI_6$. The x = 0.5, 0.75, 0.9, and x = 1 samples were too resistive for accurate measurements. (c) The carrier concentration, n_e (filled teal triangles), and carrier mobility, μ_e (open pink diamonds), for x = 0, 0.05 and x = 0.1 are reduced upon Te substitution, as determined by Hall voltage measurements. Error bars denote the propagation of uncertainty from the sample dimensions for all samples, except for x = 0.05 which denotes the standard deviation of 3 transport specimens.

2.3.2 Crystal Structures

High-resolution time-of-flight neutron powder diffraction data for Cs_2SnI_6 and Cs_2TeI_6 collected at T = 300 K and T = 10 K reveal cubic crystal structures, as shown in Figures 2.3 and 2.4. Structural parameters and refinement statistics can be found in Table 2.1. The diffraction patterns are all consistent with the cubic, vacancy-ordered double perovskite structure shown in Figure 2.1 ($Fm\bar{3}m$, Figure 2.3 and 2.4). Rietveld analysis yields lattice parameters of

11.65272(4) Å and 11.7088(1) Å for Cs_2SnI_6 and Cs_2TeI_6, respectively at T = 300 K. The lack of sharp Bragg features beyond $Q > 8$ Å^{-1} at T = 300 K suggests the presence of significant rotational disorder of the BI_6 octahedral units, which is not uncommon in crystalline materials containing isolated polyhedra,[203,204] and is reflected in the somewhat large I anisotropic displacement parameters (U_{22}, U_{33}) generated during the refinement (Table 2.1). The radius ratios of Cs_2SnI_6 (r_A/r_H = 0.94) and Cs_2TeI_6 (r_A/r_H = 0.97) fall in the range $0.89 < r < 1$, and thus these materials are not expected to undergo symmetry-lowering phase transitions upon cooling, consistent with neutron scattering data collected at T = 10 K.[80,205–207]

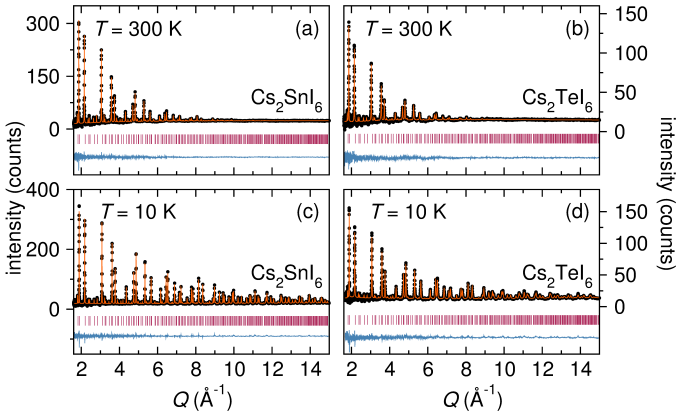

Figure 2.3: Rietveld refinements of high-resolution time-of-flight neutron scattering data of (a,c) Cs_2SnI_6 and (b,d) Cs_2TeI_6 collected from wavelength frame 2 on the POWGEN diffractometer at the Spallation Neutron Source, Oak Ridge National Laboratory. Data collected at T = 300 K are shown in panels (a) and (b) and data collected at T = 10 K are shown in panels (c) and (d). Refinements were performed using data collected from wavelength frames 2 and 4 of the POWGEN diffractometer. Black circles are the data, the orange line is the fit, and the blue line is the difference. The pink tick marks indicate the location of predicted Bragg reflections for the cubic structure.

The crystallography is further supported by the absence of any entropy-releasing anomalies in the experimentally measured low-temperature heat capacity, shown in Figure 2.5. Instead, the specific heat reveals the presence of low-energy localized lattice vibrations, as described by the summation of the Einstein and Debye models of specific heat. Analysis of the data according to these models yields Debye temperatures of Θ_D =149(2) K and Θ_D = 122(2) K and localized

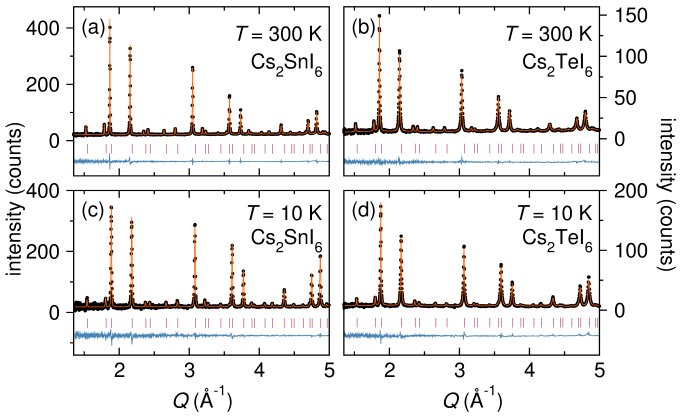

Figure 2.4: Rietveld refinements of high-resolution time-of-flight neutron scattering data of (a,c) Cs_2SnI_6 and (b,d) Cs_2TeI_6 collected from wavelength frame 4 of the POWGEN diffractometer at the Spallation Neutron Source, Oak Ridge National Laboratory. Data collected at T = 300 K are shown in panels (a) and (b) and data collected at T = 10 K are shown in (c) and (d). The structural models were refined jointly against data from wavelength frames 2 and 4. Black circles are the data, the orange line is the fit, and the blue line is the difference. The pink tick marks indicate the location of predicted Bragg reflections for the cubic structure.

Table 2.1: Structural parameters and refinement statistics for Cs_2SnI_6 and Cs_2TeI_6 from high-resolution neutron diffraction data at T = 300 K and T = 10 K.[a]

		Cs_2SnI_6	Cs_2TeI_6
T = 300 K	a (Å)	11.65272(4)	11.7088(1)
	I (x, 0, 0), 24e	0.2452(1)	0.2498(2)
	U_{iso}(Cs) (Å^2)	0.0393(4)	0.0445(7)
	U_{iso}(B) (Å^2)	0.0159(4)	0.0262(7)
	U_{11}(I) (Å^2)	0.0104(3)	0.0142(6)
	U_{22} = U_{33}(I) (Å^2)	0.0396(2)	0.0444(4)
	Red. χ^2	2.55	1.958
	wR	3.27%	3.88%
T = 10 K	a (Å)	11.53346(3)	11.5895(1)
	I (x, 0, 0), 24e	0.2481(1)	0.2514(2)
	U_{iso}(Cs) (Å^2)	0.00435(9)	0.0064(2)
	U_{iso}(B) (Å^2)	0.0054(1)	0.0114(4)
	U_{11}(I) (Å^2)	0.00308(3)	0.00497(7)
	U_{22} = U_{33}(I) (Å^2)	0.00277(8)	0.0052(1)
	Red. χ^2	4.498	4.399
	wR	4.43%	6.03%

[a] Space group: $Fm\bar{3}m$. Sn position, 4a: (0, 0, 0); Cs position, 8c: (0.25, 0.25, 0.25).

(Einstein) oscillator energy of ϵ = 3.58(4) meV and ϵ = 3.27(4) meV for Cs_2SnI_6 and Cs_2TeI_6, respectively, and is consistent with the presence of localized octahedral rotations.[208]

High-resolution synchrotron powder X-ray diffraction (SXRD) data collected for all members in the $Cs_2Sn_{1-x}Te_xI_6$ series at room temperature confirm solid-solution behavior. SXRD

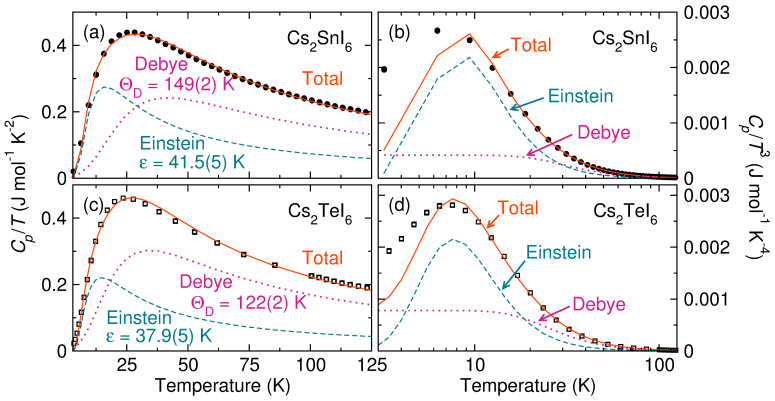

Figure 2.5: Heat capacity data of Cs_2SnI_6 (a,b) and Cs_2TeI_6 (c,d). The data are shown as filled black circles for Cs_2SnI_6 and open black squares for Cs_2TeI_6. The orange line is the total fit to the sum of the Debye and Einstein models of the heat capacity, and the separate contributions from each model are shown in pink dotted (Debye) and teal dashed (Einstein) lines. In (c) and (d) the data are shown at C_p/T^3 to highlight the deviation of the Debye model from the data at low temperatures.

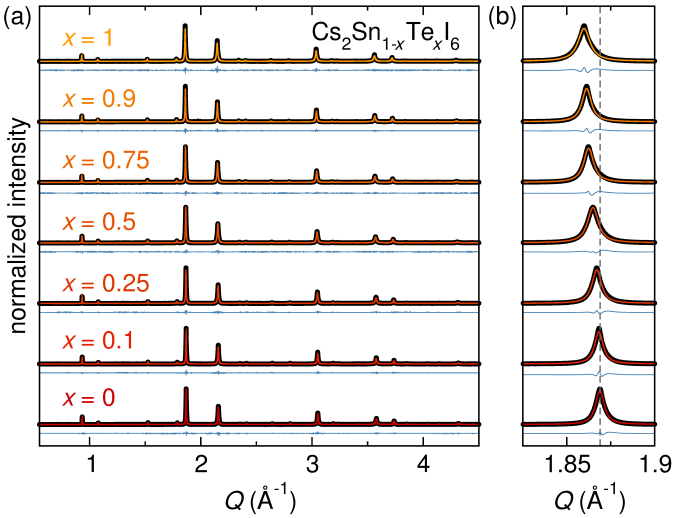

Figure 2.6: (a) High-resolution synchrotron X-ray diffraction data (11-BM) and Rietveld refinements of the solid solution series $Cs_2Sn_{1-x}Te_xI_6$ collected at room temperature (black circles represent data, colored lines represent the fit, and blue lines are difference curves). (b) The strongest reflection, {222} at $Q = 1.87$ Å^{-1} shifts to lower Q with increasing tellurium substitution.

data for the entire solid solution present reflections consistent with the cubic vacancy-ordered double perovskite structure (Figure 2.6a), and the noticeable shift in the reflection positions to lower Q with increasing x is consistent with an expansion of the unit cell upon substitution of the larger tellurium ion, as shown in Figure 2.6b. Structural models for the solid solution were constructed by modifying the Sn/Te occupancy to reflect the nominal stoichiometry uti-

lized during the syntheses. The resulting Rietveld refinements are shown in Figure 2.6, and the structural parameters and refinement statistics are compiled in Table 2.2.

Table 2.2: Structural parameters and refinement statistics for $Cs_2Sn_{1-x}Te_xI_6$ from Rietveld refinements of high-resolution synchrotron powder X-ray diffraction data.

x	0	0.1	0.25	0.5	0.75	0.9	1
stoichiometric x	0	0.101	0.2498	0.5007	0.7505	0.9003	1
a (Å)	11.64572(2)	11.64912(2)	11.65697(2)	11.67028(3)	11.68567(3)	11.69277(3)	11.70220(4)
I (x, 0, 0)	0.24516(4)	0.24579(5)	0.24668(5)	0.24809(5)	0.24916(5)	0.24984(5)	0.25039(6)
U_{iso}(Cs) (Å^2)	0.0402(2)	0.0401(2)	0.0413(2)	0.0415(2)	0.0434(3)	0.0433(2)	0.0447(3)
U_{iso}(B) (Å^2)	0.0276(3)	0.0331(3)	0.0308(3)	0.0299(3)	0.0290(3)	0.0270(3)	0.0302(4)
U_{11}(I) (Å^2)	0.0202(2)	0.0190(2)	0.0236(4)	0.0237(2)	0.0225(4)	0.0201(3)	0.0231(5)
$U_{22} = U_{33}$(I) (Å^2)	0.0444(1)	0.0458(1)	0.0450(2)	0.0446(1)	0.0470(2)	0.0484(2)	0.0489(3)
Red. χ^2	4.054	3.692	5.384	6.341	6.352	7.462	4.397
wR	7.49%	8.60%	7.99%	8.06%	8.04%	8.85%	8.60%

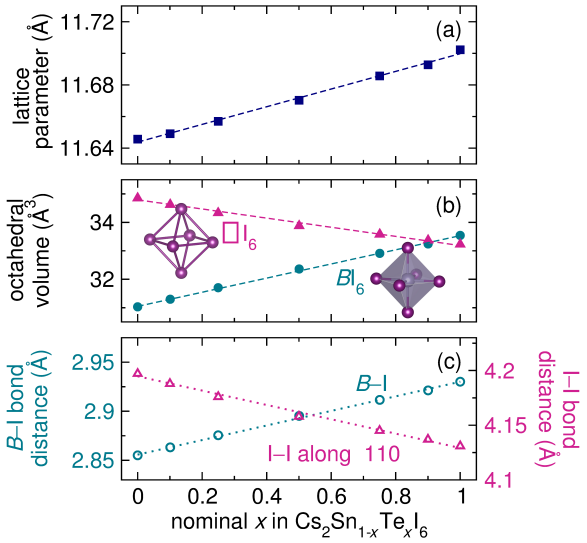

Figure 2.7: Crystal structure parameters across the solid solution series, $Cs_2Sn_{1-x}Te_xI_6$, as determined from high-resolution synchrotron X-ray diffraction at room temperature. (a) The refined lattice parameters are plotted as a function of nominal x in $Cs_2Sn_{1-x}Te_xI_6$. The dashed line represents Vegard's law interpolated from the end members. (b) The average polyhedral volumes of the BI_6 octahedra and $\square I_6$ void regions show that the voids become smaller as the [BI_6] octahedra become larger. (c) The average B–I bond distances and I–I contact distances along the ⟨110⟩ directions in the unit cell reflect the trend shown in (b). Dashed lines in (b) and (c) are linear regressions.

The refined lattice parameters follow a linear increase upon tellurium substitution, as shown in Figure 2.7a. While the increase in unit cell volume is not altogether unsurprising given

the increase in *B*-site ionic radius from r_{Sn} = 0.69 Å to r_{Te} = 0.97 Å,[206] the 0.5% increase in unit cell parameter is insufficient to account for the the 40.5% increase in ionic radius from Sn^{4+} to Te^{4+}. From the crystallographic analysis of the structures with only one free internal structural coordinate, the iodine position, (*x*, 0, 0), the larger Te^{4+} ion is accommodated into the structure with an increase of the average *B*–I bond length by 1.6% at the expense of the I–I contact distances between octahedra (inter-octahedral), as shown in Figure 2.7c.

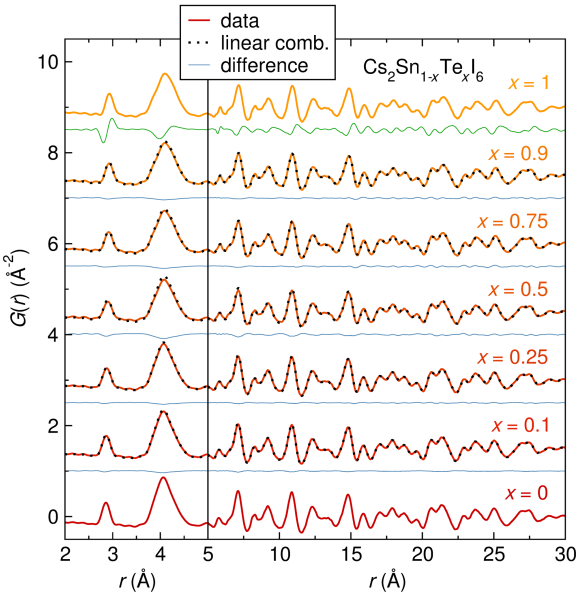

Figure 2.8: Synchrotron X-ray pair distribution function analysis of all compounds in the solid solution series from data collected at room temperature. The XPDF data for all compounds can be constructed by a linear combination of the XPDF data for the end members (*i.e.*, XPDF = (1–*x*)$XPDF_{Sn}$ + (*x*)$XPDF_{Te}$. The data are shown as solid colored lines, and the computed linear combinations for each member are overlain as a black dotted line. The difference between the data and the linear combinations are shown as blue lines. The difference curve shown below *x* = 1 (green line) is the difference between end-members and illustrates the apparent shift in bond lengths across the solid solution. Note the split *x*-axis to highlight the nearest-neighbor (*B*–I) and next-nearest-neighbor (I–I) pair correlations.

In order to rule out the presence of distortions in the local coordination environment or stereochemical lone-pair activity of the Te(IV) $5s^2$ electrons, the X-ray pair distribution function (XPDF) for each compound in the solid solution was computed from synchrotron X-ray total scattering data (beam line 11-ID-B). As shown in Figure 2.8, the XPDFs are nearly identical across the solid solution, with the exception of the increasing coordination distance of the

nearest neighbor (*B*–I) and decreasing coordination distance of the next-nearest neighbor (I–I) pair correlations, as highlighted in the left panel of Figure 2.8. Interestingly, we have found that the PDFs of the intermediate members of the solid solution can be modeled as a linear combination of the end member PDFs (*i.e.*, XPDF($Cs_2Sn_{1-x}Te_xI_6$) = (1–*x*)$XPDF_{Sn}$ + (*x*)$XPDF_{Te}$), which indicates that the local structure of the solid solution is identical to that of the end members. This analysis is shown in Figure 2.8. The XPDFs extracted from the experimental data are shown as colored lines and the computed linear combinations are overlain as dotted lines. The differences between the data and the linear combination analyses are shown as blue lines below.

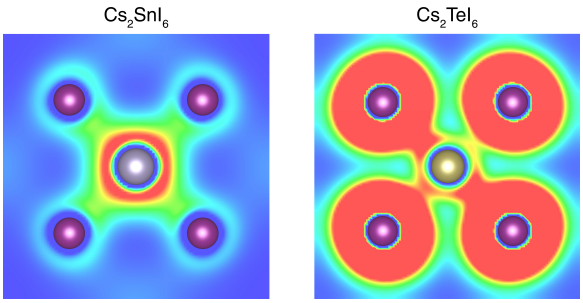

Figure 2.9: Charge density isosurfaces of the occupied ns^2 states in Cs_2SnI_6 and Cs_2TeI_6. Sn, Te, and I atoms are denoted by grey, gold, and purple spheres, respectively. Contours shown from 0 (blue) to 0.002 eV Å^{-3} and 0.0034 eV Å^{-3} (red) for Cs_2SnI_6 and Cs_2TeI_6, respectively.

Density functional calculations of the longitudinal optical-transverse optical phonon (LO-TO) splitting for Cs_2SnI_6 and Cs_2TeI_6 further support the experimental observation that the ns^2 electrons are stereochemically-inactive, and are in good agreement with LO-TO splittings determined experimentally.[209] As shown in Table 2.3, the largest splitting across both compounds is 21 cm^{-1}, which is similar in magnitude to other materials with stereochemically inactive lone-pairs such as PbTe (52 cm^{-1})[210] and significantly smaller than in materials with distorted local geometries, such as GeS (322 cm^{-1})[211] and the cubic perovskite oxides (typically $\sim$ 700 cm^{-1}).[212] Analysis of the charge-density isosurface for the electron density range containing the Sn and Te $5s^2$ electrons reveals no asymmetry in the electron density surrounding

the metals (Figure 2.9). As such, it is clear that the compounds studied here do not display a tendency to structurally distort due to lone-pair stereochemical activity.

Table 2.3: LO-TO splitting (cm^{-1}) in the phonon spectrum of Cs_2SnI_6 and Cs_2TeI_6.

Cs_2SnI_6	0.3, 3.4, 9.4, 10.8, 20.7
Cs_2TeI_6	0.3, 4.2, 11.6, 14.9

2.3.3 Optical Spectroscopy and Electronic States

UV-visible diffuse reflectance spectroscopy performed on powdered samples illustrates an increase in optical gap from Cs_2SnI_6 to Cs_2TeI_6 across the solid solution. While Tauc analysis is often used to extract the nature (direct vs. indirect) and magnitude of the band gap from diffuse reflectance data, the method often underestimates the band gap of most crystalline semiconductors, particularly those that are degenerately doped or which exhibit delocalized electronic states.[213] Therefore, the energy of the absorption onsets determined by UV-visible diffuse reflectance spectroscopy is used to approximate the optical gaps of these materials. The reflectance data were converted to absorbance, and the baseline and onset regions were fit to linear functions. The optical gap was determined by the intersection of the two fits, which yields the non-linear relationship shown as the orange circles in Figure 2.10. Values for the optical gaps were additionally extracted by transforming the raw reflectance data to the Kubelka-Munk function, F(R), and fitting a line to the onset region and extrapolating to zero absorbance. Additionally, the data were converted from reflectance to absorbance and normalized from hν = 1.25–4 eV. A line was fit to the onset region and extrapolated to zero absorbance to yield a value for the optical gap by this method. The range of values obtained by these methods are represented by the blue bars in Figure 2.10 and are shown to highlight the ambiguity in determination of the optical gaps by diffuse reflectance spectroscopy.

Two previous studies of Cs_2SnI_6 report a band gap magnitude of ~ 1.3 eV but disagree regarding the assignment of direct vs. indirect band gap,[3,11] while another report suggests a direct

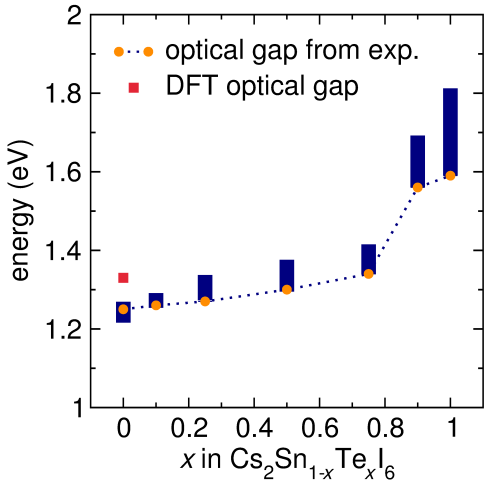

Figure 2.10: Optical gaps of the solid solution series determined from UV-visible diffuse reflectance data. The optical gaps (shown as yellow circles) are determined by converting the reflectance data to absorbance, fitting linear functions to the baseline and onset regions of the data, and determining the intersection. The blue bars represent a range of values for optical gaps determined by extracting the data by various methods and are shown to highlight the ambiguity in determining the value of the optical gap by diffuse reflectance spectroscopy. The red square represents the magnitude of the DFT-calculated optical gap arising from the dipole-allowed transition below the valence band maximum (See Figure 2.13).

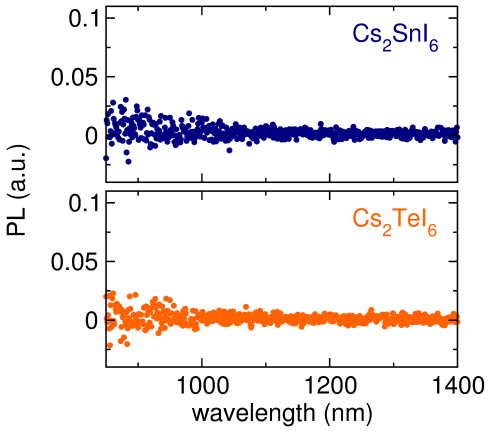

Figure 2.11: Room-temperature photoluminescence (PL) measurements of (a) Cs_2SnI_6 and (b) Cs_2TeI_6.

band gap of 1.6 eV for thin-film samples.[12] The analysis performed here suggests an optical gap of ~ 1.25 eV for Cs_2SnI_6. The same analysis for Cs_2TeI_6 gives an optical gap of ~ 1.59 eV, which is in reasonable agreement with the previously reported indirect band gap of 1.5 eV.[214] However, determination of the optical gap for Cs_2TeI_6 is complicated by the presence of exciton-like features near the absorption edge, which are also consistent with single-ion excited states arising from the Te(IV) $5s^2$ electron configuration.[215–218] Photoluminescence (PL) measurements

attempted on a cold-pressed polycrystalline pellet of Cs_2SnI_6 and Cs_2TeI_6 did not show any measurable PL intensity, as shown in Figure 2.11. We note that PL was observed in thin-films of Cs_2SnI_6,[12] and thus we anticipate that the lack of signal is due to phonon quenching and differences arising from bulk vs. thin film nature of the specimens.

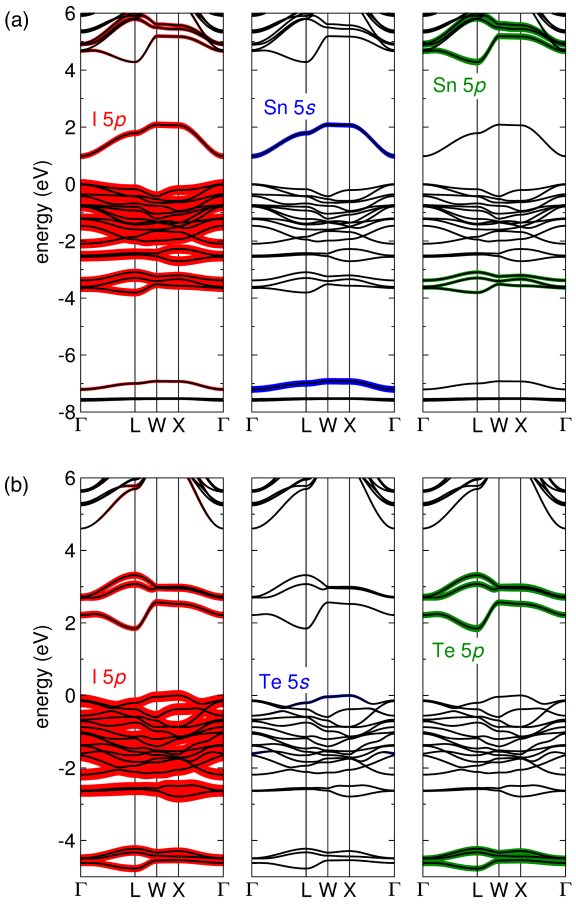

Figure 2.12: Band structures, including orbital projection analysis, of (a) Cs_2SnI_6 and (b) Cs_2TeI_6, showing the contributions of: the I p states in red, the B 5s states in blue, and the B 5p states in green.

As shown in Figure 2.10, the optical gaps of these materials shift to higher energy with increased tellurium substitution. Between $x = 0$ and $x = 0.75$, the gaps increase steadily (and nearly linearly), and the spectra present well-defined onset regions. The optical gaps of the $x = 0.9$ and $x = 1$ compounds do not follow the linear trend; however, determination of the optical gaps for the $x = 0.9$ and $x = 1$ members of the solid solution is somewhat ambiguous, given the presence of peaks near the absorption edge. With that being said, the optical gaps are monotonically in-

creasing across the solid solution and do not follow a parabolic band-bowing relationship [*e.g.*, $E_g = (1-x)E_g^{\mathrm{Sn}}(x) + xE_g^{\mathrm{Te}}(x) - bx(x-1)$], as often observed in solid-solutions.[219–222]

Density functional calculations of the electronic structures provide insight to the experimental observations. The calculations were performed using the Vienna *Ab initio* simulation package (VASP),[176–179] with the HSE06 hybrid functional[181] to provide an accurate description of the electronic structure; the calculations also included an explicit treatment of spin-orbit coupling (SOC) effects. The band structures are shown in Figure 2.12. The band structure of Cs_2SnI_6 illustrates a direct band gap, E_g^{dir} = 0.97 eV, at the Γ-point, which is smaller than the experimentally-observed optical gap of E_{opt} = 1.25 eV. Calculation of the optical absorption reveals an onset that occurs at 1.33 eV, which is considerably larger than the direct band gap of 0.97 eV (Figure 2.10, red square). The direct VB-CB optical transition at the Γ-point is dipole forbidden in Cs_2SnI_6, as illustrated in Figure 2.13.[223–225] As such, prior reports may have employed artificially large amounts of Hartree-Fock exchange to fit the fundamental band gap to the experimental optical gap.[12,103,105] In agreement with the HSE06+SOC calculations presented here, *GW0* calculations of Cs_2SnI_6 indicate a direct band gap of 0.88 eV.[209]

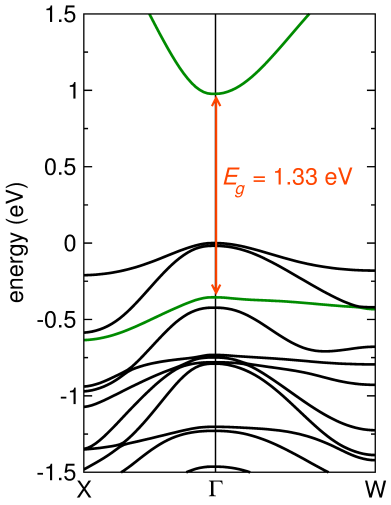

Figure 2.13: Band structure of Cs_2SnI_6 depicting the fundamental band gap at Γ. The bands resulting in the fundamental allowed optical band gap are indicated in green. The valence band maximum is set to 0 eV.

The band structure of Cs_2TeI_6 indicates an indirect band gap with a magnitude E_g^{ind} = 1.83 eV, which is larger than the experimentally-observed optical gap of 1.59 eV. In Cs_2TeI_6, the highest occupied and lowest unoccupied bands appear at the X and L points in the first Brillouin zone, respectively, with the direct band gap (E_g^{dir} = 2.05 eV) occurring at L. The discrepancy between the DFT-calculated band gap and the experimentally-determined optical gap may arise from the fact that VASP calculations do not take into account absorption arising from configuration interactions with different excited states,[215–218] which may obscure the absorption edge.

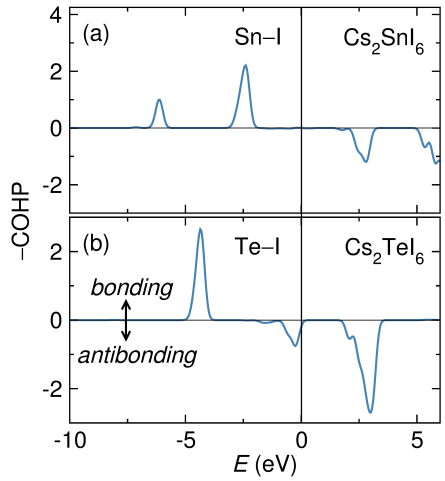

Figure 2.14: Crystal orbital Hamilton population (COHP) analysis of (a) Cs_2SnI_6 and (b) Cs_2TeI_6, in which the density of states is partitioned for Sn–I and Te–I interactions, with the sign indicating bonding or anti-bonding character, and the magnitude related to the strength of the interaction. The valence band maximum is set to 0 eV.

Analysis of the orbital character of Cs_2SnI_6 and Cs_2TeI_6 reveals that the highest occupied bands in both compounds are comprised of I 5*p* character (Figure 2.12). For Cs_2SnI_6, the states at the highest occupied band are primarily non-bonding, but are anti-bonding in character for Cs_2TeI_6, as determined by crystal orbital Hamilton population (COHP) analysis of the *B*–I interactions (Figure 2.14).[191] Similar to previous hybrid DFT studies on Cs_2SnI_6,[103,105] there are occupied Sn 5*s* states around 7 eV below the highest occupied band due to the strong covalent interaction between Sn and I.[105] For Cs_2TeI_6, the conduction band is of anti-bonding Te 5*p*

and I 5p character (Figure 2.14), as consistent with the formal charge, Te(IV), that would have occupied 5s and unoccupied 5p states. The occupied 5s states in Cs_2TeI_6 are predominately localized around $E \sim -12$ eV, but also have a small projection just below the Fermi energy.

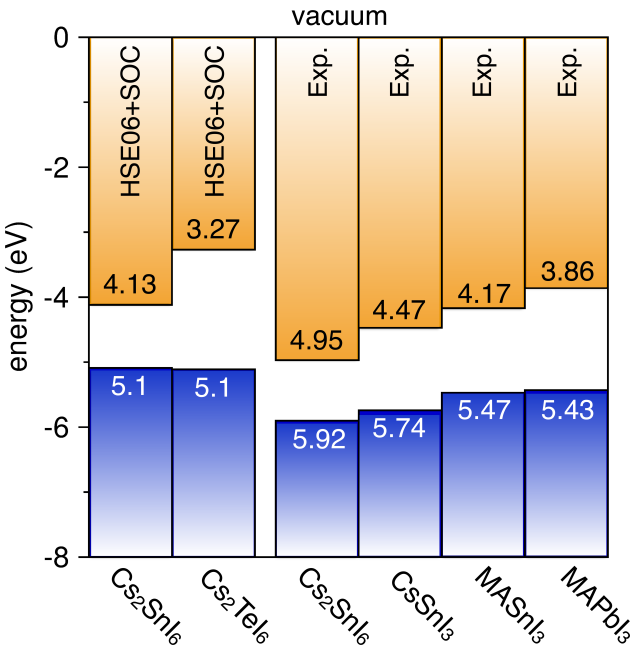

Figure 2.15: Comparison of DFT-calculated band alignments for Cs_2SnI_6 and Cs_2TeI_6 (HSE06 + SOC) to experimentally-determined band alignments. The experimental valence band maximum position of Cs_2SnI_6 was determined by XPS and the conduction band minimum was positioned 0.97 eV above (HSE06 + SOC band gap). The experimental values are shown for $CsSnI_3$,[3] $MASnI_3$,[4] and $MAPbI_3$[5] (where MA = $CH_3NH_3^+$).

From analysis of the calculated electronic structures, the band gaps and optical gaps in these materials are dictated by the energies of the empty Sn 5s and Te 5p states at the lowest unoccupied band (as illustrated in Figure 2.15). The calculated ionization potentials of both Cs_2SnI_6 and Cs_2TeI_6 are ~5.1 eV, with the I 5p states comprising the highest occupied bands, thus providing support that the valence band energy levels are pinned across the solid-solution. The electron affinities (EA) of each material, 4.13 eV and 3.27 eV, respectively, are therefore controlled by the energy of the unoccupied states of Sn or Te. Density functional calculations of the band gaps across the solid solution (25%, 50%, 75%, 88%, and 91% Te concentration) are consistent with this notion, and show a nearly linear increase in band gap across the solid so-

lution (Figure 2.16). In contrast to the calculated band gaps, the experimentally-determined optical gaps increase steadily from $x = 0$ to $x = 0.75$ until a rapid increase for $x = 0.9$ and $x = 1$. One possible explanation for the non-linear trend in optical gaps arises from the nature of the optical transition compared to the fundamental band gap. As discussed previously, the DFT calculations reveal that the optical gap of Cs_2SnI_6 is derived from dipole-allowed transitions originating from below the valence band maximum. These transitions may persist across part of the solid solution, which would yield discrepancies between the experimental and calculated band gaps. Another possibility arises from the introduction of Te-derived states ~ 0.85 eV above the conduction band minimum upon substitution of Te for Sn in Cs_2SnI_6. These states may not immediately influence the magnitude of the band gap until the concentration of tellurium exceeds the percolation threshold for the face-centered cubic lattice (12% Sn, 88% Te),[226] at which point the optical gap becomes reflective of the larger, indirect gap of Cs_2TeI_6.

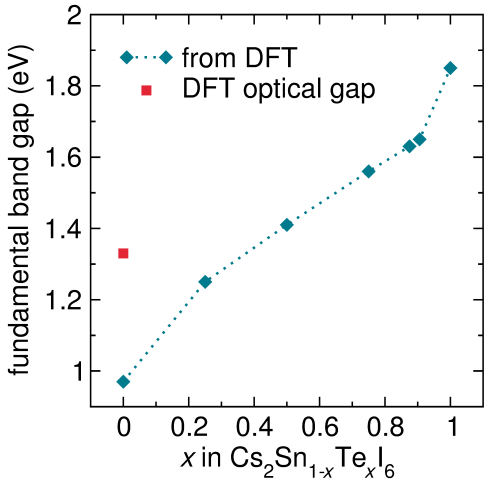

Figure 2.16: Fundamental band gaps calculated using HSE06+SOC for several members of the solid solution. The calculated dipole-allowed optical transition for Cs_2SnI_6 is shown as a red square for reference.

X-ray photoelectron spectroscopy (XPS) was performed to align the ionization potential with related perovskite halides (Figure 2.17). The ionization potential is –5.92(5) eV, as shown in Figure 2.15, and is in good agreement with previous measurements of bulk powders of Cs_2SnI_6 (–5.40 eV,[11] –5.94 eV[3]), but not with thin-film samples (–6.1 eV[12]). Here, the conduction band

was positioned using the 0.97 eV band gap calculated using DFT (HSE06+SOC). The discrepancy between calculation and experiment is likely due to the extreme sensitivity of Cs_2SnI_6 to the nature of the exchange correlation functional used in the density functional calculations and/or from the surface sensitivity of the XPS measurements.

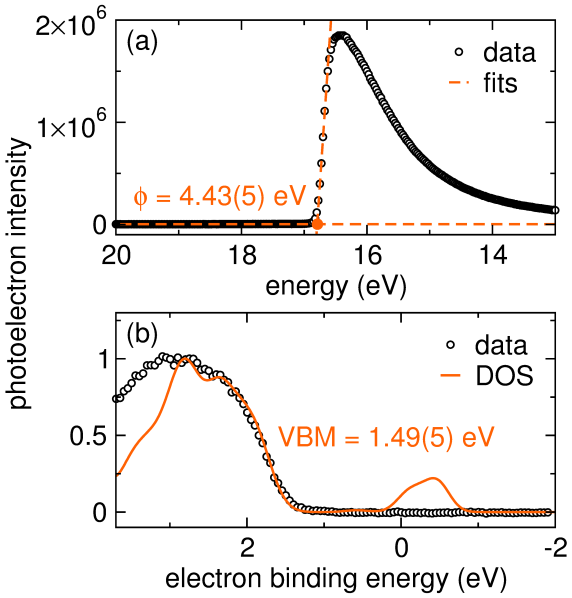

Figure 2.17: X-ray photoelectron spectroscopy data for Cs_2SnI_6. (a) The work function is extrapolated from the secondary electron cutoff. (b) The DOS convoluted with a 350 meV Gaussian allows interpolation of the XPS data to yield the valence band maximum with respect to Fermi level.

The band structures of both Cs_2SnI_6 and Cs_2TeI_6 present fairly dispersive conduction band states, indicative of significant orbital overlap despite the presence of ordered *B*-site vacancies. Calculation of the electron effective masses for Cs_2SnI_6 yield $m_e^* = 0.48\ m_0$ (along $\Gamma \rightarrow$ X, in the [0.5 0 0.5] direction) and $m_e^* = 0.92\ m_0$ ($\Gamma \rightarrow$ L, along [0.5 0.5 0.5]), reflecting its intrinsic *n*-type behavior. The hole effective masses are considerably larger: $m_h^* = 1.32\, m_0$ ($\Gamma \rightarrow$ X) and $m_h^* = 2.75\ m_0$ ($\Gamma \rightarrow$ L). These calculations are consistent with recently reported calculations.[12] Cs_2TeI_6 presents highly anisotropic electron and hole effective masses, with the lightest masses appearing along L $\rightarrow$ W ($m_e^* = 0.22\ m_0$) and X $\rightarrow \Gamma$ ($m_h^* = 0.97\ m_0$) and the other directions producing significantly heavier charge carriers: $m_e^* = 1.40\ m_0$ (L $\rightarrow \Gamma$) and $m_h^* = 4.40\ m_0$ (X $\rightarrow \Gamma$). The electron effective masses in these systems are all relatively light, albeit larger than that seen

in the hybrid perovskites $CH_3NH_3PbI_3$ and $CH_3NH_3SnI_3$ ($m_e^* = 0.15\ m_0$ and $0.28\ m_0$).[140,227] Interestingly, unlike in the hybrid perovskites where the hole effective masses are smaller than the electron effective masses ($m_h^* = 0.12\ m_0$ and $0.13\ m_0$ for $CH_3NH_3PbI_3$ and $CH_3NH_3SnI_3$, respectively),[140,227] here no such trend is observed. The lighter electron effective masses in Cs_2TeI_6 correlates with the reduced inter-octahedral distances observed in the crystal structures. The reduced electrical conductivity in tellurium-doped Cs_2SnI_6, despite the presence of dispersive conduction band states and small electron effective masses, suggests that the origin of this insulating behavior instead arises from the nature of carrier generation and mobility from intrinsic defects.

2.3.4 Intrinsic Defects

By varying the chemical potentials, μ_i, as calculated from DFT, we can simulate the effect of experimentally varying the partial pressures in the formation of Cs_2SnI_6 and Cs_2TeI_6 and the resulting native defects. The accessible range of chemical potentials for Cs_2SnI_6 and Cs_2TeI_6, are shown in Figure 2.18 in a two-dimensional (μ_{Cs}, μ_{Te}) plane.[228,229] Through varying the chemical potentials, μ_i, we can simulate the effect of experimentally varying the partial pressures in the formation of Cs_2SnI_6 and Cs_2TeI_6. These potentials are defined within the global constraint of the calculated enthalpy of the host, in this case: Cs_2SnI_6: $2\mu_{Cs} + \mu_{Sn} = \Delta H_f^{Cs_2SnI_6}$ and Cs_2TeI_6: $2\mu_{Cs} + \mu_{Te} = \Delta H_f^{Cs_2TeI_6}$. To avoid precipitation into solid elemental Cs, I, and Sn or Te, we also require $\mu_{Cs} \leq 0$, $\mu_I \leq 0$, $\mu_{Sn} \leq 0$, and $\mu_{Te} \leq 0$. Lastly, the chemical potentials are further constrained in order to avoid decomposition into a range of binary and ternary compounds. In the case of Cs_2SnI_6 these are: $\mu_{Cs} + \mu_{Sn} + 3\mu_I = \Delta H_f^{CsSnI_3}$, $\mu_{Sn} + 4\mu_I = \Delta H_f^{SnI_4}$, $\mu_{Cs} + \mu_I = \Delta H_f^{CsI}$, and $\mu_{Cs} + 3\mu_I = \Delta H_f^{CsI_3}$. On the other hand, Cs_2TeI_6 is limited by: $\mu_{Cs} + 4\mu_I = \Delta H_f^{CsI_4}$, $\mu_{Cs} + 3\mu_I = \Delta H_f^{CsI_3}$, $\mu_{Cs} + \mu_I = \Delta H_f^{CsI}$, and $\mu_{Te} + 4\mu_I = \Delta H_f^{TeI_4}$.

Previous studies have performed similar calculations using the HSE functional but have adjusted the amount of non-local Hartree-Fock exchange (α) to fit the fundamental band gap to the experimental optical band gap, without consideration of the optical allowed transitions.

However, as we have demonstrated, the fundamental band gap of Cs_2SnI_6 is dipole disallowed and HSE06 does not need to be altered to yield a reasonable description of the electronic structure of Cs_2SnI_6. As such, the close agreement between the calculated HSE06 electronic properties and the experimental optical band gap gives us confidence in our model.

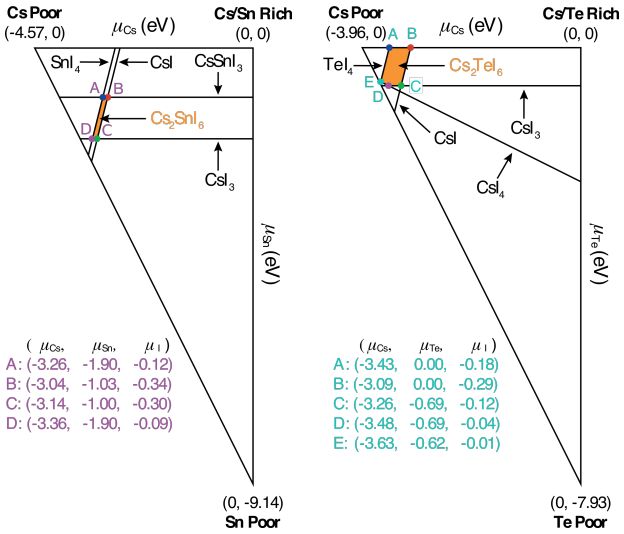

Figure 2.18: Illustration of the accessible chemical potential ranges of (a) Cs_2SnI_6 and (b) Cs_2TeI_6. Constraints imposed by the formation of competing binary and ternary compounds result in the stable region indicated in orange.

Focusing on the formation of *n*-type defects to provide a theory-based understanding of the experimental data, calculations of Cs_2SnI_6 indicate that the formation energies of iodine vacancies (V_I) are small (0.14–0.39 eV). Additionally, the +1/0 transition level is only 0.07 eV below the lowest unoccupied band and is therefore likely to be the source of the native *n*-type conductivity observed in this material. While previous defect calculations of Cs_2SnI_6 have identified iodine vacancies as deep donor states with an ionization level of 0.52 eV,[103] the large size of the supercells used in our calculations as well as the improved accuracy of the fundamental band gap provides a representation of these defect states consistent with the intrinsic *n*-type conductivity and equilibrium carrier concentration on the order of $\sim 10^{16}$ cm^{-3}.[230] Cs_2SnI_6 appears to be intrinsically doped and is tolerant of the native iodine vacancy defects.

Cs_2TeI_6, on the other hand, yields an electronic structure that is less amenable for introducing mobile carriers. The formation energy of V_I in Cs_2TeI_6 is much larger (0.56–0.84 eV) than in Cs_2SnI_6, which is likely responsible for the reduction in carrier concentration and insulating behavior upon tellurium substitution (Figure 2.19). The factor of 2-to-4-fold increase in defect formation enthalpy translates to a reduction in defect concentration by $\sim 10^6$–10^8 upon substitution of Sn by Te. Furthermore, the energy of the (+1/0) transition level is effectively pinned across the solid solution at $E = 0.9$ eV above E_F. Therefore, the depth of the defect level is largely dependent upon the energy of the empty B states that comprise the lowest unoccupied bands. In Cs_2SnI_6, V_I defect states form ~ 0.07 eV below the unoccupied Sn 5s states, and therefore can behave as donor states. In Cs_2TeI_6, the defect transition level is deep in the band gap, with the lowest unoccupied band ~ 0.85 eV higher in energy, such that the native defects are likely to behave as deep trap states for charge carriers. These dramatic changes can account for the reduction in carrier concentration, mobility, and thus conductivity upon tellurium substitution.

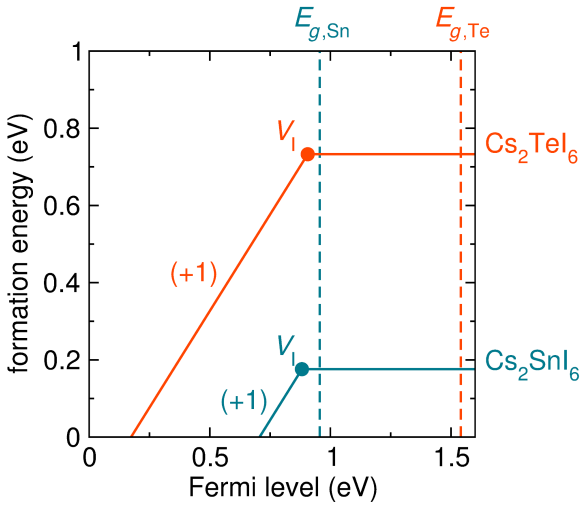

Figure 2.19: Formation energies for iodine vacancies in Cs_2SnI_6 (teal) and Cs_2TeI_6 (orange), under tin-poor conditions (point C in Figure 2.18). Sloped lines indicate the +1 charge state, and the solid dots represent the transitions levels $\epsilon(q/q')$. The dashed lines represent the fundamental band gap of each material.

The general structure-property relationships in these materials follow from the close-packed anionic lattice and the interaction between the B-site ions and the halides. The main

difference between the electronic band structures of Cs_2SnI_6 and Cs_2TeI_6 is the position and symmetry of the conduction band, since the valence bands are pinned by the I 5*p* states. The increased Pauling electronegativity of Te^{4+} (χ = 2.1) compared to Sn^{4+} (χ = 1.8)[231] increases the covalency of the [TeI_6] octahedral units relative to [SnI_6]. This notion is further supported by Bader charge analysis of Cs_2SnI_6 and Cs_2TeI_6 (Table 2.4), which shows reduced Bader charges for Te relative to Sn. The average integrated COHP (ICOHP) value for each *B*–I bond was found to be –3.4 and –2.0 for Cs_2SnI_6 and Cs_2TeI_6. This would suggest a more covalent interaction for the Sn–I bonds relative to the Te–I bonds; however, we note that this computational result likely results from the shorter bond lengths in Cs_2SnI_6. The Born effective charges for the *B*-site cation in Cs_2SnI_6 and Cs_2TeI_6 are 3.9 and 4.4, respectively, which indicate a higher degree of covalency for the Te–I bonds[232] in support of the Bader charge analysis and the Pauling electronegativities.

While the close-packed iodine sublattice is responsible for the dispersive conduction band states, increased covalency of the Te–I bonds relative to Sn–I affect the electronic structure and defect chemistry in these materials. The increased covalency of Te–I bonding likely prevents the formation of iodine vacancies in the material and raises the energy of the conduction band, which yields defect states that form deep within the band gap. While the smaller band gap and more ionic [SnI_6] units in Cs_2SnI_6 yields a defect-tolerant material with shallow donor states, the larger band gap and more molecular [TeI_6] units render the material intolerant to crystallographic defects.

Table 2.4: Bader charges generated for Cs_2SnI_6 and Cs_2TeI_6.

	Cs	*B*	I
Cs_2SnI_6	0.84	1.31	–0.50
Cs_2TeI_6	0.84	0.89	–0.43

2.4 Conclusions

Vacancy-ordered double perovskite halides present a fertile testbed to explore structure-property relationships in complex semiconductors with potential for transformative applications in photovoltaics. From the preparation of the solid-solution of $Cs_2Sn_{1-x}Te_xI_6$, the end member, Cs_2SnI_6, exhibits intrinsic *n*-type conductivity, yet substitution of tin by tellurium is accompanied by a reduction in conductivity, carrier concentration and carrier mobility. The poor conductivity of Cs_2TeI_6 is attributed mostly to the electronic structure and hindered formation of intrinsic iodine vacancy donor defects, despite a predicted increase in carrier mobility, as further supported from hybrid-functional DFT calculations. This conclusion is based upon extensive structural characterization by high-resolution time-of-flight neutron powder diffraction, synchrotron powder X-ray diffraction, and X-ray pair distribution function analysis, which together, reveal that tellurium does not induce structural distortions or instabilities across this series of materials, as one might hypothesize from the potential for stereochemical activity of the formal $5s^2$ valence electron configuration. Even when there is no three-dimensional covalent *B*–*X*–*B* connectivity in the crystal structure, the close-packed anionic lattice of large halides (such as iodine) forms dispersive frontier electronic bands with light carriers, provided that the *B*-site ions occupying the interstitial voids provide the right bonding environment to stabilize the highly-symmetric structure *and* to stabilize shallow defect states to provide mobile charge carriers.

Chapter 3

Anharmonicity and Octahedral Tilting in Hybrid Vacancy-Ordered Double Perovskites[3]

3.1 Introduction

Perovskite halides are a technologically relevant family of crystalline materials for optical and electronic applications including light-emitting diodes and photovoltaics.[233] Significant research interest in perovskite halide semiconductors has been spurred by the demonstration of up to 20% efficiency of photovoltaic devices containing the hybrid organic-inorganic perovskite methylammonium lead iodide ($CH_3NH_3PbI_3$).[134] The high efficiency of hybrid perovskite photovoltaic devices is attributed to unique properties such as tolerance to crystallographic defects[1,161] and long excited state carrier lifetimes.[21,51,234] The excellent performance of main group metal halide perovskites in thin-film photovoltaic devices motivates further study of these materials, in an effort to elucidate a fundamental crystal-chemical understanding of their advantageous properties.

The conventional ABX_3 perovskite structure is characterized by corner-sharing $[BX_6]$ octahedra with the *A*-site cation residing in the cuboctahedral void formed by twelve neighboring *X*-site anions. In perovskite halides, the *B*-site is typically occupied by a main-group metal such as Pb^{2+} or Sn^{2+}, while the *X*-site is a halide (Cl^-, Br^-, or I^-). The *A*-site is occupied by a monovalent cation such as Cs^+ or larger, dipolar organic cations such as methylammonium ($CH_3NH_3^+$) or formamidinium ($CH(NH_2)_2^+$). In most perovskite halide semiconductors, the electronic states of the $[BX_6]$ octahedral framework comprise the valence and conduction band

[3]Substantial portions of this chapter have been reproduced with permission from A. E. Maughan, A. M. Ganose, A. M. Candia, J. T. Granger, D. O. Scanlon, and J. R. Neilson, *Chem. Mater.*, **2018**, *30*, 472–483.[6]

edges and dictate light absorption and charge transport processes,[186,235,236] while the *A*-site cation serves to stabilize the octahedral perovskite framework.[81]

A unique feature of main-group metal perovskite halides, compared to conventional compound semiconductors, is the "softness" of the lattice. Deformations of the [$PbBr_6$] octahedral framework in $CH_3NH_3PbBr_3$ and $CsPbBr_3$ enable the formation of large polarons that may protect charge carriers and prolong excited state lifetimes.[58] This notion provides an explanation for long carrier diffusion lengths despite having modest carrier mobilities.[25,60] Recently, it has been hypothesized that carrier mobilities may be further reduced in $CH_3NH_3PbX_3$ perovskites compared to $CsPbX_3$ via "dielectric drag," in which movement of charges necessitates molecular reorientations of $CH_3NH_3^+$ cations.[77] These molecular reorientations have been shown to occur on picosecond timescales and are coupled to the dynamics of the surrounding inorganic framework.[62–64,66,71] Given that the dynamics of the organic cations are intimately coupled to the soft inorganic lattice,[52,65,67] decoupling cooperative octahedral tilting modes of the soft inorganic framework from molecular dynamics presents a challenge for understanding the underlying charge transport behavior of hybrid perovskites.

Defect-ordered perovskites provide a structural framework to study organic-inorganic coupling in a lattice with relatively decoupled octahedra. Vacancy-ordered double perovskites are a family of perovskite derivatives with the general formula $A_2B\square X_6$, where $\square$ represents a vacancy. The structure is formed by removing every other *B*-site cation from the fully-occupied perovskite to yield rock-salt ordering of [$\square I_6$] and isolated [BX_6] octahedral units. Despite the absence of octahedral connectivity, the semiconductor Cs_2SnI_6 exhibits a direct optical gap of about 1.3 eV and native *n*-type conductivity.[7,11] The origin of this behavior lies in the close-packed iodine sub-lattice, which provides a dispersive conduction band. Similarly to conventional perovskite materials, the valence and conduction band edges are derived from the inorganic framework.[7,9] As states of the *X*-site anion comprise the edges of both the valence and conduction bands, substitution at the *X*-site will subsequently affect charge transport and optical absorption properties through changes in band dispersion.[9] This has been illustrated in

the series Cs_2SnX_6 where $X = I^-$, Br^-, Cl^-; incorporation of the smaller and more electronegative Cl^- and Br^- anions increases the magnitude of the band gap and reduces charge transport through reduced conduction band width.[209] Further, substitution at the *B*-site dictates the nature (direct vs. indirect) and magnitude of the band gap, as well as tolerance to intrinsic defects, as has been shown in the solid solution series $Cs_2Sn_{1-x}Te_xI_6$.[7] Though the electronic states of the *A*-site cation do not comprise the band edges, changing the size of the *A*-site cation can indirectly influence electronic and optical behavior by changing the close-packing of the halogen sub-lattice through cooperative rotations of the octahedral units to lower symmetry, as is illustrated by the A_2TeI_6 series ($A = K^+$, Rb^+, Cs^+). While Cs_2TeI_6 adopts the cubic vacancy-ordered double perovskite structure,[7] cooperative octahedral tilting to lower symmetries is favorable to improve coordination to the smaller Rb^+ and K^+ ions.[9,83,84] These cooperative octahedral tilting distortions are also observed as a series of structural phase transitions from cubic ($Fm\bar{3}m$) to tetragonal ($P4/mnc$) to monoclinic ($P2_1/n$) upon cooling, due to condensation of the octahedral rotary phonon mode.[85,208] The temperature dependence of these phase transitions trends with the "radius ratio" of the radius of the *A*-site cation to the radius of the enclosing 12-coordinate void; smaller *A*-site cations tend to yield higher transition temperatures.[80] These phase transitions may be further affected by introduction of molecular species such NH_4^+ or alkylammonium cations which are capable of hydrogen-bonding interactions with the surrounding *X*-site framework and thus can influence the temperature-dependence, phase transition mechanism, and low-temperature structural behavior by coupling to the rotational dynamics of the $[BX_6]$ octahedral units.[95–97,237]

In this work, we have exploited the isolated octahedral framework of the "soft" vacancy-ordered double perovskite structure to understand the influence of organic-inorganic coupling on the structural, optical, and electronic properties of these materials. We have synthesized the series of vacancy-ordered double perovskites A_2SnI_6, where $A = Cs^+$, $CH_3NH_3^+$ (methylammonium), and $CH(NH_2)_2^+$ (formamidinium) and have drawn connections between crystallographic structure, local bonding environment, and optical and electronic behavior. Cs_2SnI_6 ex-

hibits native *n*-type conductivity,[7,11,103] yet replacement of Cs^+ with the polar organic $CH_3NH_3^+$ and $CH(NH_2)_2^+$ cations reduces both carrier concentration and carrier mobility across the series. Despite nearly identical crystal structures observed by powder X-ray diffraction, the local coordination environment reveals deviations in the inter-octahedral I–I distances seen in X-ray pair distribution function analysis due to anharmonic lattice dynamics, which is modeled as rotational disorder of the $[SnI_6]$ octahedral units. This anharmonicity is enhanced in the hybrid $(CH_3NH_3)_2SnI_6$ and $(CH(NH_2)_2)_2SnI_6$ compounds, which we attribute to the formation of hydrogen bonds and coupled organic-inorganic dynamics. Soft, anharmonic lattice dynamics give rise to stronger electron-phonon coupling and reduced carrier mobilities, as supported by calculation of Hellwarth electron mobilities within a temperature-dependent polaron transport model, to which we attribute the trends in electronic behavior across the series. The combination of organic cations within a framework of relatively decoupled octahedra provides insight into the influence of organic-inorganic coupling on the optical and electronic behavior of perovskite halide semiconductors.

3.2 Methods and Materials

Note on author contributions: This chapter was published in *Chemistry of Materials*, **2018**, volume 30, pages 472–483 by Annalise E. Maughan, Alex M. Ganose, Andrew M. Candia, Juliette T. Granger, David O. Scanlon, and James R. Neilson. AEM, AMC, and JTG performed the syntheses and experiments and AMG and DOS performed density functional calculations. AEM and JRN analyzed the data. AEM wrote the initial draft of the manuscript, and JRN supervised the project. All authors contributed to editing and finalization of the manuscript.

Methylamine hydrochloride (~0.5 g) was added to 2.0 mL of hydriodic acid (57%, aqueous, 1.5% H_3PO_2) and 3.0 mL of absolute ethanol and stirred to dissolve. Once dissolved, the solution was cooled in an ice bath while stirring. The cooled solution was crashed with diethyl ether to yield a sparkly white precipitate. The precipitate was washed thoroughly with diethyl ether to remove any trace of yellow color and collected by centrifugation. The product was

dried overnight. Energy dispersive X-ray spectroscopy yields a molar ratio of [Cl]:[I] content as 0.04(2).

Formamidinium acetate (~ 1 g) was added to 10 mL of absolute ethanol and 2.50 mL of hydriodic acid (57%, aqueous, 1.5% H_3PO_2). The solution was heated gently to T = 50 °C until the solid had fully dissolved. Once dissolved, the solution was crashed with diethyl ether to yield a white precipitate. The product was then recrystallized 4-5 times from ethanol to yield pure formamidinium iodide.[238] The purification step proves critical for later syntheses. In particular, early recrystallization products often contained an unidentified impurity evidenced by a peak in the powder diffraction pattern at $Q \simeq 1.5$ Å^{-1} that does not index to the reported crystal structure of formamidinium iodide and persists through later syntheses of $(CH(NH_2)_2)_2SnI_6$. Repeated recrystallizations remove this impurity and yield a powder diffraction pattern consistent with the reported crystal structure.[238] Proton NMR spectra of the final product dissolved in D_2O are consistent with the previously published NMR spectrum of pure formamidinium iodide.[239]

Tin metal (0.3108 g, 2.62 mmol) and iodine (1.3347 g, 5.26 mmol) were reacted in an evacuated fused silica ampoule (P < 10 mTorr). The ampoule was heated in a furnace at 200 °C for 60 h, or until the purple vapor had subsided, which was air-quenched to yield bright orange-yellow SnI_4 powder.

Cs_2SnI_6 was synthesized by previously reported methods.[7,74]

$(CH_3NH_3)_2SnI_6$ was prepared by grinding methylamine hydroiodide (0.2366 g, 1.49 mmol) and tin(IV) iodide (0.4661 g, 0.74 mmol) in an agate mortar and pestle for 30 m. Upon grinding, the white and orange powders gradually turned black. We note that this effect is amplified in more humid environments (30%-40%), and we suspect that atmospheric moisture facilitates slight solubility of the precursors and enables reactivity. Once ground, the black powder was pressed into pellets and annealed at T = 150 °C for 48 h in a fused silica ampoule sealed under vacuum (P < 10 mTorr). Energy dispersive X-ray spectroscopic analysis yields a molar ratio of [Cl]:[I] content as 0.005(2).

$(CH(NH_2)_2)_2SnI_6$ was prepared by grinding powders of fomamidinium iodide (0.2544 g, 1.48 mmol) and tin(IV) iodide (0.4633 g, 0.74 mmol) in an agate mortar and pestle for 30 m. Upon grinding, the white and orange powders gradually turned olive green and eventually black. Similarly to $(CH_3NH_3)_2SnI_6$, this color change occurs faster at higher humidities. Once ground, the black powder was pressed into pellets and annealed at $T = 150\,^{\circ}C$ for 48 h in a fused silica ampoule sealed under vacuum ($P < 10$ mTorr).

The solid state mechanochemical synthetic route used to prepare methylammonium tin(IV) iodide and formamidinium tin(IV) iodide was employed due to the similar solubilities of the precursors and final products, which did not permit the synthesis of these materials via solution precipitation methods.

Characterization

Laboratory powder X-ray diffraction data were collected on a Bruker D8 Discover X-ray diffractometer using Cu Kα radiation and a Lynxeye XE-T position-sensitive detector. Samples were prepared on a (510) cut zero-diffraction Si wafer.

Synchrotron X-ray scattering data suitable for pair distribution function (PDF) analysis were collected at beamline 11-ID-B at the Advanced Photon Source, Argonne National Laboratory, using 86 keV photons and sample-detector distance of 25 cm. Powdered samples were loaded into polyimide capillaries and measured in transmission mode at room temperature using a Perkin Elmer amorphous silicon image plate detector.[240] Experimental PDFs were extracted using PDFgetX2[241] and analyzed using PDFgui.[170] The program Fit2D[168] was used to calibrate the sample to detector distance and detector alignment with data from a CeO_2 powder standard. Raw scattering data was integrated into Q-space spectra, applying a mask and polarization correction during integration. The normalized total scattering patterns, $S(Q)$ were produced in PDFgetX2 by subtracting polyimide container scattering, utilizing the appropriate sample composition, and applying standard corrections for the area detector setup.[240] Pair distribution function patterns, $G(r)$, were calculated via Fourier transformation of the total scat-

tering data utilizing a Q maximum of 23.8 Å^{-1} for Cs_2SnI_6 and $(CH(NH_2)_2)_2SnI_6$ and 20 Å^{-1} for $(CH_3NH_3)_2SnI_6$. Values of Q_{damp} = 0.034127 Å^{-1} and Q_{broad} = 0.021102 Å^{-1} were extracted from refinement of a TiO_2 anatase standard in PDFgui. A description of the mathematical relationships used to extract the pair distribution function are described in Appendix I.

The diffraction patterns for the tilted supercells of cesium tin(IV) iodide, methylammonium tin(IV) iodide, and formamidinium tin(IV) iodide were calculated by inverse Fourier transform of the pair distribution function, as described in Appendix A.

UV-visible diffuse reflectance spectroscopy was performed on powdered samples diluted to 15wt% in $BaSO_4$, using $BaSO_4$ as a baseline. Spectra were acquired using a Thermo Nicolet Evolution 300 spectrophotometer with a Praying Mantis mirror setup from λ = 600–1000 nm at a scan rate of 240 nm/min.

Electrical resistance measurements were performed on cold-pressed polycrystalline pellets using Pt wires and Au-paste (Cs_2SnI_6 and $(CH_3NH_3)_2SnI_6$) or Ag-paste ($(CH(NH_2)_2)_2SnI_6$) contacts in a 4-probe configuration using a Physical Properties Measurement System (Quantum Design, Inc.). Hall measurements were collected on cold-pressed polycrystalline pellets in the Van der Pauw configuration at T = 300 K. We note that the resistivity of $(CH(NH_2)_2)_2SnI_6$ is near the maximum impedance of the Physical Properties Measurement System (PPMS), and thus these values should be regarded as approximate. Sample geometries (in cm) for the 4-probe measurements are as follows: Cs_2SnI_6: l = 0.21(1), w = 0.14(1), h = 0.01(1); $(CH_3NH_3)_2SnI_6$: l = 0.45(1), w = 0.35(1), h = 0.15(1); $(CH(NH_2)_2)_2SnI_6$: l = 0.42(1), w = 0.48(1), h = 0.09(1).

Energy-dispersive X-ray spectroscopy (EDS) measurements were performed in a JEOL JSM-6500F field emission scanning electron microscope equipped with an Oxford 80 X-MAX (80mm) SDD detector using a 15 keV beam. Measurements were performed on polycrystalline powders of CH_3NH_2·HI and $(CH_3NH_3)_2SnI_6$ adhered to Cu tape. The average molar [Cl]:[I] ratios were determined from the average of 6 scans (5×30 s scans and 1×5 m scan) taken at 1000× magnification in macroscopically-separate locations on the samples.

VESTA was used to visualize and render all crystal structures presented here.[171]

DFT Calculations

Calculations were performed within the framework of density functional theory (DFT), using the Vienna *ab initio* Simulation Package (VASP).[176–178] A plane-wave basis set was used, with the interactions between core and valence electrons described using the Projector Augmented Wave (PAW) method.[180] Two functionals were employed in this study: PBEsol,[242] a version of the Perdew, Burke and Erzorhof (PBE) functional[182] revised for solids, and the hybrid functional HSE06 which combines 75% exchange and 100% of the correlation energies from PBE, together with 25% exact Hartree-Fock (HF) exchange at short range.[181]

PBEsol has been shown to accurately reproduce the structural properties of many compounds containing weakly dispersive interactions, such as in the vacancy ordered double perovskites and other layered halide systems, and accordingly was used for geometry optimizations.[243,244] For band structure, density of states and high-frequency dielectric response calculations, special attention was paid to accurately modeling electron–electron interactions and the relativistic effects seen in Sn and I, through use of scalar relativistic PAW pseudopotentials, explicit treatment of spin-orbit coupling (SOC) effects,[245] and the HSE06 functional.

This combination of HSE06+SOC has been shown to provide an accurate description of the electronic structure of many metal–halide containing semiconductors.[196,246] A plane wave cut-off of 350 eV and Γ centered, 3 × 3 × 3 *k*-point sampling were found to provide convergence of the total energy to 1 meV for all systems studied. Structural relaxations were performed at the experimentally determined lattice constants, with the ionic forces converged to 0.01 eV Å^{-1}, using a larger cut-off energy of 455 eV. In all cases, the initial starting geometry was based on cells refined from powder X-ray diffraction data, with the *A*-site cation oriented along the (111) and (110) directions for $(CH_3NH_3)_2SnI_6$ and $(CH(NH_2)_2)_2SnI_6$, respectively. During optimizations, all atomic positions were allowed to relax.

Static dielectric constants were calculated using the PBEsol functional within density functional perturbation theory (DFPT),[247] with a denser 6×6×6 Γ-centered *k*-point mesh necessary to reach convergence. The high-frequency real and imaginary dielectric functions were calcu-

lated from the optical transition matrix elements within the transversal approximation,[248] obtained at a denser 6 × 6 × 6 Γ-centered *k*-point mesh, from which the absorption coefficient was also derived.

The electron mobilities were calculated within a temperature-dependent Feynman polaron model as implemented in the codes produced by Frost.[249] A full description of the self-consistent process described by Hellwarth necessary to calculate the mobilities has been described in detail elsewhere in the literature.[250] In this method, the electron–phonon coupling is approximated without empirical parameters using a highly idealized model.[38,251,252] The band structure is represented only as the effective mass approximation, with the physical response of the lattice given by the optical and static dielectric constants and an effective phonon-response frequency. This method has recently been shown to provide excellent agreement with the experimental electron mobilities in the hybrid perovskites.[250]

3.3 Results and Discussion

We have prepared the series of vacancy-ordered double perovskite semiconductors A_2SnI_6, where A = Cs^+, $CH_3NH_3^+$ (methylammonium), and $CH(NH_2)_2^+$ (formamidinium). All three compounds in the series crystallize in the cubic vacancy-ordered double perovskite structure (space group $Fm\bar{3}m$, K_2PtCl_6 structure type), as determined by laboratory powder X-ray diffraction (PXRD) shown in Figure 3.1. The structural models were refined against the diffraction data using the Rietveld method implemented in TOPAS, and structural parameters generated from the refinements can be found in Table 3.1. The structures are characterized by a face-centered lattice of isolated $[SnI_6]^{2-}$ octahedral units bridged by *A*-site cations in the cuboctahedral voids, as shown in Figure 3.2. From refinement of the structures shown in Figure 3.2, we find that the larger methylammonium and formamidinium cations are accommodated into the structure by an expansion of the unit cell and the inter-octahedral I–I contact distances from 4.213(1) Å to 4.402(2) Å to 4.606(2) Å across the series. Refinement of the iodine anisotropic atomic displacement parameters (ADPs) result in large ADPs for the plane perpendicular to the

Sn–I bond ($U_{22} = U_{33}$), particularly in $(CH_3NH_3)_2SnI_6$ and $(CH(NH_2)_2)_2SnI_6$. Unique positions for the methylammonium and formamidinium cations could not be identified due to dynamic disorder, and thus these ions were modeled with partially occupied carbon and nitrogen positions on high symmetry sites with fixed ADPs within the cubic perovskite structure to capture the nominal stoichiometry. Hydrogen atoms were excluded from the refinements for simplicity and because their contribution to the diffraction intensity is negligible.

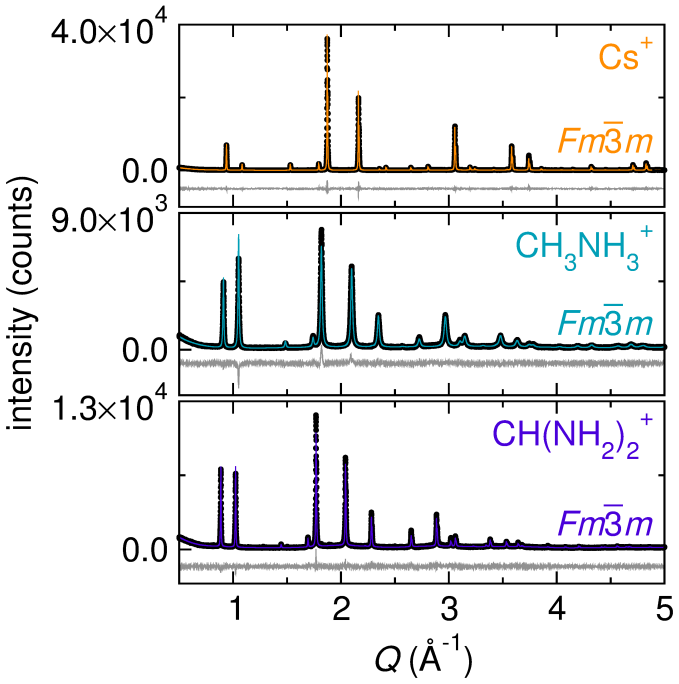

Figure 3.1: Laboratory powder X-ray diffraction patterns and Rietveld refinements showing phase purity of the A_2SnI_6 series, where $A = Cs^+$, $CH_3NH_3^+$ (methylammonium), and $CH(NH_2)_2^+$ (formamidinium). Data are shown as black circles, the fit is the colored line, and difference curves are shown as grey lines.

These compounds appear to be isostructural by diffraction, though the semiconducting behavior varies significantly across the series. Resistivity measurements indicate that all members of the series exhibit semiconducting behavior, as evidenced by the increase in resistivity upon cooling, as shown in Figure 4.5. While Cs_2SnI_6 exhibits a room temperature resistivity of $\rho \simeq 12\ \Omega\cdot$cm,[7,11] replacement of cesium with the organic methylammonium or formamidinium cations yields a ~ 100-fold or ~ 10^5-fold increase in resistivity, respectively.

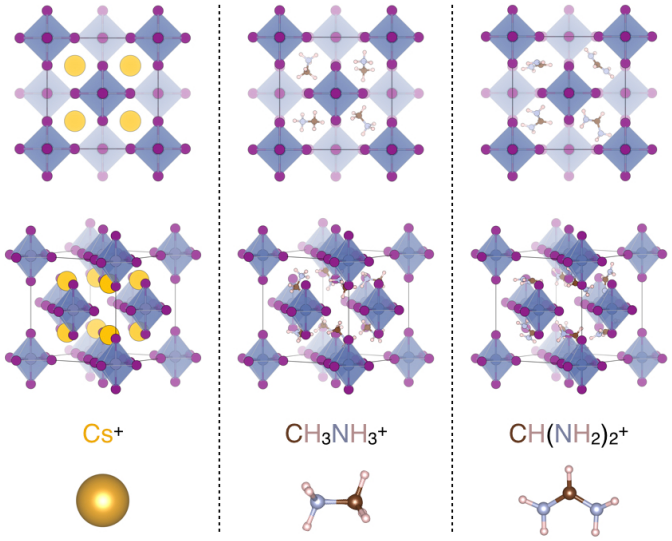

Figure 3.2: Structures of Cs_2SnI_6, $(CH_3NH_3)_2SnI_6$, and $(CH(NH_2)_2)_2SnI_6$ showing the isolated octahedral units. Tin atoms are shown in blue, iodine are purple, cesium are yellow, carbon are brown, nitrogen are light blue, and hydrogen are eggshell. The structures are shown with random orientations of the methylammonium and formamidinium cations.

Hall effect measurements were performed on polycrystalline pellets to further probe the origin of the observed electronic properties across the series. All compounds exhibit native *n*-type conductivity, consistent with the formation of shallow iodine vacancy donor states, to which the *n*-type conductivity of Cs_2SnI_6 is attributed.[7,103] In Figure 3.4, the carrier concentrations and mobilities determined from Hall effect measurements are plotted as a function of Goldschmidt tolerance factor, as ubiquitously used for ABX_3 perovskites. Effective radii of 2.17 Å and 2.53 Å were used for $CH_3NH_3^+$ and $CH(NH_2)_2^+$, respectively in calculation of the tolerance factors.[160] The trends in carrier concentrations and carrier mobilities appear to follow the trends in tolerance factor. Of the A_2SnI_6 series, the tolerance factor of Cs_2SnI_6 is closest to unity (0.998), and Cs_2SnI_6 exhibits the highest carrier mobility of ~ 9 cm^{-2} V^{-1} s^{-1}. Replacement of Cs^+ with the larger $CH_3NH_3^+$ and $CH(NH_2)_2^+$ cations yields tolerance factors of 1.07 and 1.16 and is accompanied by $\sim$ 4-fold and 25-fold reductions in carrier mobilities, respectively. Similarly, the observed carrier concentrations are reduced by an order of magnitude from cesium tin(IV) iodide to methylammonium tin(IV) iodide and by a further two orders of magnitude for formamidinium tin(IV) iodide (Table 3.2).

Table 3.1: Structural parameters extracted from Rietveld refinements of the cubic structural models against laboratory powder X-ray diffraction patterns of the A_2SnI_6 series.

	Cs_2SnI_6	$(CH_3NH_3)_2SnI_6$	$(CH(NH_2)_2)_2SnI_6$
Crystal system	Cubic	Cubic	Cubic
Space group	$Fm\bar{3}m$	$Fm\bar{3}m$	$Fm\bar{3}m$
Cell parameters (a) (Å)	11.64822(4)	12.0022(2)	12.3364(1)
I (x, 0, 0)	0.24425(5)	0.23975(6)	0.2367(1)
A U_{iso} (Å^2)	0.0495(4)	0.025	0.025
Sn U_{iso} (Å^2)	0.0338(5)	0.0315(7)	0.066(1)
I U_{11} (Å^2)	0.0239(6)	0.0181(8)	0.058(1)
I $U_{22} = U_{33}$ (Å^2)	0.0494(4)	0.0867(7)	0.184(1)
R_w	10.945%	10.314%	9.182%

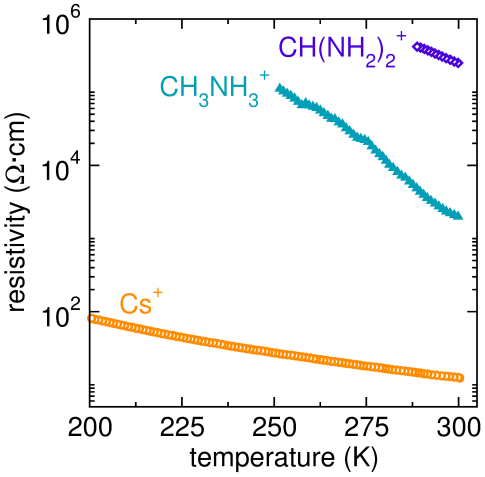

Figure 3.3: Electrical resistivity as a function of temperature for each member of the A_2SnI_6 series. Data were collected on cold-pressed polycrystalline pellets using a 4-wire configuration with Au paste for $A = Cs^+$ and $CH_3NH_3^+$ and Ag paste for $CH(NH_2)_2^+$.

UV-visible diffuse reflectance spectroscopy measurements were performed on powdered samples diluted in $BaSO_4$. The spectra were converted to pseudo-absorbance via the Kubelka-Munk transform and the optical gaps were estimated by extrapolating the linear onset region to zero absorbance as shown in Figure 4.6. This method yields an optical gap of ~1.23(3) eV for Cs_2SnI_6, consistent with previous reports.[7,11] Incorporation of the larger methylammonium and formamidinium ions yields a monotonic increase in optical gap to ~1.35(2) eV and ~1.37(2) eV, respectively. Cs_2SnI_6 is known to be a (nearly) degenerately-doped n-type semiconductor,[7] which presents challenges for accurate determination of the optical gap.[213]

Table 3.2: Room temperature resistivities (ρ_{300K}), carrier concentrations (n_e), and carrier mobilities (μ_e) for the A_2SnI_6 series.

Cation	ρ_{300K} (Ω·cm)	n_e (cm^{-3})	μ_e ($cm^2\ V^{-1}\ s^{-1}$)
Cs^+	12(2)	$5.6(3) \times 10^{16}$	9(2)
$CH_3NH_3^+$	$2.0(3) \times 10^3$	$1.3(1) \times 10^{15}$	2.5(5)
$CH(NH_2)_2^+$	$2.5(3) \times 10^5$	$7(1) \times 10^{13}$	0.36(6)

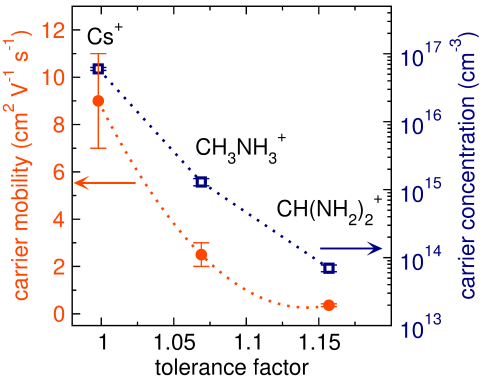

Figure 3.4: Carrier concentrations (blue squares) and carrier mobilities (orange circles) for the A_2SnI_6 series determined by Hall effect measurements. The dotted lines are shown as a guide to the eye.

The observed changes in electronic and optical behavior across the series were further examined through calculations performed within the framework of density functional theory. Structural relaxations, performed using the PBEsol functional, indicate increased I–I distances between octahedra upon substitution of Cs^+ (4.17 Å) with $CH_3NH_3^+$ (4.41 Å) and $CH(NH_2)_2^+$ (4.66 Å), as expected due to the increase in cation size. The increase in interatomic I–I distance is coupled with a decrease in conduction band width, as can be observed in the band structures presented in Figure 4.10, which leads to a slight increase in charge carrier effective masses (Table 4.2). The electron effective masses are smallest in Cs_2SnI_6 ($m_e^* = 0.25$) and increase in $(CH_3NH_3)_2SnI_6$ ($m_e^* = 0.31$) and $(CH(NH_2)_2)_2SnI_6$ ($m_e^* = 0.43$). This yields a trend in decreasing $1/m_e^*$ that cannot match the experimental decrease in mobilities and necessitates further discussion. The change in conduction band width also provides a possible explanation for the variation in observed carrier concentrations across the series. While Cs_2SnI_6 is a (nearly) degenerate doped *n*-type semiconductor,[7] assuming a rigid and level V_I donor defect, the donor states will presumably come deeper in nature as the conduction band edge moves higher upon

cation substitution. In general, the hole effective masses are much larger, with the conduction band composed of Sn 5*s* and I 5*p* states remaining quite disperse in all three compounds.

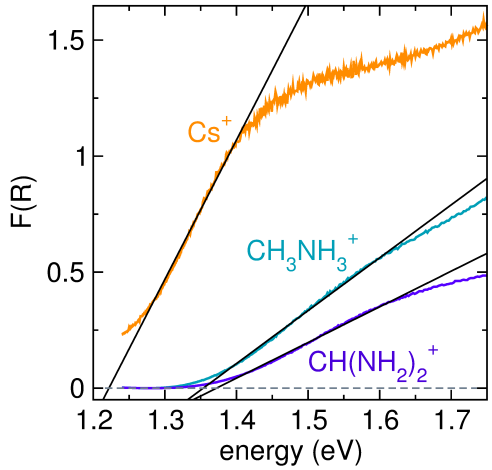

Figure 3.5: UV-visible diffuse reflectance spectra collected for the A_2SnI_6 series. The data were converted to pseudo-absorbance, F(R), by the Kubelka-Munk function, and the absorption onsets determined by extrapolating the linear onset region to zero absorbance. The transformed data are shown as colored lines and the fits the the linear regions are shown as black lines. Zero absorbance is demarcated by the dashed grey line.

Incorporation of the larger methylammonium and formamidinium cations is accompanied by an increase in the DFT-calculated band gaps across the series, consistent with the trend in optical gap observed by diffuse reflectance spectroscopy. We attribute this observation to changes in close-packing of the iodine sub-lattice and subsequent changes in conduction band dispersion upon substitution of the larger methylammonium and formamidinium cations. This hypothesis is supported by calculations of the cubic Cs_2SnI_6 lattice, as well as variations of the structure in which both the Cs and Sn cations are removed ($\square_2\square I_6$) and only the Sn cations are removed ($Cs_2\square I_6$), as shown in Figure 3.7. In these calculations, we charge balance the loss of the cations by the addition of the corresponding number of electrons. In all three cases, the valence band is effectively pinned to the non-bonding I 5*p* states.[7] Cs is strongly electropositive and thus will not affect the positions nor dispersions of the valence and conduction band, illustrated by comparison of the band structures for ($\square_2\square I_6$) and ($Cs_2\square I_6$). In contrast, removal of the Sn cations destabilizes the conduction band minimum due to the hybridization of the

Sn 5*s* and I 5*p* states to form a manifold of antibonding states.[7] However, the Sn–I interactions remain relatively unchanged across the A_2SnI_6 series due to the covalency of the [SnI_6] octahedral units, and thus the band gaps of the series are dictated primarily by the dispersion of the conduction band dominated by close-packing of the iodine sub-lattice.

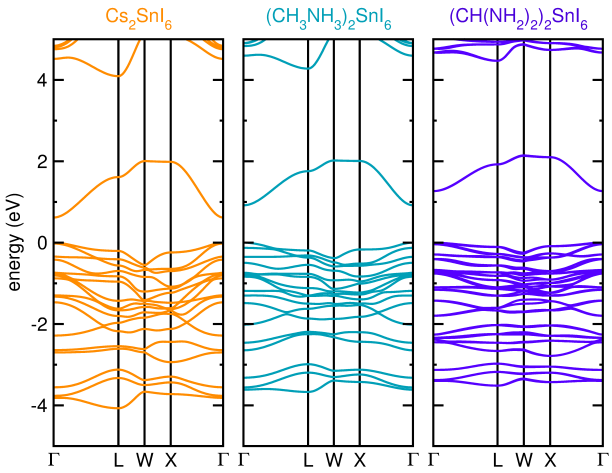

Figure 3.6: Band structures calculated using HSE06+SOC for cesium tin(IV) iodide, methylammonium tin(IV) iodide, and formamidinium tin(IV) iodide. The valence band maximum is set to 0 eV in all cases.

To further investigate the trends in carrier mobilities across the series, we have calculated the limits of electron mobility within a temperature-dependent Feynman polaron transport model, as recently applied to the cubic hybrid perovskites.[250] The parameters used in this model were all calculated *ab initio* as described above and are provided in Table 4.3. The electron band effective masses, m_e^*, used in the calculation are reported in Table 4.2. This model quantifies the degree of electron–phonon coupling (α) and its effect on the polaron mobility (calculated within the Hellwarth model, μ_e^H),[38] phonon-drag mass-renormalization (m_r), and relaxation time (τ). The Hellwarth electron mobilities at T = 300 K across the series, calculated using publicly available codes developed by Frost,[249] are presented in Table 4.4. While this model is highly idealized, with the physical response of the lattice parametrized only by the optical and static dielectric constant and effective dielectric-response frequency, this method has been shown to provide excellent agreement with experiment in the hybrid perovskites and

should therefore perform well for the related A_2SnI_6 series. As only the interaction between the polaron state and characteristic optical-phonon frequency is considered, the calculated mobilities will form an upper bound for a perfect crystal in the absence of other carrier scattering processes.

Table 3.3: Band gaps (E_g), conduction band widths ($\Delta\epsilon_{CB}$) and charge carrier effective masses (m^*), calculated using HSE+SOC, for the A_2SnI_6 series. Band gaps and widths provided in eV, effective masses given in units of the bare electron mass, m_0

Cation	E_g	$\Delta\epsilon_{CB}$	m_e^*	m_h^*
Cs^+	0.62	1.39	0.25	0.81
$CH_3NH_3^+$	0.92	1.10	0.31	0.99
$CH(NH_2)_2^+$	1.27	0.88	0.43	1.61

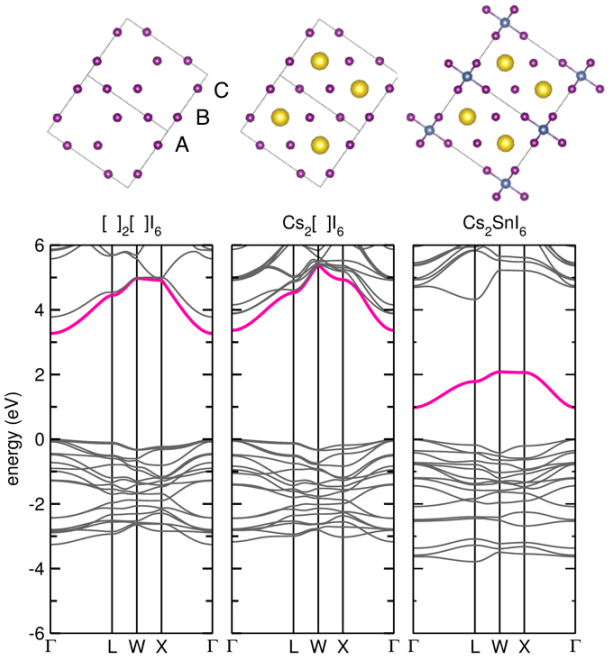

Figure 3.7: Band structure calculations of the cubic vacancy-ordered double perovskite structure of Cs_2SnI_6 in which both the Cs and Sn cations are removed, the Sn cations are removed, and Cs_2SnI_6. The structures used in the calculations are shown above. The states at the bottom of the conduction band are colored pink for clarity.

The experimental trend in electron mobilities is broadly reproduced by our calculations, with the mobility of Cs_2SnI_6 (98 $cm^2\ V^{-1}\ s^{-1}$) nearly 2 times larger than that of $(CH_3NH_3)_2SnI_6$ (52 $cm^2\ V^{-1}\ s^{-1}$) and approximately 4 times larger than in $(CH(NH_2)_2)_2SnI_6$ (27 $cm^2\ V^{-1}\ s^{-1}$). The relatively high calculated mobility (98 $cm^2\ V^{-1}\ s^{-1}$) seen in Cs_2SnI_6, comparable to that calculated for $CH_3NH_3PbI_3$ (136 $cm^2\ V^{-1}\ s^{-1}$),[250] results from a weak electron–phonon coupling constant that produces only minimal polaron mass renormalization (the additional phonon drag produces a 26% increase in the electron effective mass) and a long relaxation time (0.16 ps). Larger I–I contact distances in $(CH_3NH_3)_2SnI_6$ reduces the high-frequency dielectric constant and increases band effective masses, resulting in greater electron–phonon coupling (1.88) and mass renormalization (42%). The reduced mobility seen in $(CH(NH_2)_2)_2SnI_6$ arises due to further reduction in the high-frequency dielectric response and a softening of the phonon modes, leading to greater optical scattering at lower temperatures. It is interesting to note that while the electron-phonon coupling constant of $(CH(NH_2)_2)_2SnI_6$ (2.48) is nearly comparable to that of $CH_3NH_3PbI_3$ (2.39),[250] the greater electron effective mass produces polaron mobilities a factor of 5 times smaller in $(CH(NH_2)_2)_2SnI_6$. Overall, the Hellwarth mobilities obtained from the polaron model are much greater than those seen in experiment, as expected due to the polycrystalline nature of the samples and the absence of electron–electron, impurity, electron–phonon, and grain-boundary scattering effects in our calculations.

Table 3.4: Parameters of the Feynman polaron model. High frequency (ϵ_∞) and static (ϵ_S) dielectric constants given in units of the permittivity of free space (ϵ_0). Characteristic phonon frequency (f) given in THz.

Cation	ϵ_∞	ϵ_S	f
Cs^+	4.28	7.20	3.53
$CH_3NH_3^+$	3.72	6.82	4.32
$CH(NH_2)_2^+$	3.39	6.06	3.88

The relationship between experimental carrier mobility, μ_e and calculated electron band effective mass, m_e^* were examined to provide insight into the influence of carrier scattering

Table 3.5: Hellwarth electron mobilities at T = 300 K (μ_e^H, cm^2 V^{-1} s^{-1}), electron-phonon coupling (α), polaron effective mass renormalization (m_r, %) and polaron relaxation time (τ, ps) calculated within the polaron model for the A_2SnI_6 series

Cation	μ_e^H	α	m_r	τ
Cs^+	98	1.45	26	0.16
$CH_3NH_3^+$	52	1.88	42	0.11
$CH(NH_2)_2^+$	27	2.48	54	0.08

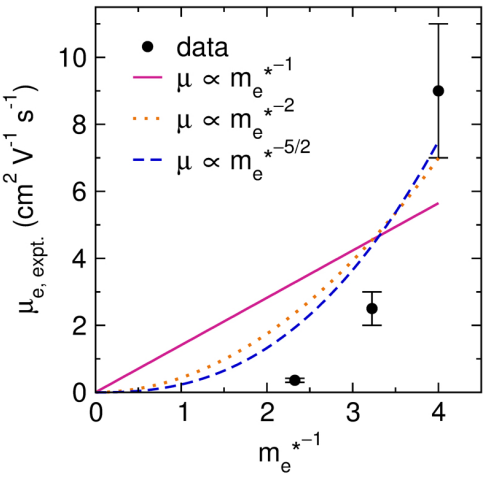

Figure 3.8: Experimental mobility, μ_e plotted as a function of band effective mass, m_e^{*-1}. Fits to the data for m_e^{*-1} (pink solid line), m_e^{*-2} (orange dotted line), and $m_e^{*-5/2}$ (blue dashed line).

mechanisms on the observed trends in mobility (Figure 3.8). From the relationship $\mu_e = e\tau/m_e^*$, the mobility scales as $\mu_e \propto 1/m_e^*$ in the absence of carrier scattering mechanisms. Scattering processes from zero-order optical deformation potential scattering yields $\mu_e \propto m_e^{*-2}$,[253] while carrier scattering due to acoustic deformation potential scattering yields $\mu_e \propto m_e^{*-5/2}$.[254,255] As shown by the fit lines in Figure 3.8, the trends in carrier mobilities are not well-described by the aforementioned scattering mechanisms, further suggesting there are additional factors contributing to the charge transport across the A_2SnI_6 series.

Investigation of the local coordination environment through X-ray pair distribution function (XPDF) analysis provides additional insight into the observed electronic behavior. Preliminary modeling of the XPDF was performed using the cubic structural models obtained by Rietveld refinement of the laboratory PXRD data. Despite identical cubic structures by diffraction, the XPDF reveals deviations in the local coordination environment that cannot be mod-

eled by the cubic structure with harmonic atomic displacements. The XPDF fits from the cubic structure were performed over short-range ($2 \leq r \leq 5.5$ Å) and long range ($5.5 \leq r \leq 30$ Å) correlations, as shown in Figure 3.9. From $5.5 \leq r \leq 30$ Å, the data are reasonably well-modeled by the average structure observed by diffraction, particularly for Cs_2SnI_6 and $(CH_3NH_3)_2SnI_6$. For $(CH(NH_2)_2)_2SnI_6$, the long range correlations can only be described with the inclusion of extremely large anisotropic ADPs for iodine atoms, which is consistent with Rietveld refinements of the diffraction data (Table 3.1). We note that the magnitude of the iodine anisotropic ADPs increases significantly across the series, suggesting increasing thermal or static disorder as cesium is replaced with methylammonium and formamidinium, which can be observed visually through broadening of the longer-r pair correlations.

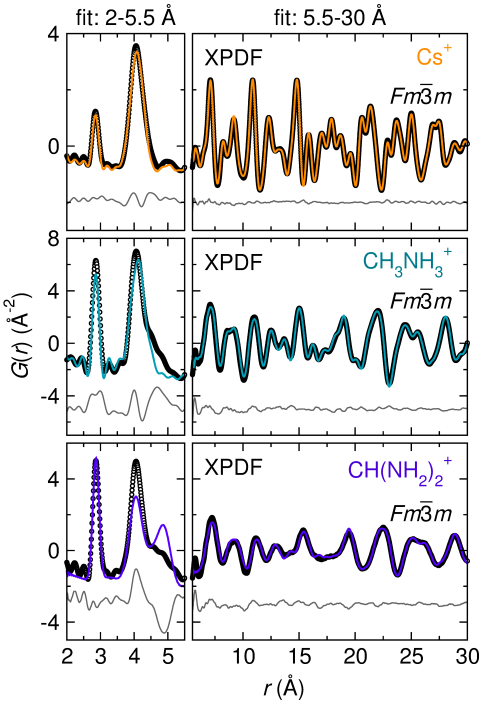

Figure 3.9: X-ray pair distribution function analysis of cesium tin(IV) iodide, methylammonium tin(IV) iodide, and formamidinium tin(IV) iodide. The data were modeled with the cubic structural models determined by powder X-ray diffraction, with fit ranges of $2 \leq r \leq 5.5$ Å (left panels) and $5.5 \leq r \leq 30$ Å (right panels). The data are shown as black circles, the fit is the colored line, and the difference is the grey line.

Distortions in the local coordination environment are observed in the next-nearest neighbor pair correlation at $r \sim 4$-4.1 Å corresponding to *A*–I and I–I pairs. In Cs_2SnI_6, this manifests as a small peak asymmetry, while $(CH_3NH_3)_2SnI_6$ and $(CH(NH_2)_2)_2SnI_6$ exhibit significant tailing on the high-r side of the peak. In all three compounds the nearest-neighbor Sn–I pair correlations at $r \sim 2.86$ Å remain symmetric, indicating little deviation in their bond lengths that accompanies distortion of the octahedral units, in contrast to many Sn^{2+}-based perovskites that exhibit distorted octahedra due to stereochemically-active ns^2 electrons.[256–259] Rather, we propose that the distortions reported here result from anharmonic atomic displacements resulting in an asymmetric distribution of inter-octahedral I–I contact distances, which can be modeled as random rotations of relatively rigid [SnI_6] octahedral units.

To address the hypothesis of anharmonic displacements, we employed a pseudo-smallbox rigid-body modeling routine. For each A_2SnI_6 compound, a $3 \times 3 \times 3$ supercell of the cubic structure is constructed with random orientations of the methylammonium or formamidinium cations with molecular geometries taken from Lee *et al.*[74] and Petrov *et al.*,[238] respectively. The isolated octahedral units, with geometries determined by Rietveld refinements of the cubic structures against the PXRD data, are also rotated about each Euler angle as rigid bodies by a distribution of random angles ranging from 0° to θ_{max}. The pair distribution function is calculated for different supercells with distinct values of θ_{max} and compared to the data. The largest allowed rotation angle that provides the best goodness-of-fit to the XPDF is retained and further optimized using the least-squares procedure implemented in PDFGUI to obtain relevant fitting parameters, including scale factor, correlated motion parameter (δ_2), lattice parameters, and atomic displacement parameters constrained by chemical identity. From this analysis, we find $\theta_{max} = 6.6(7)°$, $11.2(9)°$, and $11.7(6)°$ for Cs_2SnI_6, $(CH_3NH_3)_2SnI_6$, and $(CH(NH_2)_2)_2SnI_6$, respectively. The best-fit supercells for each compound are shown in Figure B.2. As shown in the fits to the low-r range in Figure 3.11, the asymmetry observed in the next-nearest-neighbor pair correlation is captured with the octahedral tilting model in all three compounds. Further, the longer r pair correlations are also reasonably approximated by the rigid-body model, as shown

in the fits from $5.5 \leq r \leq 30$ Å. The observation that the XPDF at long r can be described by both the tilted and cubic structures (Figures 3.9 and 3.11) indicates that any anharmonic displacements are effectively averaged into the cubic structure observed by powder X-ray diffraction, which has been similarly observed in ABX_3 perovskites.[45,67,260] Portions of the *ad hoc* Python code used to generate the tilted supercells are included in Appendix B.

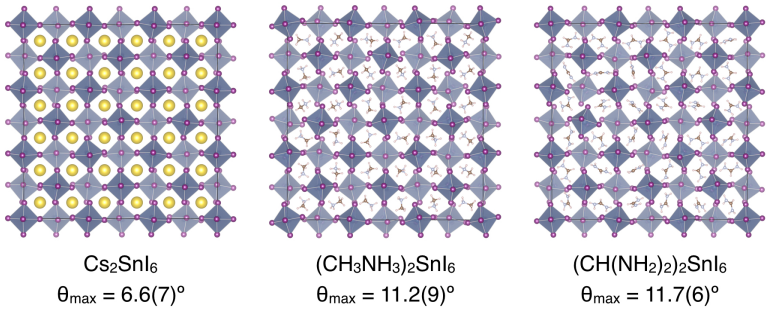

Figure 3.10: Supercells for a) Cs_2SnI_6, b) $(CH_3NH_3)_2SnI_6$, and c) $(CH(NH_2)_2)_2SnI_6$ with the corresponding θ_{max} determined by the pseudo-rigid-body modeling routine.

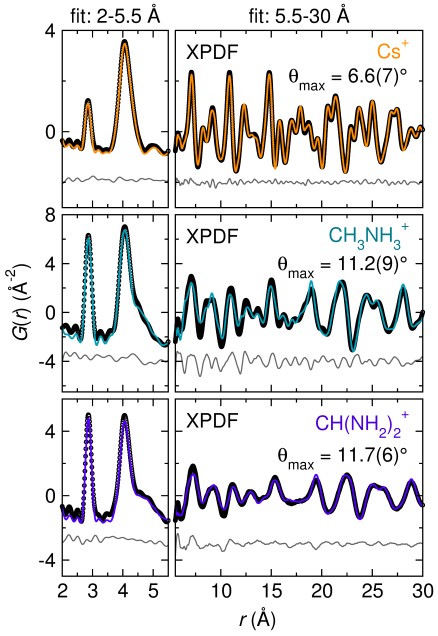

Figure 3.11: X-ray pair distribution function analysis of cesium tin(IV) iodide, methylammonium tin(IV) iodide, and formamidinium tin(IV) iodide with fits from the tilted models shown in Figure B.2. In the left panels, the data are fit from $2 \leq r \leq 5.5$ Å, while the right panels show the fits from $5.5 \leq r \leq 30$ Å. Black circles are the data, colored lines are the fit, and grey lines are the difference curve.[6]

The supercell models also reproduce the observed diffraction data. Figure A.1 illustrates a comparison of the calculated $I(Q)$ and the experimental powder X-ray diffraction data convolved with a broadened Gaussian distribution to account for the finite size of the supercell. The calculated diffraction patterns retain the major features present in the experimental data, even with the removal of internal symmetry elements and finite size of the model. The close resemblance of the calculated and experimental diffraction patterns lends further support of this rigid-body modeling approach.

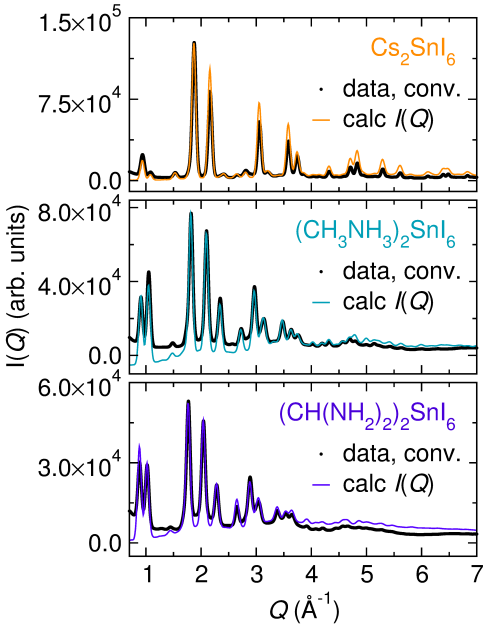

Figure 3.12: Comparison of powder X-ray diffraction data convolved with a Gaussian to diffraction patterns ($I(Q)$) calculated from $G(r)$ of the tilted supercells. Black lines are the convolved data, while colored lines represent the calculated $I(Q)$ for each compound in the A_2SnI_6 series.

Anharmonicity can manifest as peak asymmetry in the pair distribution function. Currently, there are not trivial ways to accurately model anharmonic atomic displacements in the PDF. In the case of PbTe, anharmonic displacements artificially manifest as off-centering of the Pb atoms when projected onto the radial distribution function.[261] Here, we use the octahedral rotation model as a proxy for the anharmonic displacements in order to extract atomistic insights into the pair correlations responsible for the anharmonic interactions. Using the

exported structures from the 3 × 3 × 3 supercells, we have computed the potential of mean force, $w_{\text{I-I}}(r)$, from the partial PDF of the intra- and inter-octahedral I–I contact distances using $w_{\text{I-I}}(r) = -ln(g_{\text{I-I}}(r))/k_BT$. As shown by the dashed lines in Figure 3.13, the intra-octahedral I–I contacts show the expected harmonic potential well for the regular [SnI_6] octahedra. In contrast, the inter-octahedral I–I potentials move to higher *r* and becomes increasingly anharmonic as cesium is replaced with the methylammonium and formamidinium cations.

The considerable differences in anharmonicity, as measured by effective octahedral tilt angle, between all-inorganic Cs_2SnI_6 (θ_{max} = 6.6(7)°) and the hybrid compounds $(CH_3NH_3)_2SnI_6$ (θ_{max} = 11.2(9)°) and $(CH(NH_2)_2)_2SnI_6$ (θ_{max} = 11.7(6)°) can be rationalized by the coupling of organic molecules with the surrounding iodine framework through hydrogen bonding. These interactions likely deviate from a harmonic potential due to reorientational dynamics of the molecules transiently coupled to the lattice. Though we cannot unequivocally determine if the octahedral tilting disorder in these compounds is static or dynamic through analysis of the XPDF data, previous studies of the vacancy-ordered double perovskite family by nuclear quadrupole resonance reveal dynamic octahedral rotations with frequencies on the order of ω_{rot} = 55–75 cm^{-1} (~6–9 meV) for compounds such as A_2PtCl_6 (A = K^+, Rb^+, Cs^+).[86,87] Further, studies of the related compounds $(CH_3NH_3)_2SnCl_6$ and $(CH_3NH_3)_2PtCl_6$ compounds by ^{35}Cl nuclear quadrupole resonance and proton magnetic resonance have revealed dynamic octahedral rotations and methylammonium reorientations occurring simultaneously at room temperature.[98,99,262] We propose that dynamic rotations of the [SnI_6] octahedra in $(CH_3NH_3)_2SnI_6$ and $(CH(NH_2)_2)_2SnI_6$ are coupled to molecular dynamics through hydrogen bonding interactions. This notion is supported by studies of $(NH_4)_2SiF_6$, which reveal that rotations of the [SiF_6] octahedral units are hindered by hydrogen bonding interactions with dynamic ammonium cations.[95,96] Further analysis through *ab initio* molecular dynamics calculations may provide further insight into the correlated nature of octahedral rotations and molecular reorientations.

The presence of anharmonic lattice dynamics via high-amplitude octahedral rotations may contribute to charge transport behavior in the A_2SnI_6 series through electron-phonon inter-

actions such as in polaron formation, which have been implicated in the modest carrier mobilities observed in many hybrid organic-inorganic perovskites.[25,52,54,60,61,263,264] The origin of these interactions in methylammonium lead halide perovskites have been suggested to stem from the relative "softness" of the lattice, which results in low Debye temperatures and low phonon activation energies.[39,265] It is therefore conceivable that carrier mobilities would be similarly affected, and perhaps to a greater extent, in the more softly-bonded vacancy-ordered double perovskite lattice. Indeed, calculation of the Hellwarth electron mobilities reported in this contribution reveals softening of the lattice dynamics across the A_2SnI_6 series due to larger I–I distances, which facilitates the formation of tightly-bound polarons that subsequently localize charge carriers. We hypothesize that this effect is amplified by organic-inorganic coupling through hydrogen bonding interactions in $(CH_3NH_3)_2SnI_6$ and $(CH(NH_2)_2)_2SnI_6$ which further soften the lattice and manifest in the increasingly anharmonic inter-octahedral I–I potential wells shown in Figure 3.13.

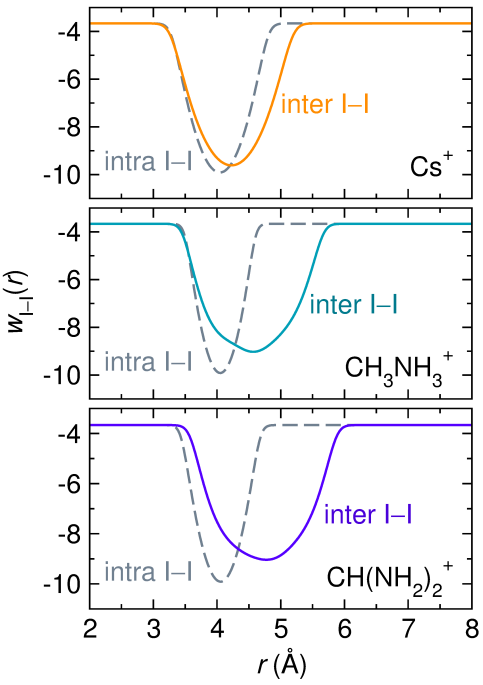

Figure 3.13: Mean-force potentials calculated from the structural models with tilted octahedra shown in Figure B.2. The intra-octahedral I–I potentials are shown as the grey dashed line, while the inter-octahedral I–I potentials are shown as solid colored lines.

3.4 Conclusions

We have synthesized the tin iodide-based vacancy-ordered double perovskite series A_2SnI_6, where A = Cs^+, $CH_3NH_3^+$, and $CH(NH_2)_2)_2SnI_6$. Measurement of the electronic behavior indicates that all compounds are native *n*-type semiconductors, but replacement of cesium with the larger, organic methylammonium and formamidinium cation is accompanied by a reduction in conductivity through reduced carrier concentrations and carrier mobilities. Analysis of the local coordination environment by X-ray pair distribution function analysis reveals asymmetry in the inter-octahedral I–I pair correlations that can be modeled by rotational displacements of the isolated [SnI_6] octahedral units. These displacements, which we attribute to high-amplitude, anharmonic lattice dynamics, appear to be exaggerated by organic-inorganic coupling in the hybrid compounds. Calculation of the electron-phonon coupling strength supports the observed trend in carrier mobilities through formation of more tightly-bound polarons across the series, a consequence of softer and more anharmonic lattice dynamics. These materials offer the opportunity to study the influence of lattice anharmonicity, brought about by the interplay of organic cations with molecular-like inorganic units, on the charge transport properties of halide perovskite derivatives for optoelectronic applications.

Chapter 4

Tolerance Factor and Cooperative Tilting Effects in Vacancy-Ordered Double Perovskite Halides[4]

4.1 Introduction

Inorganic perovskite halide-based materials have presented a paradigm shift in the search for new high performance semiconductors. The high amplitude lattice dynamics and low elastic moduli, yet excellent carrier dynamics and electronic behavior, suggests that elucidation of structure-dynamics-property relationships is required in order to fully understand these materials.[53,233] The perovskite family is typified by the general formula ABX_3, and the structure is formed by a network of corner sharing $[BX_6]$ octahedra bridged by A-site cations in the cuboctahedral void. A hallmark of the perovskite family is cooperative octahedral tilting (static and dynamic) of the $[BX_6]$ framework, which typically arises from a size mismatch between the A-site cation and the cuboctahedral void formed by twelve neighboring X-site anions, as predicted by the Goldschmidt tolerance factor, $t = (r_A + r_X)/(\sqrt{2}(r_B + r_X))$.[46,48,81] Octahedral tilting distortions are well-known to influence the optoelectronic properties of perovskite halides, as the electronic states of the B- and X-site ions dominate the conduction and valence band edges.[266] Static octahedral tilting distortions affect the electronic dispersions of the B and X states through deviation in the X–B–X bond angle from 180°, yielding smaller carrier mobilities and higher resistivities.[114] Changes in these bond angles also affect the relative energies of the conduction and valence band edges, resulting in a widening of the band gap with correspondingly larger octahedral tilting distortions.[150,236,267,268] Further, dynamic octahedral tilting of the $[BX_6]$ framework has recently been implicated in the formation of polarons via electron-

[4]Substantial portions of this chapter have been reproduced with permission from A. E. Maughan, A. M. Ganose, M. A. Almaker, D. O. Scanlon, and J. R. Neilson, *Chem. Mater.*, **2018**, *30*, 3909–3919.[8] ©2018 the American Chemical Society

phonon coupling; large polarons are hypothesized to protect carriers, thereby prolonging carrier excited state lifetimes and reducing carrier mobilities.[25,51,52,58,61,260]

Vacancy-ordered double perovskites are a subset of the ordered double perovskite family with the general formula A_2BX_6. The structure is formed by a face-centered lattice of isolated [BX_6] octahedral units bridged by *A*-site cations, and can alternatively be thought of as an ordered double perovskite lattice with rock-salt ordering of *B*-site cations and vacancies. Similar to ordered double perovskites, vacancy-ordered double perovskites undergo successive octahedral tilting distortions according to the group-subgroup relationship: $a^0a^0a^0$ ($Fm\bar{3}m$) → $a^0a^0c^+$ ($P4/mnc$) → $a^+b^-b^-$ ($P2_1/n$),[78,269] and the proclivity of these materials to undergo octahedral tilting can be predicted by the "radius ratio", which is defined as the ratio of the *A*-site cation radius to the radius of the cuboctahedral site formed by the X_{12} cage.[9,80] As in conventional ABX_3 perovskites, the electronic properties of vacancy-ordered double perovskites are directly dictated by the electronic states of the *B*- and *X*-site ions at the valence and conduction band edges. Close-packing of the halogen framework provides dispersive electronic states and a framework for mobile carriers, while the interaction of the *B*-site cations with the coordinating *X*-site anions dictates the band positions, optical gaps, and tolerance to crystallographic defects.[7,9,12,103] Although the electronic states of the *A*-site cations are typically far from the frontier electronic states in vacancy-ordered double perovskites,[9] varying the identity of the *A*-site can indirectly influence characteristics such as carrier mobilities and band gap through changes in the dynamics of the surrounding inorganic framework. Our recent study of the vacancy-ordered double perovskites A_2SnI_6, where $A = Cs^+$, $CH_3NH_3^+$ (methylammonium), and $CH(NH_2)_2^+$ (formamidinium) revealed significant lattice anharmonicity in the hybrid compounds, resulting in more tightly-bound polarons and subsequently reduced carrier mobilities across the series.[6] Due to the large sizes and hydrogen bonding capabilities of the $CH_3NH_3^+$ and $CH(NH_2)_2^+$ cations, the anharmonic effects appear to manifest as random rotations of the isolated [SnI_6] octahedral units rather than through typical cooperative tilting motifs.

In this contribution, we present a study of the tin(IV) iodide-based vacancy-ordered double perovskite Rb_2SnI_6 and compare the observed structural and electronic properties to those of Cs_2SnI_6 and other A_2SnI_6 compounds. Both Rb_2SnI_6 and Cs_2SnI_6 exhibit native n-type conductivity, though Rb2SnI6 exhibits carrier mobilities that are reduced by 50-fold relative to Cs_2SnI_6. Crystallographic analysis reveals that Rb_2SnI_6 crystallizes in the tetragonal modification of the vacancy-ordered double perovskite structure at room temperature due to cooperative tilting of the [SnI_6] octahedral units. Upon cooling, Rb_2SnI_6 undergoes further octahedral tilting to a lower-symmetry monoclinic structure. X-ray and neutron pair distribution function analysis reveal that the local coordination environment is best described by the monoclinic structure at all temperatures. This can be rationalized through bond valence sum analysis, which suggests that the Rb^+ ion coordination is optimized in the monoclinic structure. Calculation of the phonon dispersions indicate that, although the tetragonal structure is dynamically stable, the lowest-frequency optical phonon polarization corresponds to cooperative octahedral tilting that yields the monoclinic structure. This strongly implicates octahedral rotational dynamics in driving the structural phase transition. Density functional calculations reveal that cooperative octahedral tilting in Rb_2SnI_6 results in marginally smaller electron effective masses due to subtle changes in the close-packed iodide framework, which alone cannot account for the changes in carrier mobility observed experimentally. Rather, we find that the lower symmetry of Rb_2SnI_6 relative to Cs_2SnI_6 yields stronger electron–phonon coupling due to the larger number of non-degenerate low-frequency phonons that contribute to the dielectric response of the lattice and produce more tightly bound polarons that reduce charge carrier mobilities. From these results we show that simple models such as bond valence sum and the perovskite tolerance factor serve as effective predictors for charge transport behavior in vacancy-ordered double perovskite semiconductors.

4.2 Methods and Materials

Note on author contributions: This chapter was published in *Chemistry of Materials*, **2018**, volume 30, pages 3909–3919 by Annalise E. Maughan, Alex M. Ganose, Mohammed A. Almaker, David O. Scanlon, and James R. Neilson. AEM performed the syntheses and experiments and analyzed the data, AMG and DOS performed density functional calculations, and MAA assisted in synthesis and data analysis. AEM wrote the initial draft of the manuscript, and JRN supervised the project. All authors contributed to editing and finalization of the manuscript.

Materials Synthesis

SnI_4 [6,7] and Cs_2SnI_6 [7,11] were prepared by previously reported methods. Rb_2SnI_6 was synthesized via solution precipitation. To a 20 mL scintillation vial was added 0.2 g of SnI_4, 10.0 mL of isopropanol, and 1.0 mL of hydriodic acid (57% aq., unstabilized). The solution was heated to $T = 60$ °C while stirring to dissolve the entire mass of SnI_4. In a separate scintillation vial was added a stoichiometric amount of Rb_2CO_3 to 2.0 mL of hydriodic acid and stirred to dissolve the solid. We note that it is important to minimize the length of time over which the Rb_2CO_3 is allowed to sit in the hydriodic acid, to prevent the formation of RbI_3. Once the solids had dissolved in both solutions, the RbI solution was added all at once to the warm SnI_4/isopropanol solution. The scintillation vial was capped and stirred gently for 30 min to cool to room temperature. The solution was further cooled in an ice bath for an additional 30 min while stirring to induce precipitation. The black precipitate was collected via centrifugation and washed with a small amount of cold isopropanol. The product was dried in air at $T = 60$ °C for 24 h. We note that unstabilized hydriodic acid is required for successful precipitation of the final product; use of HI containing the H_3PO_2 stabilizer typically results in precipitation of bright orange crystals, which are presumably due to precipitation of the SnI_4 precursor.

Structural Characterization

High-resolution synchrotron powder X-ray diffraction data for Rb_2SnI_6 were collected from the diffractometer on beam line 11-BM-B at the Advanced Photon Source, Argonne National Laboratory at T = 295 K and T = 100 K.[167] The data were analyzed with the Rietveld method implemented in GSAS/EXPGUI.[165,166] VESTA was used to visualize and render all crystal structures presented here.[171]

Synchrotron X-ray scattering data suitable for pair distribution function (PDF) analysis were collected at beamline 11-ID-B at the Advanced Photon Source, Argonne National Laboratory, using 86 keV photons and sample-detector distance of 25 cm. Powdered samples of Rb_2SnI_6 were loaded into polyimide capillaries and measured in transmission geometry at room temperature using a Perkin Elmer amorphous silicon image plate detector.[240] The program Fit2D[168] was used to calibrate the sample to detector distance and detector alignment with data from a CeO_2 powder standard. Raw scattering data was integrated into Q-space spectra, applying a mask and polarization correction during integration. Experimental PDFs were extracted using PDFgetX2[241] and analyzed using PDFgui.[170] The normalized total scattering pattern, $S(Q)$, was produced in PDFgetX2 by subtracting polyimide container scattering, utilizing the appropriate sample composition, and applying standard corrections for the area detector setup.[240] The pair distribution function pattern, $G(r)$, was calculated via sine Fourier transformation of the total scattering data utilizing a maximum Q of 23.8 Å^{-1}. Values of Q_{damp} = 0.034127 Å^{-1} and Q_{broad} = 0.021102 Å^{-1} were extracted from refinement of a TiO_2 anatase standard in PDFgui and used for further refinement.

Neutron scattering measurements were performed on the NOMAD instrument at the Spallation Neutron Source, Oak Ridge National Laboratory. A powdered sample of Rb_2SnI_6 was loaded into a 6 mm Vanadium sample can and sealed under a He atmosphere. Total scattering data were collected at T = 2, 10, 150, 250, and 300 K in the cryostat sample environment. Data were normalized against scattering data collected for a vanadium rod and background scattering from the vanadium can was subtracted. Total scattering data of Cs_2SnI_6 at T = 10 K

were collected on a powdered sample of Cs_2SnI_6 sealed into a 6 mm Vanadium sample can under a He atmosphere utilizing the cryostat sample environment. Data were normalized against scattering data collected for a vanadium rod and background scattering from the vanadium can was subtracted. Total scattering data of Cs_2SnI_6 at T = 90 K and T = 300 K were collected on powdered samples of Cs_2SnI_6 sealed into a quartz capillary (capillary diameter = 3.0 mm) in the multi-sample changer. Data were normalized against scattering data collected for an empty glass capillary, and background scattering from the empty capillary was subtracted.

For all neutron total scattering experiments, the data were merged to the total scattering structure function using the IDL codes developed for the NOMAD instrument.[270] The pair distribution function was then produced through the sine Fourier transform of the total scattering structure function utilizing Q_{max} = 31.4 Å^{-1}. For Rb_2SnI_6 at all temperatures, values of Q_{damp} = 0.0245 Å^{-1} and Q_{broad} = 0.0196 Å^{-1} were extracted from refinement of a silicon standard in PDFgui. For Cs_2SnI_6 at T = 90 K and T = 300 K, values of Q_{damp} = 0.0201 Å^{-1} and Q_{broad} = 0.0196 Å^{-1} were extracted from refinement of a diamond standard in PDFgui. For Cs_2SnI_6 at T = 10 K, values of Q_{damp} = 0.01766 Å^{-1} and Q_{broad} = 0.01918 Å^{-1} were extracted from refinement of a silicon standard. Analysis of the nPDFs was performed using PDFgui.

Optical and Electronic Properties

UV-visible diffuse reflectance spectroscopy was performed on powdered samples of Rb_2SnI_6 diluted to 15wt% in $BaSO_4$, using $BaSO_4$ as a baseline. Spectra were acquired using a Thermo Nicolet Evolution 300 spectrophotometer with a Praying Mantis mirror setup from λ = 600-1000 nm at a scan rate of 240 nm/min.

Electrical resistance measurements were performed on cold-pressed polycrystalline pellets of Rb_2SnI_6 using a Physical Properties Measurement System (Quantum Design, Inc.). The measurements were collected in a linear 4-probe configuration using Pt wires and Ag-paste contacts. Similar results were obtained when Au paste was used. Hall measurements were collected on a cold-pressed polycrystalline pellet in the Van der Pauw configuration at T=300 K with Pt

wires contacted to the edge of the cylindrical pellet using Ag paste. 4-probe sample geometry: $l = 0.35(1)$ cm, $w = 0.35(1)$ cm, $h = 0.05(1)$ cm. Hall probe sample thickness: $t = 0.08(1)$ cm.

Density Functional Theory Calculations

Density functional theory calculations were performed using the Vienna *ab initio* Simulation Package (VASP).[176–179] A plane-wave basis set was employed, with the interactions between core and valence electrons described using the Projector Augmented Wave (PAW) method.[180] This study employed two functionals: PBEsol,[242] a version of the Perdew, Burke and Erzorhof (PBE) functional[182] revised for solids, and the hybrid functional HSE06 which combines 75% exchange and 100% of the correlation energies from PBE, together with 25% exact Hartree-Fock (HF) exchange at short range.[181] PBEsol has been shown to reproduce the structural and vibrational properties of many compounds containing weakly dispersive interactions, such as in the vacancy-ordered double perovskites[6] and other layered halide systems.[243,271] The band structures were calculated along a reciprocal space path defined between all high-symmetry points in the Brillouin zone, as detailed by Bradley and Cracknell.[272] For density of states, band structure, and high-frequency dielectric response calculations, special attention was paid to capturing the effects of electron–electron interactions through use of the HSE06 hybrid functional.[273,274] Furthermore, the relativistic effects in Sn and I were accounted for through use of scalar relativistic pseudopotentials and explicit treatment of spin-orbit coupling effects.[245] This combination of HSE06+SOC has been shown to provide an accurate description of the electronic structure of many metal–halide containing semiconductors.[196,246] A k-point sampling mesh of Γ centered 3 × 3 × 2 and plane wave energy cut-off of 350 eV were found to converge the total energy to 1 meV/atom for all systems studied. The structures were relaxed using HSE06 until the forces on all atoms totaled less than 0.01 eV Å^{-1}. The HSE06 optimized crystal structures can be found online in a public repository.[275]

The ionic contribution to the dielectric constants were calculated using the PBEsol functional within density functional perturbation theory (DFPT),[247] with a denser 6 × 6 × 4 Γ-

centered *k*-point mesh necessary to reach convergence. The phonon band structure was calculated using the finite-displacement method in a 3 × 3 × 2 (324 atom) supercell using a 1 × 1 × 1 *k*-point mesh. The DFPT calculations were performed on structures relaxed using PBEsol, due to the high computational expense of performing DFPT calculations using hybrid DFT. The high-frequency real and imaginary dielectric functions were calculated from the optical transition matrix elements within the transversal approximation,[248] obtained at a denser 6 × 6 × 3 Γ-centered *k*-point mesh. Band alignments were performed using a vacuum–slab model (35 Å slab, 35 Å vacuum) with a (101) surface. The corresponding electrostatic potential was averaged along the *c*-direction using the MacroDensity package,[276] with the energy of the potential at the plateau used as the external vacuum level. Slab calculations were performed using the HSE06 functional, with a correction for the valence band energy and band gap taken from the HSE06+SOC calculated bulk.

Polaron mobilities were calculated within a temperature-dependent Feynman model, as implemented in the codes produced by Frost.[249] A full definition of the methodology is described elsewhere in the literature.[250] Crucially, the electron–phonon coupling is approximated without empirical parameters, using a highly idealized model.[38,251,252] The band structure is represented only as the effective mass approximation, with the physical response of the lattice given by the optical and static dielectric constants and an effective phonon-response frequency. This method has recently been applied to calculate the the electron mobilities in the hybrid perovskites[250] and other vacancy-ordered double perovskites.[6]

4.3 Results

4.3.1 Structural Characterization

Rubidium tin(IV) iodide crystallizes in the tetragonal modification of the vacancy-ordered double perovskite structure (space group $P4/mnc$) at room temperature, in contrast to a previous report of a cubic structure.[277] The structure is characterized by in-phase cooperative octahedral rotations about the *c*-axis by ∼11° ($a^0a^0c^+$ in Glazer notation) relative to the cubic

aristotype, as shown in Figure 4.1a and b. The tetragonal structural model was refined against high-resolution synchrotron powder X-ray diffraction (SXRD) data shown in Figure 4.2a and b.

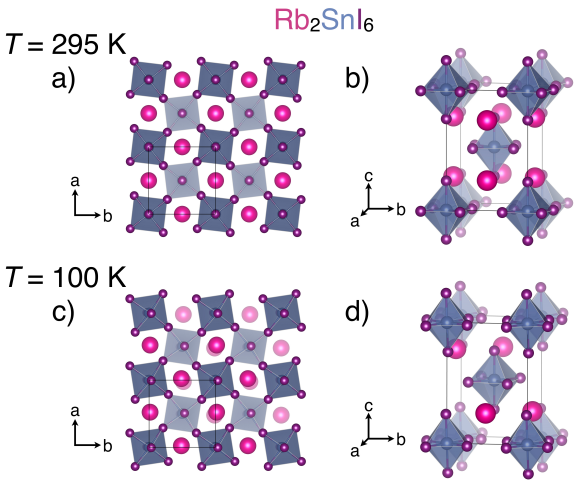

Figure 4.1: Crystal structures of Rb_2SnI_6 at T = 295 K and T = 100 K. In (a) and (c), the structures are projected down the *c*-axis to highlight the octahedral tilting and rotation, while unit cell descriptions are shown in b) and d). Rubidium atoms are shown in pink, tin atoms in blue, and iodine atoms are shown in purple.

Upon cooling to T = 100 K, Rb_2SnI_6 undergoes a phase transition to monoclinic symmetry (space group $P2_1/n$), characterized by out-of-phase tilting of the octahedra in the *ab* plane by ~5° ($a^-a^-c^+$), in addition to the 11° tilt about the *c*-axis. The transition is evidenced by splitting of the (202) reflection in the SXRD patterns shown in Figure 4.2c,d, and is consistent with the series of symmetry-lowering phase transitions commonly observed in other members of the vacancy-ordered double perovskite family and with those predicted for ordered double perovskites.[78,158,278] Structural and statistical parameters from Rietveld refinements of the tetragonal and monoclinic structural models against the SXRD data can be found in Table 4.1.

Temperature-dependent neutron diffraction data were collected from Bank 2 (31° bank) of the NOMAD instrument at the Spallation Neutron Source, Oak Ridge National Laboratory to gain insight into the phase transition behavior of Rb_2SnI_6. 5-minute scans were collected continuously upon cooling from T = 298 K to T = 14 K. As shown in Figure 4.3, the reflections shift to higher Q upon cooling, consistent with lattice contraction; a change in dQ/dT is observed at

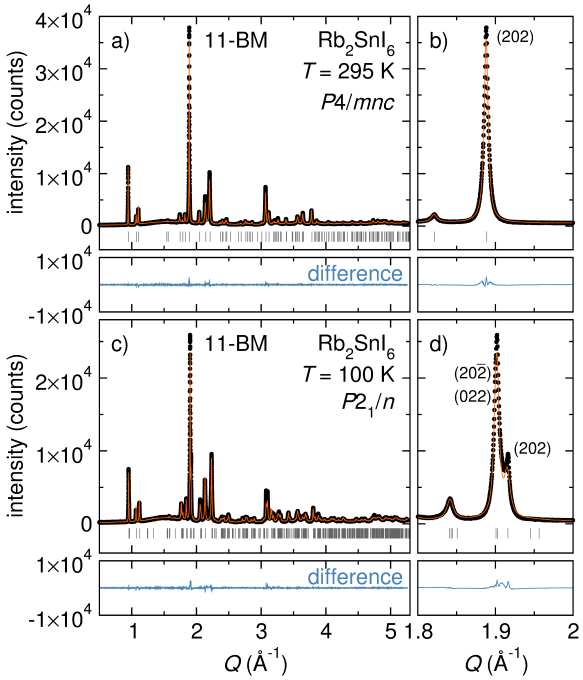

Figure 4.2: Rietveld refinements of the tetragonal and monoclinic structural models of Rb_2SnI_6 against high resolution synchrotron powder X-ray diffraction patterns collected at $T = 295$ K (a,b) and $T = 100$ K (c,d) on the high-resolution 11-BM diffractometer. Data are shown as black circles, the fit is the orange line, and the difference is shown in blue. Plots b) and d) highlight the splitting of the most intense reflection (202) at $Q \sim 1.9$ Å^{-1} upon cooling through the phase transition.

Table 4.1: Structural parameters and refinement statistics for Rb_2SnI_6 at $T = 295$ K and $T = 100$ K.

	295 K	100 K
Crystal System	Tetragonal	Monoclinic
Space Group	$P4/mnc$	$P2_1/n$
a (Å)	8.07056(6)	7.9426(1)
b (Å)	8.07056(6)	7.9758(9)
c (Å)	11.7650(1)	11.7876(2)
α (°)	90	90
β (°)	90	90.484(1)
γ (°)	90	90
U_{iso}(Rb) (Å^2)	0.0564(8)	0.0245(7)
U_{iso}(Sn) (Å^2)	0.0245(6)	0.0194(7)
U_{iso}(I1) (Å^2)	0.0587(7)	0.0296(5)
U_{iso}(I2) (Å^2)	0.0521(4)	0.0262(5)
U_{iso}(I3) (Å^2)	–	0.0219(5)
Red. χ^2	5.373	9.046
wR	8.41%	10.92%

$T \sim 189$ K for the peak located near $Q \sim 2.15$ Å^{-1}. The white horizontal line at $T = 189$ K denotes the estimated phase transition temperature from sequential refinements of the data. Though a split in the most intense reflection is observed in the $T = 100$ K synchrotron powder X-ray diffraction data (Figure 4.2), we lack the resolution to truly observe this splitting in the neutron powder diffraction data and thus cannot assign a phase transition temperature from qualitative inspection of these data.

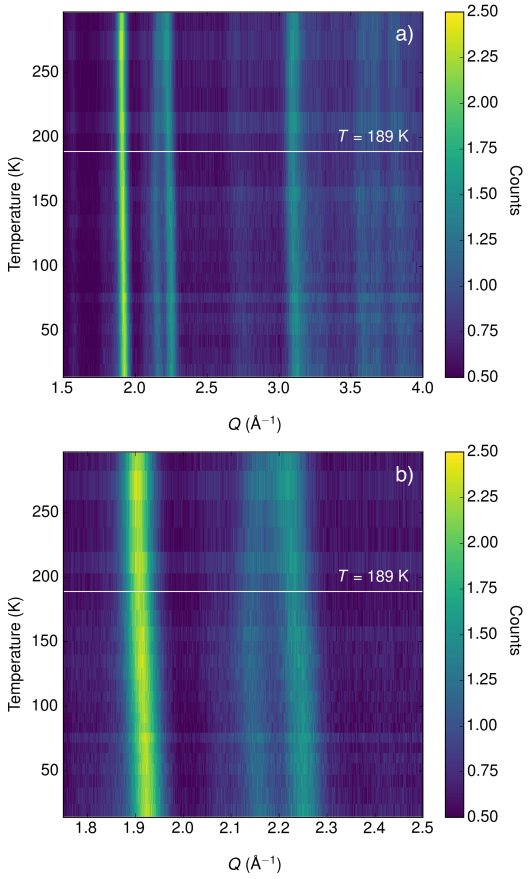

Figure 4.3: Neutron diffraction data of Rb_2SnI_6 collected upon cooling on the 31° bank of the NOMAD instrument. In a), the data are shown from $Q = 1.5$–4.0 Å^{-1}. In panel b), the data are shown over shorter Q-ranges ($Q = 1.75$–2.5 Å^{-1}) to highlight the most intense reflections in the diffraction pattern. The white horizontal line at $T = 189$ K denotes the estimated phase transition temperature of Rb_2SnI_6.

Sequential Rietveld refinements of the diffraction data were performed from low to high temperatures using the $P2_1/n$ structural model for all temperatures, and lattice parameters and atom positions were allowed to refine. Examination of the β angle as a function of temperature

reveals two regions of interest, as shown in Figure 4.4. Below $T \sim 189$ K, the refined values for the β angle are relatively constant near 90°, consistent with the value of 90.484(1)° refined from the $T = 100$ K SXRD data. Between $T \sim 189$ K and $T \sim 200$ K, the β angle undergoes a dramatic increase to ~93° and levels off between ~92-93° for temperatures above $T \sim 189$ K. The drastic change in β angle at $T \sim 189$ K provides an estimation of the phase transition temperature to be near $T \sim 189$ K. Though we note there is not sufficient resolution nor signal-to-noise to accurately assess the correct space group symmetry, the change in coefficient of expansion suggests the onset of a phase transition.

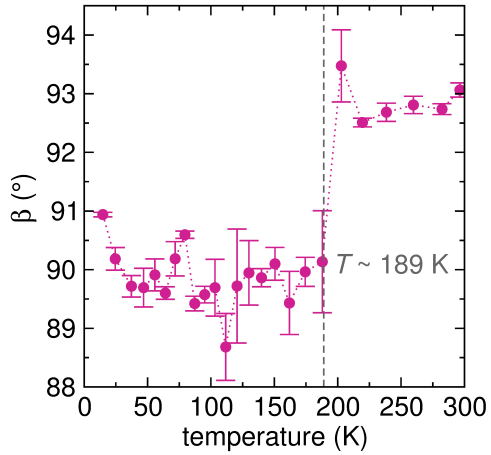

Figure 4.4: Monoclinic β angle plotted as a function of temperature extracted from sequential Rietveld refinements of the $P2_1/n$ structural model of Rb_2SnI_6 against neutron diffraction data collected on the NOMAD instrument.

4.3.2 Electronic and Optical Properties

Electrical resistivity measurements of Rb_2SnI_6 performed in a 4-probe configuration reveal semiconducting behavior, as evidenced by increasing resistivity upon cooling shown in Figure 4.5. At $T = 300$ K, Rb_2SnI_6 exhibits a bulk resistivity of $\rho = \sim 5 \times 10^5$ Ω·cm, which is approximately five orders of magnitude larger than that reported for Cs_2SnI_6 ($\rho = 12$ Ω·cm).[7] Hall effect measurements at $T = 300$ K reveal that Rb_2SnI_6 exhibits native n-type conductivity, consistent with the formation of iodine vacancy defect states that form as shallow donors to the conduc-

tion band, as in other tin(IV)-iodide based vacancy-ordered perovskites.[6,7,103] The higher resistivity of Rb_2SnI_6 compared with Cs_2SnI_6 arises from a reduction in both carrier concentration and carrier mobility. From Hall effect measurements, Rb_2SnI_6 exhibits a carrier concentration on the order of $n_e \sim 10^{12}$ cm^{-3} and a carrier mobility of $\mu_e \sim 0.22(3)$ cm^2 V^{-1} s^{-1}, which are reduced by factors of ~10^4 and ~50 respectively compared with $n_e \sim 5(1)\times10^{16}$ cm^{-3} and $\mu_e \sim 8.6(5)$ cm^2 V^{-1} s^{-1} reported for Cs_2SnI_6.[7]

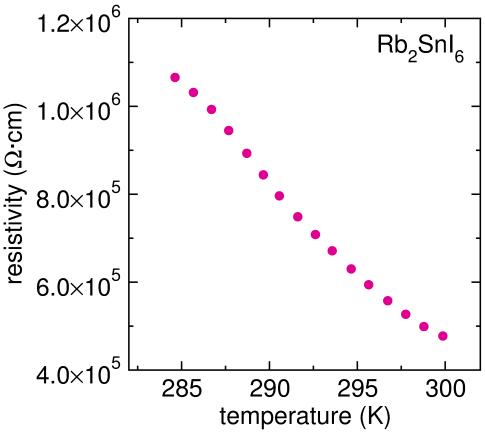

Figure 4.5: Temperature-dependent resistivity data of rubidium tin(IV) iodide collected using a 4-probe configuration with Pt wires and Ag paste.

Analysis of UV-visible diffuse reflectance spectroscopy data for Rb_2SnI_6 yields an optical gap of 1.32(2) eV, consistent with the black color of the compound. The optical gap was extracted by converting the raw reflectance data to pseudo-absorbance, $F(R)$, using the Kubelka-Munk function. The optical gap was determined by extrapolating the linear absorption onset region to zero absorbance, as shown in Figure 4.6. The optical gap of 1.32(2) eV is slightly larger than the value of 1.23(3) eV determined for Cs_2SnI_6 by the same method.[6,7]

4.3.3 Local Coordination Environment

X-ray and neutron pair distribution function (XPDF, nPDF) analyses were employed to correlate changes in the local coordination environment with the observed structural and electronic behavior. The XPDF of rubidium tin(IV) iodide at T = 300 K in shown in Figure 4.7.

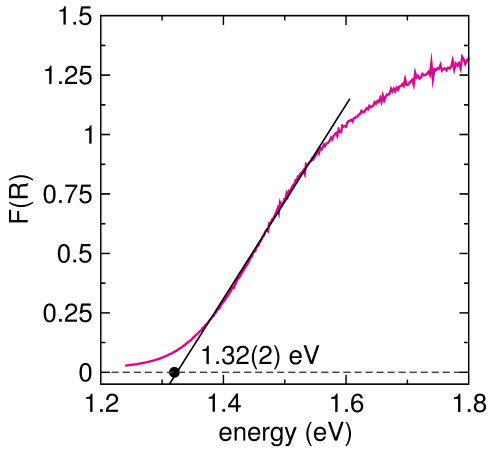

Figure 4.6: UV-visible diffuse reflectance spectrum for Rb_2SnI_6. The data were converted to pseudo-absorbance via the Kubelka-Munk transform and the optical gap was determined by extrapolating the onset region to zero absorbance, as shown by the black fit. The pink line is the transformed data, the fit is the black line, and zero absorbance is shown as the grey dashed line. The intersection point of the fit and zero absorbance is shown by the black dot.

The local coordination environment of Rb_2SnI_6 is moderately well-described by the tetragonal structural model observed in the powder X-ray diffraction data. Modeling the data with this structural model requires the inclusion of large, anisotropic atomic displacement parameters (ADPs) for the iodine and rubidium atoms, as represented by the thermal ellipsoids on the structural models shown adjacent to the fit. Yet, the model still does not capture the shape of the next-nearest neighbor I–I pair correlation at $r \sim 4$ Å. The large ADPs required to provide an adequate fit to the data suggest the presence of disorder (static or dynamic) of the iodine and rubidium atoms within the structure. The fit to the XPDF is significantly improved, both statistically and visually, with the use of the low-temperature monoclinic structural model determined from the $T = 100$ K SXRD data, as shown in Figure 4.7b. The addition of out-of-phase octahedral tilting into the *ab* plane permitted by the lower symmetry of the monoclinic structure results in significantly smaller isotropic ADPs for all atoms, as shown by the thermal ellipsoids in the corresponding structural model.

This analysis indicates that the local coordination environment at $T = 300$ K is best modeled by the monoclinic structural modification, despite the higher-symmetry tetragonal structure observed by SXRD. This observation is consistent with previous reports of other perovskite

halide materials, in which dynamic and cooperative octahedral rotations manifest as a lower-symmetry instantaneous structure[279] in the local coordination environment, yet they average to higher symmetry structures observed by diffraction.[6,45,52,67,86,259,260] The large thermal ellipsoids observed for both iodine and rubidium atoms implies that there is strong coupling between octahedral tilting and Rb^+ displacements, as has been previously presented.[46]

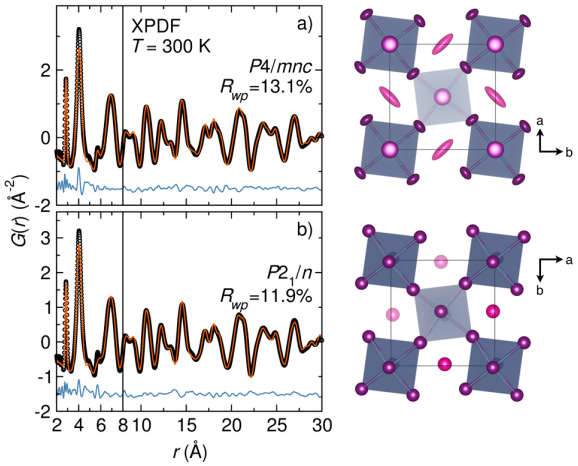

Figure 4.7: The X-ray pair distribution function of Rb_2SnI_6 fit to the a) tetragonal ($P4/mnc$) and b) monoclinic ($P2_1/n$) structural models. In a), the XPDF is fit to the tetragonal ($P4/mnc$) model using anisotropic atomic displacement parameters for iodine and rubidium ions, and in b) the XPDF is fit to the monoclinic ($P2_1/n$) structural model using isotropic displacement parameters for all atoms. The thermal ellipsoids in the corresponding structural models are shown at 95% probability.

Temperature-dependent neutron pair distribution function analysis (nPDF) was performed to probe changes in the local coordination environment of Cs_2SnI_6 and Rb_2SnI_6 as a function of temperature. At all temperatures, the local coordination environment of Cs_2SnI_6 is well-described by the cubic structural model, with no evidence of symmetry-lowering phase transitions, consistent with the corresponding neutron diffraction patterns shown in Figure 4.8b and with our previous report.[7] We note that a slight asymmetry of the next-nearest neighbor I–I pair correlation at $r \sim 4$ Å is observed at $T = 300$ K, which has been previously attributed to anharmonic lattice dynamics.[6] The fits of the cubic structural model to the nPDF are shown in Figure 4.8a, and Rietveld refinements of the cubic structural model against the corresponding diffraction data are shown in Figure 4.8b.

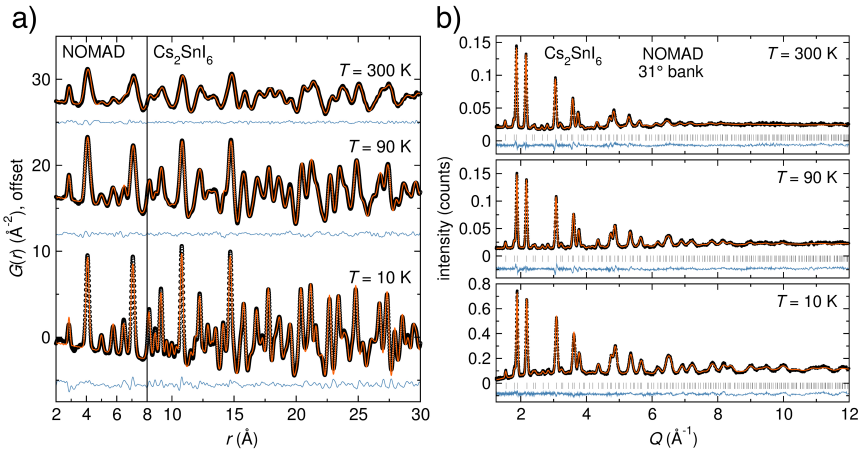

Figure 4.8: a) Temperature-dependent neutron pair distribution function analysis (nPDF) of Cs_2SnI_6 extracted from neutron total scattering collected on NOMAD. The x-axis is split to highlight the low-r pair correlations. Rietveld refinements of the corresponding neutron diffraction patterns collected from bank 2 (31° bank) of NOMAD are shown in b). Both the nPDF and neutron diffraction data are modeled by the cubic ($Fm\bar{3}m$) structural model at all temperatures. Black circles are the data, the orange lines are the fits, and the blue lines are difference curves. In b), the grey tick marks indicate the positions of predicted reflections from the $Fm\bar{3}m$ structure.

Temperature-dependent nPDFs of Rb_2SnI_6 provide further insight into the structural behavior observed by SXRD and XPDF. For $T > 150$ K, the nPDF can be modeled with the tetragonal structural model with the inclusion of large, anisotropic ADPs for the iodine atoms or with the monoclinic structural model with isotropic ADPs, consistent with analysis of the XPDF shown in Figure 4.7. Upon cooling to $T = 150$ K, a low-r shoulder to the next-nearest neighbor I–I pair correlation at $r = 4$ Å appears, which is only captured by the monoclinic structural model, as shown in Figure 4.9a. The appearance of this shoulder results in a poor fit to the nPDF when modeling with the higher-symmetry tetragonal structure. Rietveld refinements of the corresponding neutron diffraction data are shown Figure 4.9b. Data collected at temperatures above $T = 150$ K are modeled with the tetragonal $P4/mnc$ structure, while data collected at $T = 150$ K and below are modeled by the $P2_1/n$ structure.

4.3.4 Electronic Structure Calculations

Density functional calculations were performed to gain insight into the optical and electronic properties of rubidium tin(IV) iodide. The orbital-projected band structures of Rb_2SnI_6

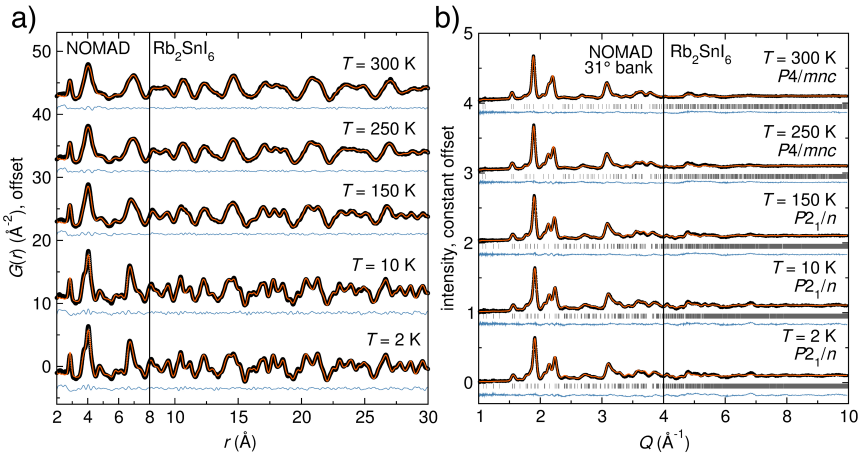

Figure 4.9: a) Temperature-dependent neutron pair distribution function analysis (nPDF) of Rb_2SnI_6 extracted from neutron total scattering collected on NOMAD. The nPDFs are best modeled by the monoclinic ($P2_1/n$) structure at all temperatures. The x-axis is split to highlight the low-r pair correlations, and the data are offset vertically for clarity. Rietveld refinements of the neutron diffraction data from bank 2 (31° bank) of NOMAD are shown in b). For $T > 150$ K, the data are modeled with the tetragonal ($P4/mnc$) structure. For $T \leq 150$ K, the data are modeled by the monoclinic ($P2_1/n$) structure. Black circles are the data, the orange lines are the fits, and the blue lines are difference curves. In b), the grey tick marks indicate the positions of predicted reflections from the $P4/mnc$ and $P2_1/n$ structures. The x-axis is split to highlight the lower-Q reflections, and the data are offset vertically for clarity.

in the $P4/mnc$ and $P2_1/n$ structures, calculated using HSE06+SOC, are shown in Figure 4.10. Both symmetries yield direct band gaps, with fundamental band gaps of 1.13 eV and 1.32 eV occurring at the Γ point (Table 4.2). Spin-orbit coupling was found to play a role on the size of the band gaps, with a band gap renormalization of 0.19 eV and 0.21 eV seen, respectively, mainly though raising of the valence band maximum. For both compounds, the orbital projections reveal the upper valence band to be dominated by I 5p states, with the conduction band minimum derived from hybridization between Sn 5s and I 5p states, in agreement with other A_2SnI_6 perovskite materials.[6,7] We note that the calculated fundamental band gap of the $P4/mnc$ phase is significantly smaller than the optical band gap measured in experiment (1.32 eV). Analysis of the transition dipole moments reveals that, consistent with other A_2SnI_6 materials,[7] the fundamental band gap is dipole disallowed in both symmetries. Instead, the optical band gap results from transitions originating from the bands ~0.30 eV below the valence band maximum.

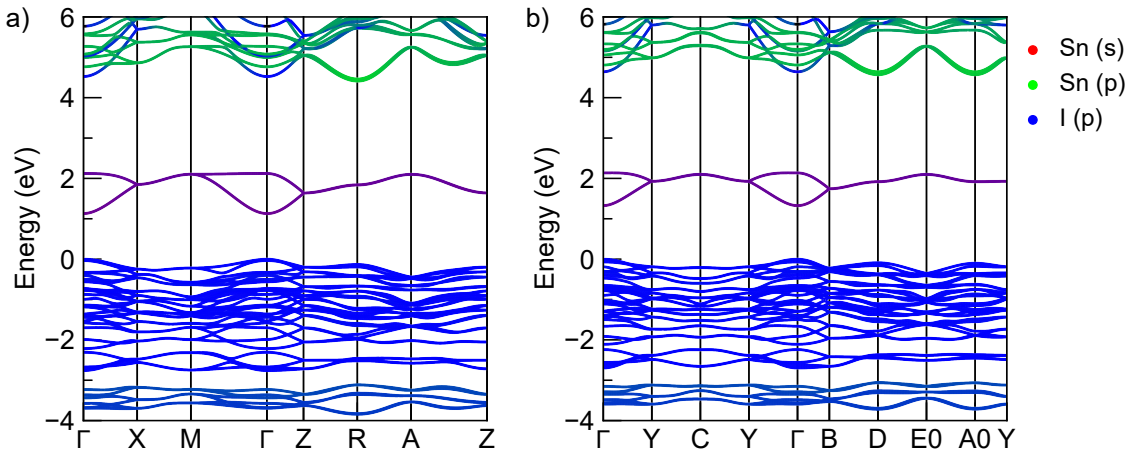

Figure 4.10: Band structures calculated using HSE06+SOC for the a) $P4/mnc$ and b) $P2_1/n$ phases of Rb_2SnI_6. The color of the band indicates the orbital contribution to that band, with Sn 5*s*, Sn 5*p*, and I 5*p* represented by red, green and blue, respectively. The resulting color of the bands is obtained by mixing each color in proportion to the orbital contributions. The valence band maximum is set to 0 eV in all cases.

Table 4.2: Band gaps (E_g), conduction bandwidths ($\Delta\epsilon_{CB}$) and charge carrier effective masses (m^*), calculated using HSE06+SOC, for the $P4/mnc$ and $P2_1/n$ phases of Rb_2SnI_6. Band gaps and widths provided in eV, effective masses given in units of the bare electron mass, m_0.

Phase	E_g	$\Delta\epsilon_{CB}$	m_e^*	m_h^*
$P4/mnc$	1.13	0.99	0.39	0.98
$P2_1/n$	1.32	0.81	0.44	1.07

The carrier effective masses, calculated based on parabolic fits of the band edges in three directions around the Γ point, indicate electrons will be relatively mobile, with masses of 0.39 m_0 and 0.44 m_0 seen for the $P4/mnc$ and $P2_1/n$ phases, respectively. These are marginally larger than the electron effective masses in Cs_2SnI_6 (m_e^* = 0.25 m_0),[6] likely due to deviations in the close-packed iodine sublattice from octahedral tilting. These changes further manifest as a reduction in the conduction bandwidth, $\Delta\epsilon_{CB}$, from 1.39 eV seen in Cs_2SnI_6, to 0.99 eV and 0.81 eV, for the $P4/mnc$ and $P2_1/n$ phases, respectively.

DFT calculations of isolated slab structures surrounded by vacuum reveal that the band gap differences between the two phases of Rb_2SnI_6 are driven by changes in the position of both the valence band maximum and conduction band minimum. For the $P4/mnc$ phase, the HSE06+SOC calculated ionization potential and electron affinity are 5.82 eV and 4.70 eV, respec-

tively. Moving to the low temperature $P2_1/n$ phase, the ionization potential is deeper relative to the vacuum level (5.92 eV), whereas the electron affinity becomes more shallow (4.60 eV). Again, these changes can likely be attributed to subtle distortions of the close-packed iodine sublattice, and the reduction in bandwidth of both the upper valence and lower conduction bands. We note that the band alignments are close to those calculated for Cs_2SnI_6, which shows an ionization potential and electron affinity of 5.79 eV and 4.80 eV, respectively; this is not unexpected due to the similar orbital composition of the valence and conduction bands in these materials.

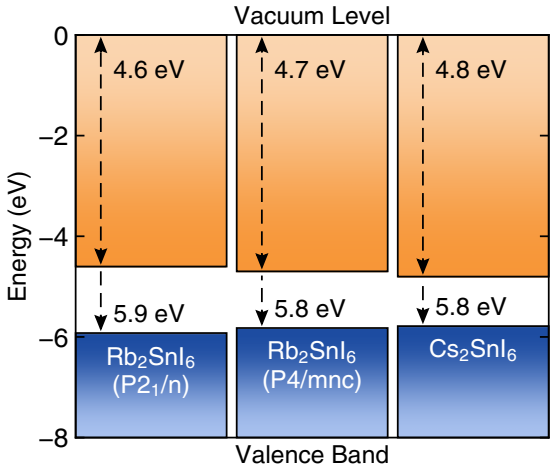

Figure 4.11: Calculated band alignment (HSE06+SOC) of the $P4/mnc$ and $P2_1/n$ structured phases of Rb_2SnI_6 relative to those of Cs_2SnI_6.

To further investigate the carrier mobilities in Rb_2SnI_6, we have calculated the limits of electron mobility within a temperature-dependent Feynman polaron transport model. This method has recently been applied to the cubic hybrid perovskites[250] and other members of the A_2SnI_6 series.[6] All required parameters were calculated *ab initio* and are provided in Table 4.3. The electron effective masses necessary for the calculations, m_e^*, are provided in Table 4.2. Within this model, the extent of electron–phonon coupling (α) is used to evaluate the polaron mobility (μ_e^H,calculated within the Hellwarth model),[38] along with the associated phonon-drag mass-renormalization (m_r^*) and relaxation time (τ). The Hellwarth electron mobilities, μ_e^H, at

$T = 300$ K are presented in Table 4.4. This model is highly idealized, with the physical response of the lattice parametrized by the optical and static dielectric constants and effective-response frequency. Despite this, previous work applying this method to the hybrid perovskites has shown excellent agreement with experiment. We note that this method does not take into account other scattering processes; therefore, the results will form an upper bound for electron mobilities for a perfect crystal.

Table 4.3: Parameters of the Feynman polaron model. High frequency (ϵ_∞) and static (ϵ_S) dielectric constants given in units of the permittivity of free space (ϵ_0). Frequency (f) is in THz.

Space group	ϵ_∞	ϵ_S	f
$P4/mnc$	3.61	8.38	4.01
$P2_1/n$	3.64	8.48	4.32

Table 4.4: Hellwarth electron mobilities at $T = 300$ K (μ_e^H, cm^2 V^{-1} s^{-1}), electron–phonon coupling (α), effective mass renormalization (m_r^*, units of m^*) and polaron relaxation time (τ, ps), calculated within a temperature-dependent polaron model, for the $P4/mnc$ and $P2_1/n$ phases of Rb_2SnI_6.

Space group	μ_e^H	α	m_r^*	τ
$P4/mnc$	24.4	2.83	1.71	0.07
$P2_1/n$	19.8	2.98	1.64	0.06

The calculated Hellwarth electron mobilities for the $P4/mnc$ (24 cm^2 V^{-1} s^{-1}) and $P2_1/n$ (20 cm^2 V^{-1} s^{-1}) phases of Rb_2SnI_6 are significantly smaller than those calculated for Cs_2SnI_6 (98 cm^2 V^{-1} s^{-1}). The increase in electron effective masses seen in the Rb_2SnI_6 phases will play a crucial role; however, when considered alone, they are insufficient to account for the dramatic difference between the experimental mobilities. Instead, the trend can be attributed to two additional factors: Firstly, the Rb_2SnI_6 phases show considerably larger static dielectric constants (~8.4) than Cs_2SnI_6 (7.2), due to an increase in the ionic component of the dielectric response. Analysis of the zone center phonon eigenvalues and eigenvectors reveals that this is due to an increase in the number of *low*-frequency polar phonon modes that can contribute to the dielec-

tric response of the lattice. These additional modes and their increased polarity result from the symmetry breaking in the Rb_2SnI_6 phases, which reduces the degeneracy of several modes in the highly degenerate Cs_2SnI_6 phonon spectrum. Secondly, the high-frequency dielectric constants of the Rb_2SnI_6 phases are slightly reduced, likely due to the changes in the iodine sublattice. Together, these factors result in significantly larger electron–phonon coupling constants (α) of 2.83 and 2.98 for the $P4/mnc$ and $P2_1/n$ phases of Rb_2SnI_6, in comparison to just 1.45 for Cs_2SnI_6. The increased coupling, combined with larger effective masses, results in significant effective mass renormalization and small polaron relaxation times. We note that the effective-response frequency is larger in Rb_2SnI_6 than in Cs_2SnI_6, suggesting a stiffening of the lattice. Further investigation into the IR response of the modes indicates that the symmetry breaking also allows for increased polarity of the higher-frequency phonon modes, thereby increasing the effective-response frequency, with the stiffness of the lattice remaining largely unchanged.

Further examination of the phonon band structure of tetragonal Rb_2SnI_6 reveals that the tetragonal structure is dynamically stable within the harmonic approximation of forces calculated by DFPT, as evidenced by the lack of imaginary phonon modes (Figure 4.12). The lowest-energy optical phonon occurs at 0.25 THz (1.03 meV, 8.27 cm^{-1}) at the Γ point, as denoted by the orange circle in Figure 4.12. Analysis of the polarization eigenvectors indicates that this mode corresponds to displacements of the iodine and rubidium ions within the structure, which are consistent with cooperative octahedral tilting out of the *ab* plane coupled to Rb^+ displacements and map onto the lower-symmetry ($a^-a^-c^+$) monoclinic structure observed at low temperatures. This observation is consistent with the structural behavior of Rb_2SnI_6 observed experimentally. At higher temperatures, dynamic octahedral tilting averages to the tetragonal structure observed by diffraction, yet it gives rise to the lower symmetry suggested from the local coordination environment. Upon cooling, the octahedral tilts freeze in to yield the lower-symmetry monoclinic structure observed in the crystallography. This notion is supported by previous studies of the vacancy-ordered double perovskite family, which have shown that the symmetry-lowering phase transitions in these materials are driven by condensation of the octa-

hedral rotary phonon mode.[85,86,93] The lack of imaginary modes in these calculations suggests that anharmonicity may play a role in driving the structure to the monoclinic ground state.

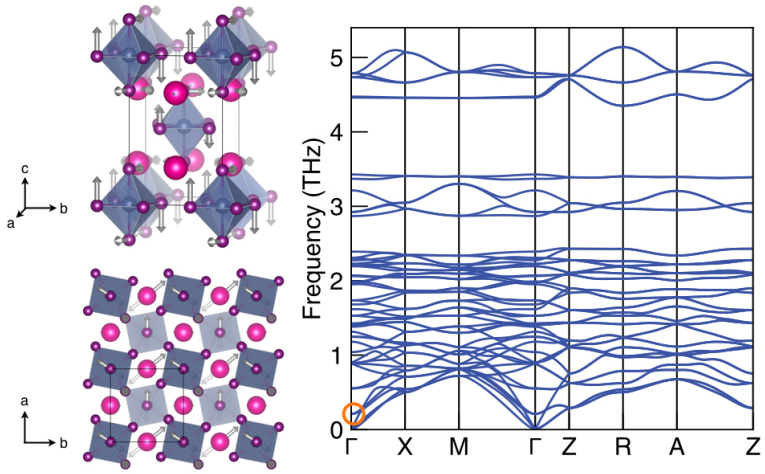

Figure 4.12: The phonon band structure of rubidium tin(IV) iodide in the tetragonal $P4/mnc$ structure ($a^0a^0c^+$). The lowest-frequency optic mode at 0.25 THz (1.03 meV, 8.27 cm^{-1}) (denoted by the orange circle) corresponds to displacements of the rubidium and iodine atoms, as shown by the displacement vectors in the structural representations. Together, these displacements map to the octahedral tilting out of the ab plane coupled with Rb^+ displacements observed in the lower-symmetry monoclinic structure, ($a^-a^-c^+$).

4.4 Discussion

Rb_2SnI_6 adopts a tetragonal ($P4/mnc$) variant of the vacancy-ordered double perovskite structure at room temperature characterized by cooperative octahedral tilting, and undergoes a phase transition to monoclinic ($P2_1/n$) upon cooling. Temperature-dependent phase transitions in perovskites are typically driven by a size mismatch between the A-, B-, and X-site ions, and cooperative rotation and tilting of the octahedral units occur to improve coordination to the A-site cation by the neighboring X-site anions by collapsing the A-site void.[46,78,81,280] Bond valence sum (BVS) analysis of Cs_2SnI_6 reveals that the coordination provided to the Cs^+ ion by the I_{12} cage results in a Cs valence of 1.156, indicating that the cesium is potentially over-bonded by the surrounding iodine network in the cubic structure (using tabulated parameters). This analysis provides an explanation for the observation that Cs_2SnI_6 does not appear to be suscep-

tible to temperature-dependent phase transitions or distortions of the local coordination environment. BVS analysis of the previously reported cubic structure of Rb_2SnI_6 yields an underbonded BVS for the Rb^+ ions of 0.891, indicating that the Rb–I bond distances are too long to provide adequate coordination to the rubidium ions in that structural model.[277] The bond valence of rubidium is improved in the tetragonal (0.939) and monoclinic (1.069) structural models, consistent with the observation that Rb_2SnI_6 adopts both the tetragonal and monoclinic variants of the vacancy-ordered double perovskite family, as well as with DFT-based calculations that show the dominating role of electrostatics in determining octahedral tilting patterns in perovskite halides.[81] Further, this lends support to our hypothesis that dynamic octahedral tilting occurs readily at room temperature to yield the tetragonal structure by diffraction yet reduced symmetry in the local coordination environment. This notion is further supported by analysis of the phonon spectrum of Rb_2SnI_6, which indicates that the lowest-energy optical phonon corresponds to octahedral tilting and rubidium ion displacements that together map onto the lower-symmetry monoclinic structure. Parameters used in the BVS analysis are shown in Table 5.1.

Table 4.5: Bond valence sum analysis for Cs–I and Rb–I bonds in Cs_2SnI_6 and Rb_2SnI_6.

	B[281]	R_0 (Å)[281]	BVS
Cs–I ($Fm\bar{3}m$)	0.609	2.6926	1.156
Rb–I ($Fm\bar{3}m$)	0.638	2.4509	0.891
Rb–I ($P4/mnc$)	0.638	2.4509	0.939
Rb–I ($P2_1/n$)	0.638	2.4509	1.069

Analysis of the band effective masses suggests that static cooperative octahedral tilting does not play a strongly significant role in dictating the charge transport behavior in Rb_2SnI_6. While octahedral tilting in Rb_2SnI_6 induces subtle changes in the close-packed iodine framework and yields slightly larger carrier effective masses than in the cubic Cs_2SnI_6 (by a factor of 1.5-1.8), these structural changes alone are not sufficient to account for the trend in carrier mobilities observed experimentally. Rather, calculation of the electron-phonon coupling characteristics

of Rb_2SnI_6 indicates that the lower symmetry due to octahedral tilting yields a larger number of low-frequency polar phonons that contribute to a large static dielectric constant and subsequently stronger electron–phonon coupling that significantly reduces carrier mobilities. Therefore, interpreting the electronic properties from the perspective of static cooperative octahedral tilting is insufficient to fully understand the charge transport behavior in vacancy-ordered double perovskites, and a dynamic understanding of these structural deviations is necessary to account for the observed behavior.

While lattice dynamics play a critical role in dictating the electronic properties of vacancy-ordered double perovskites, the interplay between octahedral tilting and charge transport in Rb_2SnI_6 can be generalized to a set of guiding principles for predicting charge transport behavior in vacancy-ordered double perovskites based upon the geometric model of the perovskite tolerance factor. A highly simplified use of the Goldschmidt tolerance factor, $t = (r_A + r_X)/(\sqrt{2}(r_B + r_X))$, where B = Sn(IV) and X = I ($r_{Sn} = 0.69$ Å and $r_I = 2.2$ Å)[207] captures the observed trends in carrier mobilities for these vacancy-ordered double perovskites. Of the A_2SnI_6 family ($A = Rb^+$, Cs^+, $CH_3NH_3^+$, and $CH(NH_2)_2^+$), the tolerance factor for Cs_2SnI_6 is 0.998 and Cs_2SnI_6 exhibits the largest carrier mobility of ~ 9 cm^2 V^{-1} s^{-1} (Figure 4.13). Incorporation of the larger $CH_3NH_3^+$ and $CH(NH_2)_2^+$ ions yields tolerance factors of 1.07 and 1.16 and carrier mobilities of ~ 2.5 cm^2 V^{-1} s^{-1} and ~ 0.36 cm^2 V^{-1} s^{-1}, respectively.[6] Replacement of Cs^+ with Rb^+ yields a tolerance factor of 0.959 and a carrier mobility of $\mu_e \sim 0.22(3)$ cm^2 V^{-1} s^{-1}. Further, the trends in carrier mobilities observed experimentally are captured by the computationally-derived Hellwarth electron mobilities (μ_e^H), as also shown in Figure 4.13. Therefore, we might expect that vacancy-ordered double perovskite materials with tolerance factors closest to unity will exhibit weaker electron–phonon coupling interactions and higher carrier mobilities. Cations that are too large for the A-site can introduce soft, anharmonic lattice dynamics that produce tightly-bound polarons that localize charge carriers and impede charge transport, as in $(CH_3NH_3)_2SnI_6$ and $(CH(NH_2)_2)_2SnI_6$.[6] In contrast, cations that are too small yield structures of reduced symmetry, as characterized by cooperative octahedral tilting and rotation. This slightly distorts the

close-packed halogen sublattice and increases the number of low-lying phonon modes that contribute to stronger electron–phonon coupling interactions and reduce carrier mobilities.

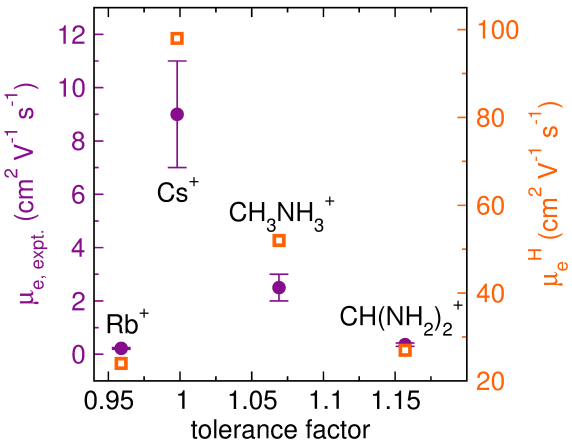

Figure 4.13: Experimentally- ($\mu_{e,\text{expt.}}$) and computationally-derived Hellwarth (μ_e^H) electron mobilities of the A_2SnI_6 vacancy-ordered double perovskites plotted as a function of perovskite tolerance factor. Experimental electron mobilities are shown as filled purple circles on the left axis, while the calculated Hellwarth electron mobilities are denoted by open orange squares on the right axis. Values for the carrier mobilities of Cs_2SnI_6, $(CH_3NH_3)_2SnI_6$, and $(CH(NH_2)_2)_2SnI_6$ are taken from a previous study.[6] For Rb_2SnI_6, the μ_e^H value is calculated from the tetragonal structure.

4.5 Conclusions

Replacing Cs^+ with the smaller Rb^+ ion in the vacancy-ordered double perovskite Rb_2SnI_6 is accompanied by significant changes in structural and electronic behavior. Electrical conductivity measurements of Rb_2SnI_6 indicate that, similarly to Cs_2SnI_6, Rb_2SnI_6 is a native n-type semiconductor. However, the carrier mobility is reduced by a factor of ~50 for Rb_2SnI_6 compared to Cs_2SnI_6. Structural analysis through high-resolution synchrotron powder X-ray diffraction indicates that Rb_2SnI_6 crystallizes in a lower-symmetry structural modification of the vacancy-ordered double perovskite structure, characterized by cooperative tilting of the [SnI_6] octahedra ($a^0a^0c^+$). Upon cooling, Rb_2SnI_6 undergoes further octahedral tilting to a monoclinic structure ($a^-a^-c^+$). X-ray and neutron pair distribution function analysis reveals that the bonding environment is best described by the monoclinic structure at all temperatures, which becomes

thermally averaged to higher symmetry at ambient temperature. No structural distortions are observed for Cs_2SnI_6 to $T = 10$ K. Density functional calculations reveal that the reduced carrier mobilities observed experimentally in Rb_2SnI_6 relative to Cs_2SnI_6 arise from stronger electron–phonon interactions and subsequently smaller Hellwarth electron mobilities in Rb_2SnI_6 due to an increase in the number of low-frequency phonons that contribute to the dielectric response of the lattice, rather than a trivial increase in band effective mass. This observation suggests that the polaron characteristics and charge transport behavior in the vacancy-ordered double perovskite family can be tuned by introducing cooperative octahedral tilting distortions through judicious choice of *A*-site cation and further predicted bond valence sum and the perovskite tolerance factor.

Chapter 5

Bond Valences and Anharmonicity in Vacancy-Ordered Double Perovskite Halides[5]

5.1 Introduction

Lattice dynamics play a crucial role in dictating materials properties, including thermal conductivity,[282] ionic and electronic transport,[60,283] optical emission,[284,285] piezoelectricity and ferroelectricity,[286,287] and superconductivity,[288] to name a few. Divergence from a purely harmonic vibrational landscape further manifests interesting physical behavior. High amplitude anharmonic vibrations in systems such as the tin and lead chalcogenides introduce vibrational disorder to which their low thermal conductivities and advantageous performance in thermoelectric devices are attributed.[261,289,290] Anharmonic rattling of guest atoms within host structures has been exploited as a mechanism to disrupt thermal conductivity in other candidate thermoelectric materials such as skutterudites.[291] Additionally, ionic conductivity may be enhanced in materials in which the mobile ion occupies a flat and broad anharmonic potential well,[292,293] while lower-energy anharmonic vibrational modes can couple to mobile electrons to reduce electron mobilities.[25,60] Despite the extensive influence of anharmonicity upon functional properties in crystalline materials, a unified understanding of the structural and bonding motifs necessary to leverage anharmonic behavior to target particular materials properties is fundamentally lacking.

Halide-based perovskite materials are redefining the paradigm of semiconductor materials design principles, in that they appear to follow a set of structure-dynamics-property relationships that are distinct from conventional semiconductors. The perovskite structure adopts the general formula ABX_3, and the structure is composed of corner sharing BX_6 octahedra with *A*-

[5]Substantial portions of this chapter have been reproduced with permission from A. E. Maughan, A. A. Paecklar and J. R. Neilson, *J. Mater. Chem. C*, **2018**, DOI: 10.1039/c8tc03527j.

site cations in the 12-coordinate void. Anharmonic lattice dynamics in perovskite halides have been shown to arise from rotational instabilities of the soft, deformable BX_6 octahedral framework coupled with motions of the *A*-site cation.[45,260,294] These dynamic instabilities yield an anharmonic double potential well, resulting in an instantaneous local structure characterized by cooperative octahedral tilting that averages to a higher-symmetry, untilted structure.[45,67,260,294] Anharmonicity has been further correlated with the remarkable photoconversion efficiencies of halide perovskite materials in photovoltaic devices.[134,233] Of particular note is the observation of long carrier excited-state lifetimes,[21,51,234] which are hypothesized to arise from the formation of polarons that protect photogenerated charge carriers and prevent recombination.[25,51–53,61,77,295,296] The intimate link between anharmonic lattice dynamics and functional properties motivates a fundamental understanding of the structural and compositional origins of anharmonicity in perovskite halides.

Vacancy-ordered double perovskites present a materials family to study anharmonicity in a lattice with additional dynamic degrees of freedom. The vacancy-ordered double perovskite structure is formed by doubling the conventional ABX_3 perovskite unit cell and removing every other *B*-site cation to form a face-centered lattice of isolated BX_6 octahedral units bridged by *A*-site cations in the void. Alternatively, the structure can be thought of as an ordered double perovskite of the formula $A_2B\square X_6$, with rock salt ordering of BX_6 and $\square X_6$ octahedra, where $\square$ denotes a vacancy, as shown in Figure 5.1. Anharmonicity in the vacancy-ordered double perovskites Cs_2SnI_6, $(CH_3NH_3)_2SnI_6$, and $(CH(NH_2)_2)_2SnI_6$ has been correlated with reduced carrier mobilities.[6] Replacing the inorganic Cs^+ with the molecular methylammonium ($CH_3NH_3^+$) and formamidinium ($CH(NH_2)_2^+$) cations is accompanied by a significant reduction in electron mobilities due to softer, more anharmonic lattice dynamics that result in stronger electron-phonon coupling interactions. In order to leverage anharmonicity as a design principle for perovskite halide semiconductors, a fundamental understanding of the structural and compositional origins of anharmonic lattice dynamics are required.

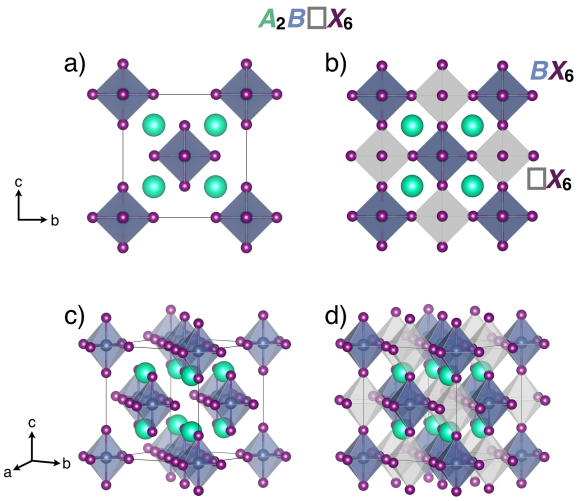

Figure 5.1: Unit cell representation of the cubic vacancy-ordered double perovskite structure. *A*-site cations are shown in teal, *B*-site cations are shown in blue, and *X*-site anions are shown in purple. Panels (a) and (c) highlight the isolated BX_6 octahedral units. In (b) and (d), the grey, transparent octahedra represent the ordered vacancies, denoted as $\square X_6$.

In this contribution, we assess the structural origins of anharmonicity in the series of inorganic vacancy-ordered double perovskites $Cs_2Sn_{1-x}Te_xI_6$. X-ray pair distribution function analysis reveals asymmetry in the local coordination environment of Cs_2SnI_6, which systematically decreases and vanishes with increasing tellurium content. Neutron total scattering of Cs_2SnI_6 reveals that the peak asymmetry becomes increasingly pronounced at higher temperatures, indicating that this feature is likely due to a dynamic effect rather than a static structural distortion. We attribute the subtle deviations in the local coordination environment of the $Cs_2Sn_{1-x}Te_xI_6$ series to anharmonic lattice dynamics brought about by octahedral rotations and Cs^+ displacements, consistent with the concave-down shape of the atomic displacement parameter vs. temperature curves for cesium and iodine. This assertion is supported by pseudo-rigid-body Reverse Monte Carlo simulations of Cs_2SnI_6 and Cs_2TeI_6. From the RMC-optimized structures, we find that the Cs–I and $I–I_{inter}$ partial pair correlations exhibit a broad, asymmetric distribution, indicating that the anharmonicity arises from these atom pairs. We further quantified the trend in anharmonicity in the XPDFs of $Cs_2Sn_{1-x}Te_xI_6$ using a modified anharmonic Toda potential and find a strong correlation of the peak asymmetry with the calculated bond valence of the Cs^+ cation, suggesting that the anharmonicity arises due to dissatisfied bonding

preferences of the Cs^+ cation within the cuboctahedral void, giving rise to dynamic octahedral rotations coupled to displacements of the Cs^+ ions. The relationship between bonding and anharmonicity provides a hand-hold for tuning the vibrational properties in vacancy-ordered double perovskite semiconductors.

5.2 Methods and Materials

Note on author contributions: This chapter has been accepted for publication in *Journal of Materials Chemistry C*, **2018**, DOI: 10.1039/c8tc03527j by Annalise E. Maughan, Arnold A. Paecklar, and James R. Neilson. AEM performed the experiments, wrote the initial draft, and collected and analyzed the data. AAP performed the RMC simulations. JRN supervised the project. All authors contributed to editing and finalization of the manuscript.

Synthesis of $Cs_2Sn_{1-x}Te_xI_6$

The solid solution series $Cs_2Sn_{1-x}Te_xI_6$ was prepared by previously reported methods.[7]

Structural Characterization

Synchrotron X-ray scattering data suitable for pair distribution function (PDF) analysis were collected at beamline 11-ID-B at the Advanced Photon Source, Argonne National Laboratory, using 86 keV photons and sample-detector distance of 19 cm. Powdered samples of $Cs_2Sn_{1-x}Te_xI_6$ were loaded into polyimide capillaries and measured in transmission mode at room temperature using a PerkinElmer amorphous silicon image plate detector.[240] Experimental PDFs were extracted using PDFgetX3[169] and analyzed using PDFgui.[170] The program Fit2D[168] was used to calibrate the sample to detector distance and detector alignment with data from a CeO_2 powder standard. Raw scattering data were integrated into Q-space spectra, applying a mask and polarization correction during integration. The normalized total scattering pattern, $S(Q)$, was produced in PDFgetX3 by subtracting polyimide container scattering, utilizing the appropriate sample composition, and applying standard corrections for the area

detector setup.[240] The pair distribution function pattern, $G(r)$, was calculated via Fourier transformation of the total scattering data utilizing a maximum $Q = 30$ Å^{-1}. $G(r)$ for each member of the series was extracted for several values of Q_{max} to infer the influence of Fourier termination ripples in our subsequent analyses. Values of $Q_{damp} = 0.0538$ Å^{-1} and $Q_{broad} = 0.003$ Å^{-1} were extracted from refinement of a Ni standard in PDFgui and used for further refinement.

Neutron total scattering measurements of Cs_2SnI_6 were performed on the Nanoscale Ordered Materials Diffractometer (NOMAD) at the Spallation Neutron Source, Oak Ridge National Laboratory. For measurements collected at $T = 90$, 300, and 500 K, a powdered sample of Cs_2SnI_6 was loaded and sealed in a quartz capillary (capillary diameter = 3.0 mm) in the multisample changer. Data were normalized against scattering data collected for an empty quartz capillary, and background scattering from the quartz capillary was subtracted. For measurements at $T = 10$ K, a powdered sample of Cs_2SnI_6 was loaded into a 6 mm vanadium canister under He atmosphere. Data were normalized against scattering collected for a vanadium rod, and background scattering from the vanadium can was subtracted.

Temperature-dependent neutron total scattering data were merged to the total scattering structure function using the IDL codes developed for the NOMAD instrument.[270] The pair distribution function was then produced through the sine Fourier transform of the total scattering structure function using $Q_{max} = 31.4$ Å^{-1}. For Cs_2SnI_6 at $T = 90$, 300, and 500 K, values of $Q_{damp} = 0.0201$ Å^{-1} and $Q_{broad} = 0.0196$ Å^{-1} were extracted from refinement of a diamond standard in PDFgui. For Cs_2SnI_6 at $T = 10$ K, values of $Q_{damp} = 0.01766$ Å^{-1} and $Q_{broad} = 0.01918$ Å^{-1} were extracted from refinement of a silicon standard. Analysis of the nPDFs was performed using PDFgui.

Reverse Monte Carlo simulations

Reverse Monte Carlo (RMC) simulations were performed with $6 \times 6 \times 6$ supercells of the cubic structures of Cs_2SnI_6 ($a = 69.830$ Å) and Cs_2TeI_6 ($a = 70.212$ Å), each containing 7,776 atoms. The simulations were constrained in reciprocal-space by $S(Q)$-1 data, and in real-space by the

X-ray pair distribution function, $G(r)$. $S(Q)$-1 was convolved with a Gaussian function with a full-width-half-maximum of $^1/_2$ the length of the supercell edge prior to use in simulations in order to capture appropriate peak broadening due to finite size of the box.[297] The experimental data were simulated within the fullrmc package and the simulations were run for 89,882,085 steps.[298]

Pseudo-rigid-body RMC simulations were implemented, in which the [SnI_6] and [TeI_6] octahedra were randomly rotated and tilted as rigid units, prior to and after their free relaxation. The Sn–I/Te–I bond lengths were constrained between 2.65 Å–3.05 Å and the I–Sn–I and I–Te–I bond angles were constrained to 80-100° and 170-180°. After initiating the refinements with only the intraoctahedron bonds, the refinement range was increased step-wise to include longer-range pair correlations while all atoms were permitted to displace in the Cartesian reference. After the fitting range reached r = 17.45 Å and after a finite number of atomic displacements, the octahedra were constrained as rigid bodies (Sn/Te–I bond lengths and angles were frozen) and allowed to tilt about the center of the octahedra around all three Euler angles up to a maximum tilt angle of 10°. The entire fitting process was reiterated twice from the start to achieve the final configuration.

VESTA was used to visualize and render all crystal structures presented here.[171]

5.3 Results

All members of the $Cs_2Sn_{1-x}Te_xI_6$ series crystallize in the cubic vacancy-ordered double perovskite structure shown in Figure 5.1.[7] The Sn(IV) and Te(IV) ions randomly occupy the *B*-site coordinated to six I^- ions at the *X*-site, and the Cs^+ cations occupy the cuboctahedral *A*-site void.

The local coordination environment probed by XPDF analysis is consistent with solid solution behavior between Cs_2SnI_6 and Cs_2TeI_6. In Figure 5.2a, the the X-ray pair distribution function (XPDF) of each member of the $Cs_2Sn_{1-x}Te_xI_6$ series are modeled with the cubic structural model with appropriate fractional occupancies of tin and tellurium. Over medium and

long length scales ($r > 6$ Å), the XPDFs are fairly well described by the cubic structural model, consistent with each member of the series adopting the cubic vacancy-ordered double perovskite structure; however, the fit quality is worse closer to Cs_2SnI_6 (Figure 5.2b). As shown in Figure 5.3a, tellurium substitution is accommodated by a linear increase in the lattice parameter, consistent with Vegard's law. Further, the larger tellurium ion results in an increase in the average *B*–I bond length (Figure 5.3b) at the expense of the inter-octahedral I–I contact distances along the ⟨110⟩ directions (Figure 5.3c). This also results in a slight increase in the average Cs–I bond lengths across the series (Figure 5.3d). The structural parameters extracted from the XPDF fits in Figure 5.3 are plotted with the previously reported parameters from analysis of high-resolution synchrotron powder X-ray diffraction data.[7]

Although all members of the series appear to adopt nearly identical crystalline structures by both SXRD and XPDF, the local coordination environment over short length scales reveals subtle differences across the series. The first nearest-neighbor pair correlation at $r \sim 2.85$-2.9 Å due to Sn–I/Te–I bonds moves to higher r due to an increase in the average *B*–I bond length with substitution of the larger tellurium ion. Despite mixed Sn–I and Te–I bond lengths, this peak remains symmetric across the series and is well-described by the cubic structural model, consistent with regular, undistorted BX_6 octahedral units.

In contrast, deviations in the next-nearest-neighbor (*nnn*) pair correlation at $r \sim 4.1$ Å, due to I–I and Cs–I pairs, are observed across the series, manifesting as a slight asymmetry of the high-r side of the peak present in the difference curves in Figure 5.2. The apparent asymmetry is most pronounced in Cs_2SnI_6 and gradually decreases with increasing tellurium content, consistent with the nearly monotonic decrease in R_{wp} with x shown in Figure 5.2b. Our previous work found that the XPDFs of the intermediate members could be obtained by a linear combination of the XPDFs of the Cs_2SnI_6 and Cs_2TeI_6 end members,[7] indicating that this apparent asymmetry evolves smoothly as a function of tellurium content. As the BI_6 octahedra remain relatively undistorted and all members of the solid solution adopt nearly identical crystal struc-

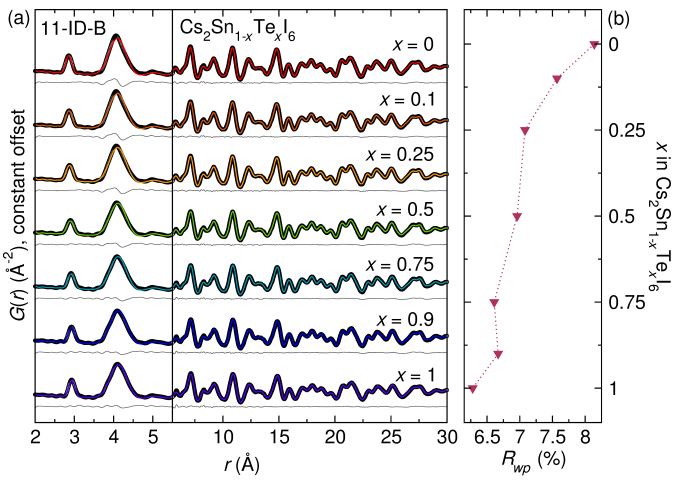

Figure 5.2: (a) X-ray pair distribution functions of the solid solution $Cs_2Sn_{1-x}Te_xI_6$ modeled with the cubic vacancy-ordered double perovskite structure with isotropic, harmonic atomic displacement parameters. The data are shown as black circles, the fits are colored lines, and the difference is shown in grey. The x-axis is split to highlight the low-r pair correlations, particularly the asymmetry of the next-nearest neighbor pair correlation at $r \sim 4.1$ Å. The R_{wp} for each fit is shown in (b).

tures by X-ray diffraction, we propose that this asymmetry may be due to anharmonic lattice dynamics rather than a static structural distortion.

Neutron total scattering experiments of Cs_2SnI_6 reveal a temperature-dependence of the asymmetry observed in the local coordination environment. Neutron diffraction data of Cs_2SnI_6 collected from the 31° bank (bank 2) of NOMAD at T = 10, 90, 300, and 500 K reveal that Cs_2SnI_6 adopts the cubic vacancy-ordered double perovskite structure at all measured temperatures, as shown in the Rietveld refinements in Figure 5.4. The neutron pair distribution functions (nPDF) extracted from total scattering data are shown in Figure 5.5. At all temperatures the nPDFs were modeled with the cubic vacancy-ordered double perovskite structure of Cs_2SnI_6, consistent with previous reports[7,8] and with the corresponding diffraction data that indicate Cs_2SnI_6 adopts the cubic structure at all temperatures (Figure 5.4). At T = 10 K, the pair correlations are sharp, narrow, and symmetric, consistent with low-amplitude harmonic thermal vibrations at this temperature. Increasing temperature to T = 90 K and T = 300 K is accompanied by broadening of all pair correlations. The *nnn* pair correlation becomes visibly asymmetric with increasing temperature, with a slight tailing on the high-r side of the peak revealed in the difference curves. At T = 500 K, the peaks in the nPDF are significantly broadened

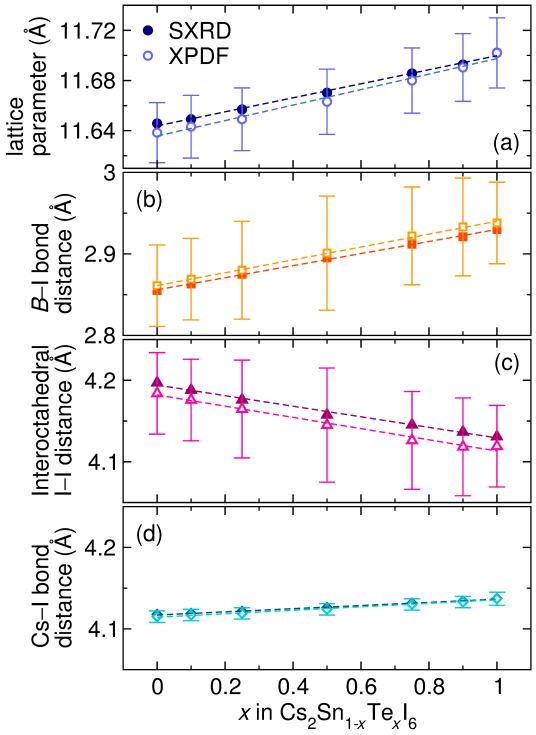

Figure 5.3: Structural parameters for the $Cs_2Sn_{1-x}Te_xI_6$ solid solution from refinement of the cubic structural models against high-resolution synchrotron powder X-ray diffraction (SXRD) data (filled symbols) and X-ray pair distribution function analysis (open symbols). In (a), the lattice parameters for each member of the solid solution follow Vegard's law. In (b), the average *B*–I bond lengths increase linearly with substitution of the larger tellurium ion at the expense of the interoctahedral I–I contact distance along the ⟨110⟩ direction shown in (c). In (d), the average Cs–I bond length increases. The dashed lines represent linear regressions performed for each data set. Error bars are shown for the parameters extracted from the XPDF fits. The error bars for the SXRD parameters are within the size of the symbol and are therefore omitted for clarity. The structural parameters from the SXRD data are taken from Ref.[7]

and dampened, and we observe significant asymmetry of the *nnn* pair correlation that is not captured by the cubic structural model. The nPDFs for Cs_2SnI_6 at T = 10, 90, and T = 300 K are taken from our previous study and re-fit here for comparison with the T = 500 K data.[8]

Temperature-dependent peak asymmetries have been observed in the XPDF of the related perovskite $CsSnBr_3$.[258,259] At T = 300 K, the nearest-neighbor pair correlation due to Sn–Br bonds is symmetric, but becomes noticeably asymmetric on the high-r side of the peak at higher temperatures. The emergence of this asymmetry with temperature, termed "emphanisis", has been attributed to dynamic off-centering of the Sn^{2+} ion within the $SnBr_6$ octahedra, which arises from stereochemically-active $5s^2$ electrons. While the formal [Kr]$4d^{10}5s^0$ electron

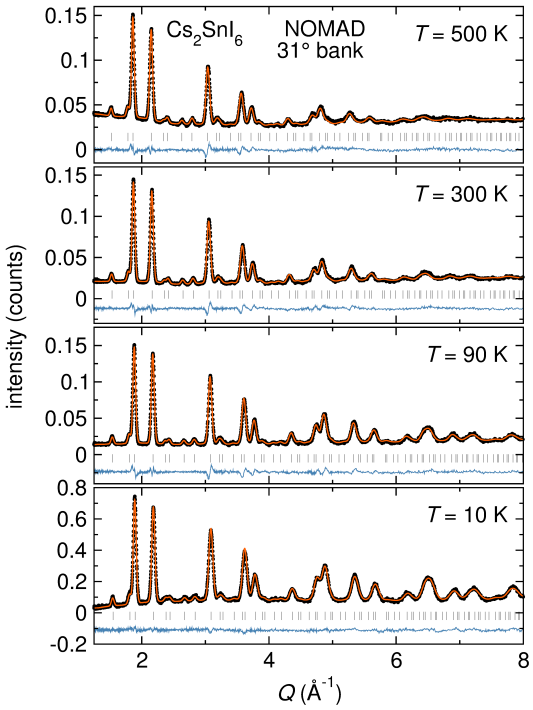

Figure 5.4: Rietveld refinements of temperature-dependent neutron diffraction of Cs_2SnI_6 at T = 10, 90, 300, and T = 500 K from the 31° bank (bank 2) of the NOMAD instrument at the Spallation Neutron Source, Oak Ridge National Laboratory. The data are modeled with the cubic vacancy-ordered double perovskite structure at all temperatures. Black circles are the data, the orange line is the fit, the blue line is the difference, and the grey tick marks represent positions of anticipated reflections for the $Fm\bar{3}m$ vacancy-ordered double perovskite structure. The data at T = 10, 90, and T = 300 K have been previously reported.[8]

configuration of Sn^{4+} in Cs_2SnI_6 precludes the presence of stereochemically-driven structural distortions, the temperature dependence of the peak asymmetry suggests that this effect arises from high-amplitude anharmonic lattice vibrations rather than a static structural distortion.

To gain insight into the atomistic contributions to the anharmonicity and peak asymmetry in Cs_2SnI_6, we extracted values for the atomic displacement parameters (ADPs) from the Rietveld refinements of the neutron diffraction data shown in Figure 5.4. The iodine ADPs were refined anisotropically; U_{11} corresponds to displacements along the Sn–I bond, while $U_{22} = U_{33}$ corresponds to displacements perpendicular to the Sn–I bond. As shown in Figure 5.6, the ADPs for Cs and I ($U_{22} = U_{33}$) increase monotonically (though not linearly) with increasing temperature, while the ADPs for Sn and I (U_{11}) increase only slightly from T = 10 K to T = 500 K. In systems with harmonic interactions, the relationship between the atomic displacement parameter

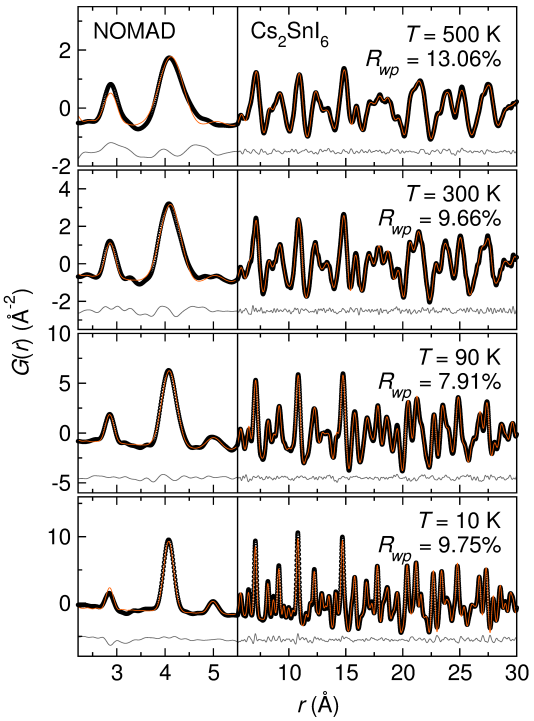

Figure 5.5: Temperature-dependent neutron pair distribution function analysis of Cs_2SnI_6 at T = 10, 90, 300, and T = 500 K. The data are modeled with the cubic vacancy-ordered double perovskite structure at all temperatures. Black circles are the data, orange lines are the fits, and grey lines are the difference curves. The x-axis is split to highlight the low-r pair correlations and the increasing asymmetry of the next-nearest-neighbor pair correlation at $r \sim 4$ Å with increasing temperature. The nPDFs at T = 10, 90, and T = 300 K have been previously reported and are re-fit here for comparison with the T = 500 K data.[8]

(U_{iso}) and temperature is well-described by a Debye-Waller model.[299,300] In Cs_2SnI_6, however, the ADPs for Cs and I $U_{22} = U_{33}$ follow a concave-down shape with increasing temperature, a trend which has previously been attributed to anharmonic dynamics in the $VAl_{10+\delta}$ system due to rattling of the Al atoms within the structural voids.[300] Similarly, neutron diffraction studies of $CsPbX_3$ halide perovskites reveal anomalously large atomic displacement parameters of the Cs and X ions that diverge from the harmonic Debye-Waller model, indicating the presence of anharmonic effects due to coupled displacements of the Cs^+ and X^- ions.[301] The similarities observed between the $VAl_{10+\delta}$ and $CsPbX_3$ systems and Cs_2SnI_6 suggests that the trends in ADP vs. temperature arises from anharmonic dynamics of the Cs and I atoms in Cs_2SnI_6. Furthermore, the observation that iodine displacements perpendicular to the Sn–I bond ($U_{22} = U_{33}$) follow the same trend as the atomic displacement parameter for cesium and are significantly

larger than iodine displacements along the Sn–I bond (U_{11}) may suggest the presence of [SnI_6] octahedral rotations coupled to Cs^+ displacements as the source of anharmonicity. Prior nuclear quadrupole resonance studies of the vacancy-ordered double perovskite family support this assertion, as dynamics in these materials originate predominantly from rotations of the rigid octahedral units.[85–87,89]

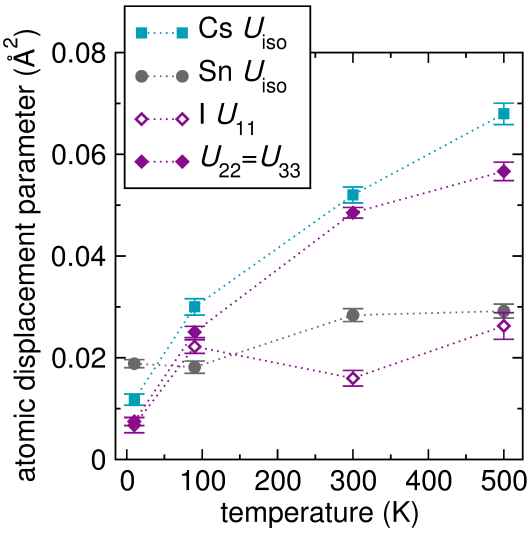

Figure 5.6: Atomic displacement parameters (ADPs) extracted from the temperature-dependent neutron diffraction data for Cs_2SnI_6 using Rietveld analysis. Isotropic atomic displacement parameters were refined for cesium and tin. The ADPs for iodine were refined anisotropically, such that U_{11} corresponds to iodine displacements along the Sn–I bond and $U_{22} = U_{33}$ corresponds to displacements perpendicular to the Sn–I bond. The dotted lines are a guide to the eye to highlight the trends in ADP for each atom.

Reverse Monte Carlo (RMC) simulations of Cs_2SnI_6 and Cs_2TeI_6 were performed to provide atomistic insights into the asymmetry observed in the XPDFs. As the dominant lattice dynamics in vacancy-ordered double perovskites arise from octahedral rotations rather than deformations of the octahedra,[85–87,89] we elected to use a pseudo-rigid-body RMC approach, in which the isolated [SnI_6] and [TeI_6] octahedra were allowed to tilt as rigid bodies, to encourage chemically reasonable descriptions of the anharmonicity. The constraint of rigid-bodies has been shown to improve RMC simulation results, especially in cases with dynamics such as rigid-unit modes.[302] From this approach, we find that the XPDFs are best described by structures with random rotations of the SnI_6 and TeI_6 octahedra and displacements of the Cs^+ ions away from

their crystallographic positions, as shown in the optimized supercells in Figure 5.7 and in the fits to the XPDF shown in Figure 5.8a and b.

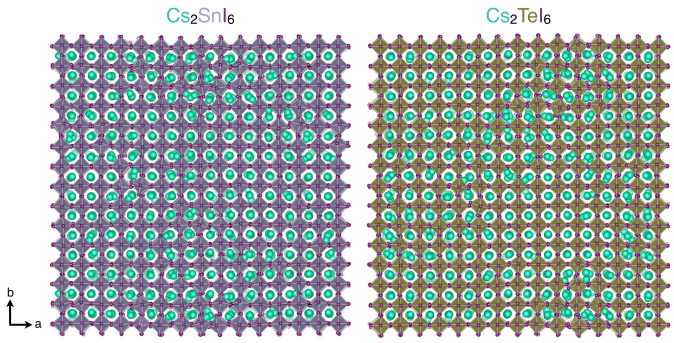

Figure 5.7: Supercell structures of Cs_2SnI_6 and Cs_2TeI_6 optimized from pseudo-rigid-body RMC simulations.

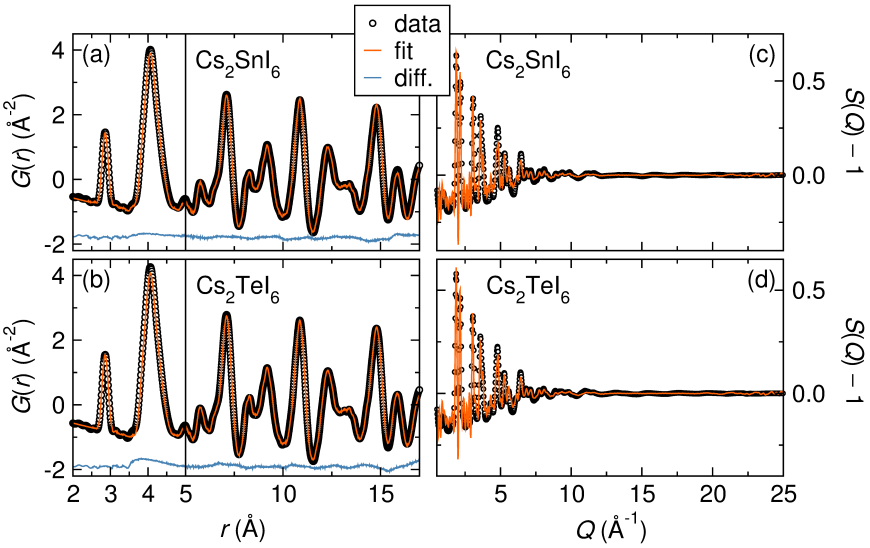

Figure 5.8: Calculated $G(r)$ and $S(Q)$-1 from pseudo-rigid-body RMC-optimized supercells of Cs_2SnI_6 and Cs_2TeI_6 compared against the experimental $G(r)$ and $S(Q)$-1 from X-ray total scattering data. Experimental data are shown as open circles, the fits from the RMC optimizations are shown as orange lines, and the difference curves are shown as blue lines. The x-axes in (a) and (b) are split to highlight the low-r pair correlations.

To determine the atom pair contributions to the asymmetry observed in the next-nearest-neighbor pair correlation at $r \sim 4$ Å, the partial radial distribution functions (RDF) for the intraoctahedral I–I ($I–I_{intra}$), interoctahedral I–I ($I–I_{inter}$), and Cs–I pairs were extracted from the

RMC-optimized supercells. As shown in Figure 5.9, the partial RDFs are relatively consistent between both Cs_2SnI_6 and Cs_2TeI_6 and show only subtle variations between the two compounds. In both compounds, the I–I_{intra} RDFs for Cs_2SnI_6 and Cs_2TeI_6 are fairly well-described by a Gaussian function. In contrast, both the I–I_{inter} and Cs–I partials exhibit an asymmetric peak shape evidenced by the deviations from a Gaussian function shown in Figure 5.9, indicating that the overall peak asymmetry arises due to these atom pairs. It is important to note that the I–I_{inter} and Cs–I pairs in both Cs_2SnI_6 and Cs_2TeI_6 exhibit slightly asymmetric peak shapes, and therefore we cannot unambiguously assign one compound as being more anharmonic than the other from these simulations. Instead, these simulations are consistent with the notion that anharmonicity in these compounds arises from octahedral rotations coupled with displacements of the Cs^+ cations.

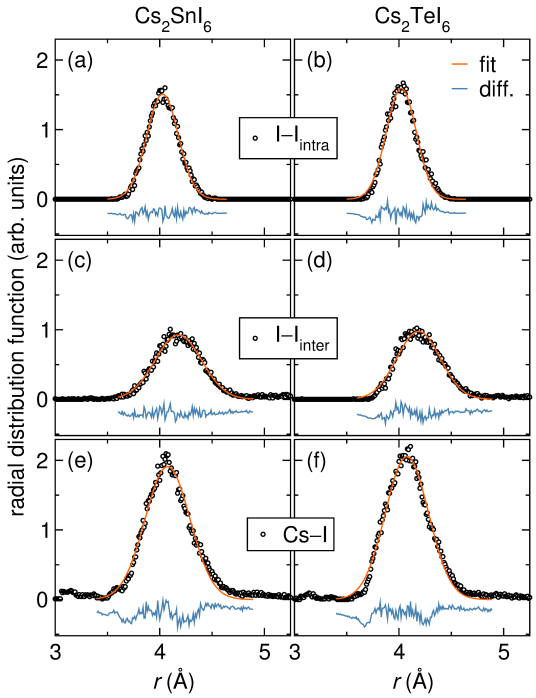

Figure 5.9: Partial radial distribution functions for I–I_{intra} (a,b), I–I_{inter} (c,d), and Cs–I (e,f) pair correlations in Cs_2SnI_6 and Cs_2TeI_6 obtained from pseudo-rigid-body Reverse Monte Carlo simulations (circles). The distributions are fit with Gaussian functions, shown by the orange line. The difference curves are shown in blue and reveal asymmetries in the I–I_{inter} and Cs–I RDFs.

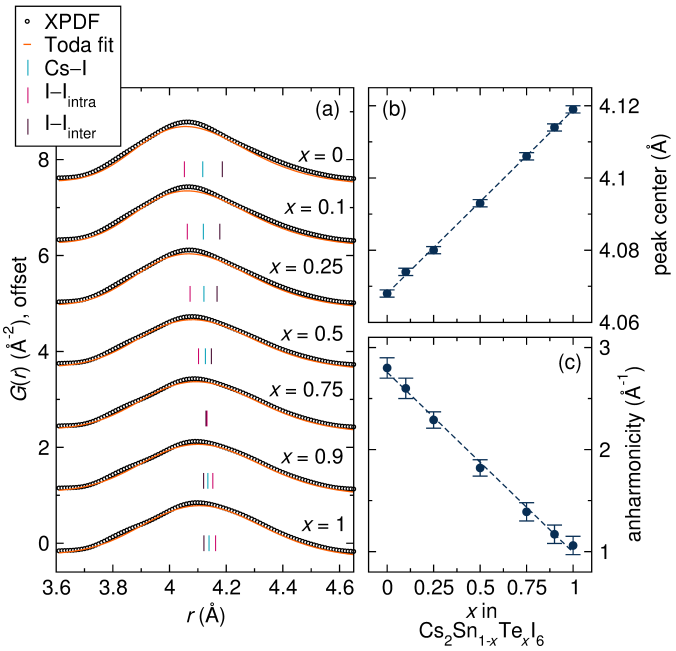

Figure 5.10: (a) Toda potential fits to the next-nearest-neighbor pair correlation in the X-ray pair distribution function analysis for $Cs_2Sn_{1-x}Te_xI_6$. The data are shown as black circles and the fit is the orange line. The PDF data are fit with one Toda potential peak, and are offset vertically for comparison and clarity. In (b) and (c), the interatomic distance (b) and degree of anharmonicity (β) are plotted as a function of x in $Cs_2Sn_{1-x}Te_xI_6$, respectively. The colored tick marks in (a) represent the contact distances for Cs–I (teal), intraoctahedral I–I (pink), and interoctahedral I–I (purple) atom pairs taken from the refinements of the cubic model against the XPDF data from Figure 5.2. Dashed lines in (b) and (c) represent linear regressions.

In order to quantify the trends in anharmonicity across the intermediate members of the $Cs_2Sn_{1-x}Te_xI_6$ series, the asymmetry of the *nnn* pair correlation was modeled with a modified Toda potential, which has been previously used to describe anharmonic interactions between nearest-neighbors in a linear atomic chain.[303,304] This modified Toda potential, $U(r)$, takes the form

$$U(r) = \frac{\mu}{\beta^2} e^{-\beta(r-b)} + \frac{\mu}{\beta}(r-b) - \frac{\mu}{\beta^2}, \tag{5.1}$$

where μ is the elastic constant, β is the degree of anharmonicity, and b is the interatomic distance. Harmonic interactions are described in the limit as $\beta \to 0$. The potential, $U(r)$, was approximated as the potential of mean force and then transformed to the reduced pair distribution function, $G(r)$, via $G(r) = [(k_B T e^{-U(r)})/r] - 4r\pi\rho_0$, where ρ_0 is the average number density,

N/V, of each member of the series. The transformed Toda potential was fit to the asymmetric pair correlation at ~4.1 Å in the XPDF for each member of the $Cs_2Sn_{1-x}Te_xI_6$ series (Figure 5.10a) using a non-linear least squares optimizer implemented in Python. In Figure 5.10b and c, the fitted parameters for the interatomic distance (b) and the degree of anharmonicity (β) are plotted as a function of x in $Cs_2Sn_{1-x}Te_xI_6$. From this analysis, we find that the interatomic distance (b) increases linearly with increasing tellurium content, consistent with the increase in Cs–I bond length extracted from fits to the XPDF data shown in Figure 5.3d. Of particular significance is the trend in the degree of anharmonicity (Figure 5.10b), which decreases linearly with increasing tellurium content, consistent with qualitative inspection of the fits to the XPDFs shown in Figure 5.2. We note that the Toda potential is conventionally used to describe anharmonic interactions in a linear atomic chain, and thus our use of the Toda potential to describe the more complex interactions in this system serves as a comparative analysis of the trends in anharmonicity between members of the $Cs_2Sn_{1-x}Te_xI_6$ series.

5.4 Discussion

Previous studies of anharmonicity in perovskite halides provide further insight into the atomistic origins of anharmonicity in the inorganic vacancy-ordered double perovskites presented here. In our previous study of the vacancy-ordered double perovskites $(CH_3NH_3)_2SnI_6$ and $(CH(NH_2)_2)_2SnI_6$, we observed significant tailing of the A–I/I–I pair correlation of the XPDFs of the hybrid compounds. In the hybrid compounds, the extensive tailing observed in the XPDF was attributed to coupled organic-inorganic dynamics via hydrogen bonding interactions resulting in a distinctly anharmonic potential.[6] However, the lack of hydrogen bonding interactions available in Cs_2SnI_6, yet asymmetry in the local coordination environment, indicates that the anharmonicity originates from a different source.

We propose that the subtle deviations in the Cs–I/I–I pair correlations of the $Cs_2Sn_{1-x}Te_xI_6$ series arise from anharmonic lattice dynamics originating from $[BI_6]$ octahedral rotations coupled with displacements of the Cs^+ ions. Octahedral rotations in vacancy-ordered double per-

ovskites have been studied at length by nuclear quadrupole resonance, which reveal that these modes are the dominant source of dynamics in these materials.[85–87,89] Furthermore, prior studies of inorganic perovskite halides $CsPbX_3$ and $CsSnX_3$ have shown that anharmonic lattice dynamics originate from cooperative tilting of the BX_6 octahedral units coupled with small displacements of the *A*-site cations within the cuboctahedral void.[45,46,260] In the present study, the presence of octahedral rotations coupled with Cs^+ displacements is supported by analysis of the neutron total scattering experiments of Cs_2SnI_6; the concave-down shape of the curves for the Cs atoms and the I $U_{22} = U_{33}$ atomic displacement parameters with increasing temperature follow a similar trend observed for localized vibrations associated with an ion rattling in a cage.[300] Notably, the iodine atomic displacement parameter parallel to the Sn–I bond (U_{11}) remains relatively constant while the perpendicular displacements ($U_{22} = U_{33}$) increase significantly with temperature. This observation indicates that iodine displacements perpendicular to the Sn–I bond dominate over those parallel to the Sn–I bond, lending further support to the notion of octahedral tilting as the primary source of dynamics and anharmonicity in Cs_2SnI_6.

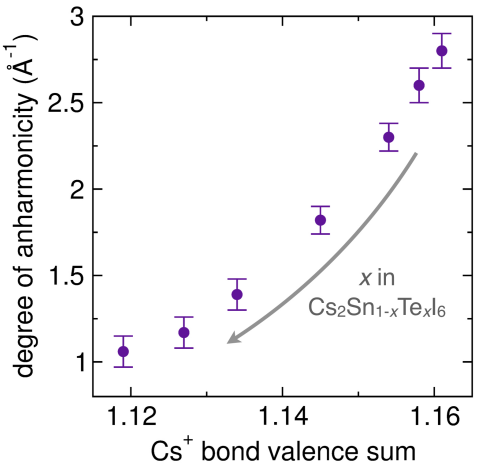

Figure 5.11: The degree of anharmonicity from the Toda potential fits plotted as a function of the Cs^+ bond valence sum.

Anharmonicity in the vacancy-ordered double perovskites $Cs_2Sn_{1-x}Te_xI_6$ can be correlated with the bonding preferences of the cesium cation within the cuboctahedral void. In Fig-

Table 5.1: Bond valence sum analysis for Cs–I bonds in $Cs_2Sn_{1-x}Te_xI_6$. Cs–I bond lengths were taken from the XPDF and SXRD analyses. Values of $B = 0.609$ and $R_0 = 2.6926$ Å were used in calculation of the bond valence sum.[305]

	XPDF		SXRD	
x	Cs–I length (Å)	BVS	Cs–I length (Å)	BVS
0	4.115	1.161	4.118	1.156
0.1	4.117	1.158	4.119	1.154
0.25	4.119	1.154	4.122	1.149
0.5	4.124	1.145	4.126	1.140
0.75	4.130	1.134	4.132	1.130
0.9	4.133	1.127	4.134	1.125
1	4.137	1.119	4.137	1.119

ure 5.11, the degree of anharmonicity extracted from the Toda potential fits are plotted as a function of the Cs^+ bond valence sum. For $x = 1$ (Cs_2TeI_6), the degree of anharmonicity is the lowest and corresponds with a bond valence sum of ~1.12, suggesting that the Cs^+ is most optimally bonded in Cs_2TeI_6. As tellurium is replaced with tin, the bond valence sum of Cs^+ increases concomitantly with an increase in the degree of anharmonicity, reaching a maximum bond valence of ~1.16 for Cs_2SnI_6. This analysis suggests that the anharmonicity is minimized when the size of the cuboctahedral void satisfies the bonding preferences of the Cs^+ cation. Conversely, increasingly anharmonic lattice dynamics are therefore expected as the bond valence of the Cs^+ ion diverges from ideal coordination.

The bond valence sum has previously been applied to other perovskite halide systems to predict the presence of dynamic and cooperative octahedral tilting distortions.[8,46,81,268] Bond valence sum calculations of the vacancy-ordered double perovskite Rb_2SnI_6 indicate that the coordination to the smaller Rb^+ ion is optimized by symmetry-lowering cooperative octahedral tilting distortions,[8] as is also observed in the $Cs_{1-x}Rb_xPbX_3$ ($X = Cl^-$, Br^-) series.[268] In the $Cs_2Sn_{1-x}Te_xI_6$ series, the Cs^+ coordination is nearly optimal in the cubic structural models, consistent with the observation that neither Cs_2SnI_6 nor Cs_2TeI_6 undergo structural phase transitions down to $T = 10$ K.[7] Rather, the slight deviations in bond valence sum in this system manifest as a small degree of anharmonicity. Therefore, anharmonic effects in vacancy-ordered

double perovskites may be expected when the bond valence sum of the *A*-site cation deviates slightly from ideal, while more significant structural changes due to cooperative octahedral tilting may be expected if the *A*-site is significantly underbonded. As the properties of halide perovskites are intimately linked to (anharmonic) lattice dynamics, the bond valence sum provides a simple tool for predicting the presence and extent of anharmonicity and may further be leveraged as a design principle for materials with desired structure-dynamic-property relationships.

5.5 Conclusion

The series of vacancy-ordered double perovskites $Cs_2Sn_{1-x}Te_xI_6$ presents an interesting test case for anharmonic lattice dynamics. While each member of the series adopts the cubic vacancy-ordered double perovskite structure by high-resolution powder X-ray diffraction, the local coordination environment probed by X-ray pair distribution function analysis reveals subtle deviations. These deviations manifest as an emergent asymmetry of the next-nearest-neighbor pair correlation due to Cs–I and I–I atom pairs in Cs_2SnI_6, which gradually disappears with increasing tellurium content. Through analysis of temperature-dependent neutron pair distribution function analysis for Cs_2SnI_6, we propose that this asymmetry arises due to anharmonic lattice dynamics associated with coupled motions between the isolated SnI_6 octahedra and the Cs^+ ions within the cuboctahedral void, supported by RMC simulations and the trends in atomic displacement parameters for the Cs and I atoms extracted from neutron diffraction data. Using bond valence sum analysis, we find that the valence for Cs^+ is optimized when tellurium occupies the *B*-site rather than tin. This observation is consistent with the trends in anharmonicity extracted from Toda potential fits, and suggests that the asymmetry observed in the Cs–I/I–I pair correlation in the XPDFs of Sn-rich samples originates from dissatisfied bonding preferences of the Cs^+ cation with the surrounding iodide cage. We further demonstrate that bond valence sum analysis can be correlated with anharmonic behavior in halide perovskites and used as a simple tool for predicting anharmonicity in perovskite halide systems.

Chapter 6

Hybrid Inorganic–Organic Materials with an Optoelectronically-Active Aromatic Cation: $(C_7H_7)_2SnI_6$ and $C_7H_7PbI_3$[6]

6.1 Introduction

Growing and novel technologies necessitate the discovery of new materials with robust and tunable properties. Hybrid materials – which, in the present context we use to denote compounds composed of an inorganic lattice and primarily non-coordinating organic ions (*i.e.*, not coordination polymers) – are an advantageous subset of functional materials that exhibit a wide range of optical and electronic properties.[306–308] Such materials are of particular interest for device applications because the properties and structures are easily tuned by chemical modification of either the inorganic and organic components.[306,309] Furthermore, the often solution-based synthetic routes used to prepare hybrid compounds enables facile production of films for device fabrication.[310,311] Specifically, main-group metal–halide-based hybrids are among the most widely researched, and often the observed properties derive primarily from the inorganic connectivity.[312] For example, lead and tin halide perovskites, including both purely inorganic (*e.g.*, $CsSnI_3$ and $CsPbI_3$) and hybrid compounds (*e.g.*, $CH_3NH_3SnI_3$ and $CH_3NH_3PbI_3$), show exceptionally high carrier mobilities and offer great promise in solar photoconversion applications;[114,313] replacement of the smaller Cs^+ cation with the larger methylammonium ($CH_3NH_3^+$) cation induces a lattice expansion and alteration of octahedral tilting that influences, among other characteristics, the band gap and mobility.[314,315] Similar effects can be achieved by replacing or substituting the smaller Br^- or Cl^- anions for the larger I^- anion, and

[6]Substantial portions of this chapter have been reproduced with permission from A. E. Maughan, J. A. Kurzman, and J. R. Neilson, *Inorg. Chem.*, **2015**, *54*, 370–378.[204] ©2015 the American Chemical Society.

collectively these compositional variations can be exploited to enhance factors such as moisture stability,[316,317] a key factor in practical device longevity.

With significant research interest devoted to utilizing Pb–I and Sn–I frameworks as the inorganic component in functional hybrid materials, the size and functionality of the organic cation has been shown to greatly influence the dimensionality and connectivity of the inorganic lattice.[312,318] Small organic cations such as methylammonium and formamidinium result in three-dimensional hybrid perovskites,[114,306] while slightly larger primary cyclic ammonium cations like cyclobutylammonium form two-dimensional layered perovskites.[116,317] Larger cations often produce frameworks of reduced dimensionality; 1-D infinite chains of face- or edge-sharing octahedra are commonly observed.[113,319,320] Although lower dimensional compounds exhibit interesting photoluminescence properties, the structural connectivity typically inhibits carrier mobilities.[31] Additionally, zero-dimensional molecular compounds containing isolated polyhedra or small inorganic clusters tend to result when large organic ions or higher charged inorganic cations are present;[321] these compounds exhibit absorption features characteristic of the constituents rather than broad band spectral absorption.[322]

While the choice of organic cation can drastically affect the structure of the inorganic framework in hybrid materials, it does not always influence the optoelectronic properties, owing to the fact that they are typically optoelectronically inactive in UV or visible light. Another approach to tune the properties of hybrid materials is to introduce an organic component with desirable optical and electronic properties. An exemplary molecule is the cycloheptatrienyl (tropylium) ion; tropylium is a seven-membered aromatic ring containing a delocalized positive charge and is a compelling choice for use in hybrid materials. Tropylium exhibits extraordinary charge transfer properties that are easily tuned by altering the polarity of the solvent environment.[323] Because of its aromaticity, the positive charge of tropylium is delocalized; therefore, the ion maintains its planar structure and is chemically stable as a reactant. This enables tropylium to be readily retained under a variety of synthetic conditions.[324,325] By introducing the tropylium ion into lead- and tin-iodide frameworks, the electronic properties may be enhanced

through coupling of the inorganic lattice to the delocalized electron density in the aromatic tropylium ring.

Here, we report the preparation, crystal structures, and optoelectronic properties of tropylium tin iodide, $(C_7H_7)_2SnI_6$, and tropylium lead iodide, $C_7H_7PbI_3$, which are the first hybrid materials to incorporate the tropylium ion as the organic constituent. Tropylium tin iodide, $(C_7H_7)_2SnI_6$, is a black powder that crystallizes in space group *An* and contains isolated tin(IV)-iodide octahedra [Figure 6.1a and b]; tropylium lead iodide, $C_7H_7PbI_3$, crystallizes as a bright red-orange powder in space group *Pnma* and contains one-dimensional lead(II)-iodide chains [Figure 6.1c and d]. The crystal structures of these compounds were solved *ab initio* from high-resolution synchrotron X-ray powder diffraction data (SXRD), and high-resolution time-of-flight neutron diffraction was used to confirm the structure of tropylium tin iodide. The optical properties of tropylium tin iodide are commensurate with the molecular nature of the compound, evidenced by a large absorbance feature in the ultraviolet (UV) region consistent with intramolecular electronic transitions of the tropylium ion. Electronic structure calculations indicate localized states consistent with the zero-dimensional inorganic components, well-separated tropylium cations, and extremely high measured electrical resistivity. The deep black color of $(C_7H_7)_2SnI_6$ and density functional theory (DFT) calculations suggest that charge transfer is not likely due to any inorganic–organic coupling, but rather is solely due to the inorganic constituents. On the other hand, the bright red-orange color of tropylium lead iodide suggests increased charge transfer between the organic component and the inorganic lattice, evidenced by the fact that 1-D iodoplumbates typically range from colorless to yellow to orange.[113,319,320] DFT calculations of the band and *k*-point decomposed charge densities are used to probe the nature of optical transitions across the fundamental gaps, and support the presence of localized charge transfer to tropylium in $C_7H_7PbI_3$.

6.2 Methods and Materials

Note on author contributions: This chapter was published in *Inorganic Chemistry*, **2015**, volume 54, pages 370–378 by Annalise E. Maughan, Joshua A. Kurzman, and James R. Neilson. AEM performed the syntheses, experiments, analyzed the data, and wrote the initial draft of the manuscript. JAK performed density functional calculations and assisted in data analysis. JRN supervised the project. All authors contributed to editing and finalization of the manuscript.

Materials

HI (57% aq., 1.5% H_3PO_2)-Sigma Aldrich, 99.99%; Tropylium tetrafluoroborate-Alfa Aesar, 99.99%, kept in an Argon inert atmosphere until use; Tin Metal Shot-Alfa Aesar; Iodine-Macron Chemicals. All chemicals were used without further purification.

Preparation of Tin (IV) Iodide (SnI_4)

Tin metal (0.3108 g, 2.62 mmol) and iodine (1.3347 g, 5.26 mmol) were reacted in an evacuated fused silica ampoule (P <10 mTorr). The ampoule was heated in a furnace at T = 200 °C for 48 h, which was air-quenched to yield bright orange-yellow SnI_4.

Preparation of Tropylium Iodide (C_7H_7I)

At 60 °C, finely ground tropylium tetrafluoroborate (0.5177 g, 2.91 mmol) was added to 60 mL ethanol in a 250 mL round bottom flask with an air condenser; this solution was stirred vigorously to dissolve into a light yellow-brown solution. After boiling the ethanol for 5 m, the flask was removed from heat. When the rolling boil had subsided to a very gentle boil, 500 μL of stabilized HI solution (57% aq., 1.5% H_3PO_2) was added. This turned the solution dark red. After about 1 min of stirring, a bright red precipitate formed. The solution was stoppered and allowed to stir gently until cool. The flask was then submerged in an ice bath and stirred gently for 1 h. The solution and the precipitate were washed with anhydrous ether and centrifuged, which was repeated three times. The bright red precipitate was dried in an oven at T = 37 °C

for 24 h, yielding a fine red powder of tropylium iodide (C_7H_7I, $R\bar{3}m$) with a small tropylium tetrafluoroborate impurity.[326]

Preparation of Tropylium Tin Iodide $(C_7H_7)_2SnI_6$

A 100 mL 2-necked round bottom flask was charged with 7.0 mL of stabilized HI (57% aq., 1.5% H_3PO_2). The mixture was degassed with nitrogen for 1 m and the flask was kept under nitrogen for the duration of the experiment. The flask was heated in an oil bath to T = 100 °C, and tin(IV) iodide (0.1834 g, 0.292 mmol) was added, then stirred vigorously until the solid had dissolved completely. Tropylium iodide (0.1279 g, 0.586 mmol) was then added to the flask, which immediately resulted in a black precipitate. The solution was stirred for an additional 15 m, at which time the heat was removed and the flask was allowed to air-cool while stirring gently. The solution and precipitate were washed with anhydrous ether and centrifuged three times. The black product was dried at T = 37 °C for 24 h. Compositional analysis confirms C 12.77%, H 1.11%, Sn 14.3%, and I 73.08% (Predicted: C 15.83%, H 1.33%, Sn 11.17%, I 71.67%).

Preparation of Tropylium Lead Iodide $(C_7H_7PbI_3)$

A 100 mL 2-necked round bottom flask was charged with 11.0 mL of HI (57% aq., 1.5% H_3PO_2) and a stir bar. The solution was degassed with nitrogen for 1 m and the flask was kept under nitrogen for the duration of the experiment. The flask was heated in an oil bath to T = 45 °C while stirring, at which point lead iodide (0.6438 g, 1.395 mmol) was added all at once and stirred vigorously to dissolve, resulting in a translucent bright yellow solution. The flask was heated to T = 55 °C at which point finely ground tropylium tetrafluoroborate (0.2483 g, 1.396 mmol) was added, turning the solution bright orange-red. The heat was immediately turned off and the flask was allowed to cool in the warm oil bath while stirring gently. Once the temperature of the oil bath decreased to T = 40 °C, the flask was removed and allowed to air-cool to room temperature while stirring gently. Once cool, the solution and red precipitate were washed with ethanol and centrifuged. The remaining product was then washed with anhydrous ether and centrifuged three times. The resulting bright red precipitate was dried at T = 37 °C for

24 h. Compositional analysis confirms C 12.25%, H 1.07%, Pb 31.2%, and I 55.23% (Predicted: C 12.38%, H 1.04%, Pb 30.52%, I 56.06%).

Characterization

Products were characterized by high-resolution synchrotron powder X-ray diffraction data obtained from the diffractometer on beam line 11-BM-B at the Advanced Photon Source, Argonne National Laboratory.[167] Room temperature powder neutron diffraction data were collected on a sample sealed in a vanadium canister at the Spallation Neutron Source (SNS) at the Oak Ridge National Laboratory using the POWGEN diffractometer (BL-11A). After determination of the lattice parameters with DICVOL[327] and deduction of the space group from systematic absences, structural models were constructed using Free Objects for Crystallography (FOX).[328] The data were analyzed with the Rietveld method using GSAS/EXPGUI.[165,166] In order to generate the CIF files the carbon-carbon bond distances were restrained to 1.35(5) Å and the bond angles were restrained to 128.6(1)° to create an idealized structural representation of the tropylium rings within the inorganic framework. X-ray scattering data suitable for pair distribution function (PDF) analysis were collected at beamline 11-ID-B at the Advanced Photon Source, Argonne National Laboratory, using 58 keV photons and sample-detector distance of ~17 cm. Experimental PDFs were extracted using PDFgetX3[169] and analyzed using PDFgui.[170] VESTA was used to visualize and render all crystal structures presented in this manuscript.[171]

Proton and fluorine nuclear magnetic resonance studies were performed on an Agilent (Varian) 400 MHz NMR spectrometer in deuterated d_6-DMSO. Fourier transform infrared spectroscopy (FT-IR) was performed on solid samples on a Thermo Nicolet iS50 FT-IR spectrometer from 650 cm^{-1} to 4000 cm^{-1}. UV-visible diffuse reflectance spectroscopy was performed on powdered samples of all three tropylium compounds diluted to 15 wt% in $BaSO_4$, using $BaSO_4$ as a baseline; spectra were acquired using a Thermo Nicolet Evolution 300 spectrophotometer with a Praying Mantis mirror setup from λ = 200 to 1000 nm at a scan rate of 240 nm/min. Compositional analyses were performed at Galbraith laboratories. Electronic resistance mea-

surements on pellets with Au-paste contacts and Pt wires were attempted using a Physical Properties Measurement System (Quantum Design, Inc.); however, the resistivity exceeded that of the sensitivity of the instrument.

DFT Calculations

The electronic structures of $(C_7H_7)_2SnI_6$ and $C_7H_7PbI_3$ were calculated using density functional theory within the plane-wave code VASP (*Vienna Ab initio Simulation Package*).[177,179] The Perdew–Burke–Ernzerhof (PBE) functional[182] was used to treat the effects of exchange-correlation at the generalized gradient approximation (GGA) level of theory. Valence–core interaction was described with the projector augmented wave method, and cores of [Kr]$4d^{10}$ for Sn and I, [Xe]$4f^{14}5d^{10}$ for Pb, and [He] for C were used. The structures of both compounds were relaxed within the constraints of the experimentally determined cells; attempts to determine the equilibrium structures by relaxing at a series of volumes were impeded by difficulty converging forces on the tropylium ring when the cell shape was allowed to change (for a fixed volume). Relaxations of the ionic positions were conducted using $2 \times 6 \times 4$ for $(C_7H_7)_2SnI_6$ and $6 \times 4 \times 2$ for $(C_7H_7PbI_3)$ Γ-centered k-point meshes and an energy cutoff of 520 eV. Relaxations were deemed to have converged when forces on all the ions were less than 0.02 eV Å^{-1}. The density of states of tropylium tin iodide was calculated using a $4 \times 8 \times 6$ Γ-centered k-mesh with a total of 70 irreducible k points, and the band structure was calculated using 20 point interpolations along high symmetry directions of the first Brillouin zone (100 irreducible k points). The density of states of tropylium lead iodide was calculated using a $10 \times 8 \times 6$ gamma-centered k-point mesh and the band structure was calculated using 15 point interpolations, both involving 120 irreducible k points.

6.3 Results and Discussion

Tropylium tin iodide was prepared by reaction of SnI_4 and tropylium iodide in aqueous hydroiodic acid, which resulted in a crystalline black product that rapidly precipitated out of

the solution. As a control, preparation was attempted by reaction with tin(II) iodide; the final product was identical but contained a significant fraction of SnI_4, as supported by the facile oxidation of tin(II) to tin(IV).[329] Tropylium lead iodide was prepared by reaction of tropylium tetrafluoroborate and PbI_2 in aqueous hydroiodic acid, which resulted in a bright red-orange crystalline powder. There was no difference in the final product when tropylium iodide was synthesized first, followed by reaction with PbI_2.

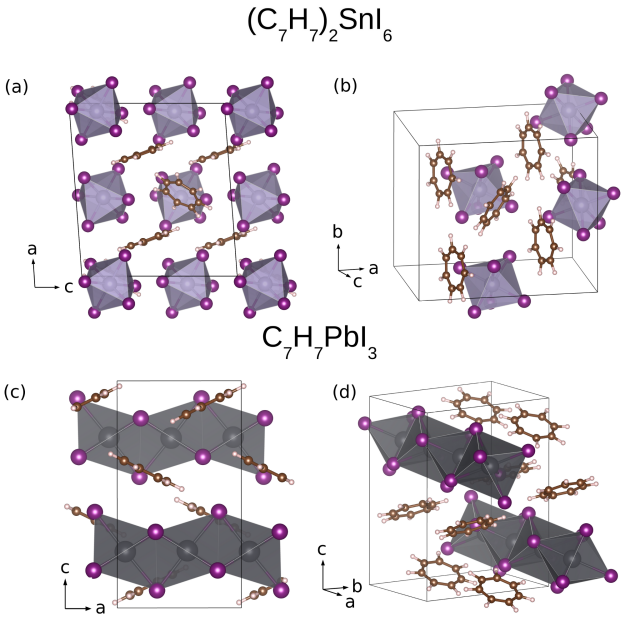

Figure 6.1: DFT-relaxed crystal structures of tropylium tin iodide ((a), (b)), and tropylium lead iodide ((c), (d)). Lavender spheres denote tin, purple denote iodine, charcoal denote lead, brown denote carbon, and eggshell denote hydrogen.

6.3.1 FT-IR and ^{1}H NMR Studies

FT-IR spectra of compacted powders shows the expected vibrational modes for the aromatic ring in all three tropylium containing compounds, C_7H_7I, $(C_7H_7)_2SnI_6$, and $C_7H_7PbI_3$ (Figure 6.2). The sharp peak at 3000 cm^{-1} indicates C–H stretching, while sharp signals at approximately 1460 cm^{-1} and 1050 cm^{-1} identify C=C stretching and in-plane C–H bending, respectively. The feature at 650 cm^{-1} corresponds to an aromatic out-of-plane ("oop") C–H bend.[330,331]

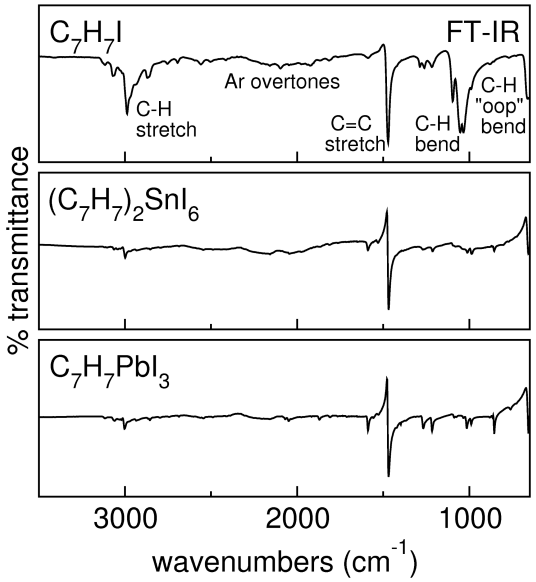

Figure 6.2: FT-IR spectra of tropylium iodide, tropylium tin iodide, and tropylium lead iodide, indicating the vibrational modes of the aromatic (Ar) $[C_7H_7]^+$ ring. "oop" refers to "out-of-plane" bending.

^{1}H and ^{19}F NMR spectroscopies were performed on solutions prepared from dissolving tropylium iodide, tropylium tin iodide, and tropylium lead iodide in d_6-DMSO. The proton spectra of all three compounds show a large singlet at a chemical shift of 9.33 ppm, which is consistent with the seven hydrogens of the aromatic tropylium ring [Figure 6.3]. The small peaks between 4–7 ppm in the ^{1}H NMR spectra indicate a benzaldehyde impurity, which may have formed from oxidation of the tropylium ion by hydroiodic acid. However, the concentration of this impurity is small compared to that of tropylium, was undetectable by other analytical methods, and does not appear to influence the structure of the lead and tin containing products. The ^{19}F NMR spectrum of tropylium iodide (not shown) reveals minor contributions from a tetrafluoroborate impurity, which is also confirmed by powder X-ray diffraction (14(6)mol%); however, there was no evidence for this impurity in the $(C_7H_7)_2SnI_6$ or $C_7H_7PbI_3$ products by ^{19}F NMR.

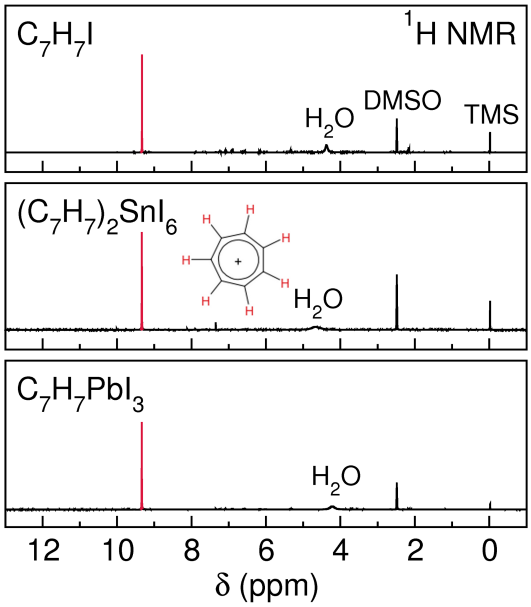

Figure 6.3: ^{1}H NMR spectra of tropylium iodide, tropylium tin iodide, and tropylium lead iodide redissolved in d_6-DMSO. The singlet at δ = 9.33 ppm corresponds to the seven hydrogens of the aromatic tropylium ion, which are highlighted in red for clarity. Tetramethylsilane (TMS) was used as an internal standard.

6.3.2 The crystal structures of tropylium tin iodide, $(C_7H_7)_2SnI_6$, and tropylium lead iodide, $C_7H_7PbI_3$

The crystal structures of tropylium tin iodide and tropylium lead iodide were solved *ab initio* from SXRD data. Unit cells were determined using DICVOL;[327] the large number of well-resolved reflections provided a lone plausible cell solution for each compound. Space group assignments were deduced by examining systematic absences in the data, as discussed in detail below. Inspection of X-ray pair distribution function (PDF) data enabled an *a priori* elucidation of tin and lead coordination environments. Sn–I pair correlations are observed at 2.9(2) Å, consistent with tetravalent SnI_6 octahedra rather than SnI_4 tetrahedra. Bond valence calculations for six-coordinate Sn with an average Sn–I bond distance of 2.9 Å are also consistent with the Sn^{4+} oxidation state.[281,332,333]

X-ray PDF data of tropylium lead iodide reveals a Pb–I pair correlation at 3.2(1) Å consistent with PbI_6 octahedra. The heavy atoms in both tropylium tin iodide and tropylium lead iodide were located utilizing the Monte-Carlo algorithm implemented in FOX[328] by introducing rigid

octahedral units with metal–ligand bond distances taken from the PDF data. Once the heavy atoms were located, electron density Fourier difference maps were generated from Rietveld refinements of the heavy atom positions against the SXRD data, which revealed rings of positive electron density consistent with the size of tropylium ions (Figure 6.4a and c). Carbon positions were located manually via maxima in the difference density, and also using rigid-body modeling (FOX) with frozen metal and iodide positions as determined from heavy-atom-only refinements. We elected to restrain the tropylium C–C bond distances to 1.35(5) Å and the internal angles of the ring to 128.6(1)° to encourage chemically rational representations of the aromatic ring,[334] the presence of which is confirmed by the FT-IR and ^{1}H NMR studies. Despite the success in locating carbon positions, the models most likely reflect the average positions of tropylium, which is liable to be rotationally disordered in both compounds.

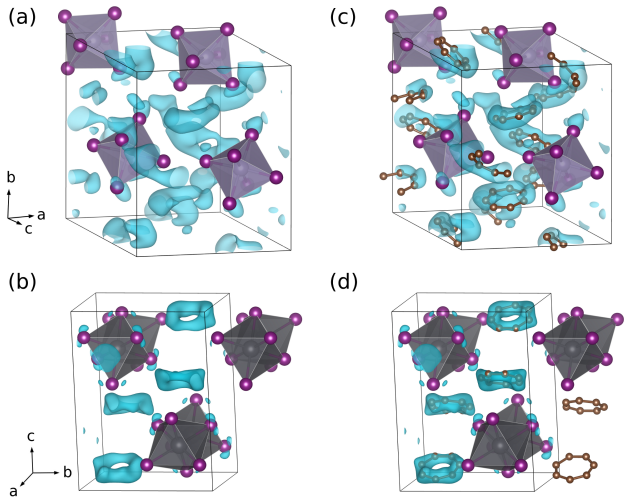

Figure 6.4: Visualization of the residual electron density after location of the heavy atoms in tropylium tin iodide (a) and tropylium lead iodide (b). Crystal structures of tropylium tin iodide (c) and tropylium lead iodide (d) superposed on the respective Fourier difference maps. Hydrogen atoms have been omitted for clarity, lavender spheres denote tin atoms, charcoal are lead, purple are iodine, and brown are carbon.

Tropylium tin iodide, $(C_7H_7)_2SnI_6$, crystallizes in the monoclinic space group *An* with lattice parameters a = 14.5120(1) Å, b = 12.5472(1) Å, c = 13.0163(1) Å, and β = 94.303(1)°. Observed reflections in the SXRD data are consistent with space groups deriving from the $A1n1$ extinction symbol, namely *An* and $A2/n$. Although the atomic positions can be described by signifi-

cantly fewer symmetry distinct atoms in $A2/n$, the presence of inversion symmetry necessitates that one of the two troplyium ions in the asymmetric unit be described by split sites. A split-site (half-occupied) model to account for the carbon positions is not necessarily inappropriate, considering the expectation of rotational disorder, but such a model is challenging to restrain for refinement. Despite a larger number of free parameters, site-splitting is avoided with the use of space group An, which also provided for convenient generation of a fully-occupied model as required for density functional calculations.

In Figure 6.4b, the structure of $(C_7H_7)_2SnI_6$ is superposed on the Fourier difference map generated from a heavy-atom-only Rietveld refinement. A joint Rietveld refinement against the SXRD data and high-resolution time-of-flight neutron diffraction data was performed with all of the atoms in the unit cell, including hydrogen, and offers strong support of the An structural model determined using solely X-ray data (Figure 6.5). Although it was anticipated that incoherent scattering by hydrogen might dominate the pattern, the data present well-resolved reflections (Figure 6.5b). In addition to C–C bond distance and angle restraints, the inclusion of hydrogen necessitated C–H distance [1.10(5) Å] and C–C–H angle [115.7(1)°] restraints to preserve the planarity of the tropylium ion. While the smeared electron density present in Figure 6.4a/b is suggestive of rotational disorder of tropylium, the refined atomic displacement parameter (ADP, U_{iso}, Table 6.1) on carbon is consistent with a lesser degree of disorder than expected; this lends support to the choice of space group An rather than $A2/n$ to model the compound. The X-ray refinement shown in Figure 6.5a exhibits diffuse features at higher Q, and despite the exceptional flux and signal-to-noise provided by the 11-BM diffractometer there were no observable Bragg features beyond $Q = 6\,\text{Å}^{-1}$. These observations indicate orientational disorder of the isolated $[SnI_6]$ octahedra, which is a common consequence of isolated octahedral units (*cf.*, SF_6[335] and K_3AlF_6[203]). This is also reflected in the large heavy-atom U_{iso} values obtained from the refinement.

Tropylium lead iodide, $C_7H_7PbI_3$, crystallizes in the orthorhombic space group $Pnma$ with lattice parameters a = 8.05443(2) Å, b = 11.18714(3) Å, and c = 14.71927(5) Å. On the basis of

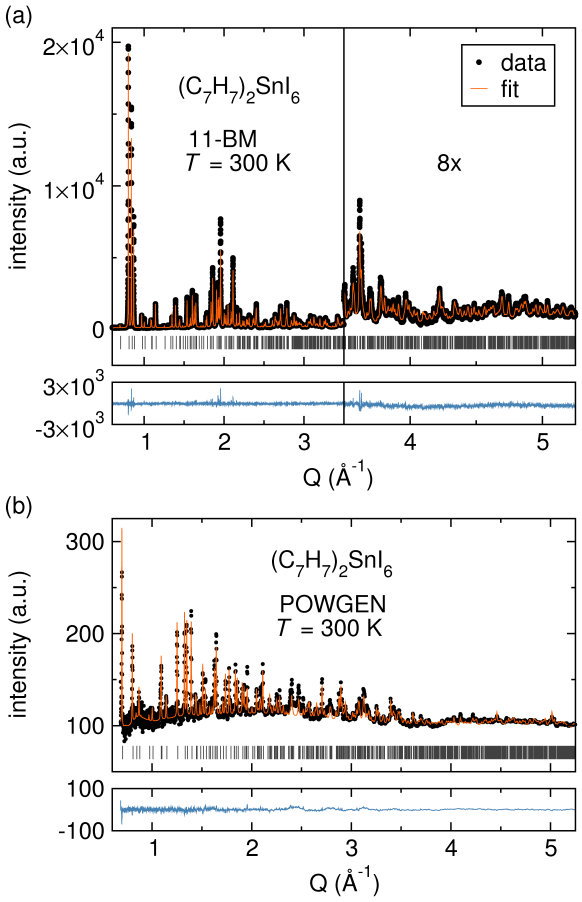

Figure 6.5: Joint Rietveld refinement of high-resolution X-ray powder diffraction data (a) with high-resolution time-of-flight neutron diffraction data (b). The right panel in (a) is multiplied by 8 to show the sharp decrease in intensity at $Q > 4$ Å^{-1} and diffuse features. The grey tick marks indicate the locations of predicted Bragg reflections of $(C_7H_7)_2SnI_6$. Refinement parameters can be found in Table 6.1.

the observed extinctions (extinction symbol *P*–*cn*), two possible space groups were identified, $P2_1cn$ and *Pmcn*; the conventional settings, $Pna2_1$ and *Pnma*, were adopted for structure determination and refinement. Analogous topologies containing one-dimensional chains of face-sharing PbI_6 octahedra were found for both space group possibilities. In $Pna2_1$, for which the 4*a* general position is the only Wyckoff position, three unique iodines are required in the asymmetric unit. In space group *Pnma*, the same topology is described by one Pb and two I atoms, with one of the crystallographically distinct iodine atoms residing on the 8*d* general position. The larger number of atoms required in $Pna2_1$ and lack of statistical improvement despite the increase in free parameters support the selection of *Pnma*.[336] Tropylium ions are described by

four crystallographically-distinct carbon atoms, one of which resides on a mirror plane normal to b (the 4c position). In Figure 6.4d, the resulting structural model is superposed on the difference map generated from the carbon-free model.

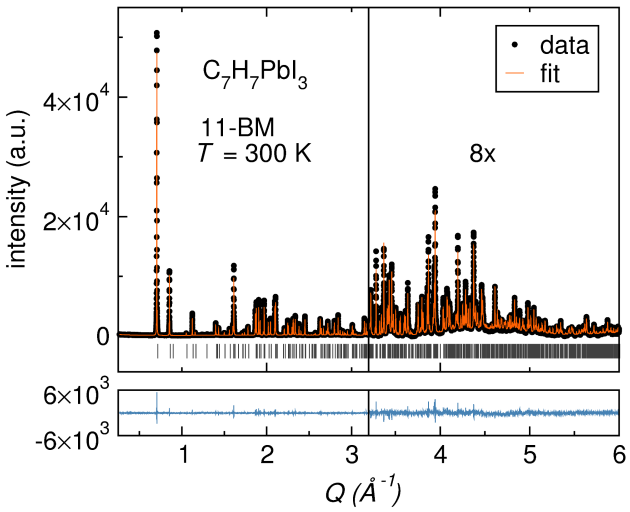

Figure 6.6: Rietveld refinement of tropylium lead iodide. The data for $Q > 3.2$ Å^{-1} are multiplied by 8 in order to enhance the diffuse features at higher Q. The grey tick marks indicate the locations of predicted Bragg reflections for $C_7H_7PbI_3$.

As similarly noted for the tin compound, the diffraction pattern of $C_7H_7PbI_3$ presents diffuse components in the higher Q region (Figure 6.6), and there are no observable Bragg features beyond $Q = 7$ Å^{-1}. This indicates that Pb and I are also somewhat disordered in tropylium lead iodide, as reflected by the ADPs (Table 6.1). While large ADPs could be an indication of an error in space group selection, we note that slighly larger U_{iso} values were obtained in refinements using space group $Pna2_1$, which further supports the space group selection and the notion of intrinsic structural disorder. The $Pna2_1$ and $Pnma$ structures differ with respect to the tropylium orientation, which is slightly canted in the bc plane in $Pna2_1$. Density functional relaxation in both space groups, constrained to the experimentally determined cell, suggest a slight stabilization of 35 meV per formula unit in $Pna2_1$. However, as discussed in more detail below, since this is not the DFT equilibrium cell volume, it is difficult to be certain which structure is more energetically favorable. Despite identical Rietveld refinement statistics, the fewer

number of structural parameters required to describe $C_7H_7PbI_3$ in *Pnma* is consistent with the room temperature structure adopting this space group.

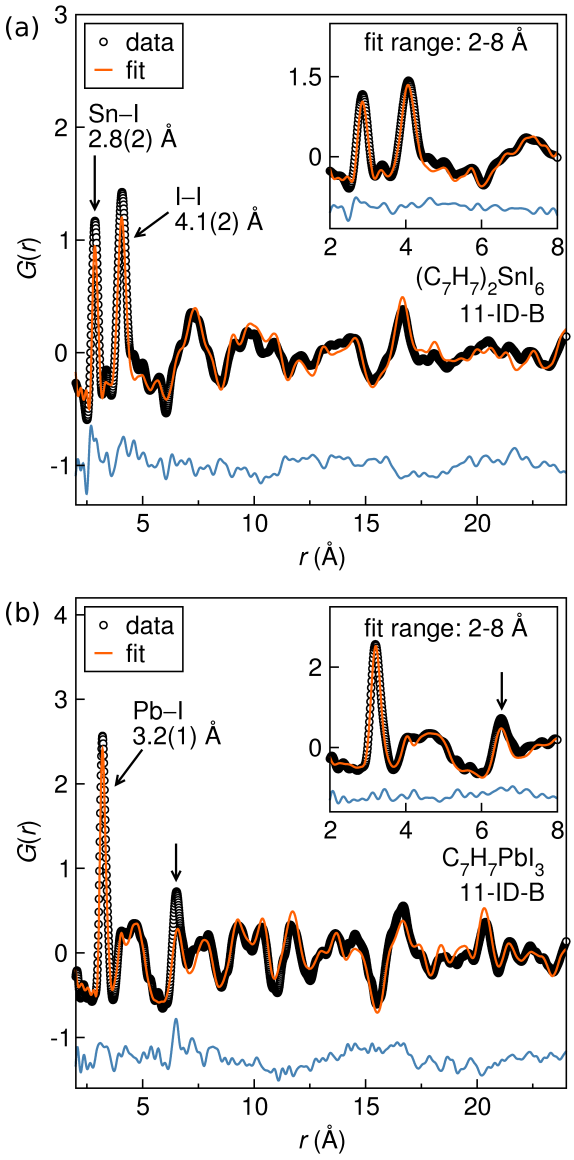

Figure 6.7: X-ray PDF analysis of (a) tropylium tin iodide and (b) tropylium lead iodide over a fit range of $2 < r < 24$ Å. The insets of (a) and (b) show the refinements resulting from a fit range of $2 < r < 8.5$ Åand $2 < r < 8$ Å, respectively. The large feature in (a) at $r = 2.83$ Å corresponds to the octahedral tin-iodide bond distance, while the peak at $r = 4.44$ Å reflects the distance between iodine atoms within an octahedron. In (b) the arrows show that, over shorter refinement ranges, the predicted intensity of the feature at r~6.4 Å is improved.

Further refinement of the $(C_7H_7)_2SnI_6$ and $C_7H_7PbI_3$ models against X-ray PDF data indicates that the local structures are described well by the average structures, as shown in Figure 6.7a and b, respectively. Medium-range structural disorder, however, is reflected in the poorly predicted intensities of intra-octahedon features in full-range refinements: in tropylium tin iodide, the Sn–I (r = 2.9(2) Å) and *cis*-I–I (r = 4.1(2) Å) intensities are poorly fit; in tropylium lead iodide, the *trans*-iodide feature at r = 6.4 Å (denoted by an arrow in Figure 6.7b) is poorly fit. The hypothesis of *inter*-octahedral disorder in both compounds is confirmed by refining the data over shorter correlation distances to minimize the effects of reduced coherence at longer length scales. As shown in the insets of Figure 6.7a and b, the predicted intensities of these low r features are notably improved by excluding longer r correlations. This strongly supports our assertions that the large ADPs obtained in Rietveld refinements arise from medium-range disorder, rather than due to problems inherent to the models. In $C_7H_7PbI_3$, the disorder is attributed to torsional distortions of the one-dimensional Pb–I chains.

Table 6.1: Structural parameters and refinement statistics for tropylium tin iodide and tropylium lead iodide. With the exception of the two chemically distinct iodine atoms in $C_7H_7PbI_3$ (indicated by Wyckoff site), like elements were constrained to the same atomic displacement parameter. Refinement statistics for $(C_7H_7)_2SnI_6$ are reported for the joint X-ray and neutron refinement.

	$(C_7H_7)_2SnI_6$	$C_7H_7PbI_3$
Crystal System	Monoclinic	Orthorhombic
Space Group	*An*	*Pnma*
a (Å)	14.5120(1)	8.05443(2)
b (Å)	12.5472(1)	11.18714(3)
c (Å)	13.0163(1)	14.71927(5)
α (°)	90	90
β (°)	94.303(1)	90
γ (°)	90	90
U_{iso}(M) (Å^2)	0.051(1)	0.0461(2)
U_{iso}(I) (Å^2)	0.0422(2)	0.0685(5); 8d
		0.0640(6); 4c
U_{iso}(C) (Å^2)	0.0164(6)	0.102(4)
U_{iso}(H) (Å^2)	0.064(3)	—
Red. χ^2	4.8	3.31
wR_p	4.7 %	10.2 %

6.3.3 Optical Properties and Electronic Structures

UV-Visible Diffuse Reflectance Spectroscopy

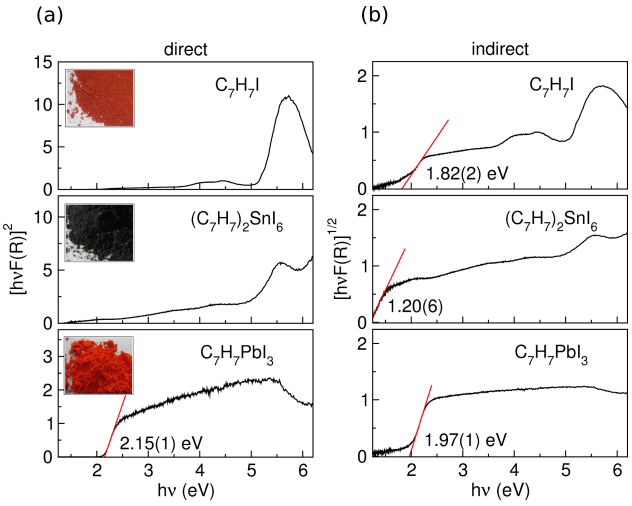

Figure 6.8: Tauc plots of UV-visible diffuse reflectance spectra used to determine the (a) direct optical gaps and (b) indirect optical gaps of tropylium iodide, tropylium tin iodide, and tropylium lead iodide (diluted in $BaSO_4$). The insets in (a) are brightfield photographs of the sample powders of tropylium iodide, tropylium tin iodide, and tropylium lead iodide.

The Kubelka-Munk transform was performed on UV-visible diffuse reflectance spectra collected on powders of tropylium iodide, tropylium tin iodide and tropylium lead iodide, and Tauc plots were generated to highlight possible direct and indirect absorption edges, as shown in Figure 6.8a and b, respectively. When the spectra are plotted as $[h\nu F(R)]^2$ (panel a), both tropylium iodide and tropylium tin iodide do not exhibit a well-defined direct optical band edge within the examined energy range. However, there is a strong absorption feature between 5 eV and 6 eV that corresponds to UV absorption by the tropylium ring, indicating that the electronic states of the tropylium ion are not strongly influenced by the surrounding inorganic constituents in $(C_7H_7)_2SnI_6$; this feature reflects the molecular nature of tropylium iodide and tropylium tin iodide. In contrast, tropylium lead iodide clearly shows a linear region in the Tauc plot that indicates a direct optical band gap of 2.15(1) eV when extrapolated to zero absorption. Additionally,

the strong absorption feature characteristic of the $[C_7H_7]^+$ moeity is not resolved, which could be attributed to increased inorganic-organic interaction in the form of charge transfer.

When the diffuse reflectance data are plotted as $[h\nu F(R)]^{1/2}$ to highlight potential indirect band edges (Figure 6.8b), linear regions for tropylium iodide, tropylium tin iodide, and tropylium lead iodide are visible; extrapolation to zero absorption results in indirect gaps of 1.82(2) eV, 1.20(6) eV, and 1.97(1) eV, respectively. Although the Tauc plots of all three compounds exhibit broad absorption features across the range of energies examined, the absorption feature characteristic of the tropylium rings is still visible in the spectra of tropylium iodide and tropylium tin iodide, which supports the notion that there is minimal electronic coupling to the organic. In the absorption spectrum of tropylium lead iodide the absorption peak of the tropylium ring is not resolved, which once again suggests that it may be obscured by inorganic-organic charge transfer.

We attribute the deep colors of tropylium tin iodide and tropylium lead iodide to charge-transfer processes, although the origin of these processes is not immediately apparent upon inspection of the optical spectra. In tropylium tin iodide, the charge-transfer processes are not likely due to any interaction between the tropylium cations and the isolated SnI_6 octahedra, due to the fact that the absorption feature of tropylium is highly pronounced. Therefore, it is much more likely that ligand-to-metal charge transfer is occurring between iodine and tin, thus resulting in the deep black color. In the case of tropylium lead iodide, it is interesting to compare the color of this compound to the colors of compounds with similar topologies. Typically, hybrid materials containing one-dimensional chains of face-sharing lead-iodide octahedra are reported to range in color from colorless to yellow-orange, regardless of the choice of organic constituent.[319,337,338] The anomalous bright red-orange color of the tropylium lead iodide powder suggests that there is strong charge transfer between the tropylium ions and the inorganic lattice, thus resulting in the unresolved absorption feature of tropylium in the absorbance spectrum of tropylium lead iodide.

DFT Calculations

The structures of tropylium tin iodide and tropylium lead iodide were optimized within density functional theory and the relaxed structures were used in static electronic structure calculations. Due to the slow convergence of forces on tropylium rings when the lattice shape (*i.e.*, cell dimensions) was allowed to relax at a fixed volume, ionic relaxations were constrained to the experimentally determined cells with respect to both volume and shape. Thus, the calculations presented here do not represent the electronic structures at equilibrium cell volumes, which may influence the magnitude of the calculated gaps. The DFT relaxed structures are in excellent agreement with the experimentally determined structures.

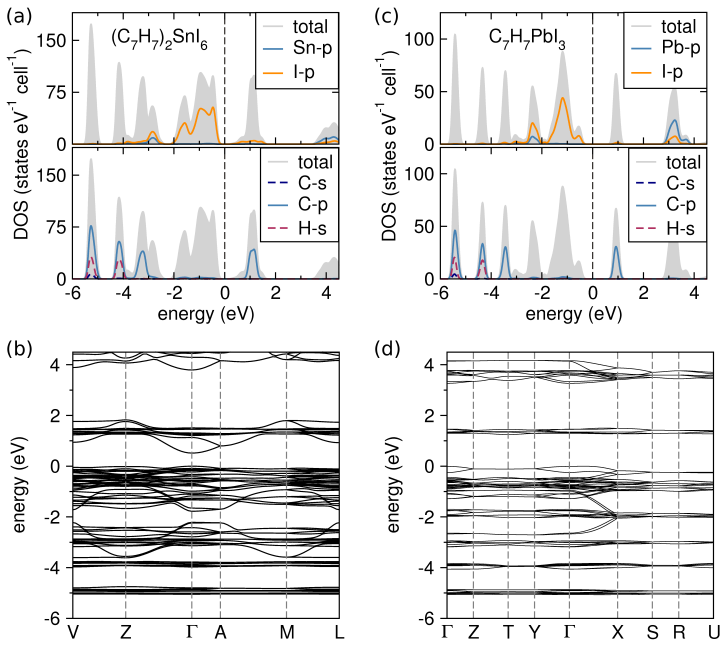

Figure 6.9: Total and local density of states for tropylium tin iodide (a) and tropylium lead iodide (c). The contribution from the inorganic constituents are shown in the upper panels, while the contribution from the tropylium rings is shown in the lower panels. The calculated band diagrams for tropylium tin iodide and tropylium lead iodide are shown in (b) and (d), respectively. The Fermi energy is referenced to the top of the valence band, set to 0 eV.

Total and local densities of states (DOS) and band structure diagrams are shown for both compounds in Figure 6.9. Tropylium tin iodide (panels a and b) is predicted to have a direct gap of 0.52 eV at the Γ point, which is consistent with the black color of the solid. The indirect gap

between Γ and A is calculated to be 0.80 eV. Near the Fermi energy the valence band is composed of primarily iodine *p* states, while the low-lying unoccupied states are predominantly iodine and, at slightly higher energies, carbon *p* states (panel a). The majority of bands present flat dispersions, with a few exceptions arising from a short I–I distance in the crystal structure. Orientational disorder of SnI_6 octahedra would relieve this contact and induce a narrowing of the dispersions, and the electronic states are probably more localized than reflected here. The generally localized states are consistent with tropylium tin iodide comprising isolated SnI_6 octahedra and tropylium ions, and this is reflected in a very high measured electrical resistivity. In this light, it is interesting to note that Cs_2SnI_6, a zero-dimensional "perovskite" containing regular isolated $[SnI_6]^{2-}$ units, exhibits high electron and hole mobility due to wider band dispersions that arise from increased overlap of iodine and tin states.[11]

The calculated DOS and band structure of tropylium lead iodide are shown in Figure 6.9c and d. An indirect gap of 1.25 eV is predicted to occur between roughly the Γ and T points; the highest occupied state actually occurs between Γ and X. The 1.3 eV direct gap at Γ is only slightly larger. In general, $C_7H_7PbI_3$ presents some similar electronic structural features as $(C_7H_7)_2SnI_6$, with localized carbon states suggesting minimal coupling between tropylium rings and metal/halide states. In contrast to tropylium tin iodide, however, the DOS indicate that the lowest-lying unoccupied states in $C_7H_7PbI_3$ have significant carbon character. Occupied iodine *p* states between –2.5 eV and 0 eV are somewhat disperse due to orbital overlap within the 1D chains.

Although the DFT calculations suggest that neither compound presents features expected to yield mobile charge carriers, supported by experimentally measured electrical resistivities in excess of $\sim 3 \times 10^7$ Ω·cm, the DOS and band structures are reflective of the observed optical absorption behavior. To gauge the character of band-edge optical transitions, band and *k*-point decomposed charge densities were calculated at the valence band maxima (HOB, highest occupied band) and conduction band minima (LUB, lowest unoccupied band), presented in Figure 6.10. The HOB of $(C_7H_7)_2SnI_6$ (panel a) is composed of localized iodine *p* states while the

LUB (panel b) contains significant Sn character, suggesting that near-edge optical absorption arises from ligand-to-metal charge transfer in tropylium tin iodide. The situation is distinct in $C_7H_7PbI_3$, in which charge density is localized on I and Pb at the HOB (panel c) but is almost entirely tropylium derived (π^* character) at the LUB (panel d). This scenario is highly suggestive of iodine-to-tropylium charge transfer, indicating stronger inorganic–organic interactions in the lead compound than in the tin.

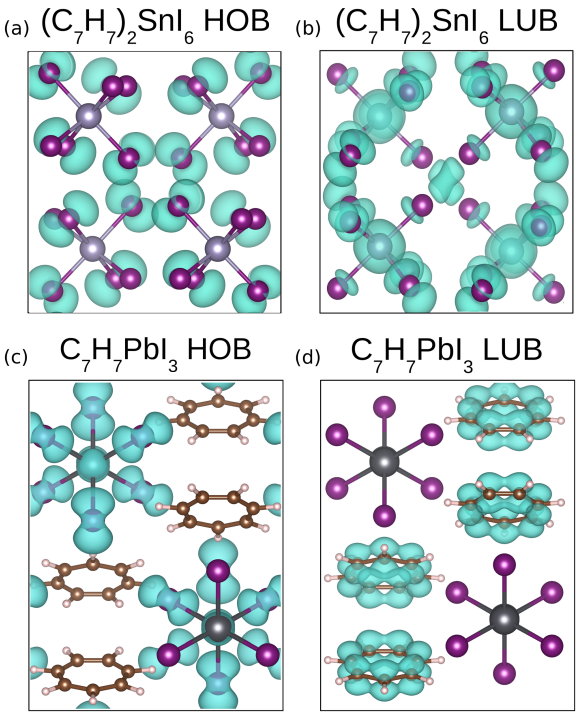

Figure 6.10: Band decomposed charge densities for tropylium tin iodide and tropylium lead iodide. Panel (a) shows the charge density associated with the highest occupied band (HOB) of tropylium tin iodide, while (b) shows the charge density of the tropylium tin iodide lowest unoccupied band (LUB). The band decomposed charge densities of tropylium lead iodide are shown in (c) and (d), where (c) illustrates the charge density of the HOB and (d) shows the charge density for the LUB. The tropylium rings have been omitted from panels (a) and (b) for clarity.

6.4 Conclusions

We have prepared two hybrid materials containing the tropylium ion, an optoelectronically active unfunctionalized aromatic organic ion. The crystal structures of tropylium tin

iodide, $(C_7H_7)_2SnI_6$, and tropylium lead iodide, $C_7H_7PbI_3$, were solved using high-resolution synchrotron powder X-ray diffraction informed by X-ray pair distribution function data. High-resolution time-of-flight neutron diffraction confirms the tropylium tin iodide structural model, which contains isolated $Sn^{IV}I_6$ octahedra. Tropylium lead iodine presents 1D chains of face-sharing $Pb^{II}I_6$ octahedra. The low dimensionality of both compounds contribute to high measured electrical resistivities, in excess of $\sim 3 \times 10^7$ Ω·cm. The diffuse reflectance spectrum of tropylium tin iodide reveals a large absorption feature characteristic of the tropylium ion, suggesting that the optoelectronic properties result from intramolecular transitions of the SnI_6 octahedra and tropylium ion. Tropylium lead iodine, on the other hand, exhibits a broad spectral absorption, suggestive of increased electronic coupling between tropylium ions and the inorganic lattice. These conclusions are supported by density functional calculations of the band and *k*-point decomposed charge densities at the highest occupied and lowest unoccupied bands. The larger degree of organic–inorganic coupling observed in tropylium lead iodide motivates a search for tropylium-containing hybrids with higher inorganic dimensionality, which may further increase the electronic coupling while also enabling improved carrier mobility.

Chapter 7

Perspectives and Design Principles of Vacancy-Ordered Double Perovskite Semiconductors

7.1 Introduction

The above work represents a significant contribution towards an understanding of the structure-dynamics-property relationships in vacancy-ordered double perovskite semiconductors. This chapter will expand upon the work presented in this document within the context of recent experimental and computational studies in the literature to construct a set of guiding principles to explain and predict the optical and electronic properties of vacancy-ordered double perovskites with relevance for potential applications in photovoltaics. We then propose avenues of future study for vacancy-ordered double perovskite semiconductors.

Note on author contributions: This chapter was written through contributions from Annalise E. Maughan, Alex M. Ganose, David O. Scanlon and James R. Neilson. AEM wrote the initial draft. AMG and DOS contributed significant portions of the *Electronic Dispersion and Low Carrier Effective Masses* section and (Figure 7.4 and Figure 7.5). JRN supervised the project.

7.2 Optical Gap and Band Alignment

The band gap and optical absorption of vacancy-ordered double perovskites is dictated by the electronic states of the *B*- and *X*-site ions. We first consider the impact of the *X*-site halogen upon the band alignment and optical gap. Incorporation of smaller halogens across the series $I^- \rightarrow Br^- \rightarrow Cl^-$ results in a progressive widening of the band gap, as illustrated in a computational study by Cai *et al.*[9] As shown in Figure 7.1, the calculated band gaps of the iodide-based vacancy-ordered double perovskites are, in general, smaller than those of the bromide and chloride analogs, and the band gaps increase monotonically within a compositional fam-

ily in which the *A*- and *B*-site cations are unchanged. This notion is evidenced by the trend in experimentally-determined optical gaps for the Cs_2SnX_6 and Cs_2TiX_6 series. Cs_2SnI_6 is reported to exhibit an experimental optical gap of ~1.3 eV,[7,11,209,339] yet replacing I^- with Br^- and Cl^- increases the optical gap to 2.7 eV and 3.9 eV, respectively.[10,209] Similarly, Cs_2TiI_6 exhibits an optical gap of 1.02 eV while a larger optical gap of 1.78 eV is observed for Cs_2TiBr_6.[340] This trend is conserved across all members of the vacancy-ordered double perovskite family for a given combination of *A*- and *B*-site cations.

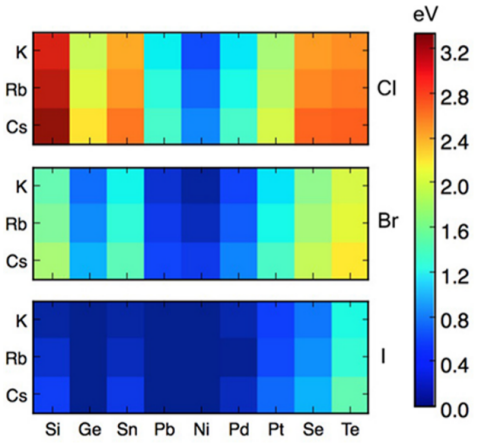

Figure 7.1: DFT-calculated band gaps of the A_2BX_6 compounds in which the *A*-, *B*-, and *X*-sites were systematically varied. Figure reproduced with permission from Cai, Xie, Ding, Chen, Thirumal, Wong, Mathews, Mhaisalkar, Sherburne, Asta, *Chem. Mater.*, **2017**, *29*, 7740–7749.[9]

The impact of the *X*-site upon the optical gap stems from the strong presence of halogen states at the valence and conduction band edges. In most members of the vacancy-ordered double perovskite family, the valence band maximum (VBM) is derived exclusively from the halogen *p* states, and thus the energy of the valence band is dictated predominantly by the choice of halogen. This notion is exemplified by the Cs_2SnX_6 series ($X = I^-$, Br^-, Cl^-) and is illustrated through simplified molecular orbital diagrams of the Sn–*X* interactions within the octahedra. As shown in Figure 7.2, the highest occupied states are derived from the halogen non-bonding *p* states. Upon incorporation of the smaller halides, these states move to lower energies as the ionization potential of the halogen *p* orbitals decreases across the $I^- \rightarrow Br^- \rightarrow$

Cl^- series, resulting in a widening of the optical gap observed experimentally.[209] Substitution at the X-site has been employed to tune the band gap in the mixed halide series $Cs_2SnI_{6-x}Br_x$ and $Cs_2TiI_{6-x}Br_x$, though the optical gaps do not change linearly with respect to halide concentration.[10,340]

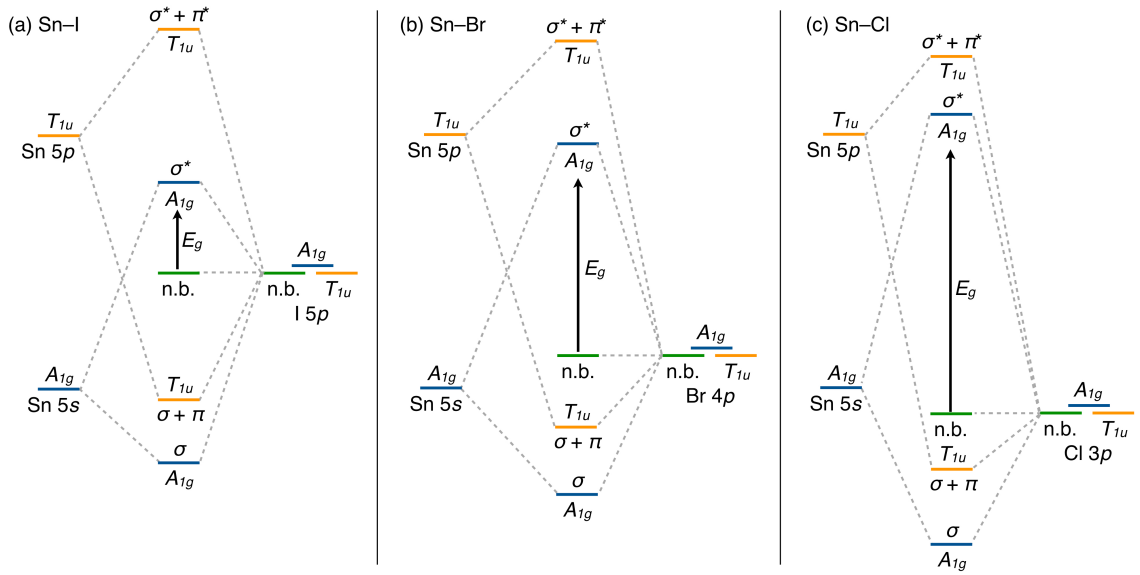

Figure 7.2: Molecular orbital theory perspective of the frontier states of (a) Cs_2SnI_6, (b) Cs_2SnBr_6, and (c) Cs_2SnCl_6 considering the interactions between the Sn and I orbitals.

The X-site anion further contributes to the band gap through interactions with the B-site cation at the center of the octahedra to dictate the energy of the conduction band minimum. In the Cs_2SnX_6 series, the conduction band minimum is derived from hybridized Sn 5s and X p states,[6–8,11,209] as predicted by the molecular orbital theory diagram in Figure 7.2. As the halogen p states fall closer in energy to the Sn 5s states, the energy of the lowest unoccupied states are pushed higher in energy as their interaction becomes more covalent. The increase in band gap for the smaller halogens is therefore due to a combination of the valence band moving to lower energies with an increase in energy of the conduction band minimum. It has been noted recently that the proportional change in band gap across the Cs_2SnX_6 ($X = I^-$, Br^-, Cl^-) series is significantly larger than is observed for the $CsSnX_3$ perovskites.[341] In $CsSnX_3$, the calculated band gaps lie between E_g = 1.3–2.7 eV from $X = I^- \rightarrow Br^- \rightarrow Cl^-$ for the cubic $Pm\bar{3}m$ perovskite

phase,[342] while the band gaps in Cs_2SnX_6 span a much larger range from E_g = 1.3−3.9 eV.[209,341] In the $CsSnX_3$ series, the formally filled Sn 5*s* orbitals result in a valence band maximum derived from hybridized Sn 5*s*/halogen *p* states, while the conduction band minimum is derived from hybridized Sn 5*p*/halogen *p* states.[342] Due to the hybridization of the Sn/halogen states at the valence band maximum, incorporation of smaller halogens with lower ionization potentials depresses the valence band energy only slightly. In contrast, the valence band maximum of the Cs_2SnX_6 vacancy-ordered double perovskites is derived exclusively from the non-bonding halogen states, and thus the valence band maximum is depressed concomitantly with the ionization potential of the halogen. This results in a significant widening and larger proportional increase of the band gap upon incorporation of smaller halogens in the Cs_2SnX_6 vacancy-ordered double perovskites compared to the the $CsSnX_3$ compounds. As most vacancy-ordered double perovskites exhibit similar orbital character at the valence and conduction band edges, the molecular orbital theory diagrams shown in Figure 7.2 serve as a simple predictive tool to understand the influence of *B*- and *X*-site substitution upon the band gap.

The trends in band gap reported in the literature and predicted by the molecular orbital theory perspective shown in Figure 7.2 are further supported by the reported band alignments of several members of the vacancy-ordered double perovskite family. As shown in Figure 7.3, the ionization potentials for the bromide-based vacancy-ordered double perovskites lie at lower energies than their iodide analogs. For example, the experimental ionization potentials for Cs_2SnI_6 range from −5.42 eV to −5.94 eV and the electron affinities range from −4.12 eV to −4.95 eV for polycrystalline samples.[3,7,10,11] In contrast, the ionization potential of polycrystalline Cs_2SnBr_6 falls deeper in energy at −6.62 eV, and the electron affinity is pushed higher in energy to reside at −3.77 eV, consistent with the large increase in band gap.[10] A similar observation is expected for Cs_2SnCl_6, though photoelectron spectroscopy studies are likely complicated by the high electrical resistivity of this compound.[209]

While both conduction and valence band edges exhibit character from the halogen *p* states, deviations in the close-packing of the halogen sublattice do not appear to strongly influence

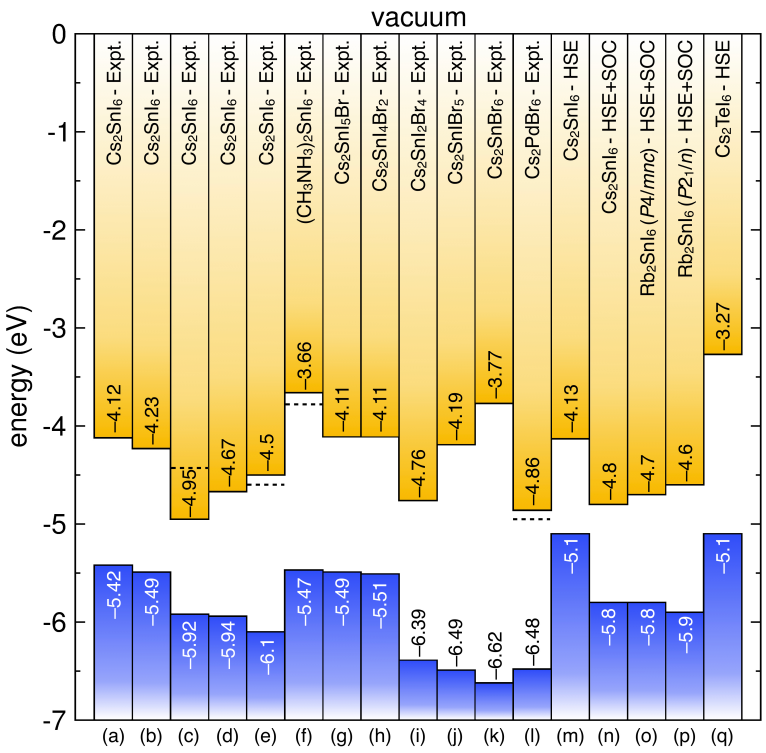

Figure 7.3: Comparison of the experimentally- and computationally-determined ionization potentials and electron affinities of several members of the vacancy-ordered double perovskite family. Dashed lines represent the reported Fermi levels. Values were taken from (a),[10] (b),[11] (c),[7] (d),[3] (e),[12] (f),[13] (g),[10] (h),[10] (i),[10] (j),[10] (k),[10] (l),[14] (m),[7] (n),[8] (o),[8] (p),[8] (q).[7]

the optical gap and band alignment in the vacancy-ordered double perovskites. In Rb_2SnI_6, the smaller size of the Rb^+ ion yields a tetragonal variant of the vacancy-ordered double perovskite structure characterized by cooperative octahedral tilting, and further undergoes a phase transition to a monoclinic structure with additional tilting motifs.[8] Tetragonal Rb_2SnI_6 exhibits an optical gap of 1.32(2) eV, which is only slightly higher than the value of 1.23(3) eV determined for Cs_2SnI_6 by the same method. This observation is further mirrored in the DFT-calculated band alignments. Despite the lower-symmetry structure, the valence band maxima of both cubic Cs_2SnI_6 and tetragonal Rb_2SnI_6 are calculated to reside at −5.8 eV (Figure 7.3). The electron affinity of Rb_2SnI_6 (−4.7 eV) moves to slightly higher energy than that of Cs_2SnI_6 (−4.8 eV), likely responsible for the slight increase in optical gap observed experimentally. The band alignments of the monoclinic variant are also relatively unchanged. Taken together, these observations sug-

gest that cooperative octahedral tilting does not strongly affect the optical absorption behavior or electronic structure of vacancy-ordered double perovskite semiconductors. Rather, the optical absorption can be considered as a metal to metal/ligand charge transfer process within the [BX_6] octahedra, lending further credence to the predictive capability of the molecular orbital theory approach.

The interaction of the *B*-site with the halide ligands of the octahedra dictates the magnitude of and direct vs. indirect nature of the band gap. While Cs_2SnI_6 possesses a direct band gap of ~1.3 eV,[7,11,209,339] replacing Sn(IV) with Te(IV) at the *B*-site yields a larger, indirect band gap of 1.59 eV for Cs_2TeI_6.[7] The larger magnitude of the band gap in Cs_2TeI_6 arises due to covalent interaction of the Te 5*p* states with the I 5*p* states that pushes the conduction band higher in energy, as shown in the molecular orbital diagram in Figure 7.4. As the valence band is pinned at the iodine 5*p* states that dominate the valence band, the band gap is determined exclusively by the energy of the Te/I states at the conduction band minimum. Consideration of the orbital symmetry and character enables prediction of the direct vs. indirect nature of the band gaps in Cs_2SnI_6 and Cs_2TeI_6. From the molecular orbital theory perspective of the Sn–I interactions within an [SnI_6] octahedron, the highest occupied states of Cs_2SnI_6 are derived from a triply degenerate T_{1g} I 5*p* orbital set, while the lowest unoccupied state is A_{1g} character derived from the Sn 5*s*/I 5*p* orbitals (Figure 7.4a). By considering the interactions of the T_{1g} I 5*p* orbital set between octahedra, the highest energy state occurs when these orbitals are out of phase with those of the neighboring octahedra at the Γ point. At the conduction band minimum, the lowest energy state occurs at the Γ point and corresponds to in-phase interactions between the A_{1g} orbitals, as shown in Figure 7.5. This produces a direct band gap at the Γ point. In Cs_2TeI_6, the valence band maximum is derived predominantly from the T_{1g} I 5*p* orbital set, similarly to that observed for Cs_2SnI_6. We note that the reported band structure for Cs_2TeI_6 exhibits a small contribution from the Te 5*s* states, however the valence band is overwhelmingly I 5*p* character by comparison. The conduction band minimum is derived of a triply degenerate T_{1u} orbital set derived from Te 5*p* and I 5*p* states. As the frontier states of Cs_2TeI_6 are both composed of states

with p orbital symmetry, the nature of the band gap is necessarily indirect, occurring between the L and X points in the Brillouin zone.

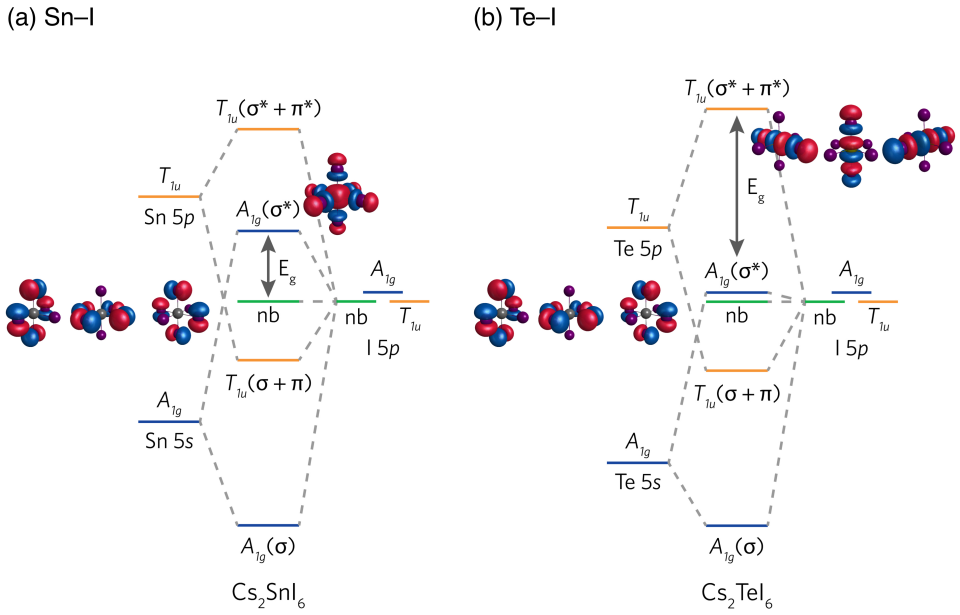

Figure 7.4: Molecular orbital theory perspective of the frontier states of (a) Cs_2SnI_6 and (b) Cs_2TeI_6 with orbital representations of the highest occupied and lowest unoccupied states of [SnI_6] and [TeI_6] octahedra calculated using GAMESS.

Consideration of the orbital character at the band edges provides insight into the nature of the band gap of the transition-metal-based vacancy-ordered double perovskites. In these compounds, the halogen p states comprise the valence band maximum while the d states of the Ti(IV), Pd(IV), or Pt(IV) ions comprise the conduction band minimum. In the Cs_2TiX_6 system, the conduction band is derived predominantly from fairly localized Ti 3d states, with a small contribution from the halogen p states near the conduction band edge, resulting in an indirect band gap.[340] Similarly to Cs_2SnI_6, the highest occupied states in Cs_2PdBr_6 are derived from the Br 4p orbitals to yield a triply degenerate orbital set with the highest energy state at the Γ point.[14] The conduction band is composed of Pd 4d and Br 4p states. A 3D projection of the wavefunction distribution at the conduction band minimum of Cs_2PdBr_6 indicate that the lowest unoccupied state is composed of hybridized Pd dz^2 and Br 4p orbitals within the octahedra

occurring at the X point in the Brillouin zone, presumably due to lower-energy in phase interactions between neighboring octahedra. This orbital configuration produces an indirect band gap between the Γ and X points of the Brillouin zone. The vacancy-ordered double perovskite $(NH_4)_2PtI_6$ is also reported to exhibit an indirect band gap of ~2 eV arising from transitions between I 5*p* character at the Γ point to the Pt 5*d* e_g states at X.[102] The reported optical gaps of other members of the hybrid Pt–I family are included in Table 7.1 for comparison, though only $(NH_4)_2PtI_6$ crystallizes in the cubic vacancy-ordered double perovskite structure.[102] A table of experimentally-determined optical gaps and the direct vs. indirect nature of the band gap of several members of the vacancy-ordered double perovskite family compiled in Table 7.1.

It is important to note that the fundamental band gap, determined as the energy gap between the valence band maximum and conduction band minimum, is not necessarily reflective of the true *optical gap* or *absorption onset* observed by absorption spectroscopy in some members of the vacancy-ordered double perovskite family. In the A_2SnI_6 (A = Rb^+, Cs^+, $CH_3NH_3^+$, $CH(NH_2)_2^+$) series, the direct transition at the Γ point is dipole-forbidden, and thus the dominant optical absorption occurs from states slightly below the valence band edge.[6–8] Similarly, the indirect band gap of Cs_2PdBr_6 from Γ-X is dipole-forbidden, though Sakai *et al.* note that transitions become allowed by moving slightly away from the X point.[14] The presence of disallowed transitions at the fundamental gap results in significant discrepancies between the calculated band gap and the experimental optical gap in these materials. As such, computational studies of these materials may also invoke an artificially large amount of Hartree-Fock exchange to fit the fundamental band gap to the experimentally observed optical gap.[12,103,105] For Cs_2SnI_6, the calculated band gap from GW0 calculations predict a band gap of ~0.88 eV,[7,209] though the optical gap determined by UV-visible diffuse reflectance spectroscopy is nearly 0.5 eV larger at ~1.3 eV.[7,11,209,339] The optical gaps of Cs_2SnBr_6 (2.7 eV) and Cs_2SnCl_6 (3.9 eV) are also underestimated by the GW0 calculated band gaps of 2.241 eV and 3.226 eV, respectively,[209] suggesting that the direct fundamental band gap is also dipole-disallowed in these materials; this observation likely stems from the fact that the electronic structures of the Cs_2SnX_6 are de-

rived of nearly identical orbital character and symmetry at both the valence and conduction band edges.[209]

One finds discussion in the literature regarding the true valence state of the Sn ions in Cs_2SnI_6. Formal oxidation state and electron counting yields tetravalent Sn with an electron configuration of [Kr]$5s^0 5p^0$. A computational study by Xiao *et al.* proposed that the true valence state of the Sn ion is divalent as in $CsSnI_3$ rather than tetravalent due to population of the Sn 5*s* states.[105] A more recent combined experimental and computational study demonstrated that the loss of two electrons (addition of two holes) upon oxidation of Sn^{2+} to Sn^{4+} from $CsSnX_3$ to Cs_2SnX_6 is accompanied by a rearrangement of the hybridized Sn 5*s* and *X p* orbitals that redistributes the charge over the Sn–*X* bond, rather than localizing in the Sn orbitals.[341] This effect occurs due to covalency between the tin and halide ions, and is therefore predicted to occur to a much lesser extent in members of the Cs_2SnX_6 series with strongly ionic interactions (*e.g.*, the hypothetical Cs_2SnF_6). While the covalent nature of the Sn–I interactions may result in changes to the electron density within the octahedra, formal oxidation states and electron counting provides an excellent predictor of the orbital character of the valence and conduction bands, and the nature and magnitude of the band gap, as illustrated in Figure 7.2 and Figure 7.4.

7.3 Electronic Dispersion and Charge Transport

Due to the absence of extended polyhedral connectivity between the [BX_6] octahedra, vacancy-ordered double perovskites are often referred to as "zero-dimensional" perovskite derivatives. However, this name is misleading, as it implies that the octahedra are isolated electronically from one another. Rather, vacancy-ordered double perovskites retain a close-packed framework of halides familiar to ABX_3 perovskites that can engage in orbital overlap with neighboring octahedra to produce dispersive electronic states. It is therefore important to consider the *electronic dimensionality*, rather than structural dimensionality, when deriving structure-property relationships in these materials.[345]

Table 7.1: Experimentally-determined optical gaps of several vacancy-ordered double perovskite halide semiconductors.

Compound	Optical gap (eV)	Direct/Indirect	Reference
Cs_2SnI_6	1.26	direct	[11]
Cs_2SnI_6	1.25	direct	[7]
Cs_2SnI_6 (thin film)	1.62	direct	[12]
Cs_2SnI_5Br	1.38	direct	[10]
$Cs_2SnI_4Br_2$	1.40	direct	[10]
$Cs_2SnI_3Br_3$	1.43	direct	[343]
$Cs_2SnI_2Br_4$	1.63	direct	[10]
Cs_2SnIBr_5	2.3	direct	[10]
Cs_2SnBr_6	2.7	direct	[209]
Cs_2SnBr_6	2.9	direct	[10]
Cs_2SnCl_6	3.9	direct	[209]
Cs_2PdBr_6	1.6	indirect	[14]
$(NH_4)_2PtI_6$	~2	indirect	[102]
$(CH_3NH_3)_2PtI_6$*non-VODP	~2	indirect	[102]
$(CH(NH_2)_2)_2PtI_6$	~2	indirect	[102]
$(C(NH_2)_3)_2PtI_6$*non-VODP	~2	indirect	[102]
Cs_2TiI_6	1.02	indirect	[340]
$Cs_2TiI_4Br_2$	1.15	indirect	[340]
$Cs_2TiI_2Br_4$	1.38	indirect	[340]
Cs_2TiBr_6	1.78	indirect	[340,344]
Cs_2TeI_6	1.59	indirect	[7]
Rb_2SnI_6	1.32(2)	direct	[8]
$(CH_3NH_3)_2SnI_6$	1.35(2)	direct	[6]
$(CH_3NH_3)_2SnI_6$ (thin film)	1.81	direct	[13]
$(CH(NH_2)_2)_2SnI_6$	1.37(2)	direct	[6]

As the valence band of vacancy-ordered double perovskites is derived predominantly from the halogen *p* states, the electronic dispersion of the valence band and thus the hole effective masses and transport are dictated by the orbital overlap within the close-packed halide framework. As such, replacing the larger iodide with bromide is accompanied by an increase in the hole effective mass due to reduced overlap between the smaller orbitals of the bromide sublattice. This notion is demonstrated by comparison of the cubic vacancy-ordered double perovskites Cs_2TiI_6 and Cs_2TiBr_6 and Cs_2PdI_6 and Cs_2PdBr_6. The calculated hole effective masses of Cs_2TiI_6 range from 0.79-1.58m_0, yet replacing iodide with bromide increases the hole effective masses to 0.9-1.79m_0.[340] Similarly, Cs_2PdI_6 exhibits a hole effective mass of 0.85m_0[9]

while a larger hole effective mass of $1.37m_0$ is reported for Cs_2PdBr_6.[14] The conduction band of vacancy-ordered double perovskites is often comprised of both *B*- and *X*-site electronic states, and thus the calculated electron effective masses are also impacted by orbital overlap within the close-packed halogen framework. Substitution of bromide for iodide in Cs_2TiX_6 increases the electron effective mass from $1.58m_0$ to $1.79m_0$.[340] Similarly, the reported electron effective mass of Cs_2PdI_6 is $0.47m_0$,[9] which is increased to $0.53m_0$ for the bromide analog.[14] The impact of halogen substitution on both the electron and hole effective masses speaks to the prominence of the close-packed halide framework in dictating the charge transport behavior in vacancy-ordered double perovskites.

The dispersive conduction band states in Cs_2SnI_6 and other vacancy-ordered double perovskites are further dictated by interactions of the hybridized *B*- and *X*-site states between neighboring octahedra. To illustrate this point, we have calculated charge density isosurfaces of the lowest conduction band of Cs_2SnI_6 (Figure 7.5), at the Γ and X points in the Brillouin zone. At the Γ point, the A_{1g} antibonding orbital is in phase with the A_{1g} orbital in the adjacent cell (Figure 7.5b), leading to a bonding interaction between neighboring octahedra (Figure 7.5c). This interaction occurs across a distance of ~4 Å between octahedra, due to the disperse projection of the iodine $5p$ orbitals into the interoctahedral void and acts to stabilize the bonding at this *k*-point. In contrast, at the X point, the A_{1g} antibonding orbital is out of phase with the A_{1g} orbital in the adjacent cell (Figure 7.5d), resulting in an antibonding interaction between neighboring octahedra (Figure 7.5e).[15] As such, the energy of the interaction at the X point is significantly higher, giving rise to reasonably high band dispersion. The large conduction band dispersion of Cs_2SnI_6 leads to calculated electron effective masses as low as $0.25m_0$.[6] A similar argument can be made for the dispersive conduction band of Cs_2TeI_6 by considering the interaction of the triply degenerate T_{1u} orbital sets between octahedra that produces electron effective masses ranging from $0.22m_0$ to $0.97m_0$.[7,9]

Similarly to the main-group metal-halide vacancy-ordered double perovskites, the palladium and platinum-based vacancy-ordered double perovskites $(NH_4)_2PtI_6$ and Cs_2PdBr_6

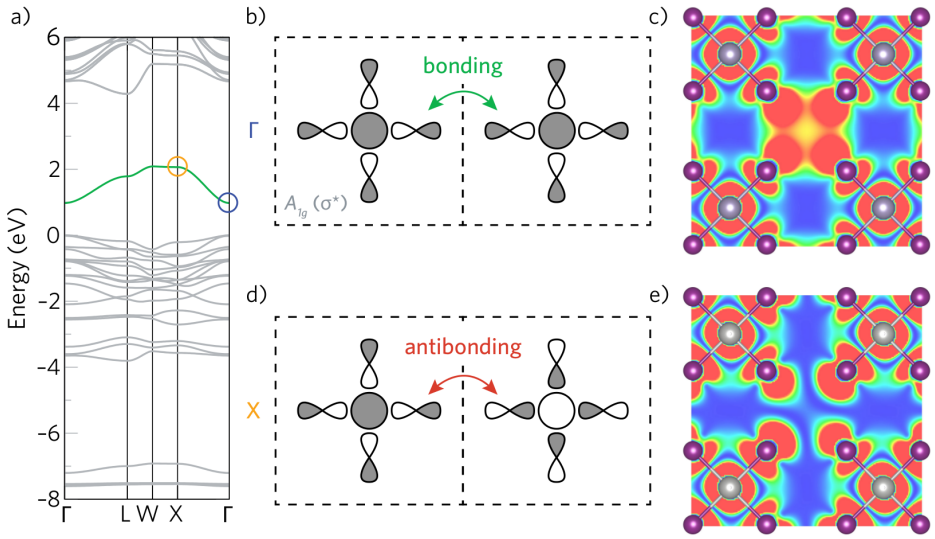

Figure 7.5: Band structure of Cs_2SnI_6, highlighting the A_{1g} antibonding states. Simplified bonding diagram (a and d) and charge density isosurfaces (c and e) of the highlighted band at the Γ and X points. The isosurface level was set to 0.008 eV Å^{-3}. Figure reproduced with permission from A. M. Ganose Copyright 2018 University of College London.[15]

exhibit dispersive conduction bands and relatively low electron effective masses.[14,102] In Cs_2PdBr_6, the conduction band minimum is derived from a hybridized electronic state of the Pd $4dz^2$ orbitals with the Br $4p$ orbitals.[14] The relatively low electron effective mass of $0.53m_0$ is therefore determined by the overlap of these hybridized states with those of the neighboring octahedra. In contrast, the conduction band minimum of $(NH_4)_2PtI_6$ is comprised of only the Pt $5d$ e_g orbital set with little or no contribution from the iodine p states, which produces electron effective masses ranging from 0.38-0.43m_0.[102] While the Pd- and Pt-based vacancy-ordered double perovskites exhibit fairly dispersive conduction band states, the analogous electron-poor Ti-based compounds exhibit significantly more localized states in the conduction band.[340] In Cs_2TiX_6, the conduction band minimum is derived from the Ti $3d$ states. These localized conduction band states resulting in large electron effective masses of $1.58m_0$ and $1.79m_0$ for Cs_2TiI_6 and Cs_2TiBr_6, respectively. On the other hand, electronic dispersion from the close-packed halogen lattice produces lighter hole effective masses. As such, Cs_2TiI_6 and Cs_2TiBr_6 are the only compounds of those considered here that are expected to exhibit higher hole mobilities than electron mobilities. The reduced dispersion in Cs_2TiX_6 compared to

Cs_2PdBr_6 and $(NH_4)_2PtI_6$ may be due to the larger size of the $4d$ and $5d$ orbitals of Pd and Pt that can engage in stronger orbital overlap between neighboring octahedra compared to the smaller spatial distribution of the Ti $3d$ orbitals. The calculated electron and hole effective masses for several members of the vacancy-ordered double perovskite family are provided in Table 7.2.

Table 7.2: Calculated electron and hole effective masses for several members of the vacancy-ordered double perovskite family given in units of m_0.

Compound	Spacegroup	m_e^*	m_h^*	Reference
Cs_2SnI_6	$Fm\bar{3}m$	0.25	0.81	[6]
Cs_2SnI_6	$Fm\bar{3}m$	0.33	1.5	[9]
Cs_2SnI_6	$Fm\bar{3}m$	0.48-0.92	1.32-2.75	[7]
$(CH_3NH_3)_2SnI_6$	$Fm\bar{3}m$	0.31	0.99	[6]
$(CH(NH_2)_2)_2SnI_6$	$Fm\bar{3}m$	0.43	1.61	[6]
$(NH_4)_2PtI_6$	$Fm\bar{3}m$	0.38-0.43	0.64-25.3	[102]
Cs_2TeI_6	$Fm\bar{3}m$	0.40	1.51	[9]
Cs_2TeI_6	$Fm\bar{3}m$	0.22-0.97	1.40-4.40	[7]
Cs_2TiI_6	$Fm\bar{3}m$	1.58	0.79-1.58	[340]
Cs_2TiBr_6	$Fm\bar{3}m$	1.79	0.9-1.79	[340]
Cs_2PtI_6	$Fm\bar{3}m$	0.51	1.45	[9]
Cs_2PdI_6	$Fm\bar{3}m$	0.47	1.37	[9]
Cs_2PdBr_6	$Fm\bar{3}m$	0.53	0.85, 19.9	[14]
Rb_2PtI_6	$P4/mnc$	0.59-0.66	1.32-2.5	[9]
K_2PtI_6	$P4/mnc$	0.83-0.84	1.79-2.55	[9]
Rb_2SnI_6	$P4/mnc$	0.39	0.98	[8]
Rb_2SnI_6	$P4/mnc$	0.65	2.17-2.61	[9]
Rb_2SnI_6	$P2_1/n$	0.44	1.07	[8]
$(CH(NH_2)_2)_2PtI_6$	$P2_1/n$	0.61-0.87	1.74-1.75	[102]
$(CH_3NH_3)_2PtI_6$*nonVODP	$R\bar{3}m$	0.61-0.74	1.29-2.30	[102]
$(CH(NH_2)_3)_2PtI_6$*nonVODP	$P6_3/mmc$	2.05-32.2	3.19-6.08	[102]

7.4 Defect Chemistry

The chemistry of the *B*-site cation plays a non-trivial role in dictating the defect behavior of vacancy-ordered double perovskites. Cs_2SnI_6 exhibits native *n*-type conductivity, with free electrons generated by the formation of iodine vacancy defects that form as donor states that are nearly resonant with the conduction band.[7,11,103] The lack of trap-state defects classify Cs_2SnI_6

as a defect-tolerant semiconductor.[7] Other members of the A_2SnI_6 (A = Rb^+, Cs^+, $CH_3NH_3^+$, $CH(NH_2)_2^+$) series exhibit native n-type conductivity, presumably due to like defect chemistry arising from their similar electronic structures.[6,8] Yet, replacing Sn^{4+} with Te^{4+} significantly impacts the defect chemistry and charge transport behavior in the $Cs_2Sn_{1-x}Te_xI_6$ series. While iodine vacancies exhibit the lowest enthalpy of formation in both Cs_2SnI_6 and Cs_2TeI_6, replacing Sn with Te increases the enthalpy of formation by a factor of ~2-4, which accounts for the exponential decrease in carrier concentration observed experimentally.[7] Further, hybridization of the Te 5p and I 5p states pushes the conduction band minimum higher in energy, such that the iodine vacancy defect states reside as trap states deep within the band gap, which are proposed to localize charge carriers and inhibit charge transport.[7] The defect tolerance vs. intolerance was attributed to the differences in electronic structure brought about by the Sn–I/Te–I hybridization at the conduction band and the increased covalency of the Te–I bonds that results in higher enthalpies of defect formation in Cs_2TeI_6 relative to Cs_2SnI_6.

In contrast to defect-tolerant Cs_2SnI_6, Cs_2TiI_6 appears to be intolerant to the formation of defects. Defect calculations of Cs_2TiI_6 indicate that, under I-rich and Ti-lean conditions, iodine vacancies are the lowest enthalpy of formation defect. Under I-lean/Ti-rich conditions, Cs_i and Ti_i are the lowest enthalpy of formation defects. However, these defect states form deep within the band gap and may therefore act as a recombination center for photoexcited charge carriers. The apparent defect intolerance of Cs_2TiI_6 may be rationalized by considering the bonding vs. antibonding orbital contributions at the valence and conduction band edges. The valence band appears to be derived from non-bonding I 5p states, while the conduction band minimum is derived from Ti–I antibonding character. Semiconductors with antibonding states at the conduction band minimum have been previously identified as defect intolerant by Zakutayev *et al.*, as the defect electronic states form as deep trap states rather than as resonances within the band edges.[27] Thus, defects such as iodine vacancies in Cs_2TiI_6 are likely to form as deep trap states, rendering this material intolerant to defect formation.

7.5 Mixed Valence

Mixed-valence compounds in vacancy-ordered double perovskites occur through charge disproportionation of the formally tetravalent *B*-site cation into B^{III} and B^{V} species. In the Cs_2SbX_6 system (X = Cl^-, Br^-), the antimony ions at the *B*-site are disproportionated into Sb(III) and Sb(V) at the center of the octahedra,[346,347] as shown in the crystal structure model in Figure 7.6. Supercell ordering of $Sb^{III}X_6$ and $Sb^{V}X_6$ result in a tetragonal unit cell (space group $I4_1/amd$) rather than the cubic $Fm\bar{3}m$ K_2PtCl_6 structure.[348–350] In contrast to the O_h symmetry of the octahedra in K_2PtCl_6, the [SbX_6] octahedra in these compounds are slightly distorted to D_{2d} symmetry, resulting in two long apical Sb–*X* bonds and four short equatorial Sb–*X* bonds.[350] These compounds are unique from other vacancy-ordered double perovskite halides in that their optical absorption arises due to a strong charge transfer band from the populated 5*s* states of the Sb^{3+} centers into the empty 5*s* states of the adjacent Sb^{5+} center, likely mediated by the halide ligands.[347,351] In A_2SbCl_6, this gives rise to a deep blue-purple coloration, while a deep black coloration is observed in A_2SbBr_6.[347,348,351] These charge transfer processes are intimately linked with the vibrational properties of these mixed valence materials.[352–354] In a study by Clark and Swanson, low-temperature far infrared spectra of Cs_2SbCl_6 reveal sharp features corresponding to internal modes of the [$SbCl_6$] octahedra.[353] At higher temperatures, these features are dampened and broadened concomitantly with the onset of thermally-activated charge transfer, indicating that the lattice dynamics are strongly perturbed by the electron transfer processes in these materials.

The antimony centers in the mixed-valence vacancy-ordered double perovskites may be substituted with other trivalent or tetravalent metal cations to elicit changes in the optical absorption and carrier transport properties of these compounds. A common substitution is of Sn(IV) as in the series $A_2Sb_{1-x}Sn_xCl_6$ (A = Cs^+, NH_4^+), where tetravalent tin is randomly distributed over both Sb(III) and Sb(V) sites within the crystalline lattice.[355,356] Substitution of Sn(IV) is found to dramatically decrease the intensity of the charge-transfer band by UV-visible spectroscopy due to dilution of the Sb^{III}-Sb^{V} sublattice.[355] Higher tin concentrations are also

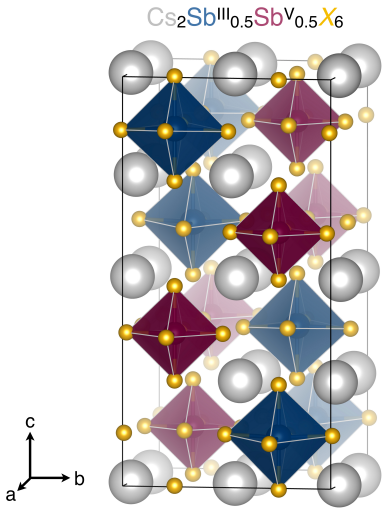

Figure 7.6: Crystal structure representation of $Cs_2Sb^{III}_{0.5}Sb^{V}_{0.5}X_6$ in the charge ordered tetragonal structure. The isolated and ordered $[Sb^{III}X_6]$ and $[Sb^{V}X_6]$ octahedra are differentiated as blue and red, respectively. Cesium ions are shown in grey and the X-site anions are shown in orange.

accompanied by a reduction in electrical conductivity due to discontinuity of the Sb sublattice through which mobile holes travel via a thermally-activated hopping process.[355,356] At Sb concentrations below 10%, the sign of the carriers changes from positive to negative, and the mechanism of charge transport is suggested to transition from electronic to ionic.[356] Trivalent metal substitution for Sb^{III} can drive both ordered and disordered configurations of the B^{III} and Sb^{V} sites.[350] For example, $Cs_2In^{III}_{0.5}Sb^{V}_{0.5}Cl_6$ exhibits disordered In^{III} and Sb^{V} centers consistent with space group $Fm\bar{3}m$, with no evidence of ordering or phase transitions down to $T = 4.2$ K. In contrast, $Cs_2Bi^{III}_{0.5}Sb^{V}_{0.5}Cl_6$ adopts the tetragonal $I4_1/amd$ structure characterized by charge-ordered Bi^{III} and Sb^{V} centers (Figure 7.6). The differences between ordered and disordered B-sites is attributed to the size of the B^{III} cation; when the $[B^{III}X_6]$ and $[Sb^{V}X_6]$ octahedra are close in size, no supercell ordering is observed, while deviations in the octahedral sizes are accompanied by the presence of supercell reflections in the neutron powder diffraction data. Similarly to the ordered $Cs_2Sb_{1-x}Sn_xCl_6$ series, the disordered $Cs_2Sb_{1-x}In_xCl_6$ series exhibits a composition-dependent charge-transfer band in the UV-visible spectroscopic data, suggesting that the arrangement of the B^{3+} and B^{5+} centers has a negligible effect on the optical properties of these materials.[355] However, ordered vs. disordered B-site cation configurations alter the

concentration-dependence of the electrical conductivity (σ). The conductivity is directly proportional to the antimony concentration in the disordered $Cs_2Sb_{1-x}In_xCl_6$ series ($\sigma \propto$ [Sb]), in contrast to the ordered $Cs_2Sb_{1-x}Sn_xCl_6$ series, in which the conductivity is proportional to the concentration squared ($\sigma \propto$ [Sb]^2).[356] The crystal-chemical origins of these differences merit further investigation.

7.6 Lattice Dynamics and Electron-Phonon Coupling

Octahedral rotations are a well-known origin of lattice dynamics in vacancy-ordered double perovskites, and are dictated by the size and bonding preferences of the *A*-site cation. In the A_2PtCl_6 series (A = K^+, Rb^+, and Cs^+), the frequency of the rotary phonon mode increases with increasing size of the alkali cation.[87] Softening of these dynamic rotations upon cooling are also responsible for symmetry lowering phase transitions characterized by frozen-in cooperative octahedral tilts.[85–93] In Rb_2SnI_6, lower symmetry structures are observed due to the smaller size of the Rb^+ ion, which is significantly underbonded in the previously reported cubic vacancy-ordered double perovskite structure;[8,277] the bond valence of the Rb^+ ion is significantly improved by cooperative octahedral tilting to the lower-symmetry tetragonal and monoclinic structural variants of the vacancy-ordered double perovskite structure. In the absence of cooperative octahedral tilting, anharmonic lattice dynamics may be observed when the coordination preferences of the *A*-site cation are dissatisfied by the cuboctahedral void. For example, both Cs_2SnI_6 and Cs_2TeI_6 crystallize in the cubic vacancy-ordered double perovskite structure, and neither compound undergoes phase transitions upon cooling, indicating that both compounds are dynamically stable.[7] However, the local coordination environment reveals signatures of anharmonicity across the solid solution $Cs_2Sn_{1-x}Te_xI_6$, attributed to octahedral rotations coupled with off-centering of the Cs^+ ion. The degree of anharmonicity is correlated with the bond valence of the Cs^+ ion, such that the anharmonicity is minimized when the Cs^+ is optimally coordinated by the surrounding octahedral framework.

Dynamic organic cations further contribute to the structural and dynamic behavior of vacancy-ordered double perovskites through hydrogen bonding interactions with the surrounding octahedra. In the A_2PtI_6 series with varied organic *A*-site cations, $(NH_4)_2PtI_6$ adopts the cubic vacancy-ordered double perovskite structure while $(CH_3NH_3)_2PtI_6$ yields a rhombohedral structural variant (space group $R\bar{3}m$). Incorporation of the larger $CH(NH_2)_2^+$ results in the monoclinic structural variant of the vacancy-ordered double perovskite structure (low-T K_2SnCl_6, space group $P2_1/n$), while $(C(NH_2)_3)_2PtI_6$ adopts the hexagonal, non-perovskite K_2MnF_6 structure. By ^{1}H NMR relaxation experiments, Evans *et al.* demonstrated that the smaller NH_4^+ and $CH_3NH_3^+$ cations undergo rapid molecular reorientations, but the larger $CH(NH_2)_2^+$ and $C(NH_2)_3^+$ cations were observed to reorient over much slower timescales. Examination of the DFT-relaxed structures of $(CH(NH_2)_2)_2PtI_6$ and $(C(NH_2)_3)_2PtI_6$ indicates orientations of the organic cations that yield N–H$\cdots$I distances that are characteristic of hydrogen bonds, suggesting an origin for the unique structural topologies and sluggish molecular dynamics in these compounds. Hydrogen bonding interactions may further drive anharmonic behavior through organic-inorganic coupling. In the hybrid vacancy-ordered double perovskites $(CH_3NH_3)_2SnI_6$ and $(CH(NH_2)_2)_2SnI_6$, coupling between the organic cations and the iodide sublattice yields soft, anharmonic lattice dynamics that manifest in the local coordination environment relative to Cs_2SnI_6, despite the observation that all three compounds crystallize in the same cubic vacancy-ordered double perovskite structure by X-ray diffraction.[6] It is further interesting to note the room-temperature structural differences between $(CH_3NH_3)_2SnI_6$ and $(CH(NH_2)_2)_2SnI_6$ and their Pt–I analogs. While the Sn-based compounds appear to adopt the cubic vacancy-ordered double perovskite structure at room temperature,[6] other structural topologies characterized by rotations and tilting of the isolated $[PtI_6]$ octahedra are observed in the Pt analogs.[102] As Sn^{4+} and Pt^{4+} exhibit similar ionic radii (r_{Sn} = 0.690 Å, r_{Pt} = 0.625 Å),[206] it may be necessary to consider the effect of Sn–I vs. Pt–I covalency and/or electronegativity and the subsequent influence upon interoctahedral I–I van der Waals interactions and N–H$\cdots$I hydrogen bonds in these compounds.

Lattice dynamics participate in the charge transport processes of perovskite halide semiconductors through electron-phonon coupling within the soft and deformable lattice. The formation of a polaron, in which an electron forms a localized deformation of the lattice, is a prevailing hypothesis to explain the long carrier excited state lifetimes yet only moderate carrier mobilities observed in perovskite halides such as methylammonium lead iodide.[25] In conventional perovskite halides, polarons form predominantly within the metal halide octahedral framework via *X*–*B*–*X* bending and *B*–*X* stretching modes, resulting in deformations and cooperative tilting of the [BX_6] octahedra.[56,58,59,357] It therefore follows that similar electron-phonon coupling processes occur in the vacancy-ordered double perovskites, and may even be enhanced by the presence of relatively decoupled octahedral units.[339,358]

As the lattice dynamics of vacancy-ordered double perovskites are intimately linked with the choice of *A*-site cation and its interaction with the surrounding octahedral framework, the electron-phonon coupling behavior in vacancy-ordered double perovskites may be predicted by the perovskite tolerance factor. As shown in Figure 7.7, the trend in experimental carrier mobilities across the A_2SnI_6 series is reproduced by computationally-derived carrier mobilities calculated within a polaron model, indicating that electron-phonon coupling processes dominate the charge transport behavior in vacancy-ordered double perovskites. These trends are also correlated with the perovskite tolerance factor. In Rb_2SnI_6, the smaller size of the Rb^+ ion yields a tolerance factor less than 1 and produces a structure characterized by cooperative octahedral tilting.[8] The lower symmetry structure further yields a larger number of non-degenerate low-frequency phonons that contribute to stronger electron-phonon coupling processes that account for experimental carrier mobilities that are ~50-fold lower than those of the cubic Cs_2SnI_6. On the other hand, introducing the larger organic $CH_3NH_3^+$ and $CH(NH_2)_2^+$ cations yields tolerance factors greater than 1 and reduced carrier mobilities relative to Cs_2SnI_6. In these compounds, the larger interoctahedral I–I distances produces softer lattices which result in stronger electron-phonon interactions and subsequently reduced carrier mobilities.[6] The highest carrier mobilities are observed for Cs_2SnI_6 with a tolerance factor of ~1, suggest-

ing that weaker electron-phonon coupling interactions are observed when the vacancy-ordered double perovskite lattice does not exhibit dynamic instabilities or anharmonicity. While polaron formation is expected to occur within the octahedral framework as in ABX_3 perovskite halides,[58,357] the choice of *A*-site cation strongly influences the charge transport characteristics of vacancy-ordered double perovskites through coupling to the neighboring octahedra.

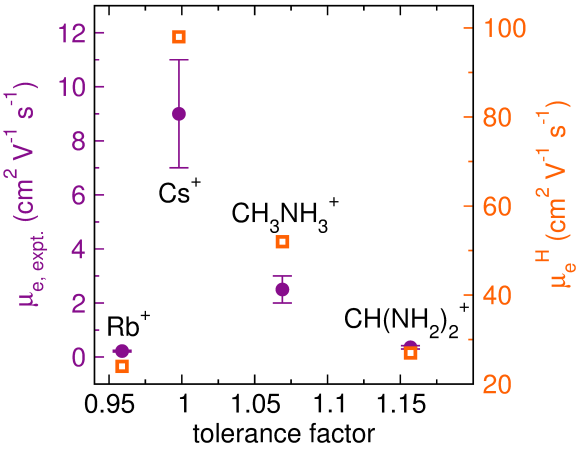

Figure 7.7: The experimental and calculated electron mobilities of the A_2SnI_6 vacancy-ordered double perovskites as a function of perovskite tolerance factor. The experimentally-determined electron mobilities are shown as filled purple circles on the left axis, while the calculated Hellwarth electron mobilities are denoted by open orange squares on the right axis. Figure reproduced with permission from Maughan, Ganose, Almaker, Scanlon, Neilson, *Chem. Mater.*, **2018**, *30*, 3909–3919.[8]

7.7 Concluding Remarks

Vacancy-ordered double perovskite semiconductors inhabit a rich compositional, structural, and dynamic phase space that may be accessed and tuned by compositional modification at all three sites to elicit desirable optical and electronic properties. Incorporating smaller *X*-site halogens is accompanied by a depression of the ionization potential and widening of the band gap due to halide *p* orbitals that dominate the valence band maximum. The close-packed lattice of large halides provides substantial orbital overlap between the neighboring isolated octahedra, yielding relatively low carrier effective masses and presumably higher carrier mobilities. Substitution of halogens with a smaller spatial distribution of the *p* orbitals results

in reduced band dispersions and larger carrier effective masses. Compositional modification at the *B*-site at the center of the octahedra offers the greatest degree of flexibility to elicit desired properties and chemistries in vacancy-ordered double perovskites due to the large variety of tetravalent ions that may be accommodated into the structure. The *B*-site cations and their interaction with the halide ligands in the octahedra dictate energy and dispersion of the conduction band, the direct vs. indirect nature of the band gap, and the defect chemistry in vacancy-ordered double perovskites. The formally tetravalent charge state of the *B*-site can also enable charge disproportionation and mixed valency, which gives rise to strong charge-transfer and unique vibronic coupling effects. The *A*-site cation does not directly participate in charge transport or optical absorption processes, but rather influences the surrounding octahedral framework through anharmonic lattice dynamics or cooperative octahedral tilting. Smaller *A*-site cations introduce cooperative octahedral tilting distortions that increase the magnitude of the band gap and carrier effective masses due to deviations in the close-packed halogen sublattice. Larger and more complex organic cations drive unique structural topologies and anharmonic lattice dynamics due to organic-inorganic coupling effects through hydrogen bonding. Changes to the dynamic landscape of vacancy-ordered double perovskites brought about by the choice of *A*-site cation further give rise to electron-phonon coupling interactions that strongly influence the charge transport behavior in these materials. Due to the large range of accessible chemistries available at all three crystallographic sites, the vacancy-ordered double perovskite structure provides an ideal framework to determine structure-dynamics-property relationships in complex semiconductors for transformative advances in sustainable energy technologies.

7.8 Outlook and Future Directions

The relatively nascent understanding of the optical and electronic behavior of vacancy-ordered double perovskites motivates further study of their properties. This section seeks to identify avenues of future study for vacancy-ordered double perovskite semiconductors, and,

where applicable, place these future studies in the broader context of the field of perovskite halide semiconductors.

In chapter two of this document, we identified the chemical bonding principles necessary to achieve defect tolerance in the vacancy-ordered double perovskite semiconductors $Cs_2Sn_{1-x}Te_xI_6$. Namely, the covalency of the Sn–I vs. Te–I bonding dictates the energy of the conduction band minimum and thus the position of the defect level within the band gap. Further, this covalency was proposed to contribute to the higher enthalpy of defect formation in Cs_2TeI_6 compared to Cs_2SnI_6.[7] The first avenue of proposed research involves expanding these design principles to other compositional derivatives of the vacancy-ordered double perovskite family. In particular, as the interaction of the *B*- and *X*-site is critical for the defect chemistry, a thorough understanding of how varying the *B*-site (*i.e.*, main-group metals vs. transition metals) affects the electronic structure and defect behavior is paramount. While there have been experimental and computational studies of the defect chemistry of several members of the vacancy-ordered double perovskite family, there have been very few studies devoted to controlling the type and concentration of dopants. Therefore, engineering native and extrinsic defects is an important step towards eliciting desirable semiconducting properties in vacancy-ordered double perovskite semiconductors for potential optoelectronic applications. Further, chemical control of the defect chemistry provides an approach to controlling and preventing material decomposition, which represents a significant challenge in the broader field of perovskite halide semiconductors.

Lattice dynamics have been strongly implicated in the charge transport properties of perovskite halide semiconductors through polaron formation. There have been numerous experimental studies aimed at understanding the mechanism of polaron formation and the subsequent influence upon charge separation and transport in ABX_3 perovskites.[25,51–58,357] The softer vacancy-ordered double perovskite lattice brought about by the isolated $[BX_6]$ octahedral framework presents a further opportunity to study electron-phonon coupling in perovskite halides. Experimental realization of the electron-phonon coupling processes in vacancy-

ordered double perovskites will provide insight into charge separation, carrier excited state lifetimes, and charge transport in these complex semiconducting materials. Further, the structurally-decoupled octahedra in the vacancy-ordered double perovskite lattice are strongly influenced by organic-inorganic coupling, as exemplified by the case of $(CH_3NH_3)_2SnI_6$ and $(CH(NH_2)_2)_2SnI_6$.[6] Thus, studies of electron-phonon coupling in hybrid vacancy-ordered double perovskites present an avenue to explore the influence of organic cation dynamics upon polaron formation, which represents an active area of research in the field of perovskite halide semiconductors.

Bibliography

[1] Steirer, K. X.; Schulz, P.; Teeter, G.; Stevanovic, V.; Yang, M.; Zhu, K.; Berry, J. J. Defect Tolerance in Methylammonium Lead Triiodide Perovskite. *ACS Energy Lett.* **2016**, *1*, 360–366.

[2] Rao, C.; Cheetham, A.; Thirumurugan, A. Hybrid inorganic–organic materials: a new family in condensed matter physics. *J. Phys. Condens. Matter* **2008**, *20*, 083202.

[3] Zhang, J.; Yu, C.; Wang, L.; Li, Y.; Ren, Y.; Shum, K. Energy barrier at the N719-dye/$CsSnI_3$ interface for photogenerated holes in dye-sensitized solar cells. *Sci. Rep.* **2014**, *4*, 6954–6959.

[4] Hao, F.; Stoumpos, C. C.; Cao, D. H.; Chang, R. P.; Kanatzidis, M. G. Lead-free solid-state organic-inorganic halide perovskite solar cells. *Nature Photon.* **2014**, *8*, 489–494.

[5] Qiu, J.; Qiu, Y.; Yan, K.; Zhong, M.; Mu, C.; Yan, H.; Yang, S. All-solid-state hybrid solar cells based on a new organometal halide perovskite sensitizer and one-dimensional TiO_2 nanowire arrays. *Nanoscale* **2013**, *5*, 3245–3248.

[6] Maughan, A. E.; Ganose, A. M.; Candia, A. M.; Granger, J. T.; Scanlon, D. O.; Neilson, J. R. Anharmonicity and Octahedral Tilting in Hybrid Vacancy-Ordered Double Perovskites. *Chem. Mater.* **2018**, *30*, 472–483.

[7] Maughan, A. E.; Ganose, A. M.; Bordelon, M. M.; Miller, E. M.; Scanlon, D. O.; Neilson, J. R. Defect tolerance to intolerance in the vacancy-ordered double perovskite semiconductors Cs_2SnI_6 and Cs_2TeI_6. *J. Am. Chem. Soc.* **2016**, *138*, 8453–8464.

[8] Maughan, A. E.; Ganose, A. M.; Almaker, M. A.; Scanlon, D. O.; Neilson, J. R. Tolerance Factor and Cooperative Tilting Effects in Vacancy-Ordered Double Perovskite Halides. *Chem. Mater.* **2018**, *30*, 3909–3919.

[9] Cai, Y.; Xie, W.; Ding, H.; Chen, Y.; Thirumal, K.; Wong, L. H.; Mathews, N.; Mhaisalkar, S. G.; Sherburne, M.; Asta, M. Computational Study of Halide Perovskite-Derived A_2BX_6 Inorganic Compounds: Chemical Trends in Electronic Structure and Structural Stability. *Chem. Mater.* **2017**, *29*, 7740–7749.

[10] Lee, B.; Krenselewski, A.; Baik, S. I.; Seidman, D. N.; Chang, R. P. Solution processing of air-stable molecular semiconducting iodosalts, $Cs_2SnI_{6-x}Br_x$, for potential solar cell applications. *Sustainable Energy Fuels* **2017**, *1*, 710–724.

[11] Lee, B.; Stoumpos, C. C.; Zhou, N.; Hao, F.; Malliakas, C.; Yeh, C.-Y.; Marks, T. J.; Kanatzidis, M. G.; Chang, R. P. Air-stable molecular semiconducting iodosalts for solar cell applications: Cs_2SnI_6 as a hole conductor. *J. Am. Chem. Soc.* **2014**, *136*, 15379–15385.

[12] Saparov, B.; Sun, J.-P.; Meng, W.; Xiao, Z.; Duan, H.-S.; Gunawan, O.; Shin, D.; Hill, I. G.; Yan, Y.; Mitzi, D. B. Thin-film deposition and characterization of a Sn-deficient perovskite derivative Cs_2SnI_6. *Chem. Mater.* **2016**, *28*, 2315–2322.

[13] Funabiki, F.; Toda, Y.; Hosono, H. Optical and Electrical Properties of Perovskite Variant $(CH_3NH_3)_2SnI_6$. *J. Phys. Chem. C* **2018**, *122*, 10749–10754.

[14] Sakai, N.; Haghighirad, A. A.; Filip, M. R.; Nayak, P. K.; Nayak, S.; Ramadan, A.; Wang, Z.; Giustino, F.; Snaith, H. J. Solution-processed cesium hexabromopalladate (IV), Cs_2PdBr_6, for optoelectronic applications. *J. Am. Chem. Soc.* **2017**, *139*, 6030–6033.

[15] Ganose, A. M. Atomic-scale insights into emergent photovoltaic absorbers. Ph.D. thesis, University College London, 2018.

[16] Green, M. A.; Hishikawa, Y.; Dunlop, E. D.; Levi, D. H.; Hohl-Ebinger, J.; Ho-Baillie, A. W. Solar cell efficiency tables (version 50). *Prog. Photovoltaics Res. Appl.* **2017**, *25*, 668–676.

[17] Bludau, W.; Onton, A.; Heinke, W. Temperature dependence of the band gap of silicon. *J. Appl. Phys.* **1974**, *45*, 1846–1848.

[18] Shockley, W.; Queisser, H. J. Detailed balance limit of efficiency of *p-n* junction solar cells. *J. Appl. Phys.* **1961**, *32*, 510–519.

[19] Yang, W. S.; Park, B.-W.; Jung, E. H.; Jeon, N. J.; Kim, Y. C.; Lee, D. U.; Shin, S. S.; Seo, J.; Kim, E. K.; Noh, J. H.; Seok, S. I. Iodide management in formamidinium-lead-halide–based perovskite layers for efficient solar cells. *Science* **2017**, *356*, 1376–1379.

[20] Wehrenfennig, C.; Eperon, G. E.; Johnston, M. B.; Snaith, H. J.; Herz, L. M. High charge carrier mobilities and lifetimes in organolead trihalide perovskites. *Adv. Mater.* **2014**, *26*, 1584–1589.

[21] Shi, D.; Adinolfi, V.; Comin, R.; Yuan, M.; Alarousu, A., Erkki andd Rothen Buin; Chen, Y.; Hoogland, A., Sjoerd anberger; Katsiev, K.; Losovy, Y.; Zhang, X.; Dowben, P. A.; Mohammed, O. F.; Sargent, E. H.; Bakr, O. M. Low trap-state density and long carrier diffusion in organolead trihalide perovskite single crystals. *Science* **2015**, *347*, 519–522.

[22] Chen, Y.; Yi, H.; Wu, X.; Haroldson, R.; Gartstein, Y.; Rodionov, Y.; Tikhonov, K.; Zakhidov, A.; Zhu, X.-Y.; Podzorov, V. Extended carrier lifetimes and diffusion in hybrid perovskites revealed by Hall effect and photoconductivity measurements. *Nat. Commun.* **2016**, *7*, 12253.

[23] Stranks, S. D.; Eperon, G. E.; Grancini, G.; Menelaou, C.; Alcocer, M. J.; Leijtens, T.; Herz, L. M.; Petrozza, A.; Snaith, H. J. Electron-hole diffusion lengths exceeding 1 micrometer in an organometal trihalide perovskite absorber. *Science* **2013**, *342*, 341–344.

[24] Kim, J.; Lee, S.-H.; Lee, J. H.; Hong, K.-H. The role of intrinsic defects in methylammonium lead iodide perovskite. *J. Phys. Chem. Lett.* **2014**, *5*, 1312–1317.

[25] Zhu, X.-Y.; Podzorov, V. Charge carriers in hybrid organic–inorganic lead halide perovskites might be protected as large polarons. *J. Phys. Chem. Lett.* **2015**, *6*, 4758–4761.

[26] Queisser, H. J.; Haller, E. E. Defects in semiconductors: some fatal, some vital. *Science* **1998**, *281*, 945–950.

[27] Zakutayev, A.; Caskey, C. M.; Fioretti, A. N.; Ginley, D. S.; Vidal, J.; Stevanovic, V.; Tea, E.; Lany, S. Defect tolerant semiconductors for solar energy conversion. *J. Phys. Chem. Lett.* **2014**, *5*, 1117–1125.

[28] Newman, R. Defects in silicon. *Rep. Prog. Phys.* **1982**, *45*, 1163.

[29] Yin, W.-J.; Shi, T.; Yan, Y. Unusual defect physics in $CH_3NH_3PbI_3$ perovskite solar cell absorber. *Appl. Phys. Lett.* **2014**, *104*, 063903.

[30] Yin, W.-J.; Shi, T.; Yan, Y. Unique properties of halide perovskites as possible origins of the superior solar cell performance. *Adv. Mater.* **2014**, *26*, 4653–4658.

[31] Umebayashi, T.; Asai, K.; Kondo, T.; Nakao, A. Electronic structures of lead iodide based low-dimensional crystals. *Phys. Rev. B* **2003**, *67*, 155405–155411.

[32] Kittel, C.; McEuen, P. *Introduction to solid state physics*; Wiley New York, 1976; Vol. 8.

[33] Stoneham, A.; Gavartin, J.; Shluger, A.; Kimmel, A.; Ramo, D. M.; Rønnow, H.; Aeppli, G.; Renner, C. Trapping, self-trapping and the polaron family. *J. Phys. Condens. Matter* **2007**, *19*, 255208.

[34] Fröhlich, H. Interaction of electrons with lattice vibrations. *Proc. R. Soc. Lond. A* **1952**, *215*, 291–298.

[35] Holstein, T. Studies of polaron motion: Part II. The "small" polaron. *Ann. Phys.* **1959**, *8*, 343–389.

[36] Shluger, A.; Stoneham, A. Small polarons in real crystals: concepts and problems. *J. Phys. Condens. Matter* **1993**, *5*, 3049.

[37] Emin, D. Optical properties of large and small polarons and bipolarons. *Phys. Rev. B* **1993**, *48*, 13691.

[38] Hellwarth, R. W.; Biaggio, I. Mobility of an electron in a multimode polar lattice. *Phys. Rev. B* **1999**, *60*, 299–307.

[39] Sun, S.; Fang, Y.; Kieslich, G.; White, T. J.; Cheetham, A. K. Mechanical properties of organic–inorganic halide perovskites, $CH_3NH_3PbX_3$ (X = I, Br and Cl), by nanoindentation. *J. Mater. Chem. A* **2015**, *3*, 18450–18455.

[40] Rakita, Y.; Cohen, S. R.; Kedem, N. K.; Hodes, G.; Cahen, D. Mechanical properties of $APbX_3$ (A= Cs or CH_3NH_3; X = I or Br) perovskite single crystals. *MRS Commun.* **2015**, *5*, 623–629.

[41] Elbaz, G. A.; Ong, W.-L.; Doud, E. A.; Kim, P.; Paley, D. W.; Roy, X.; Malen, J. A. Phonon speed, not scattering, differentiates thermal transport in lead halide perovskites. *Nano Lett.* **2017**, *17*, 5734–5739.

[42] Pisoni, A.; Jacimovic, J.; Barisic, O. S.; Spina, M.; Gaál, R.; Forró, L.; Horváth, E. Ultra-low thermal conductivity in organic–inorganic hybrid perovskite $CH_3NH_3PbI_3$. *J. Phys. Chem. Lett.* **2014**, *5*, 2488–2492.

[43] Kovalsky, A.; Wang, L.; Marek, G. T.; Burda, C.; Dyck, J. S. Thermal conductivity of $CH_3NH_3PbI_3$ and $CsPbI_3$: Measuring the effect of the methylammonium ion on phonon scattering. *J. Phys. Chem. C* **2017**, *121*, 3228–3233.

[44] Megaw, H. D. *Crystal Structures: A Working Approach*; W. B. Saunders Company, Philadelphia, London, Toronto, 1973.

[45] Yang, R. X.; Skelton, J. M.; da Silva, L.; Frost, J. M.; Walsh, A. Spontaneous Octahedral Tilting in the Cubic Inorganic Caesium Halide Perovskites $CsSnX_3$ and $CsPbX_3$ (X = F, Cl, Br, I). *J. Phys. Chem. Lett.* **2017**, *8*, 4720–4726.

[46] Bechtel, J. S.; Van der Ven, A. Octahedral tilting instabilities in inorganic halide perovskites. *Phys. Rev. Mater.* **2018**, *2*, 025401.

[47] Müller, K.; Berlinger, W.; Waldner, F. Characteristic structural phase transition in perovskite-type compounds. *Phys. Rev. Lett.* **1968**, *21*, 814.

[48] Goldschmidt, V. M. Die gesetze der krystallochemie. *Naturwissenschaften* **1926**, *14*, 477–485.

[49] Goudochnikov, P.; Bell, A. J. Correlations between transition temperature, tolerance factor and cohesive energy in 2+: 4+ perovskites. *J. Phys. Condens. Matter* **2007**, *19*, 176201.

[50] Weber, M.; Kreisel, J.; Thomas, P.; Newton, M.; Sardar, K.; Walton, R. Phonon Raman scattering of $R\mathrm{CrO_3}$ perovskites (R = Y, La, Pr, Sm, Gd, Dy, Ho, Yb, Lu). *Phys. Rev. B* **2012**, *85*, 054303.

[51] Zhu, H.; Miyata, K.; Fu, Y.; Wang, J.; Joshi, P. P.; Niesner, D.; Williams, K. W.; Jin, S.; Zhu, X.-Y. Screening in crystalline liquids protects energetic carriers in hybrid perovskites. *Science* **2016**, *353*, 1409–1413.

[52] Neukirch, A. J.; Nie, W.; Blancon, J.-C.; Appavoo, K.; Tsai, H.; Sfeir, M. Y.; Katan, C.; Pedesseau, L.; Even, J.; Crochet, J. J.; Gupta, G.; Mohite, A. D.; Tretiak, S. Polaron stabilization by cooperative lattice distortion and cation rotations in hybrid perovskite materials. *Nano Lett.* **2016**, *16*, 3809–3816.

[53] Zhu, H.; Trinh, M. T.; Wang, J.; Fu, Y.; Joshi, P. P.; Miyata, K.; Jin, S.; Zhu, X.-Y. Organic cations might not be essential to the remarkable properties of band edge carriers in lead halide perovskites. *Adv. Mater.* **2017**, *29*, 1–6.

[54] Wright, A. D.; Verdi, C.; Milot, R. L.; Eperon, G. E.; Pérez-Osorio, M. A.; Snaith, H. J.; Giustino, F.; Johnston, M. B.; Herz, L. M. Electron–phonon coupling in hybrid lead halide perovskites. *Nat. Commun.* **2016**, *7*, 11755.

[55] Zhao, D.; Skelton, J. M.; Hu, H.; La-o Vorakiat, C.; Zhu, J.-X.; Marcus, R. A.; Michel-Beyerle, M.-E.; Lam, Y. M.; Walsh, A.; Chia, E. E. Low-frequency optical phonon modes

and carrier mobility in the halide perovskite $CH_3NH_3PbBr_3$ using terahertz time-domain spectroscopy. *Appl. Phys. Lett.* **2017**, *111*, 201903.

[56] Guzelturk, B.; Belisle, R. A.; Smith, M. D.; Bruening, K.; Prasanna, R.; Yuan, Y.; Gopalan, V.; Tassone, C. J.; Karunadasa, H. I.; McGehee, M. D.; Lindenberg, A. M. Terahertz Emission from Hybrid Perovskites Driven by Ultrafast Charge Separation and Strong Electron–Phonon Coupling. *Adv. Mater.* **2018**, *30*, 1704737.

[57] Bretschneider, S. A.; Ivanov, I.; Wang, H. I.; Miyata, K.; Zhu, X.; Bonn, M. Quantifying Polaron Formation and Charge Carrier Cooling in Lead-Iodide Perovskites. *Adv. Mater.* **2018**, 1707312.

[58] Miyata, K.; Meggiolaro, D.; Trinh, M. T.; Joshi, P. P.; Mosconi, E.; Jones, S. C.; De Angelis, F.; Zhu, X.-Y. Large polarons in lead halide perovskites. *Sci. Adv.* **2017**, *3*, e1701217.

[59] Wu, X. et al. Light-induced picosecond rotational disordering of the inorganic sublattice in hybrid perovskites. *Sci. Adv.* **2017**, *3*, e1602388.

[60] Brenner, T. M.; Egger, D. A.; Rappe, A. M.; Kronik, L.; Hodes, G.; Cahen, D. Are Mobilities in Hybrid Organic–Inorganic Halide Perovskites Actually "High"? *J. Phys. Chem. Lett.* **2015**, *6*, 4754–4757.

[61] Sendner, M.; Nayak, P. K.; Egger, D. A.; Beck, S.; Müller, C.; Epding, B.; Kowalsky, W.; Kronik, L.; Snaith, H. J.; Pucci, A.; Lovrincic, R. Optical phonons in methylammonium lead halide perovskites and implications for charge transport. *Mater. Horiz.* **2016**, *3*, 613–620.

[62] Poglitsch, A.; Weber, D. Dynamic disorder in methylammoniumtrihalogenoplumbates (II) observed by millimeter-wave spectroscopy. *J. Chem. Phys.* **1987**, *87*, 6373–6378.

[63] Chen, T.; Foley, B. J.; Ipek, B.; Tyagi, M.; Copley, J. R.; Brown, C. M.; Choi, J. J.; Lee, S.-H. Rotational dynamics of organic cations in the $CH_3NH_3PbI_3$ perovskite. *Phys. Chem. Chem. Phys.* **2015**, *17*, 31278–31286.

[64] Bakulin, A. A.; Selig, O.; Bakker, H. J.; Rezus, Y. L.; Müller, C.; Glaser, T.; Lovrincic, R.; Sun, Z.; Chen, Z.; Walsh, A.; Frost, J. M.; Jansen, T. L. Real-time observation of organic cation reorientation in methylammonium lead iodide perovskites. *J. Phys. Chem. Lett* **2015**, *6*, 3663–3669.

[65] Drużbicki, K.; Pinna, R. S.; Rudić, S.; Jura, M.; Gorini, G.; Fernandez-Alonso, F. Unexpected Cation Dynamics in the Low-Temperature Phase of Methylammonium Lead Iodide: The Need for Improved Models. *J. Phys. Chem. Lett.* **2016**, *7*, 4701–4709.

[66] Kubicki, D. J.; Prochowicz, D.; Hofstetter, A.; Péchy, P.; Zakeeruddin, S. M.; Grätzel, M.; Emsley, L. Cation Dynamics in Mixed-Cation $(MA)_x(FA)_{1-x}PbI_3$ Hybrid Perovskites from Solid-State NMR. *J. Am. Chem. Soc.* **2017**, *139*, 10055–10061.

[67] Beecher, A. N.; Semonin, O. E.; Skelton, J. M.; Frost, J. M.; Terban, M. W.; Zhai, H.; Alatas, A.; Owen, J. S.; Walsh, A.; Billinge, S. J. Direct observation of dynamic symmetry breaking above room temperature in methylammonium lead iodide perovskite. *ACS Energy Lett.* **2016**, *1*, 880–887.

[68] Møller, C. K. Crystal Structure and Photoconductivity of Caesium Plumbohalides. *Nature* **1958**, *182*, 1436–1436.

[69] Onoda-Yamamuro, N.; Matsuo, T.; Suga, H. Calorimetric and IR spectroscopic studies of phase transitions in methylammonium trihalogenoplumbates (II). *J. Phys. Chem. Solids* **1990**, *51*, 1383–1395.

[70] Swainson, I. P.; Stock, C.; Parker, S. F.; Van Eijck, L.; Russina, M.; Taylor, J. W. From soft harmonic phonons to fast relaxational dynamics in $CH_3NH_3PbBr_3$. *Phys. Rev. B* **2015**, *92*, 100303.

[71] Fabini, D. H.; Hogan, T.; Evans, H. A.; Stoumpos, C. C.; Kanatzidis, M. G.; Seshadri, R. Dielectric and thermodynamic signatures of low-temperature glassy dynamics in the hybrid perovskites $CH_3NH_3PbI_3$ and $HC(NH_2)_2PbI_3$. *J. Phys. Chem. Lett.* **2016**, *7*, 376–381.

[72] Mozur, E. M.; Maughan, A. E.; Cheng, Y.; Huq, A.; Jalarvo, N.; Daemen, L. L.; Neilson, J. R. Orientational Glass Formation in Substituted Hybrid Perovskites. *Chem. Mater.* **2017**, *29*, 10168–10177.

[73] Harwell, J. R.; Payne, J. L.; Sajjad, M. T.; Heutz, F. J.; Dawson, D. M.; Whitfield, P. S.; Irvine, J. T.; Samuel, I. D.; Carpenter, M. A. Role of lattice distortion and A site cation in the phase transitions of methylammonium lead halide perovskites. *Phys. Rev. Mater.* **2018**, *2*, 065404.

[74] Lee, J.-H.; Bristowe, N. C.; Bristowe, P. D.; Cheetham, A. K. Role of hydrogen-bonding and its interplay with octahedral tilting in $CH_3NH_3PbI_3$. *Chem. Commun.* **2015**, *51*, 6434–6437.

[75] Ren, Y.; Oswald, I. W.; Wang, X.; McCandless, G. T.; Chan, J. Y. Orientation of organic cations in hybrid inorganic–organic perovskite $CH_3NH_3PbI_3$ from subatomic resolution single crystal neutron diffraction structural studies. *Cryst. Growth Des.* **2016**, *16*, 2945–2951.

[76] Yin, T.; Fang, Y.; Fan, X.; Zhang, B.; Kuo, J.-L.; White, T. J.; Chow, G. M.; Yan, J.; Shen, Z. X. Hydrogen-Bonding Evolution during the Polymorphic Transformations in $CH_3NH_3PbBr_3$: Experiment and Theory. *Chem. Mater.* **2017**, *29*, 5974–5981.

[77] Bonn, M.; Miyata, K.; Hendry, E.; Zhu, X.-Y. Role of Dielectric Drag in Polaron Mobility in Lead Halide Perovskites. *ACS Energy Lett.* **2017**, *2*, 2555–2562.

[78] Woodward, P. M. Octahedral tilting in perovskites. I. Geometrical considerations. *Acta Crystallogr. B* **1997**, *53*, 32–43.

[79] Howard, C. J.; Kennedy, B. J.; Woodward, P. M. Ordered double perovskites – a group-theoretical analysis. *Acta Crystallogr. B* **2003**, *59*, 463–471.

[80] Brown, I. D. The crystal structure of K_2TeBr_6. *Can. J. Chem.* **1964**, *42*, 2758–2767.

[81] Young, J.; Rondinelli, J. M. Octahedral Rotation Preferences in Perovskite Iodides and Bromides. *J. Phys. Chem. Lett.* **2016**, *7*, 918–922.

[82] Sidey, V.; Zubaka, O.; Stercho, I.; Peresh, E. Y. X-ray Rietveld structure refinement and bond-valence analysis of Cs_2TeI_6. *Chem. Met. Alloys* **2010**, 108–114.

[83] Abriel, W. Crystal structure and phase transition of Rb_2TeI_6. *Mat. Res. Bull.* **1982**, *17*, 1341–1346.

[84] Syoyama, S.; Osaki, K.; Kusanagi, S. X-ray Study of the Crystal Structure of K_2TeI_6 and the Symmetry of the Compounds of This Series. *Inorg. Nucl. Chem. Letters* **1972**, *8*, 181–184.

[85] O'Leary, G.; Wheeler, R. Phase transitions and soft librational modes in cubic crystals. *Phys. Rev. B* **1970**, *1*, 4409.

[86] Cooke, D. F.; Armstrong, R. L. Investigation of the Rotary Lattice Mode in R_2PtCl_6 Compounds. I. From Measurements of the ^{35}Cl Nuclear Quadrupole Resonance Frequency. *Can. J. Phys.* **1971**, *49*, 2381–2388.

[87] Armstrong, R. L.; Jeffrey, K. R. Quadrupolar Nuclear Spin–Lattice Relaxation in R_2MX_6 Compounds. *Can. J. Phys.* **1971**, *49*, 49–53.

[88] Armstrong, R. L.; Cooke, D. F. Investigation of the Rotary Lattice Mode in R_2PtCl_6 Compounds. II. From a Study of the ^{35}Cl Nuclear Quadrupolar Spin–Lattice Relaxation. *Can. J. Phys.* **1971**, *49*, 2389–2395.

[89] van Driel, H. M.; Armstrong, R. L.; McEnnan, M. M. Soft-mode behavior near the 111-K displacive phase transition in K_2ReCl_6. *Phys. Rev. B* **1975**, *12*, 488.

[90] Lynn, J.; Patterson, H.; Shirane, G.; Wheeler, R. Soft rotary mode and structural phase transitions in K_2ReCl_6. *Solid State Commun.* **1978**, *27*, 859–862.

[91] McElroy, R. G.; Armstrong, R. L. Cubic to tetragonal phase transitions in $(NH_4)_2PtBr_6$ and Rb_2PtI_6. *Phys. Rev. B* **1978**, *18*, 1352.

[92] Patterson, H.; Lynn, J. Lattice-dynamics study of Cs_2SiF_6 with application to the vibronic optical spectra of $MnF_6{}^{-2}$ in Cs_2SiF_6. *Phys. Rev. B* **1979**, *19*, 1213.

[93] Waschk, V.; Pelzl, J.; Höck, K.-H.; Eckold, G. Inelastic neutron scattering from transverse acoustic modes in K_2SnCl_6. *Solid State Commun.* **1984**, *52*, 829–831.

[94] Armstrong, R. L. Structural properties and lattice dynamics of 5d transition metal antifluorite crystals. *Phys. Rep.* **1980**, *57*, 343–396.

[95] Blinc, R.; Lahajnar, G. Magnetic Resonance Study of Molecular Motion in Cubic $(NH_4)_2SiF_6$. *J. Chem. Phys.* **1967**, *47*, 4146–4152.

[96] Strange, J.-H.; Terenzi, M. Study of ionic motion in salts of the type $(NH_4)_2MX_6$ by NMR relaxation. *J. Phys. Chem. Solids* **1972**, *33*, 923–933.

[97] Kume, Y.; Muraoka, H.; Matsuo, T.; Suga, H. Low-temperature heat capacities of ammonium hexachloroselenate and of its deuterated analogue. *J. Chem. Thermodyn.* **1994**, *26*, 211–222.

[98] Kume, Y.; Ikeda, R.; Nakamura, D. Phase transitions in rhombohedral $(CH_3NH_3)_2MCl_6$ crystals as revealed by the NQR of chlorine. *J. Magn. Reson.* **1975**, *20*, 276–278.

[99] Ikeda, R.; Kume, Y.; Nakamura, D.; Furukawa, Y.; Kiriyama, H. Motion of methylammonium ions in methylammonium hexachloroplatinate (IV) and hexachlorostannate (IV) as studied by proton magnetic resonance. *J. Magn. Reson.* **1976**, *24*, 9–20.

[100] Matsuo, T.; Ueda, M.; Suga, H. Calorimetric and spectroscopic studies of the critical phase transition in $(CH_3NH_3)_2[SnCl_6]$. *Chem. Phys. Lett.* **1981**, *82*, 577–580.

[101] Kume, Y.; Matsuo, T.; Suga, H. Calorimetric, spectroscopic and dielectric studies of a phase transition in methylammonium hexachloroplatinate. *Thermochim. Acta* **1991**, *183*, 245–268.

[102] Evans, H. A.; Fabini, D. H.; Andrews, J. L.; Koerner, M.; Preefer, M. B.; Wu, G.; Wudl, F.; Cheetham, A. K.; Seshadri, R. Hydrogen Bonding Controls the Structural Evolution in Perovskite-Related Hybrid Platinum (IV) Iodides. *Inorg. Chem.* **2018**,

[103] Xiao, Z.; Zhou, Y.; Hosono, H.; Kamiya, T. Intrinsic Defects in a Photovoltaic Perovskite Variant Cs_2SnI_6. *Phys. Chem. Chem. Phys.* **2015**, *17*, 18900–18903.

[104] Chung, I.; Song, J.-H.; Im, J.; Androulakis, J.; Malliakas, C. D.; Li, H.; Freeman, A. J.; Kenney, J. T.; Kanatzidis, M. G. $CsSnI_3$: Semiconductor or Metal? High Electrical Conductivity and Strong Near-Infrared Photoluminescence from a Single Material. High Hole Mobility and Phase-Transitions. *J. Am. Chem. Soc.* **2012**, *134*, 8579–8587.

[105] Xiao, Z.; Hosono, H.; Kamiya, T. Origin of Carrier Generation in Photovoltaic Perovskite Variant Cs_2SnI_6. *Bull. Chem. Soc. Jpn.* **2015**, *88*, 1250–1255.

[106] Mitzi, D.; Feild, C.; Harrison, W.; Guloy, A. Conducting Tin Halides with a Layered Organic-Based Perovskite Structure. *Nature* **1994**, *369*, 467–469.

[107] Stoumpos, C. C.; Cao, D. H.; Clark, D. J.; Young, J.; Rondinelli, J. M.; Jang, J. I.; Hupp, J. T.; Kanatzidis, M. G. Ruddlesden–Popper hybrid lead iodide perovskite 2D homologous semiconductors. *Chem. Mater.* **2016**, *28*, 2852–2867.

[108] Savory, C. N.; Palgrave, R. G.; Bronstein, H.; Scanlon, D. O. Spatial Electron-hole Separation in a One Dimensional Hybrid Organic–Inorganic Lead Iodide. *Sci. Rep.* **2016**, *6*, 20626.

[109] Lin, H.; Zhou, C.; Tian, Y.; Siegrist, T.; Ma, B. Low-dimensional organometal halide perovskites. *ACS Energy Lett.* **2017**, *3*, 54–62.

[110] Xu, Z.; Mitzi, D. B. SnI_4^{2-}-Based Hybrid Perovskites Templated by Multiple Organic Cations: Combining Organic Functionalities through Noncovalent Interactions. *Chem. Mater.* **2003**, *15*, 3632–3637.

[111] Mitzi, D. B. Templating and structural engineering in organic–inorganic perovskites. *Dalton Trans.* **2001**, *1*, 1–12.

[112] Mitzi, D. B.; Brock, P. Structure and optical properties of several organic-inorganic hybrids containing corner-sharing chains of bismuth iodide octahedra. *Inorg. Chem.* **2001**, *40*, 2096–2104.

[113] Wang, G.-E.; Jiang, X.-M.; Zhang, M.-J.; Chen, H.-F.; Liu, B.-W.; Wang, M.-S.; Guo, G.-C. Crystal structures and optical properties of iodoplumbates hybrids templated by in situ synthesized 1, 4-diazabicyclo [2.2.2] octane derivatives. *CrystEngComm* **2013**, *15*, 10399–10404.

[114] Stoumpos, C. C.; Malliakas, C. D.; Kanatzidis, M. G. Semiconducting Tin and Lead Iodide Perovskites with Organic Cations: Phase Transitions, High Mobilities, and Near-Infrared Photoluminescent Properties. *Inorg. Chem.* **2013**, *52*, 9019–9038.

[115] Jodlowski, A. D.; Roldán-Carmona, C.; Grancini, G.; Salado, M.; Ralaiarisoa, M.; Ahmad, S.; Koch, N.; Camacho, L.; De Miguel, G.; Nazeeruddin, M. K. Large guanidinium cation mixed with methylammonium in lead iodide perovskites for 19% efficient solar cells. *Nat. Energy* **2017**, *2*, 972.

[116] Billing, D. G.; Lemmerer, A. Inorganic-organic hybrid materials incorporating primary cyclic ammonium cations: The lead iodide series. *CrystEngComm* **2007**, *9*, 236–244.

[117] Eckhardt, K.; Bon, V.; Getzschmann, J.; Grothe, J.; Wisser, F. M.; Kaskel, S. Crystallographic insights into $(CH_3NH_3)_3(Bi_2I_9)$: a new lead-free hybrid organic–inorganic material as a potential absorber for photovoltaics. *Chem. Commun.* **2016**, *52*, 3058–3060.

[118] Xu, Z.; Mitzi, D. B.; Dimitrakopoulos, C. D.; Maxcy, K. R. Semiconducting perovskites $(2\text{-}C_6H_4C_2H_4NH_3)_2SnI_4$ (X = F, Cl, Br): steric interaction between the organic and inorganic layers. *Inorg. Chem.* **2003**, *42*, 2031–2039.

[119] Venkataraman, N.; Bhagyalakshmi, S.; Vasudevan, S.; Seshadri, R. Conformation and orientation of alkyl chains in the layered organic–inorganic hybrids: $(C_nH_{2n+1}NH_3)_2PbI_4$ (n = 12, 16, 18). *Phys. Chem. Chem. Phys.* **2002**, *4*, 4533–4538.

[120] Braun, M.; Tuffentsammer, W.; Wachtel, H.; Wolf, H. Pyrene as emitting chromophore in organic–inorganic lead halide-based layered perovskites with different halides. *Chem. Phys. Lett.* **1999**, *307*, 373–378.

[121] Braun, M.; Tuffentsammer, W.; Wachtel, H.; Wolf, H. Tailoring of energy levels in lead chloride based layered perovskites and energy transfer between the organic and inorganic planes. *Chem. Phys. Lett.* **1999**, *303*, 157–164.

[122] Kondo, K.; Matsubayashi, G.-e.; Tanaka, T.; Yoshioka, H.; Nakatsu, K. Preparation and properties of tetrathiafulvalene (ttf) and tetramethyltetraselenafulvalene salts of tin (IV) halide anions and X-ray crystal structure of $[ttf]_3[SnCl_6]$. *Dalton Trans.* **1984**, 379–384.

[123] Evans, H. A.; Lehner, A. J.; Labram, J. G.; Fabini, D. H.; Barreda, O.; Smock, S. R.; Wu, G.; Chabinyc, M. L.; Seshadri, R.; Wudl, F. $(TTF)Pb_2I_5$: A Radical Cation-Stabilized Hybrid Lead Iodide with Synergistic Optoelectronic Signatures. *Chem. Mater.* **2016**, *28*, 3607–3611.

[124] Evans, H. A.; Labram, J. G.; Smock, S. R.; Wu, G.; Chabinyc, M. L.; Seshadri, R.; Wudl, F. Mono-and Mixed-Valence Tetrathiafulvalene Semiconductors $(TTF)BiI_4$ and $(TTF)_4BiI_6$ with 1D and 0D Bismuth-Iodide Networks. *Inorg. Chem.* **2016**, *56*, 395–401.

[125] Kagan, C.; Mitzi, D.; Dimitrakopoulos, C. Organic-inorganic hybrid materials as semiconducting channels in thin-film field-effect transistors. *Science* **1999**, *286*, 945–947.

[126] Labram, J. G.; Fabini, D. H.; Perry, E. E.; Lehner, A. J.; Wang, H.; Glaudell, A. M.; Wu, G.; Evans, H.; Buck, D.; Cotta, R.; Echegoyen, L.; Wudl, F.; Seshadri, R.; Chabinyc, M. L. Temperature-dependent polarization in field-effect transport and photovoltaic measurements of methylammonium lead iodide. *J. Phys. Chem. Lett.* **2015**, *6*, 3565–3571.

[127] Dohner, E. R.; Jaffe, A.; Bradshaw, L. R.; Karunadasa, H. I. Intrinsic White-Light Emission from Layered Hybrid Perovskites. *J. Am. Chem. Soc.* **2014**, *136*, 13154–13157.

[128] Protesescu, L.; Yakunin, S.; Bodnarchuk, M. I.; Krieg, F.; Caputo, R.; Hendon, C. H.; Yang, R. X.; Walsh, A.; Kovalenko, M. V. Nanocrystals of cesium lead halide perovskites ($CsPbX_3$, X = Cl, Br, and I): novel optoelectronic materials showing bright emission with wide color gamut. *Nano Lett.* **2015**, *15*, 3692–3696.

[129] Kojima, A.; Teshima, K.; Shirai, Y.; Miyasaka, T. Organometal halide perovskites as visible-light sensitizers for photovoltaic cells. *J. Am. Chem. Soc.* **2009**, *131*, 6050–6051.

[130] Gao, P.; Grätzel, M.; Nazeeruddin, M. K. Organohalide lead perovskites for photovoltaic applications. *Energ. Environ. Sci.* **2014**, *7*, 2448–2463.

[131] Colella, S.; Mosconi, E.; Fedeli, P.; Listorti, A.; Gazza, F.; Orlandi, F.; Ferro, P.; Besagni, T.; Rizzo, A.; Calestani, G.; Gigli, G.; De Angelis, F.; Mosca, R. $MAPbI_{3-x}Cl_x$ Mixed Halide Perovskite for Hybrid Solar Cells: The Role of Chloride as Dopant on the Transport and Structural Properties. *Chem. Mater.* **2013**, *25*, 4613–4618.

[132] Eperon, G. E.; Paternò, G. M.; Sutton, R. J.; Zampetti, A.; Haghighirad, A. A.; Cacialli, F.; Snaith, H. J. Inorganic caesium lead iodide perovskite solar cells. *J. Mater. Chem. A* **2015**, *3*, 19688–19695.

[133] Chung, I.; Lee, B.; He, J.; Chang, R. P.; Kanatzidis, M. G. All-solid-state dye-sensitized solar cells with high efficiency. *Nature* **2012**, *485*, 486–489.

[134] Lee, M. M.; Teuscher, J.; Miyasaka, T.; Murakami, T. N.; Snaith, H. J. Efficient hybrid solar cells based on meso-superstructured organometal halide perovskites. *Science* **2012**, *338*, 643–647.

[135] Liu, M.; Johnston, M. B.; Snaith, H. J. Efficient planar heterojunction perovskite solar cells by vapour deposition. *Nature* **2013**, *501*, 395–398.

[136] Burschka, J.; Pellet, N.; Moon, S.-J.; Humphry-Baker, R.; Gao, P.; Nazeeruddin, M. K.; Grätzel, M. Sequential deposition as a route to high-performance perovskite-sensitized solar cells. *Nature* **2013**, *499*, 316–319.

[137] Choi, J. J.; Yang, X.; Norman, Z. M.; Billinge, S. J.; Owen, J. S. Structure of methylammonium lead iodide within mesoporous titanium dioxide: active material in high-performance perovskite solar cells. *Nano Lett.* **2013**, *14*, 127–133.

[138] Fabini, D. Quantifying the Potential for Lead Pollution from Halide Perovskite Photovoltaics. *J. Phys. Chem. Lett.* **2015**, *6*, 3546–3548.

[139] Babayigit, A.; Ethirajan, A.; Muller, M.; Conings, B. Toxicity of organometal halide perovskite solar cells. *Nat. Mater.* **2016**, *15*, 247–251.

[140] Frost, J. M.; Butler, K. T.; Brivio, F.; Hendon, C. H.; van Schilfgaarde, M.; Walsh, A. Atomistic Origins of High-Performance in Hybrid Halide Perovskite Solar Cells. *Nano Lett.* **2014**, *14*, 2584–2590.

[141] Bass, K. K.; McAnally, R. E.; Zhou, S.; Djurovich, P. I.; Thompson, M. E.; Melot, B. C. Influence of moisture on the preparation, crystal structure, and photophysical properties of organohalide perovskites. *Chem. Comm.* **2014**, *50*, 15819–15822.

[142] Wozny, S.; Yang, M.; Nardes, A. M.; Mercado, C. C.; Ferrere, S.; Reese, M. O.; Zhou, W.; Zhu, K. Controlled Humidity Study on the Formation of Higher Efficiency Formamidinium Lead Triiodide-Based Solar Cells. *Chem. Mater.* **2015**, *27*, 4814–4820.

[143] Mosconi, E.; Azpiroz, J. M.; De Angelis, F. Ab Initio Molecular Dynamics Simulations of Methylammonium Lead Iodide Perovskite Degradation by Water. *Chem. Mater.* **2015**, *27*, 4885–4892.

[144] Eames, C.; Frost, J. M.; Barnes, P. R.; O'regan, B. C.; Walsh, A.; Islam, M. S. Ionic transport in hybrid lead iodide perovskite solar cells. *Nat. Commun.* **2015**, *6*, 1–8.

[145] Leijtens, T.; Eperon, G. E.; Pathak, S.; Abate, A.; Lee, M. M.; Snaith, H. J. Overcoming ultraviolet light instability of sensitized TiO_2 with meso-superstructured organometal trihalide perovskite solar cells. *Nat. Commun.* **2013**, *4*, 2885–2892.

[146] Deretzis, I.; Alberti, A.; Pellegrino, G.; Smecca, E.; Giannazzo, F.; Sakai, N.; Miyasaka, T.; La Magna, A. Atomistic origins of $CH_3NH_3PbI_3$ degradation to PbI_2 in vacuum. *Appl. Phys. Lett.* **2015**, *106*, 131904.

[147] Bertoluzzi, L. Light induced structural changes in $CH_3NH_3PbI_3$ Perovskite Solar Cells. *J. Phys.: Conf. Series* **2015**, *609*, 012001.

[148] Sadoughi, G.; Starr, D. E.; Handick, E.; Stranks, S. D.; Gorgoi, M.; Wilks, R. G.; Baer, M.; Snaith, H. J. Observation and Mediation of the Presence of Metallic Lead in Organic-Inorganic Perovskite Films. *ACS Appl. Mater. Interfaces* **2015**, *7*, 13440–13444.

[149] Attfield, J. P.; Lightfoot, P.; Morris, R. E. Perovskites. *Dalton Trans.* **2015**, *44*, 10541–10542.

[150] Amat, A.; Mosconi, E.; Ronca, E.; Quarti, C.; Umari, P.; Nazeeruddin, M. K.; Grätzel, M.; De Angelis, F. Cation-induced band-gap tuning in organohalide perovskites: Interplay of spin–orbit coupling and octahedra tilting. *Nano Lett.* **2014**, *14*, 3608–3616.

[151] Knop, O.; Wasylishen, R. E.; White, M. A.; Cameron, T. S.; Oort, M. J. M. V. Alkylammonium lead halides. Part 2. $CH_3NH_3PbX_3$ (X = Cl, Br, I) perovskites: cuboctahedral halide cages with isotropic cation reorientation. *Can. J. Chem.* **1990**, *68*, 412–422.

[152] Anderson, M. T.; Greenwood, K. B.; Taylor, G. A.; Poeppelmeier, K. R. B-cation arrangements in double perovskites. *Prog. Solid. St. Chem.* **1993**, *22*, 197–233.

[153] McClure, E. T.; Ball, M. R.; Windl, W.; Woodward, P. M. Cs_2AgBiX_6 (X = Br, Cl): New Visible Light Absorbing, Lead-Free Halide Perovskite Semiconductors. *Chem. Mater.* **2016**, *28*, 1348–1354.

[154] Slavney, A. H.; Hu, T.; Lindenberg, A. M.; Karunadasa, H. I. A bismuth-halide double perovskite with long carrier recombination lifetime for photovoltaic applications. *J. Am. Chem. Soc.* **2016**, *138*, 2138–2141.

[155] Rössler, K.; Winter, J. Influence of d-electron configuration on phase transitions in A_2MX_6 (Hexahalometallates IV). *Chem. Phys. Lett.* **1977**, *46*, 566–570.

[156] Henkel, W.; Pelzl, J.; Höck, K.; Thomas, H. Elastic constants and softening of acoustic modes in A_2MX_6-crystals observed by Brillouin scattering. *Z. Phys. B* **1980**, *37*, 321–332.

[157] Brendel, W.; Samartzis, T.; Brendel, C.; Krebs, B. TG and DTA investigations on hexaiodometallates. *Thermochim. Acta* **1985**, *83*, 167–172.

[158] Abrahams, S.; Ihringer, J.; Marsh, P. Structural and thermal dependence of normal-mode condensations in K_2TeBr_6. *Acta Crystallogr. B* **1989**, *45*, 26–34.

[159] Kieslich, G.; Sun, S.; Cheetham, A. K. Solid-state principles applied to organic–inorganic perovskites: new tricks for an old dog. *Chem. Sci.* **2014**, *5*, 4712–4715.

[160] Kieslich, G.; Sun, S.; Cheetham, T. An Extended Tolerance Factor Approach for Organic-Inorganic Perovskites. *Chem. Sci.* **2015**, *6*, 3430–3433.

[161] Brandt, R. E.; Stevanović, V.; Ginley, D. S.; Buonassisi, T. Identifying defect-tolerant semiconductors with high minority-carrier lifetimes: beyond hybrid lead halide perovskites. *MRS Commun.* **2015**, *5*, 265–275.

[162] Walsh, A.; Scanlon, D. O.; Chen, S.; Gong, X.; Wei, S.-H. Self-Regulation Mechanism for Charged Point Defects in Hybrid Halide Perovskites. *Angew. Chem.* **2015**, *127*, 1811–1814.

[163] Jansen, M.; Wedig, U. A piece of the picture—misunderstanding of chemical concepts. *Angew. Chem. Int. Ed.* **2008**, *47*, 10026–10029.

[164] Aullón, G.; Alvarez, S. Oxidation states, atomic charges and orbital populations in transition metal complexes. *Theor. Chem. Acc.* **2009**, *123*, 67–73.

[165] Larson, A. C.; Von Dreele, R. B. Gsas. *General Structure Analysis System. LANSCE, MS-H805, Los Alamos, New Mexico* **1994**,

[166] Toby, B. H. EXPGUI, a graphical user interface for GSAS. *J. Appl. Crystallogr.* **2001**, *34*, 210–213.

[167] Wang, J.; Toby, B. H.; Lee, P. L.; Ribaud, L.; Antao, S. M.; Kurtz, C.; Ramanathan, M.; Von Dreele, R. B.; Beno, M. A. A dedicated powder diffraction beamline at the Advanced Photon Source: Commissioning and early operational results. *Rev. Sci. Instrum.* **2008**, *79*, 085105.

[168] Hammersley, A.; Svensson, S.; Hanfland, M.; Fitch, A.; Hausermann, D. Two-dimensional detector software: From real detector to idealised image or two-theta scan. *International Journal of High Pressure Research* **1996**, *14*, 235–248.

[169] Juhas, P.; Davis, T.; Farrow, C. L.; Billinge, S. J. PDFgetX3: a rapid and highly automatable program for processing powder diffraction data into total scattering pair distribution functions. *J. Appl. Crystallogr.* **2013**, *46*, 560–566.

[170] Farrow, C.; Juhas, P.; Liu, J.; Bryndin, D.; Božin, E.; Bloch, J.; Proffen, T.; Billinge, S. PDFfit2 and PDFgui: computer programs for studying nanostructure in crystals. *J. Phys.: Condens. Matter* **2007**, *19*, 335219.

[171] Momma, K.; Izumi, F. *VESTA3* for three-dimensional visualization of crystal, volumetric and morphology data. *J. Appl. Crystallogr.* **2011**, *44*, 1272–1276.

[172] Zhang, X.; Manno, M.; Baruth, A.; Johnson, M.; Aydil, E. S.; Leighton, C. Crossover From Nanoscopic Intergranular Hopping to Conventional Charge Transport in Pyrite Thin Films. *ACS Nano* **2013**, *7*, 2781–2789.

[173] Perkins, C. L.; Hasoon, F. S. Surfactant-assisted growth of CdS thin films for photovoltaic applications. *J. Vac. Sci. Technol., A* **2006**, *24*, 497–504.

[174] Kraut, E.; Grant, R.; Waldrop, J.; Kowalczyk, S. Semiconductor core-level to valence-band maximum binding-energy differences: Precise determination by x-ray photoelectron spectroscopy. *Phys. Rev. B* **1983**, *28*, 1965.

[175] Chambers, S. A.; Droubay, T.; Kaspar, T. C.; Gutowski, M.; Van Schilfgaarde, M. Accurate valence band maximum determination for $SrTiO_3$ (001). *Surf. Sci.* **2004**, *554*, 81–89.

[176] Kresse, G.; Hafner, J. *A*b Initio Molecular Dynamics for Liquid Metals. *Phys. Rev. B* **1993**, *47*, 558–561.

[177] Kresse, G.; Hafner, J. *A*b Initio Molecular-Dynamics Simulation of the Liquid-Metal Amorphous-Semiconductor Transition in Germanium. *Phys. Rev. B* **1994**, *49*, 14251–14269.

[178] Kresse, G.; Furthmüller, J. Efficiency of *A*b Initio Total Energy Calculations for Metals and Semiconductors Using a Plane Wave Basis Set. *Comput. Mater. Sci.* **1996**, *6*, 15–50.

[179] Kresse, G.; Furthmüller, J. Efficient Iterative Schemes for *A*b Initio Total-Energy Calculations Using a Plane-Wave Basis Set. *Phys. Rev. B* **1996**, *54*, 11169–11186.

[180] Kresse, G. From Ultrasoft Pseudopotentials to the Projector Augmented-Wave Method. *Phys. Rev. B* **1999**, *59*, 1758–1775.

[181] Krukau, A. V.; Vydrov, O. A.; Izmaylov, A. F.; Scuseria, G. E. Influence of the Exchange Screening Parameter on the Performance of Screened Hybrid Functionals. *J. Chem. Phys.* **2006**, *125*, 224106.

[182] Perdew, J. P.; Burke, K.; Ernzerhof, M. Generalized Gradient Approximation Made Simple. *Phys. Rev. Lett.* **1996**, *77*, 3865–3868.

[183] Chen, S.; Gong, X.; Walsh, A.; Wei, S.-H. Crystal and electronic band structure of Cu_2ZnSnX_4 (X= S and Se) photovoltaic absorbers: first-principles insights. *Appl. Phys. Lett.* **2009**, *94*, 41903.

[184] Ganose, A.; Savory, C. N.; Scanlon, D. O. $(CH_3NH_3)_2Pb(SCN)_2I_2$: A More Stable Structural Motif for Hybrid Halide Photovoltaics? *J. Phys. Chem. Lett.* **2015**, *6*, 4594–4598.

[185] Scanlon, D. O.; Walsh, A. Bandgap Engineering of $ZnSnP_2$ for High-Efficiency Solar Cells. *Appl. Phys. Lett.* **2012**, *100*, 251911.

[186] Ye, Y.; Run, X.; Hai-Tao, X.; Feng, H.; Fei, X.; Lin-Jun, W. Nature of the band gap of halide perovskites ABX_3 (A= CH_3NH_3, Cs; B= Sn, Pb; X= Cl, Br, I): First-principles calculations. *Chin. Phys. B* **2015**, *24*, 116302.

[187] Zunger, A.; Wei, S.-H.; Ferreira, L.; Bernard, J. E. Special quasirandom structures. *Phys. Rev. Lett.* **1990**, *65*, 353.

[188] Romero, A.; Cardona, M.; Kremer, R.; Lauck, R.; Siegle, G.; Serrano, J.; Gonze, X. Lattice properties of PbX (X = S, Se, Te): experimental studies and ab initio calculations including spin-orbit effects. *Phys. Rev. B* **2008**, *78*, 224302.

[189] Skelton, J. M.; Parker, S. C.; Togo, A.; Tanaka, I.; Walsh, A. Thermal physics of the lead chalcogenides PbS, PbSe, and PbTe from first principles. *Phys. Rev. B* **2014**, *89*, 205203.

[190] Togo, A.; Oba, F.; Tanaka, I. First-principles calculations of the ferroelastic transition between rutile-type and $CaCl_2$-type SiO_2 at high pressures. *Phys. Rev. B* **2008**, *78*, 134106.

[191] Dronskowski, R.; Bloechl, P. E. Crystal Orbital Hamilton Populations (COHP): Energy-Resolved Visualization of Chemical Bonding in Solids Based on Density-Functional Calculations. *J. Phys. Chem.* **1993**, *97*, 8617–8624.

[192] Maintz, S.; Deringer, V. L.; Tchougréeff, A. L.; Dronskowski, R. Analytic Projection from Plane-Wave and Paw Wavefunctions and Application to Chemical-Bonding Analysis in Solids. *J. Comput. Chem.* **2013**, *34*, 2557–2567.

[193] Paier, J.; Marsman, M.; Kresse, G. Dielectric properties and excitons for extended systems from hybrid functionals. *Phys. Rev. B* **2008**, *78*, 121201.

[194] Yang, J.; Siempelkamp, B. D.; Liu, D.; Kelly, T. L. Investigation of $CH_3NH_3PbI_3$ Degradation Rates and Mechanisms in Controlled Humidity Environments Using in Situ Techniques. *ACS Nano* **2015**, *9*, 1955–1963.

[195] Walsh, A.; Butler, K. T. Prediction of Electron Energies in Metal Oxides. *Acc. Chem. Res.* **2013**, *47*, 364–372.

[196] Ganose, A. M.; Butler, K. T.; Walsh, A.; Scanlon, D. O. Relativistic electronic structure and band alignment of BiSI and BiSeI: candidate photovoltaic materials. *J. Mater. Chem. A* **2016**, *4*, 2060–2068.

[197] Henkelman, G.; Arnaldsson, A.; Jónsson, H. A fast and robust algorithm for Bader decomposition of charge density. *Comput. Mater. Sci.* **2006**, *36*, 354–360.

[198] Tang, W.; Sanville, E.; Henkelman, G. A grid-based Bader analysis algorithm without lattice bias. *J. Phys.: Condens. Matter.* **2009**, *21*, 084204.

[199] Hacene, M.; Anciaux-Sedrakian, A.; Rozanska, X.; Klahr, D.; Guignon, T.; Fleurat-Lessard, P. Accelerating VASP electronic structure calculations using graphic processing units. *J. Comput. Chem.* **2012**, *33*, 2581–2589.

[200] Hutchinson, M.; Widom, M. VASP on a GPU: Application to exact-exchange calculations of the stability of elemental boron. *Comput. Phys. Commun.* **2012**, *183*, 1422–1426.

[201] Limpinsel, M.; Farhi, N.; Berry, N.; Lindemuth, J.; Perkins, C. L.; Lin, Q.; Law, M. An inversion layer at the surface of n-type iron pyrite. *Energ. Environ. Sci.* **2014**, *7*, 1974–1989.

[202] Shklovskii, B. L.; Efros, A. L. In *Electronic Properties of Doped Semiconductors*; Cardona, M., Fulde, P., Queisser, H. J., Eds.; 45; Springer, 1984.

[203] King, G.; Abakumov, A. M.; Woodward, P. M.; Llobet, A.; Tsirlin, A. A.; Batuk, D.; Antipov, E. V. The High-Temperature Polymorphs of K_3AlF_6. *Inorg. Chem.* **2011**, *50*, 7792–7801.

[204] Maughan, A. E.; Kurzman, J. A.; Neilson, J. R. Hybrid Inorganic–Organic Materials with an Optoelectronically Active Aromatic Cation:$(C_7H_7)_2SnI_6$ and $C_7H_7PbI_3$. *Inorg. Chem.* **2015**, *54*, 370–378.

[205] Shannon, R. t.; Prewitt, C. T. Effective ionic radii in oxides and fluorides. *Acta Crystallogr. B* **1969**, *25*, 925–946.

[206] Shannon, R.; Prewitt, C. Revised values of effective ionic radii. *Acta Crystallogr. B* **1970**, *26*, 1046–1048.

[207] Shannon, R. D. Revised effective ionic radii and systematic studies of interatomic distances in halides and chalcogenides. *Acta Crystallogr.* **1976**, *A 32*, 751–767.

[208] Swanson, B. Displacive phase transformations in K_2SnBr_6. *Phys. Status Solidi A* **1978**, *47*, K95–K98.

[209] Kaltzoglou, A.; Antoniadou, M.; Kontos, A. G.; Stoumpos, C. C.; Perganti, D.; Siranidi, E.; Raptis, V.; Trohidou, K.; Psycharis, V.; Kanatzidis, M. G.; Falaras, P. Optical-vibrational properties of the Cs_2SnX_6 (X = Cl, Br, I) defect perovskites and hole-transport efficiency in dye-sensitized solar cells. *J. Phys. Chem. C* **2016**, *120*, 11777–11785.

[210] Bencherif, Y.; Boukra, A.; Zaoui, A.; Ferhat, M. Lattice dynamics study of lead chalcogenides. *Infrared Phys. Techn.* **2011**, *54*, 39–43.

[211] Waghmare, U.; Spaldin, N.; Kandpal, H.; Seshadri, R. First-principles indicators of metallicity and cation off-centricity in the IV-VI rocksalt chalcogenides of divalent Ge, Sn, and Pb. *Phys. Rev. B* **2003**, *67*, 125111.

[212] Zhong, W.; King-Smith, R.; Vanderbilt, D. Giant LO-TO splittings in perovskite ferroelectrics. *Phys. Rev. Lett.* **1994**, *72*, 3618.

[213] Dolgonos, A.; Mason, T. O.; Poeppelmeier, K. R. Direct optical band gap measurement in polycrystalline semiconductors: A critical look at the Tauc method. *J. Solid State Chem.* **2016**, *240*, 43–48.

[214] Peresh, E. Y.; Zubaka, O.; Sidei, V.; Barchii, I.; Kun, S.; Kun, A. Preparation, Stability Regions, and Properties of M_2TeI_6 (M = Rb, Cs, Tl) Crystals. *Inorg. Mater.* **2002**, *38*, 859–863.

[215] Ranfagni, A.; Mugnai, D.; Bacci, M.; Viliani, G.; Fontana, M. The optical properties of thallium-like impurities in alkali-halide crystals. *Adv. Phys.* **1983**, *32*, 823–905.

[216] Blasse, G.; Dirksen, G.; Abriel, W. The influence of distortion of the Te(IV) coordination octahedron on its luminescence. *Chem. Phys. Lett.* **1987**, *136*, 460–464.

[217] Drummen, P.; Donker, H.; Smit, W.; Blasse, G. Jahn-Teller distortion in the excited state of tellurium(IV) in Cs_2MCl_6 (M=Zr, Sn). *Chem. Phys. Lett.* **1988**, *144*, 460–462.

[218] Donker, H.; Smit, W.; Blasse, G. On the luminescence of Te^{4+} in A_2ZrCl_6 (*A* = Cs, Rb) and A_2ZrCl_6 (A = Cs, Rb, K). *J. Phys. Chem. Solids* **1989**, *50*, 603–609.

[219] Zunger, A.; Jaffe, J. Structural origin of optical bowing in semiconductor alloys. *Phys. Rev. Lett.* **1983**, *51*, 662–665.

[220] Bellaiche, L.; Wei, S.-H.; Zunger, A. Localization and percolation in semiconductor alloys: GaAsN vs GaAsP. *Phys. Rev. B* **1996**, *54*, 17568.

[221] Wu, J.; Walukiewicz, W.; Yu, K.; Ager III, J.; Haller, E.; Miotkowski, I.; Ramdas, A.; Su, C.-H.; Sou, I.; Perera, R.; Denlinger, J. Origin of the large band-gap bowing in highly mismatched semiconductor alloys. *Phys. Rev. B* **2003**, *67*, 035207.

[222] Wu, J.; Walukiewicz, W.; Yu, K.; Denlinger, J.; Shan, W.; Ager III, J.; Kimura, A.; Tang, H.; Kuech, T. Valence band hybridization in N-rich $GaN_{1-x}As_x$ alloys. *Phys. Rev. B* **2004**, *70*, 115214.

[223] Walsh, A.; Da Silva, J. L.; Wei, S.-H.; Körber, C.; Klein, A.; Piper, L.; DeMasi, A.; Smith, K. E.; Panaccione, G.; Torelli, P. Nature of the band gap of In_2O_3 revealed by first-principles calculations and X-ray spectroscopy. *Phys. Rev. Lett.* **2008**, *100*, 167402.

[224] Kehoe, A. B.; Scanlon, D. O.; Watson, G. W. Nature of the band gap of Tl_2O_3. *Phys. Rev. B* **2011**, *83*, 233202.

[225] Godinho, K. G.; Carey, J. J.; Morgan, B. J.; Scanlon, D. O.; Watson, G. W. Understanding conductivity in $SrCu_2O_2$: stability, geometry and electronic structure of intrinsic defects from first principles. *J. Mater. Chem.* **2010**, *20*, 1086–1096.

[226] van der Marck, S. C. Percolation thresholds and universal formulas. *Phys. Rev. E* **1997**, *55*, 1514–1517.

[227] Umari, P.; Mosconi, E.; De Angelis, F. Relativistic GW calculations on $CH_3NH_3PbI_3$ and $CH_3NH_3SnI_3$ perovskites for solar cell applications. *Sci. Rep.* **2014**, *4*, 1–7.

[228] Persson, C.; Zhao, Y.-J.; Lany, S.; Zunger, A. n-type doping of $CuInSe_2$ and $CuGaSe_2$. *Phys. Rev. B* **2005**, *72*, 035211.

[229] Scanlon, D. O. Defect engineering of $BaSnO_3$ for high-performance transparent conducting oxide applications. *Phys. Rev. B* **2013**, *87*, 161201.

[230] Freysoldt, C.; Grabowski, B.; Hickel, T.; Neugebauer, J.; Kresse, G.; Janotti, A.; Van de Walle, C. G. First-principles calculations for point defects in solids. *Rev. Mod. Phys.* **2014**, *86*, 253–305.

[231] Gordy, W.; Thomas, W. O. Electronegativities of the elements. *J. Chem. Phys.* **1956**, *24*, 439–444.

[232] Ghosez, P.; Gonze, X.; Lambin, P.; Michenaud, J.-P. Born effective charges of barium titanate: Band-by-band decomposition and sensitivity to structural features. *Phys. Rev. B* **1995**, *51*, 6765.

[233] Stranks, S. D.; Snaith, H. J. Metal-halide perovskites for photovoltaic and light-emitting devices. *Nat. Nanotechnol.* **2015**, *10*, 391–402.

[234] Bi, Y.; Hutter, E. M.; Fang, Y.; Dong, Q.; Huang, J.; Savenije, T. J. Charge carrier lifetimes exceeding 15 μs in methylammonium lead iodide single crystals. *J. Phys. Chem. Lett.* **2016**, *7*, 923–928.

[235] Filip, M. R.; Eperon, G. E.; Snaith, H. J.; Giustino, F. Steric engineering of metal-halide perovskites with tunable optical band gaps. *Nat. Commun.* **2014**, *5*, 5757.

[236] Prasanna, R.; Gold-Parker, A.; Leijtens, T.; Conings, B.; Babayigit, A.; Boyen, H.-G.; Toney, M. F.; McGehee, M. D. Band Gap Tuning via Lattice Contraction and Octahedral Tilting in Perovskite Materials for Photovoltaics. *J. Am. Chem. Soc.* **2017**, *139*, 11117–11124.

[237] Berg, R. W. Low temperature vibrational spectroscopy. II. Evidence for order–disorder phase transitions due to weak C–H$\cdots$Cl hydrogen bonding in tetramethylammonium hexachloroplatinate (IV),-tellurate (IV), and-stannate (IV) and the related perdeuterated compounds. *J. Chem. Phys.* **1978**, *69*, 1325–1335.

[238] Petrov, A. A.; Goodilin, E. A.; Tarasov, A. B.; Lazarenko, V. A.; Dorovatovskii, P. V.; Khrustalev, V. N. Formamidinium iodide: crystal structure and phase transitions. *Acta. Crystallogr. E* **2017**, *73*, 569–572.

[239] Aharon, S.; Dymshits, A.; Rotem, A.; Etgar, L. Temperature dependence of hole conductor free formamidinium lead iodide perovskite based solar cells. *J. Mater. Chem. A* **2015**, *3*, 9171–9178.

[240] Chupas, P. J.; Qiu, X.; Hanson, J. C.; Lee, P. L.; Grey, C. P.; Billinge, S. J. Rapid-acquisition pair distribution function (RA-PDF) analysis. *J. Appl. Crystallogr.* **2003**, *36*, 1342–1347.

[241] Qiu, X.; Thompson, J. W.; Billinge, S. J. PDFgetX2: a GUI-driven program to obtain the pair distribution function from X-ray powder diffraction data. *J. Appl. Crystallogr.* **2004**, *37*, 678–678.

[242] Perdew, J. P.; Ruzsinszky, A.; Csonka, G. I.; Vydrov, O. A.; Scuseria, G. E.; Constantin, L. A.; Zhou, X.; Burke, K. Restoring the Density-Gradient Expansion for Exchange in Solids and Surfaces. *Phys. Rev. Lett.* **2008**, *100*, 136406.

[243] Ganose, A. M.; Savory, C. N.; Scanlon, D. O. Electronic and defect properties of $(CH_3NH_3)_2Pb(SCN)_2I_2$ analogues for photovoltaic applications. *J. Mater. Chem. A* **2017**, *5*, 7845–7853.

[244] Travis, W.; Knapp, C. E.; Savory, C. N.; Ganose, A. M.; Kafourou, P.; Song, X.; Sharif, Z.; Cockcroft, J. K.; Scanlon, D. O.; Bronstein, H.; Palgrave, R. G. Hybrid Organic–Inorganic Coordination Complexes as Tunable Optical Response Materials. *Inorg. Chem.* **2016**, *55*, 3393–3400.

[245] Hobbs, D.; Kresse, G.; Hafner, J. Fully unconstrained noncollinear magnetism within the projector augmented-wave method. *Phys. Rev. B* **2000**, *62*, 11556–11570.

[246] Savory, C. N.; Ganose, A. M.; Scanlon, D. O. Exploring the PbS-Bi_2S_3 series for next generation energy conversion materials. *Chem. Mater.* **2017**, *29*, 5156–5167.

[247] Baroni, S.; De Gironcoli, S.; Dal Corso, A.; Giannozzi, P. Phonons and related crystal properties from density-functional perturbation theory. *Rev. Mod. Phys.* **2001**, *73*, 515.

[248] Gajdoš, M.; Hummer, K.; Kresse, G.; Furthmüller, J.; Bechstedt, F. Linear optical properties in the projector-augmented wave methodology. *Phys. Rev. B* **2006**, *73*, 045112.

[249] https://github.com/jarvist/PolaronMobility-FeynmanKadanoffOsakaHellwarth, Accessed: 2017-07-26.

[250] Frost, J. M. Calculating polaron mobility in halide perovskites. *Phys. Rev. B* **2017**, *96*, 195202.

[251] Kadanoff, L. P. Boltzmann Equation for Polarons. *Phys. Rev.* **1963**, *130*, 1364–1369.

[252] Feynman, R. P.; Hellwarth, R. W.; Iddings, C. K.; Platzman, P. M. Mobility of Slow Electrons in a Polar Crystal. *Phys. Rev.* **1962**, *127*, 1004–1017.

[253] Kaasbjerg, K.; Thygesen, K. S.; Jacobsen, K. W. Phonon-limited mobility in n-type single-layer MoS_2 from first principles. *Phys. Rev. B* **2012**, *85*, 115317.

[254] Yan, J.; Gorai, P.; Ortiz, B.; Miller, S.; Barnett, S. A.; Mason, T.; Stevanović, V.; Toberer, E. S. Material descriptors for predicting thermoelectric performance. *Energ. Environ. Sci.* **2015**, *8*, 983–994.

[255] Mante, P.-A.; Stoumpos, C. C.; Kanatzidis, M. G.; Yartsev, A. Electron–acoustic phonon coupling in single crystal $CH_3NH_3PbI_3$ perovskites revealed by coherent acoustic phonons. *Nat. Commun.* **2017**, *8*, 14398.

[256] Worhatch, R. J.; Kim, H.; Swainson, I. P.; Yonkeu, A. L.; Billinge, S. J. Study of Local Structure in Selected Organic–Inorganic Perovskites in the $Pm\bar{3}m$ Phase. *Chem. Mater.* **2008**, *20*, 1272–1277.

[257] Stoumpos, C. C.; Frazer, L.; Clark, D. J.; Kim, Y. S.; Rhim, S. H.; Freeman, A. J.; Ketterson, J. B.; Jang, J. I.; Kanatzidis, M. G. Hybrid germanium iodide perovskite semiconductors: active lone pairs, structural distortions, direct and indirect energy gaps, and strong nonlinear optical properties. *J. Am. Chem. Soc.* **2015**, *137*, 6804–6819.

[258] Fabini, D. H.; Laurita, G.; Bechtel, J. S.; Stoumpos, C. C.; Evans, H. A.; Kontos, A. G.; Raptis, Y. S.; Falaras, P.; Van der Ven, A.; Kanatzidis, M. G.; Seshadri, R. Dynamic Stereochemical Activity of the Sn^{2+} Lone Pair in Perovskite $CsSnBr_3$. *J. Am. Chem. Soc.* **2016**, *138*, 11820–11832.

[259] Laurita, G.; Fabini, D. H.; Stoumpos, C. C.; Kanatzidis, M. G.; Seshadri, R. Chemical tuning of dynamic cation off-centering in the cubic phases of hybrid tin and lead halide perovskites. *Chem. Sci.* **2017**, *8*, 5628–5635.

[260] Yaffe, O.; Guo, Y.; Tan, L. Z.; Egger, D. A.; Hull, T.; Stoumpos, C. C.; Zheng, F.; Heinz, T. F.; Kronik, L.; Kanatzidis, M. G.; Owen, J. S.; Rappe, A. M.; Pimenta, M. A.; Brus, L. E. Local polar fluctuations in lead halide perovskite crystals. *Phys. Rev. Lett.* **2017**, *118*, 136001.

[261] Sangiorgio, B.; Bozin, E. S.; Malliakas, C. D.; Fechner, M.; Simonov, A.; Kanatzidis, M. G.; Billinge, S. J.; Spaldin, N. A.; Weber, T. Correlated local dipoles in PbTe. *Phys. Rev. Mater.* **2018**, *2*, 085402.

[262] Furukawa, Y.; Kiriyama, H.; Ikeda, R. The Nuclear Quadrupole Spin-Lattice Relaxation of ^{35}Cl in Methylammonium Hexachlorostannate (IV) and Hexachloroplatinate (IV). *Bull. Chem. Soc. Jpn.* **1977**, *50*, 1927–1929.

[263] Karakus, M.; Jensen, S. A.; D'Angelo, F.; Turchinovich, D.; Bonn, M.; Canovas, E. Phonon–electron scattering limits free charge mobility in methylammonium lead iodide perovskites. *J. Phys. Chem. Lett.* **2015**, *6*, 4991–4996.

[264] Milot, R. L.; Eperon, G. E.; Snaith, H. J.; Johnston, M. B.; Herz, L. M. Temperature-Dependent Charge-Carrier Dynamics in $CH_3NH_3PbI_3$ Perovskite Thin Films. *Adv. Funct. Mater.* **2015**, *25*, 6218–6227.

[265] Feng, J. Mechanical properties of hybrid organic-inorganic $CH_3NH_3BX_3$ (B = Sn, Pb; X = Br, I) perovskites for solar cell absorbers. *APL Mater.* **2014**, *2*, 081801.

[266] Walsh, A. Principles of Chemical Bonding and Band Gap Engineering in Hybrid Organic–Inorganic Halide Perovskites. *J. Phys. Chem. C* **2015**, *119*, 5755–5760.

[267] Yang, Y.; Ostrowski, D. P.; France, R. M.; Zhu, K.; Van De Lagemaat, J.; Luther, J. M.; Beard, M. C. Observation of a hot-phonon bottleneck in lead-iodide perovskites. *Nat. Photonics* **2016**, *10*, 53–59.

[268] Linaburg, M. R.; McClure, E. T.; Majher, J. D.; Woodward, P. M. $Cs_{1-x}Rb_xPbCl_3$ and $Cs_{1-x}Rb_xPbBr_3$ solid solutions: Understanding octahedral tilting in lead halide perovskites. *Chem. Mater.* **2017**, *29*, 3507–3514.

[269] Howard, C. J.; Stokes, H. Group-theoretical analysis of octahedral tilting in perovskites. *Acta Crystallogr. B* **1998**, *54*, 782–789.

[270] Neuefeind, J.; Feygenson, M.; Carruth, J.; Hoffmann, R.; Chipley, K. K. The nanoscale ordered materials diffractometer NOMAD at the spallation neutron source SNS. *Nucl. Instrum. Methods, Phys. Res. Sect. B* **2012**, *287*, 68–75.

[271] Biswas, D.; Ganose, A. M.; Yano, R.; Riley, J.; Bawden, L.; Clark, O.; Feng, J.; Collins-Mcintyre, L.; Sajjad, M.; Meevasana, W., Kim; Hoesch, M.; Rault, J.; Sasagawa, T.; Scanlon, D.; King, P. Narrow-band anisotropic electronic structure of ReS_2. *Phys. Rev. B* **2017**, *96*, 085205.

[272] Bradley, C.; Cracknell, A. *The mathematical theory of symmetry in solids: representation theory for point groups and space groups*; Oxford University Press, 2010.

[273] Heyd, J.; Scuseria, G. E.; Ernzerhof, M. Hybrid functionals based on a screened Coulomb potential. *J. Chem. Phys.* **2003**, *118*, 8207–8215.

[274] Heyd, J.; Scuseria, G. E.; Ernzerhof, M. Erratum: “Hybrid functionals based on a screened Coulomb potential"[J. Chem. Phys. 118, 8207 (2003)]. *J. Chem. Phys.* **2006**, *124*, 219906.

[275] https://github.com/SMTG-UCL/CSI-CTI, Accessed: 2016-02-01.

[276] https://github.com/WMD-group/MacroDensity, Accessed: 2018-03-13.

[277] Werker, W. Die Krystallstruktur des Rb_2SnI_6 und Cs_2SnI_6. *Recl. Trav. Chim. Pays-Bas* **1939**, *58*, 257–258.

[278] Boysen, H.; Hewat, A. W. A neutron powder investigation of the structural changes in K_2SnCl_6. *Acta Crystallogr. B* **1978**, *34*, 1412–1418.

[279] McQueeney, R. Dynamic radial distribution function from inelastic neutron scattering. *Phys. Rev. B* **1998**, *57*, 10560.

[280] Woodward, P. M. Octahedral tilting in perovskites. II. Structure stabilizing forces. *Acta Crystallogr. B* **1997**, *53*, 44–66.

[281] Brown, I.; Altermatt, D. Bond-valence parameters obtained from a systematic analysis of the inorganic crystal structure database. *Acta. Crystallogr. B* **1985**, *41*, 244–247.

[282] Dugdale, J.; MacDonald, D. Lattice thermal conductivity. *Phys. Rev.* **1955**, *98*, 1751.

[283] Muy, S.; Bachman, J. C.; Giordano, L.; Chang, H.-H.; Abernathy, D. L.; Bansal, D.; Delaire, O.; Hori, S.; Kanno, R.; Maglia, F.; Lupart, S.; Lamp, P.; Shao-Horn, Y. Tuning mobility and stability of lithium ion conductors based on lattice dynamics. *Energ. Environ. Sci.* **2018**, *11*, 850–859.

[284] Chodos, S.; Black, A.; Flint, C. Vibronic spectra and lattice dynamics of Cs_2MnF_6 and $A_2^1M^{IV}F_6$: $MnF_2{}^{-6}$. *J. Chem. Phys.* **1976**, *65*, 4816–4824.

[285] Hizhnyakov, V.; Plekhanov, V.; Shepelev, V.; Zavt, G. Hot Luminescence of Self-Trapped Excitons in Alkali Halide Crystals. *Phys. Status Solidi B* **1981**, *108*, 531–540.

[286] Freire, J.; Katiyar, R. Lattice dynamics of crystals with tetragonal $BaTiO_3$ structure. *Phys. Rev. B* **1988**, *37*, 2074.

[287] Khatib, D.; Migoni, R.; Kugel, G.; Godefroy, L. Lattice dynamics of $BaTiO_3$ in the cubic phase. *J. Phys.: Condens. Matter* **1989**, *1*, 9811.

[288] Bardeen, J.; Cooper, L. N.; Schrieffer, J. R. Microscopic theory of superconductivity. *Phys. Rev.* **1957**, *106*, 162.

[289] Dughaish, Z. Lead telluride as a thermoelectric material for thermoelectric power generation. *Physica B: Condens. Matter* **2002**, *322*, 205–223.

[290] Zhao, L.-D.; Lo, S.-H.; Zhang, Y.; Sun, H.; Tan, G.; Uher, C.; Wolverton, C.; Dravid, V. P.; Kanatzidis, M. G. Ultralow thermal conductivity and high thermoelectric figure of merit in SnSe crystals. *Nature* **2014**, *508*, 373.

[291] Shi, X.; Yang, J.; Salvador, J. R.; Chi, M.; Cho, J. Y.; Wang, H.; Bai, S.; Yang, J.; Zhang, W.; Chen, L. Multiple-filled skutterudites: high thermoelectric figure of merit through separately optimizing electrical and thermal transports. *J. Am. Chem. Soc.* **2011**, *133*, 7837–7846.

[292] Cava, R.; Reidinger, F.; Wuensch, B. Mobile ion distribution and anharmonic thermal motion in fast ion conducting Cu_2S. *Solid State Ionics* **1981**, *5*, 501–504.

[293] Yoshiasa, A.; Koto, K.; Kanamaru, F.; Emura, S.; Horiuchi, H. Anharmonic thermal vibrations in wurtzite-type AgI. *Acta Crystallogr. B* **1987**, *43*, 434–440.

[294] Patrick, C. E.; Jacobsen, K. W.; Thygesen, K. S. Anharmonic stabilization and band gap renormalization in the perovskite $CsSnI_3$. *Phys. Rev. B* **2015**, *92*, 201205.

[295] Pecchia, A.; Gentilini, D.; Rossi, D.; Auf der Maur, M.; Di Carlo, A. Role of ferroelectric nanodomains in the transport properties of perovskite solar cells. *Nano Lett.* **2016**, *16*, 988–992.

[296] Katan, C.; Mohite, A. D.; Even, J. Entropy in halide perovskites. *Nat. Mater.* **2018**, *17*, 377.

[297] Tucker, M. G.; Dove, M. T.; Keen, D. A. Application of the reverse Monte Carlo method to crystalline materials. *J. Appl. Crystallogr.* **2001**, *34*, 630–638.

[298] Aoun, B. Fullrmc, a rigid body reverse monte carlo modeling package enabled with machine learning and artificial intelligence. *J. Comput. Chem.* **2016**, *37*, 1102–1111.

[299] Lawson, A.; Goldstone, J.; Cort, B.; Sheldon, R.; Foltyn, E. Atomic thermal vibrations of the light actinide elements. *J. Alloys Compd.* **1994**, *213*, 426–428.

[300] Safarik, D.; Klimczuk, T.; Llobet, A.; Byler, D.; Lashley, J.; O'Brien, J.; Dilley, N. Localized anharmonic rattling of Al atoms in $VAl_{10.1}$. *Phys. Rev. B* **2012**, *85*, 014103.

[301] Sakata, M.; Harada, J.; Cooper, M.; Rouse, K. A neutron diffraction study of anharmonic thermal vibrations in cubic $CsPbX_3$. *Acta Crystallogr. A* **1980**, *36*, 7–15.

[302] Conterio, M. J.; Goodwin, A. L.; Tucker, M. G.; Keen, D. A.; Dove, M. T.; Peters, L.; Evans, J. S. Local structure in $Ag_3[Co(CN)_6]$: colossal thermal expansion, rigid unit modes and argentophilic interactions. *J. Phys. Condens. Matter* **2008**, *20*, 255225.

[303] Toda, M. One-dimensional dual transformation. *J. Phys. Soc. Jpn.* **1965**, *20*, 2095A–2095A.

[304] Milchev, A.; Mazzucchelli, G. Frenkel-Kontorova model with anharmonic interactions. *Phys. Rev. B* **1988**, *38*, 2808.

[305] Adams, S. Relationship between bond valence and bond softness of alkali halides and chalcogenides. *Acta Crystallogr. B* **2001**, *57*, 278–287.

[306] Mitzi, D.; Feild, C.; Schlesinger, Z.; Laibowitz, R. Transport, Optical, and Magnetic Properties of the Conducting Halide Perovskite $CH_3NH_3SnI_3$. *J. Solid State Chem.* **1995**, *114*, 159–163.

[307] Mitzi, D. B.; Chondroudis, K.; Kagan, C. R. Organic-inorganic electronics. *IBM J. Res. Dev.* **2001**, *45*, 29–45.

[308] Tan, Z.-K.; Moghaddam, R. S.; Lai, M. L.; Docampo, P.; Higler, R.; Deschler, F.; Price, M.; Sadhanala, A.; Pazos, L. M.; Credgington, D.; Hanusch, F.; Bein, T.; Snaith, H. J.; Friend, R. H. Bright light-emitting diodes based on organometal halide perovskite. *Nat. Nanotechnol.* **2014**, *9*, 687–692.

[309] Cheetham, A. K.; Rao, C.; Feller, R. K. Structural diversity and chemical trends in hybrid inorganic–organic framework materials. *Chem. Commun.* **2006**, *46*, 4780–4795.

[310] Mitzi, D. B. Solution-processed inorganic semiconductors. *J. Mater. Chem.* **2004**, *14*, 2355–2365.

[311] Sun, S.; Salim, T.; Mathews, N.; Duchamp, M.; Boothroyd, C.; Xing, G.; Sum, T. C.; Lam, Y. M. The origin of high efficiency in low-temperature solution-processable bilayer organometal halide hybrid solar cells. *Energ. Environ. Sci.* **2014**, *7*, 399–407.

[312] Knutson, J. L.; Martin, J. D.; Mitzi, D. B. Tuning the band gap in hybrid tin iodide perovskite semiconductors using structural templating. *Inorg. Chem.* **2005**, *44*, 4699–4705.

[313] Mitzi, D.; Wang, S.; Feild, C.; Chess, C.; Guloy, A. Conducting Layered Organic-Inorganic Halides Containing (100)-oriented Perovskite Sheets. *Science* **1995**, *267*, 1473–1476.

[314] Hao, F.; Stoumpos, C. C.; Chang, R. P.; Kanatzidis, M. G. Anomalous band gap behavior in mixed Sn and Pb perovskites enables broadening of absorption spectrum in solar cells. *J. Am. Chem. Soc.* **2014**, *136*, 8094–8099.

[315] Borriello, I.; Cantele, G.; Ninno, D. Ab initio investigation of hybrid organic-inorganic perovskites based on tin halides. *Phys. Rev. B* **2008**, *77*, 235214.

[316] Noh, J. H.; Im, S. H.; Heo, J. H.; Mandal, T. N.; Seok, S. I. Chemical management for colorful, efficient, and stable inorganic–organic hybrid nanostructured solar cells. *Nano Lett.* **2013**, *13*, 1764–1769.

[317] Billing, D. G.; Lemmerer, A. Synthesis and crystal structures of inorganic–organic hybrids incorporating an aromatic amine with a chiral functional group. *CrystEngComm* **2006**, *8*, 686–695.

[318] Mercier, N.; Louvain, N.; Bi, W. Structural diversity and retro-crystal engineering analysis of iodometalate hybrids. *CrystEngComm* **2009**, *11*, 720–734.

[319] Duan, H.-B.; Zhao, H.-R.; Ren, X.-M.; Zhou, H.; Tian, Z.-F.; Jin, W.-Q. Inorganic–organic hybrid compounds based on face-sharing octahedral [PbI_3] chains: self-assemblies, crys-

tal structures, and ferroelectric, photoluminescence properties. *Dalton Trans.* **2011**, *40*, 1672–1683.

[320] Zhao, S.-P.; Ren, X.-M. Toward design of multiple-property inorganic-organic hybrid compounds based on face-sharing octahedral iodoplumbate chains. *Dalton Trans.* **2011**, *40*, 8261–8272.

[321] Vincent, B. R.; Robertson, K. N.; Cameron, T. S.; Knop, O. Alkylammonium lead halides. Part 1. Isolated PbI_6^{4-} ions in $(CH_3NH_3)_4PbI_6{\cdot}2H_2O$. *Can. J. Chem.* **1987**, *65*, 1042–1046.

[322] Pradeesh, K.; Agarwal, M.; Rao, K. K.; Prakash, G. V. Synthesis, crystal structure and optical properties of quasi-one-dimensional lead (II) iodide: $C_{14}H_{18}N_2Pb_2I_6$. *Solid State Sci.* **2010**, *12*, 95–98.

[323] Kosower, E. M. The Solvent Sensitivity of the Charge-Transfer Band of Tropylium Iodide. *J. Org. Chem.* **1964**, *29*, 956–957.

[324] Doering, W.; Knox, L. Reactions of the Cycloheptatrienylium (Tropylium) Ion. *J. Am. Chem. Soc.* **1957**, *79*, 352–356.

[325] Harmon, K. M.; Harmon, A. B.; Alderman, S. D.; Gebauer, P. A.; Hesse, L. L. Iodine-cycloheptatriene system. *J. Org. Chem.* **1967**, *32*, 2012–2013.

[326] Kitaigorodskii, A.; Struchkov, Y.; Khotsyanova, T.; Vol'pin, M.; Kursanov, D. Crystal structures of tropylium perchlorate and iodide. *B. Acad. Sci. USSR* **1960**, *9*, 32–36.

[327] Boultif, A.; Louër, D. Powder pattern indexing with the dichotomy method. *J. Appl. Crystallogr.* **2004**, *37*, 724–731.

[328] Favre-Nicolin, V.; Cerny, R. FOX, free objects for crystallography: a modular approach to ab initio structure determination from powder diffraction. *J. Appl. Crystallogr.* **2002**, *35*, 734–743.

[329] Cotton, F. A.; Wilkinson, G.; Murillo, C. A.; Bochmann, M.; Grimes, R. *Advanced Inorganic Chemistry*; Wiley New York, 1999; Vol. 5.

[330] Sourisseau, C. The vibrational spectra and structure of tropylium hexachlorophosphate, $C_7H_7PCl_6$. *Spectrochim. Acta Mol. Biomol. Spectros.* **1978**, *34*, 881–887.

[331] Stuart, B. *Infrared Spectroscopy: Fundamentals and Applications.*; John Wiley & Sons, Ltd., 2004.

[332] Brese, N.; O'Keeffe, M. Bond-valence parameters for solids. *Acta. Crystallogr. B* **1991**, *47*, 192–197.

[333] Hu, S.-Z.; Xie, Z.-X.; Palenik, G. J. Bond Valence Parameters for Sn(II)X and Sn(IV)X (X=O, S, N, C, P, As, Se, Te, F, Cl, Br, I). *Acta. Phys.-Chim. Sin.* **2012he**, *28*, 19.

[334] Lämsä, M.; Suorsa, T.; Pursiainen, J.; Huuskonen, J.; Rissanen, K. Crystal structure of an inclusion complex between dibenzo-24-crown-8 and tropylium tetrafluoroborate. *Chem. Commun.* **1996**, *12*, 1443–1444.

[335] Dove, M. T.; Tucker, M. G.; Keen, D. A. Neutron total scattering method simultaneous determination of long-range and short-range order in disordered materials. *Eur. J. Mineral.* **2002**, *14*, 331–348.

[336] Hamilton, W. C. Significance tests on the crystallographic R factor. *Acta. Crystallogr.* **1965**, *18*, 502–510.

[337] Li, Y.; Zheng, G.; Lin, C.; Lin, J. Synthesis, structure and optical properties of different dimensional organic–inorganic perovskites. *Solid State Sci.* **2007**, *9*, 855–861.

[338] She, Y.-J.; Zhao, S.-P.; Tian, Z.-F.; Ren, X.-M. Inorganic–organic hybrid with one-dimensional face-sharing iodoplumbate chain showing novel dielectric anomaly and semiconductor emission. *Inorg. Chem. Commun.* **2014**, *46*, 29–32.

[339] Huang, H.-M.; Jiang, Z.-Y.; Luo, S.-J. First-principles investigations on the mechanical, thermal, electronic, and optical properties of the defect perovskites Cs_2SnX_6 (X = Cl, Br, I). *Chin. Phys. B* **2017**, *26*, 096301.

[340] Ju, M.-G.; Chen, M.; Zhou, Y.; Garces, H. F.; Dai, J.; Ma, L.; Padture, N. P.; Zeng, X. C. Earth-abundant nontoxic titanium (IV)-based vacancy-ordered double perovskite halides with tunable 1.0 to 1.8 eV bandgaps for photovoltaic applications. *ACS Energy Lett.* **2018**, *3*, 297–304.

[341] Dalpian, G. M.; Liu, Q.; Stoumpos, C. C.; Douvalis, A. P.; Balasubramanian, M.; Kanatzidis, M. G.; Zunger, A. Changes in charge density vs changes in formal oxidation states: The case of Sn halide perovskites and their ordered vacancy analogues. *Phys. Rev. Mater.* **2017**, *1*, 025401.

[342] Huang, L.-y.; Lambrecht, W. R. Electronic band structure, phonons, and exciton binding energies of halide perovskites $CsSnCl_3$, $CsSnBr_3$, and $CsSnI_3$. *Phys. Rev. B* **2013**, *88*, 165203.

[343] Kaltzoglou, A.; Antoniadou, M.; Perganti, D.; Siranidi, E.; Raptis, V.; Trohidou, K.; Psycharis, V.; Kontos, A. G.; Falaras, P. Mixed-halide $Cs_2SnI_3Br_3$ perovskite as low resistance hole-transporting material in dye-sensitized solar cells. *Electrochim. Acta* **2015**, *184*, 466–474.

[344] Chen, M.; Ju, M.-G.; Carl, A. D.; Zong, Y.; Grimm, R. L.; Gu, J.; Zeng, X. C.; Zhou, Y.; Padture, N. P. Cesium titanium (IV) bromide thin films based stable lead-free perovskite solar cells. *Joule* **2018**, *2*, 558–570.

[345] Xiao, Z.; Meng, W.; Wang, J.; Mitzi, D. B.; Yan, Y. Searching for promising new perovskite-based photovoltaic absorbers: the importance of electronic dimensionality. *Mater. Horiz.* **2017**, *4*, 206–216.

[346] Prassides, K.; Day, P.; Cheetham, A. K. Anion ordering in mixed valence dicesium hexachloroantimonate (Cs_2SbCl_6) and related salts. *J. Am. Chem. Soc.* **1983**, *105*, 3366–3368.

[347] Robin, M. B.; Day, P. *Molecules Into Materials: Case Studies in Materials Chemistry—Mixed Valency, Magnetism and Superconductivity*; World Scientific, 2007; pp 142–317.

[348] Lawton, S. L.; Jacobson, R. A. Crystal Structure Studies of Some Unusual Antimony Bromide Salts. *J. Am. Chem. Soc.* **1966**, *88*, 616–618.

[349] Lawton, S. L.; Jacobson, R. A. The Crystal Structure of Ammonium Hexabromoantimonate, $(NH_4)_4Sb^{III}Sb^{V}Br_{12}$. *Inorg. Chem.* **1966**, *5*, 743–749.

[350] Prassides, K.; Day, P.; Cheetham, A. K. Crystal structures of mixed-valency and mixed-metal salts $A_2M^{III}{}_{0.5}Sb^{V}_{0.5}X_6$ (A = Rb, Cs; M = Sb, Bi, In, Tl, Fe, Rh; X = Cl, Br). A powder neutron diffraction study. *Inorg. Chem.* **1985**, *24*, 545–552.

[351] Day, P. Spectra and constitution of antimony (III), antimony (V) hexahalide salts and related compounds. *Inorg. Chem.* **1963**, *2*, 452–456.

[352] Clark, R. J.; Trumble, W. R. Resonance Raman spectra of some mixed-valence halogeno-compounds of antimony and lead. *J. Chem. Soc. Dalton Trans.* **1976**, 1145–1149.

[353] Clark, H.; Swanson, B. I. Effects of outer-sphere electron transfer on the vibrational spectrum of dicesium antimony hexachloride. *J. Am. Chem. Soc.* **1981**, *103*, 2928–2933.

[354] Prassides, K.; Day, P. Phonons in mixed-valency and mixed-metal salts $A_2M_{0.5}Sb_{0.5}Cl_6$ (A = Rb, Cs; M = Sb, Bi, Tl): an inelastic neutron scattering study. *Inorg. Chem.* **1985**, *24*, 3035–3043.

[355] Atkinson, L.; Day, P. Charge transfer in mixed-valence solids. Part IV. Electronic spectra of hexachloroantimonates (III, V). *J. Chem. Soc. A* **1969**, 2423–2431.

[356] Atkinson, L.; Day, P. Charge transfer in mixed-valence solids. Part V. Semiconductivity of hexachloroantimonates (III, V). *J. Chem. Soc. A* **1969**, 2432–2436.

[357] Park, M.; Neukirch, A. J.; Tretiak, S.; Park, M.; Reyes-Lillo, S. E.; Lai, M.; Ellis, S. R.; Dietze, D.; Neaton, J. B.; Yang, P.; Mathies, R. A. Excited-State Vibrational Dynamics Toward the Polaron in Methylammonium Lead Iodide ($MAPbI_3$) Perovskite. *Nat. Commun.* **2018**, *9*, 1–8.

[358] Yuan, G.; Huang, S.; Niu, J.; Qin, S.; Wu, X.; Ding, H.; Lu, A. Compressibility of Cs_2SnBr_6 by X-ray diffraction and Raman spectroscopy. *Solid State Commun.* **2018**, *275*, 68–72.

[359] Egami, T.; Billinge, S. J. *Underneath the Bragg peaks: structural analysis of complex materials*; Elsevier, 2003; Vol. 16.

[360] Farrow, C. L.; Billinge, S. J. Relationship between the atomic pair distribution function and small-angle scattering: implications for modeling of nanoparticles. *Acta Crystallogr. A.* **2009**, *65*, 232–239.

[361] *International Tables for Crystallography*; International Union of Crystallography, 2006; Vol. C: Mathematical, physical, and chemical tables.

[362] Juhás, P.; Farrow, C. L.; Yang, X.; Knox, K. R.; Billinge, S. J. Complex modeling: a strategy and software program for combining multiple information sources to solve ill posed structure and nanostructure inverse problems. *Acta Crystallogr. A* **2015**, *71*, 562–568.

Appendix A

Analysis of Total Scattering Data

Analysis of X-ray and neutron total scattering data through pair distribution function (PDF) analysis was undertaken to investigate the local coordination environment of materials throughout this work. The PDF provides an experimentally-determined histogram of all atom-atom pair correlations, weighted by the average scattering factors of the two participating atoms. This method enables an examination of the bonding environment within materials independent of long-range crystallographic order, including amorphous, nanocrystalline, glassy, or paracrystalline materials. A full description of pair distribution function methods is illuminated by Egami, *et al.* and Farrow, *et al.*[359,360]

Mathematically, the PDF, $G(r)$, is extracted from X-ray and neutron total scattering data through the sine Fourier transform of the reciprocal space scattering (Equation A.1):

$$G(r) = \frac{2}{\pi}\int_0^\infty Q[S(Q)-1]\sin(Qr)dQ, \tag{A.1}$$

where Q is the reciprocal scattering vector and $S(Q)$ is the total scattering structure function, defined in Equation A.4:

$$S(Q) = \frac{I_c}{N\langle f\rangle^2} - \frac{\langle (f-\langle f\rangle)^2\rangle}{\langle f\rangle^2}. \tag{A.2}$$

In Equation A.4, N is the number of scatterers per formula unit, f is the Q-dependent atomic form factor, and I_c is the experimentally measured coherent scattering intensity, hereafter referred to as $I(Q)$.

Practically, the bounds of the integral presented in Equation A.1 are limited by the Q-range that can be measured experimentally, and thus the integral becomes

$$G(r) = \frac{2}{\pi}\int_{Q_{\min}}^{Q_{\max}} Q[S(Q)-1]\sin(Qr)dQ. \tag{A.3}$$

In chapter 3, the diffraction patterns of the 3 × 3 × 3 supercells of Cs_2SnI_6, $(CH_3NH_3)_2SnI_6$, and $(CH(NH_2)_2)_2SnI_6$ containing randomly tilted octahedra were calculated by taking the inverse sine Fourier transform of the pair distribution function. The pair distribution function, $G(r)$, of the supercells were calculated from $0.01 < r < 100$ Å in increments of 0.01 Å with $Q_{\text{damp}} = 0.034127$ Å^{-1} and $Q_{\text{broad}} = 0.021102$ Å^{-1} in PDFgui. The data were sine Fourier transformed from $0.01 < Q < 7$ Å^{-1} in 0.01 Å^{-1} increments to the total scattering structure function, $S(Q)$, following Equation A.4:

$$S(Q) = 1 + \frac{1}{Q}\int_0^{\infty} G(r)\sin(Qr)dr. \tag{A.4}$$

The diffraction intensities were simulated as $I(Q)$, which is a renormalized function of the structure factor, $S(Q)$ (Equation A.5):

$$I(Q) = N[S(Q)\langle f(Q)\rangle^2 + \langle(f(Q) - \langle f(Q)\rangle)^2\rangle] \tag{A.5}$$

where $f(Q)$ denotes the Q-dependent atomic form factor and the term $\langle(f(Q) - \langle f(Q)\rangle)^2\rangle$ describes Laue monotonic diffuse scattering due to imperfect cancellation of intensity when atomic sites are occupied by atoms of different scattering strength. The atomic form factor for each atomic species was determined using the analytical expression shown in Equation A.6:

$$f_i(Q) = \sum_{i=1}^{4} a_i \exp(-b_i(\frac{Q}{4\pi})^2) + c, \tag{A.6}$$

with coefficients of the summation a_i, b_i, and c taken from the *International Tables for Crystallography*.[361] The sample averaged scattering power, $\langle f(Q)\rangle$ is defined in Equation A.7:

$$\langle f(Q)\rangle = \sum_{\alpha} c_\alpha f(Q)_\alpha. \tag{A.7}$$

In order to compare the calculated $I(Q)$ with the experimental data, the powder X-ray diffraction patterns were truncated below $Q = 0.65$ Å^{-1} to exclude the low-Q intensity due to air scattering, convolved with a Gaussian function with a fwhm of 0.065, 0.056, and 0.060 Å for Cs_2SnI_6, $(CH_3NH_3)_2SnI_6$, and $(CH(NH_2)_2)_2SnI_6$, respectively, and linearly scaled to capture the breadth and intensity of the peaks observed in $I(Q)$, as shown in Figure A.1. Portions of the *ad hoc* Python code used to perform the above analysis are shown below.

```
import matplotlib.pyplot as plt
import numpy as np
from scipy import integrate
from matplotlib import colors

Q = np.arange(0.01,7,0.01)

##Define a function to perform the sine Fourier transform integral
def sineFT_SQ(Q,r,Gr):
    Fq = np.zeros(len(Q))
    for qi in range(len(Q)):
        Fq[qi] = np.trapz(Gr*np.sin(r*Q[qi]),dx=((r[-1]-r[0])/(len(r)-1)))
    Sq = Fq/Q + 1
    return Sq

SQCs = np.array(sineFT_SQ(Q,xCs,GrCs))
SQMA = np.array(sineFT_SQ(Q,xMA,GrMA))
SQFA = np.array(sineFT_SQ(Q,xFA,GrFA))

##Define the atomic form factors as functions
###The form factor takes the form of a summation from i=1-->4 over ai, bi, and c.
def f_H(Q):
    f = a1H * np.exp((-b1H)*(Q/(4*np.pi))**2) + a2H * np.exp((-b2H)*(Q/(4*np.pi))**2) + a3H * np.exp((-b3H
    )*(Q/(4*np.pi))**2) + a4H * np.exp((-b4H)*(Q/(4*np.pi))**2) + cH
    return f

def f_C(Q):
    f = a1C * np.exp((-b1C)*(Q/(4*np.pi))**2) + a2C * np.exp((-b2C)*(Q/(4*np.pi))**2) + a3C * np.exp((-b3C
    )*(Q/(4*np.pi))**2) + a4C * np.exp((-b4C)*(Q/(4*np.pi))**2) + cC
    return f

def f_N(Q):
    f = a1N * np.exp((-b1N)*(Q/(4*np.pi))**2) + a2N * np.exp((-b2N)*(Q/(4*np.pi))**2) + a3N * np.exp((-b3N
    )*(Q/(4*np.pi))**2) + a4N * np.exp((-b4N)*(Q/(4*np.pi))**2) + cN
    return f

def f_Cs(Q):
    f = a1Cs * np.exp((-b1Cs)*(Q/(4*np.pi))**2) + a2Cs * np.exp((-b2Cs)*(Q/(4*np.pi))**2) + a3Cs * np.exp
    ((-b3Cs)*(Q/(4*np.pi))**2) + a4Cs * np.exp((-b4Cs)*(Q/(4*np.pi))**2) + cCs
    return f

def f_Sn(Q):
    f = a1Sn * np.exp((-b1Sn)*(Q/(4*np.pi))**2) + a2Sn * np.exp((-b2Sn)*(Q/(4*np.pi))**2) + a3Sn * np.exp
    ((-b3Sn)*(Q/(4*np.pi))**2) + a4Sn * np.exp((-b4Sn)*(Q/(4*np.pi))**2) + cSn
    return f

def f_I(Q):
    f = a1I * np.exp((-b1I)*(Q/(4*np.pi))**2) + a2I * np.exp((-b2I)*(Q/(4*np.pi))**2) + a3I * np.exp((-b3I
    )*(Q/(4*np.pi))**2) + a4I * np.exp((-b4I)*(Q/(4*np.pi))**2) + cI
    return f
```

```
#Compute the average form factor for each point in Q, <f>
##each atomic form factor is multiplied by the molar fraction of each species
### <f> = summation(cafa) where ca is the fraction of that atomic species Na/N
### and fa is the atomic form factor for atom a

##Average fs (<f>) for Cs2SnI6
def avgCs2SnI6(Q,fCs,fSn,fI):
    favg = np.zeros(len(Q))
    for q in range(len(Q)):
        favg[q] = (1/9)*(2*fCs[q] + 1*fSn[q] + 6*fI[q])
    return favg

##Average fs (<f>) for (CH3NH3)2SnI6
def avgMA2SnI6(Q,fH,fC,fN,fSn,fI):
    favg = np.zeros(len(Q))
    for q in range(len(Q)):
        favg[q] = (1/17)*(6*fH[q] + 2*fC[q] + 2*fN[q] + 1*fSn[q] + 6*fI[q])
    return favg

##Average fs (<f>) for (CH(NH2)2)2SnI6
def avgFA2SnI6(Q,fH,fC,fN,fSn,fI):
    favg = np.zeros(len(Q))
    for q in range(len(Q)):
        favg[q] = (1/23)*(10*fH[q] + 2*fC[q] + 4*fN[q] + 1*fSn[q] + 6*fI[q])
    return favg

#Compute the Laue monotonic diffuse scattering term <(f-<f>)^2 weighted by molar concentration of atomic
    species
## This term is effectively the variance between a given atomic form factor and the average atomic form
    factor. This describes the "imperfect cancellation of intensity at the destructive interference
    condition when atomic sites are occupied by atoms of different scattering strength"

def varfCs2SnI6(Q,fCs,fSn,fI,favgCs2SnI6):
    varf = np.zeros(len(Q))
    for q in range(len(Q)):
        varf[q] = (1/9)*(2*(fCs[q]-favgCs2SnI6[q])**2 + 1*(fSn[q]-favgCs2SnI6[q])**2 + 6*(fI[q]-
    favgCs2SnI6[q])**2)
    return varf

def varfMA2SnI6(Q,fH,fC,fN,fSn,fI,favgMA2SnI6):
    varf = np.zeros(len(Q))
    for q in range(len(Q)):
        varf[q] = (1/17)*(6*(fH[q]-favgMA2SnI6[q])**2 + 2*(fC[q]-favgMA2SnI6[q])**2 + 2*(fN[q]-favgMA2SnI6
    [q])**2 + 1*(fSn[q]-favgMA2SnI6[q])**2 + 6*(fI[q]-favgMA2SnI6[q])**2)
    return varf

def varfFA2SnI6(Q,fH,fC,fN,fSn,fI,favgFA2SnI6):
    varf = np.zeros(len(Q))
    for q in range(len(Q)):
        varf[q] = varf[q] = (1/23)*(10*(fH[q]-favgFA2SnI6[q])**2 + 2*(fC[q]-favgFA2SnI6[q])**2 + 4*(fN[q]-
    favgFA2SnI6[q])**2 + 1*(fSn[q]-favgFA2SnI6[q])**2 + 6*(fI[q]-favgFA2SnI6[q])**2)
    return varf

##Calculate I(Q) for Cs2SnI6
IQCs = 9*(SQCs*(avgCs2SnI6(Q,fCs,fSn,fI))**2 + varfCs2SnI6(Q,fCs,fSn,fI,favgCs2SnI6))

## Convolve PXRD data with a Gaussian
def gaussianCs(r,c):
    dr = float(r[-1]-r[0])/(len(r)-1)
    x = np.arange(-10*c, 10*c, dr)
    return 1.0/(np.sqrt(2*np.pi))*np.exp(-1.0*(x)**2/(2*c**2))

QresCs=0.0275 ##width of Gaussian
ConvScaleCs = 0.38 ##scale factor for Gaussian
IQconvCs = np.convolve(ICs, gaussianCs(QdataCs,QresCs), mode="same")

FWHM_Cs = 2*np.sqrt(2*np.log(2))*QresCs
```

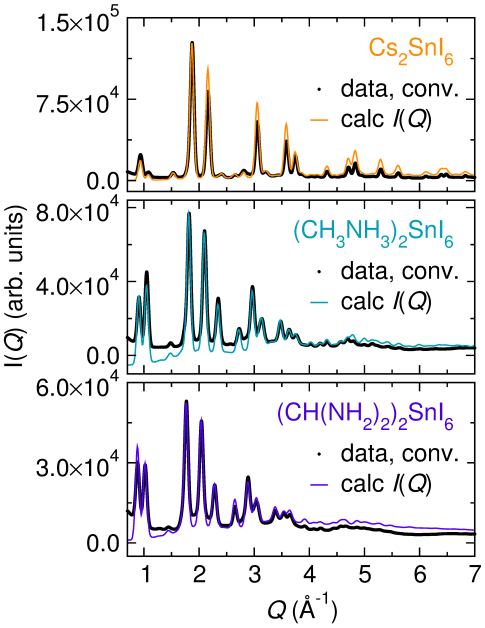

Figure A.1: Comparison of powder X-ray diffraction data convolved with a Gaussian to diffraction patterns ($I(Q)$) calculated from $G(r)$ of the tilted supercells. Black lines are the convolved data, while colored lines represent the calculated $I(Q)$ for each compound in the A_2SnI_6 series.

Appendix B

Rigid-Body Modeling of Anharmonicity in Hybrid Vacancy-Ordered Double Perovskites

In chapter 3, the hybrid vacancy-ordered double perovskites methylammonium tin(IV) iodide ($(CH_3NH_3)_2SnI_6$) and formamidinium tin(IV) iodide ($((CH(NH_2)_2)_2SnI_6$) appear to exhibit anharmonic lattice dynamics. This anharmonicity manifests in the local coordination environment as a significant tailing of the next-nearest neighbor I–I pair correlations at ~4 Å in the X-ray pair distribution function analysis. As shown in Figure B.1, this tailing is enhanced in the hybrid compounds, and cannot be modeled by the cubic structure observed by powder X-ray diffraction.

The tailing observed on the high-r side of the I–I peak is attributed to random rotations of nearly rigid SnI_6 octahedral units, which results in a distribution of inter-octahedral I–I distances. In order to test this hypothesis, supercells of the cubic A_2SnI_6 compounds were constructed, and each SnI_6 octahedron and each A-site cation was rotated about the three Euler angles by angles from 0° to θ_{max}, where θ_{max} is defined as the maximum allowed rotation angle that provides the best goodness-of-fit to the experimental XPDF. This analysis was accomplished through *ad hoc* Python code utilizing the Diffpy-CMI libraries, portions of which are included below.[362]

```
import numpy as np
from mpl_toolkits.mplot3d import axes3d
import matplotlib.pyplot as plt
from matplotlib.pyplot import cm
import numpy as np
import pandas as pd
import math
from functools import reduce
from random import uniform,randint

from scipy.optimize import curve_fit,least_squares,differential_evolution
from scipy.optimize.minpack import leastsq,least_squares

from mpl_toolkits.mplot3d import Axes3D
```

```
# Load modules from diffpy.cmi
from diffpy.Structure import loadStructure,Atom,Structure,Lattice
from diffpy.srfit.pdf import PDFContribution
from diffpy.srfit.fitbase import FitRecipe, FitResults
from diffpy.srreal.pdfcalculator import PDFCalculator


# Define functions: the rotation matrix, rotator, and periodic boundary conditions
def euler2mat(z=0, y=0, x=0):
    # take from https://afni.nimh.nih.gov/pub/dist/src/pkundu/meica.libs/nibabel/eulerangles.py
    # also looks useful: https://www.learnopencv.com/rotation-matrix-to-euler-angles/
    ''' Return matrix for rotations around z, y and x axes
    Uses the z, then y, then x convention above
    Parameters
    ----------
    z : scalar
       Rotation angle in radians around z-axis (performed first)
    y : scalar
       Rotation angle in radians around y-axis
    x : scalar
       Rotation angle in radians around x-axis (performed last)
    Returns
    -------
    M : array shape (3,3)
       Rotation matrix giving same rotation as for given angles
    When applying M to a vector, the vector should column vector to the
    right of M.  If the right hand side is a 2D array rather than a
    vector, then each column of the 2D array represents a vector.
    >>> vec = np.array([1, 0, 0]).reshape((3,1))
    >>> v2 = np.dot(M, vec)
    >>> vecs = np.array([[1, 0, 0],[0, 1, 0]]).T # giving 3x2 array
    >>> vecs2 = np.dot(M, vecs)
    Rotations are counter-clockwise.
    Notes
    -----
    The direction of rotation is given by the right-hand rule (orient
    the thumb of the right hand along the axis around which the rotation
    occurs, with the end of the thumb at the positive end of the axis;
    curl your fingers; the direction your fingers curl is the direction
    of rotation).  Therefore, the rotations are counterclockwise if
    looking along the axis of rotation from positive to negative.
    '''
    Ms = []
    if z:
        cosz = math.cos(z)
        sinz = math.sin(z)
        Ms.append(np.array(
                [[cosz, -sinz, 0],
                 [sinz, cosz, 0],
                 [0, 0, 1]]))
    if y:
        cosy = math.cos(y)
        siny = math.sin(y)
        Ms.append(np.array(
                [[cosy, 0, siny],
                 [0, 1, 0],
                 [-siny, 0, cosy]]))
    if x:
        cosx = math.cos(x)
        sinx = math.sin(x)
        Ms.append(np.array(
                [[1, 0, 0],
                 [0, cosx, -sinx],
                 [0, sinx, cosx]]))
    if Ms:
        return reduce(np.dot, Ms[::-1])
    return np.eye(3)
```

```
68
70 def XpRgen(X, a=uniform(0, 2*np.pi),b=uniform(0, 2*np.pi),c=uniform(0, 2*np.pi)):
72     # rotate a single molecule by a, b, and c angles.
74     # the default angles are:
       # uniform(0, 2*np.pi), which provides a random number between 0 and 2pi
       M = euler2mat(a,b,c)
       return np.dot(M, X.T).T
76
78 def matrixrotate(ph,th,ps):
       #https://en.wikipedia.org/wiki/Rotation_formalisms_in_three_dimensions
       costh = np.cos(th)
80     sinth = np.sin(th)
       cosph = np.cos(ph)
82     sinph = np.sin(ph)
       cosps = np.cos(ps)
84     sinps = np.sin(ps)
       M = np.array([[costh*cosps, cosph*sinps + sinph*sinth*cosps, sinph*sinps-cosph*sinth*cosps],
86                   [-1.0*costh*sinps, cosph*cosps - sinph*sinth*sinps, sinph*cosps + cosph*sinth*sinps],
                     [sinth, -1.0*sinph*costh,cosph*costh]
88                   ])
       return M
90
92 def rotateX(x,ph,th,ps):
       y=np.zeros(np.shape(x))
       for i in range(0,len(x)):
94         y[i] = np.matmul(matrixrotate(ph,th,ps),x[i])
       return y
96
98 def pbc_cfg(x):
       ## In the cfg formatted file, the positions run in fractional coordinates
100    ## from -1.0 to 1.0.
       ## Anything great than 1.0 or less than -1.0 should be corrected.
102    for i in range(len(x)):
           for j in range(3):
104            if x[i,j] < -1.0:
                   x[i,j] = x[i,j] + 1.0
106            elif x[i,j] > 1.0:
                   x[i,j] = x[i,j] - 1.0
108    return x

110 def pbc_cfg2(x):
       ## In the normal fractional coordinates, the coordinates shoul dfrom from 0 to 1.0
112    ## Anything greater than 1.0 or less than 0.0 should be corrected.
       for i in range(len(x)):
114        for j in range(3):
               if x[i,j] < 0.0:
116                x[i,j] = x[i,j] + 1.0
               elif x[i,j] > 1.0:
118                x[i,j] = x[i,j] - 1.0
       return x
120

122 def read_gr(filename,junk=28):
       with open(filename,'r') as file_in:
124        datain = file_in.readlines()
       datain = datain[junk:]
126    rvals = np.zeros(len(datain))
       ivals = np.zeros(len(datain))
128    for i in range(len(datain)):
           rvals[i] = (float(datain[i].split()[0]))
130        ivals[i] = (float(datain[i].split()[1]))
       return rvals, ivals
132
# Load in data and set up the PDF contribution
134
dataFile = "MA2SnI6-90kev.gr"
```

```
136
data_r_all , data_gr_all = read_gr(dataFile, junk=138)
138
## Plot data to make sure it loaded properly
140 plt.figure()
plt.plot(data_r_all,data_gr_all,'k-')
142
# Define a function that randomly tilts the octahedra and the CH3NH3+ orientations in the unit cell
144
def MA2SnI6_randAngle(ang,UisoI):
146     nxnxn = [3,3,3]   ## number unit cells per supercell along x, y, and z
        cellEdge = np.array([12.01615,12.01615,12.01615])  # unit cell edge lengths
148     supercellEdge = nxnxn*cellEdge
        unitcells = nxnxn[0]*nxnxn[1]*nxnxn[2]
150
152     ## Define an array of fractional coordinates for the methylammonium ion
        C1 = np.array([0.290680,0.290680,0.290680])
154     N1 = np.array([0.218910,0.218910,0.218910])

156     H1 = np.array([0.238850,0.343390,0.343390])
        H2 = np.array([0.343390,0.343390,0.238850])
158     H3 = np.array([0.343390,0.238850,0.343390])
        H4 = np.array([0.167190,0.264380,0.167190])
160     H5 = np.array([0.167190,0.167190,0.264380])
        H6 = np.array([0.264380,0.167190,0.167190])
162
        ## Put all of the atom positions into one array of arrays
164     Xo = np.zeros([8,3])
        Xo[0] = C1
166     Xo[1] = N1
        Xo[2] = H1
168     Xo[3] = H2
        Xo[4] = H3
170     Xo[5] = H4
        Xo[6] = H5
172     Xo[7] = H6

174     to = np.array([0.25,0.25,0.25])
        ## Shift the atom positions to the origin.
176     Xpo = Xo - to

178     ## define indices of atom positions:
        Cs = [0,8,16,24,32,40,48,56]
180     Ns = [1,9,17,25,33,41,49,57]
        Hs = list(range(0,64))  # start with all
182     Hs = [x for x in Hs if x not in Cs]  # remove the C
        Hs = [x for x in Hs if x not in Ns]  # remove the N
184
        ## This is the SnI6 octahedra part
186     Sn1 = np.array([0.,0.,0.])
        I1 = np.array([0.2379,0.00000,0.00000])
188     I2 = np.array([-0.2379,0.00000,0.00000])
        I3 = np.array([0.00000,0.2379,0.00000])
190     I4 = np.array([0.00000,-0.2379,0.00000])
        I5 = np.array([0.00000,0.00000,0.2379])
192     I6 = np.array([0.00000,0.00000,-0.2379])

194     ## Put all of the atom positions into one array of arrays
        Xi = np.zeros([7,3])
196     Xi[0] = Sn1
        Xi[1] = I1
198     Xi[2] = I2
        Xi[3] = I3
200     Xi[4] = I4
        Xi[5] = I5
202     Xi[6] = I6
```

```
    ## Shift the atom positions to the origin.
    ti = np.array([0.0,0.0,0.0])
    Xpi = Xi - ti

    ## define indices of atom positions:
    Sns = [0]
    Is = [1,2,3,4,5,6]

    no = 8   ## number of atoms per organic molecule
    ni = 7   ## number of atoms per inorganic molecule

    ## these lists will be specific to the spacegroup symmetry (Fm-3m)
    Cs = [0,no,2*no,3*no,4*no,5*no,6*no,7*no]
    Ns = [1,no+1,2*no+1,3*no+1,4*no+1,5*no+1,6*no+1,7*no+1]
    Hs = list(range(0,8*no))  # start with all
    Hs = [x for x in Hs if x not in Cs]  # remove the C
    Hs = [x for x in Hs if x not in Ns]  # remove the N


    ## these lists will be specific to the spacegroup symmetry (Fm-3m)
    Sns = [0,ni,2*ni,3*ni]
    Is = list(range(0,4*ni))
    Is = [x for x in Is if x not in Sns]  # remove the C

    CsXscAng = np.zeros([unitcells*len(Cs),3])
    NsXscAng = np.zeros([unitcells*len(Ns),3])
    HsXscAng = np.zeros([unitcells*len(Hs),3])
    countC=0 ; countN=0 ; countH=0

    SnsXscAng = np.zeros([unitcells*len(Sns),3])
    IsXscAng = np.zeros([unitcells*len(Is),3])
    countSn=0 ; countI=0

    ## Apply the rotation for the methylammonium ions,
    ## then shift to their respective positions in the unit cell
    for i in range(0,nxnxn[0]):
        for j in range(0,nxnxn[1]):
            for k in range(0,nxnxn[2]):
                ## Operate on organic now:
                XpRFo = np.zeros([8*no,3])
                XpRFo[0:no,:]       = XpRgen(Xpo,uniform(0, 2*np.pi),uniform(0, 2*np.pi),uniform(0, 2*np.pi
    )) + np.array([0.25, 0.25,0.25])
                XpRFo[no:2*no,:]    = XpRgen(Xpo,uniform(0, 2*np.pi),uniform(0, 2*np.pi),uniform(0, 2*np.pi
    )) + np.array([0.75, 0.25,0.25])
                XpRFo[2*no:3*no,:] = XpRgen(Xpo,uniform(0, 2*np.pi),uniform(0, 2*np.pi),uniform(0, 2*np.pi
    )) + np.array([0.25, 0.75,0.25])
                XpRFo[3*no:4*no,:] = XpRgen(Xpo,uniform(0, 2*np.pi),uniform(0, 2*np.pi),uniform(0, 2*np.pi
    )) + np.array([0.25, 0.25,0.75])
                XpRFo[4*no:5*no,:] = XpRgen(Xpo,uniform(0, 2*np.pi),uniform(0, 2*np.pi),uniform(0, 2*np.pi
    )) + np.array([0.75, 0.75,0.25])
                XpRFo[5*no:6*no,:] = XpRgen(Xpo,uniform(0, 2*np.pi),uniform(0, 2*np.pi),uniform(0, 2*np.pi
    )) + np.array([0.25, 0.75,0.75])
                XpRFo[6*no:7*no,:] = XpRgen(Xpo,uniform(0, 2*np.pi),uniform(0, 2*np.pi),uniform(0, 2*np.pi
    )) + np.array([0.75, 0.25,0.75])
                XpRFo[7*no:8*no,:] = XpRgen(Xpo,uniform(0, 2*np.pi),uniform(0, 2*np.pi),uniform(0, 2*np.pi
    )) + np.array([0.75, 0.75,0.75])

                ## convert into angstroms and shift to corresponding location in supercell:
                XpRFscoAng = (XpRFo * cellEdge) +  cellEdge*[i,j,k]

                ## break into atomic identities:
                CsXscAng[countC:(countC+len(Cs))] = XpRFscoAng[Cs]
                NsXscAng[countN:(countN+len(Ns))] = XpRFscoAng[Ns]
                HsXscAng[countH:(countH+len(Hs))] = XpRFscoAng[Hs]
                countC=countC+len(Cs)
                countN=countN+len(Ns)
                countH=countH+len(Hs)
```

```
                ## Operate on inorganic now:
                XpRFi = np.zeros([4*ni,3])
                XpRFi[0:ni,:]      = rotateX(Xpi,uniform(-1,1)*np.pi*ang/180,uniform(-1,1)*np.pi*ang/180,
    uniform(-1,1)*np.pi*ang/180) + np.array([0.0, 0.0,0.0])
                XpRFi[ni:2*ni,:]   = rotateX(Xpi,uniform(-1,1)*np.pi*ang/180,uniform(-1,1)*np.pi*ang/180,
    uniform(-1,1)*np.pi*ang/180) + np.array([0.0, 0.5,0.5])
                XpRFi[2*ni:3*ni,:] = rotateX(Xpi,uniform(-1,1)*np.pi*ang/180,uniform(-1,1)*np.pi*ang/180,
    uniform(-1,1)*np.pi*ang/180) + np.array([0.5, 0.0,0.5])
                XpRFi[3*ni:4*ni,:] = rotateX(Xpi,uniform(-1,1)*np.pi*ang/180,uniform(-1,1)*np.pi*ang/180,
    uniform(-1,1)*np.pi*ang/180) + np.array([0.5, 0.5,0.0])

                ## convert into angstroms and shift to corresponding location in supercell:
                XpRFiscAng = (XpRFi * cellEdge) +  cellEdge*[i,j,k]

                ## break into atomic identities:
                SnsXscAng[countSn:(countSn+len(Sns))] = XpRFiscAng[Sns]
                IsXscAng[countI:(countI+len(Is))] = XpRFiscAng[Is]
                countSn=countSn+len(Sns)
                countI=countI+len(Is)

    CsXsc = (CsXscAng/supercellEdge)
    NsXsc = (NsXscAng/supercellEdge)
    HsXsc = (HsXscAng/supercellEdge)
    SnsXsc = SnsXscAng/supercellEdge
    IsXsc = IsXscAng/supercellEdge

    ## This is specific to PDFgui/xyz/Cartesian:
    CsXsc = (pbc_cfg2(CsXsc))
    NsXsc = (pbc_cfg2(NsXsc))
    HsXsc = (pbc_cfg2(HsXsc))
    SnsXsc = (pbc_cfg2(SnsXsc))
    IsXsc = (pbc_cfg2(IsXsc))

    organicout = np.vstack(((np.vstack((CsXsc,NsXsc))),HsXsc))
    SnIout = np.vstack((SnsXsc,IsXsc))
    xyzout = np.vstack((SnIout,organicout))

    lattice=Lattice(12.01615*nxnxn[0],12.01615*nxnxn[1],12.01615*nxnxn[2],90,90,90)
    atomlist = ['Sn'] * len(SnsXsc) + ['I'] * len(IsXsc)+ ['C'] * len(CsXsc) + ['N'] * len(NsXsc) + ['H']
     * len(HsXsc)

    Uisos = [0.005]* len(SnsXsc) + [UisoI] * len(IsXsc)+ [0.005] * (len(CsXsc)+len(NsXsc)+len(HsXsc))
    atomitem = [None]*len(atomlist)
    for ii in range(0,len(atomlist)):
        atomitem[ii]=Atom(atomlist[ii],xyz=(xyzout[ii,0],xyzout[ii,1],xyzout[ii,2]),Uisoequiv=Uisos[ii])

    stru = Structure(atoms=atomitem,lattice=lattice,title='test')
    stru.anisotropy = False
    return stru

# Calculate the PDF using diffpy-cmi and the configurations defined in the cfg dictionary
def y(x,*params):
    scale=params[0]
    ang=params[1]
    iso=params[2]
    delta1=params[3]
    cfg = {'qmax': 30.0, 'rmin': 1.0, 'rmax': 5.5, 'delta1': delta1}
    grc = PDFCalculator(**cfg)
    MA2SnI6stru=MA2SnI6_randAngle(ang,iso)
    r, gr = grc(MA2SnI6stru)
    return gr*scale

## This is a residual function calculator
def Rp(yobs,ycalc):
    return (((yobs-ycalc)**2)/abs(yobs)).sum()

# Calculate goodness of fit as a function of maximum rotation angle
rmin = 100
```

```
rmax = 550

data_r=data_r_all[rmin:rmax]
data_gr=data_gr_all[rmin:rmax]

angles = np.linspace(0,25,50)

Rp_angles=np.zeros(len(angles))

for i in range(len(angles)):
    Rp_angles[i] = Rp(data_gr,y(data_r,*[1.1,angles[i],0.015,1.8]))
    print(i,angles[i])

# Now, find the maximum allowed rotation angle that provides the best goodness-of-fit

min_Rp = min(Rp_angles) # Find the maximum y value
x_angle = angles[Rp_angles.argmin()] # Find the x value corresponding to the minimum y value

plt.figure()
plt.plot(angles,Rp_angles,'bo')
plt.plot(x_angle,min_Rp,'kx')

## Fit RPs vs Angles to a fct. Find fct minimum.

anglefit = np.polyfit(angles,Rp_angles,6)
p = np.poly1d(anglefit)
plt.plot(angles,p(angles),'r-')

crit = p.deriv().r
p_crit = crit[crit.imag==0].real
test = p.deriv(2)(p_crit)

# compute local minima
# excluding range boundaries
angle_best = p_crit[test>0]
y_min = p(angle_best)
plt.plot( angle_best, y_min, 'k+' )

plt.ylabel('goodness of fit')
plt.xlabel('angle')
plt.xlim([-1,26])
plt.ylim([0,800])

## Print the best goodness-of-fit from
## minimum in fitting function and
## minimum goodness-of-fit value

print("Best angle from fct: %8.2f" % (angle_best))
print("Best angle from values: %8.2f" % (x_angle))

# Write out a structure that has this initially found 'best' angle:

maStructInit = MA2SnI6_randAngle(float(angle_best),0.015) ## This makes the structure using the best angle
    from the fct
maStructInit = MA2SnI6_randAngle(float(x_angle),0.015) ## This makes the structure using the lowest Rp
    from the fit to the XPDF
initfile ='MA2SnI6_3x3x3.cif'
Structure.write(maStructInit,initfile,'cif')
print("Done")
```

The 3 × 3 × 3 supercells generated from the above code are shown in Figure B.2, and fits to the XPDF are shown in Figure B.3.

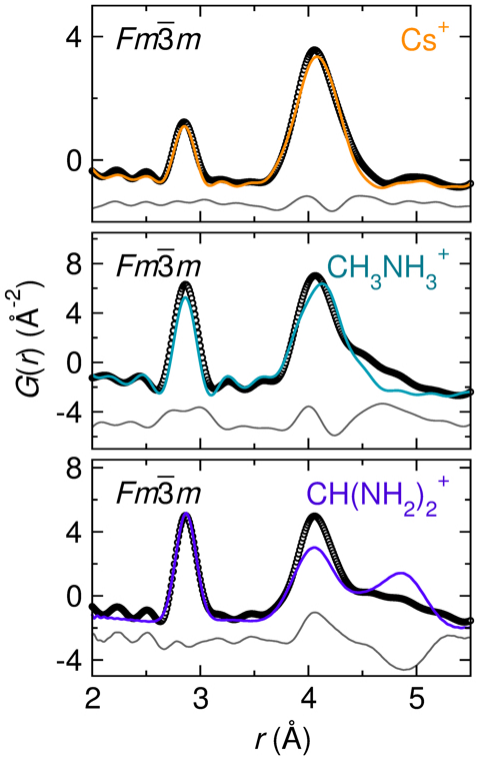

Figure B.1: X-ray pair distribution functions of Cs_2SnI_6, $(CH_3NH_3)_2SnI_6$, and $(CH(NH_2)_2)_2SnI_6$. The XPDFs are modeled with the cubic vacancy-ordered double perovskite structure observed in the powder X-ray diffraction data. While the Sn–I peak at ~2.9 Å is well described, significant tailing of the next-nearest-neighbor I–I pair correlation at ~4 Å is observed in the hybrid compounds and cannot be modeled by the cubic structural models.

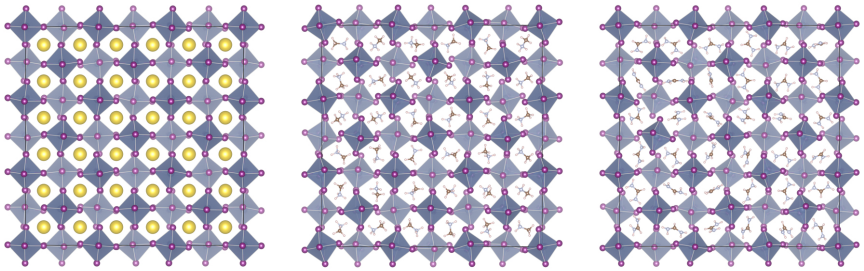

Figure B.2: Supercells for a) Cs_2SnI_6, b) $(CH_3NH_3)_2SnI_6$, and c) $(CH(NH_2)_2)_2SnI_6$ with the corresponding θ_{max} determined by the pseudo-rigid-body modeling routine.

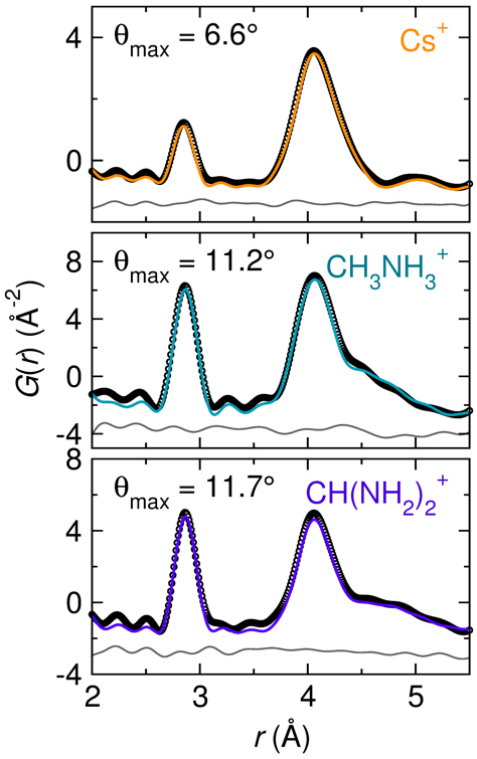

Figure B.3: X-ray pair distribution functions of Cs_2SnI_6, $(CH_3NH_3)_2SnI_6$, and $(CH(NH_2)_2)_2SnI_6$. The XPDFs are modeled with the tilted supercells of the vacancy-ordered double perovskite structures shown in Figure B.2.